



UNIVERSITÀ DI PISA
DOTTORATO DI RICERCA IN INGEGNERIA DELL'INFORMAZIONE

THE ROLE OF INTERACTION FORCES IN ROBOTIC
MANIPULATION FOR LOGISTICS: A SPECIAL FOCUS ON
DEPALLETIZING AND OBJECT DELIVERY.

DOCTORAL THESIS

Author
Chiara Gabellieri

Tutor (s)

**Prof. Lucia Pallottino, Prof. Antonio Bicchi,
Prof. Sergio Saponara, and Dr. Danilo Caporale**

Reviewer (s)

Prof. Anibal Ollero and Dr. Paolo Robuffo Giordano

The Coordinator of the PhD Program

Prof. Fulvio Gini

Pisa, April 2021

XXXIII

This Thesis is dedicated to Gemma and to my parents.

*"It is not the most intellectual of the species that survives;
it is not the strongest that survives;
but the species that survives is the one that is able best to adapt and adjust
to the changing environment in which it finds itself"*

Prof. Leon C. Megginson paraphrasing Charles Darwin,
"Lessons from Europe for American Business",
Southwestern Social Science Quarterly (1963) 44(1): 3-13, at p. 4

Acknowledgements

THIS Thesis is the result of a long journey, during which many people have guided and sustained me. First, I am deeply grateful to my supervisors, Prof. Antonio Bicchi, Prof. Lucia Pallottino, Prof. Sergio Saponara, and Dr. Danilo Caporale for their guidance. I am truly thankful to Prof. Anibal Ollero and Dr. Paolo Robuffo Giordano that have wisely revised this Thesis and to Prof. Fulvio Gini and Prof. Marco Luise, current and former coordinators of the Ph.D. program. I thank all the senior researchers of the Research Center “E. Piaggio”. Especially, appreciation is due to Manolo for his great contribution to the work contained in this Thesis. I am indebted to all the people that collaborated with me during the past years. My sincere thanks go to Prof. Antonio Franchi, who has introduced me to research and welcomed me to Laas-CNRS. I thank Marco Tognon for our fruitful collaboration. I am grateful to Prof. Min Jun Kim, Yuri, Andre, and all members of that research team who welcomed me to the German Aerospace Center (DLR).

I am very grateful to all my colleagues and friends from the Center "E. Piaggio", especially to Alessandro, Federico, Franco, and Simone. I feel lucky for the time spent with them inside and outside the lab. I particularly thank Gemma, who has been with me since the very beginning. She has been a push to do always better, a model, and a true friend. Heartfelt thanks to my boyfriend and colleague, Riccardo. I feel his support always on my side, in my profession and in my life. His determination and hard work are a source of constant inspiration.

I thank all my family for the love they have shown me all along. I thank my mom and dad, who are always so proud of me. Thanks to Anna, to my aunt Gianna and my uncle Ferdinando, and to my strong cousin Elisa for believing in me. I thank my beloved grandmother Norma. From my heart, I thank, with her, all my grandparents: Filomena, Adelmo, and Franco, whose wisdom will come along with me whenever I go. Thanks to my true friend Mariachiara and to Sandra, who has been accompanying me for a very long time, and Claudio, whom I have always admired. I am grateful to all my past teachers for what they have thought me and, most of all, for the confidence and curiosity they instilled in me, which I hope to be able to turn on again.

Ringraziamenti

LA presente Tesi è il risultato di un percorso in cui molte persone mi hanno guidata e sostenuta. Prima di tutto, ci tengo a mostrare gratitudine ai miei supervisori, Prof. Antonio Bicchi, Prof.ssa Lucia Pallottino, Prof. Sergio Saponara, e Dr. Danilo Caporale per la loro guida preziosa. Sono sinceramente grata al Prof. Anibal Ollero e al Dr. Paolo Robuffo Giordano che, con la loro esperienza, hanno revisionato questa Tesi, e al Prof. Fulvio Gini e Prof. Marco Luise, coordinatori del corso di studio in questi anni. Ringrazio tutti i ricercatori senior del Centro di Ricerca "E. Piaggio"; in particolare Manolo per il suo grande contributo ai lavori contenuti nella Tesi. Ringrazio tutte le persone che in questi anni hanno collaborato con me. Sono grata al Prof. Antonio Franchi, che mi ha introdotta alla ricerca e mi ha ospitata al Laas-CNRS. Grazie al Dr. Marco Tognon per la nostra fruttuosa collaborazione durante il mio dottorato. Ringrazio il Prof. Min Jun Kim, Yuri, Andre, e gli altri membri di quel gruppo di ricerca che mi hanno ospitata al German Aerospace Center (DLR).

Sono molto grata ai miei colleghi e amici del Centro Piaggio. Ringrazio Alessandro, Federico, Franco, e Simone: sono fortunata per il tempo speso insieme a loro dentro e fuori dal laboratorio. Ci tengo poi a ringraziare in particolar modo Gemma, che è stata con in ogni scelta professionale fino qui. Lei è per me una spinta costante a migliorarmi e a puntare più in alto, un punto di riferimento, e una vera amica. Dal cuore, ringrazio il mio ragazzo e collega, Riccardo. Sento il suo solido supporto al mio fianco, nella mia professione e nella mia vita. La sua determinazione e il suo impegno sono un'inesauribile fonte d'ispirazione.

Grazie alla mia famiglia per l'amore che mi ha mostrato e mi mostra. Ringrazio mamma e papà, che sono sempre così fieri di me. Grazie ad Anna, agli zii Gianna e Ferdinando e a mia cugina Elisa, che tifano sempre per me. Ringrazio la mia amata nonna Norma. Profondamente, con lei ringrazio tutti i miei nonni, Filomena, Adelmo e Franco; la loro saggezza mi accompagnerà ovunque andrò. Grazie alla mia cara amica Mariachiara, a Sandra, che mi accompagna da tantissimo tempo, e Claudio, che ho sempre ammirato. Sono grata a tutti i miei insegnanti passati per ciò che mi hanno trasmesso ma soprattutto per l'autostima e la curiosità che hanno ispirato in me e che spero di saper riaccendere sempre.

Summary

THAT the passive compliance embedded in their mechanical design and the active compliance conferred by their control laws have been allowing industrial robots out of the cages in which they were traditionally constrained is acknowledged. What the robots can do once out of their cages is an unfolding story that inspires this Thesis.

Robotics is trying to respond to new industrial needs, such as high flexibility required in warehouses, due especially to e-commerce, the necessity of lifting human workers from the harsh working conditions that new efficiency standards impose, and reducing the environmental impact of our activities. To do so, robots need to move in uncertain and changing environments, sometimes shared with humans, and in general not suitable for the old paradigms of high-velocity and high-precision predefined movements. Physical contacts with the environment are not to be confined at all costs anymore, but they become a useful means for adapting to an uncertain environment, thus enhancing the robot capabilities.

The focus of this Thesis is the study of the interaction forces between the robot and its surroundings, exploiting the role played by those forces in enabling novel logistic applications. The topics range from depalletizing and object picking to object delivery.

First, this Thesis presents a strategy for autonomous pallet unwrapping, namely the removal of the plastic film enclosing the parcels stacked on pallets. This is a key procedure of the intralogistic flow, the automation of which has not yet received much attention. Currently, unwrapping is performed mainly by human operators, due also to the complexity of its planning and control phases. The unwrapping robot considered in this Thesis is composed of a robotic manipulator equipped with a custom cutting end-effector. A planning method aimed to ensure a successful task execution even when the film profile is uncertain and irregularly shaped is presented. The proposed planning strategy leverages information regarding the robot collisions with the environment. Experimental results are presented to test the method.

After unwrapping the pallets, the underlying items become accessible for manipulation. This Thesis also studies a planner that enables a novel depalletizing strategy for the depalletizer robot WRAPP-up. The envisioned planner, exploiting contact force in-

formation, allows the dual-arm depalletizer to handle a large variety of goods even with non-perfectly known positions. Results of experiments conducted on different items provided by a food-delivery company are reported.

Besides bi-manual depalletizing, grasping smaller objects with a single end-effector is a relevant task also in logistics and one that WRAPP-up can accomplish, too. The problem of grasping a single object with an ad-hoc end-effector has been extensively studied in the literature both from theoretical and experimental viewpoints but it still represents an open problem, especially when no prior model of the objects is provided. This Thesis presents a method for object picking, particularly suited for soft hands, that can be used to grasp previously unseen objects. The major contribution is a data-driven planner that generates suitable grasps by relying on a *reduced* database of grasps performed by a skilled operator using the robotic hand. The basic idea is to exploit a skilled human performing experiments using the robotic hand to grasp only a set of *basic shapes* instead of general objects, dramatically reducing the number of trials. The approach is then generalized to grasp unknown objects by relying on state-of-the-art decomposition algorithms that allow approximating an object with such basic shapes. The method has been tested with the PISA/IIT SoftHand mounted on a Panda robot and has shown a success percentage of 86.7% over 105 grasps on 21 previously unseen objects.

Physical interaction capabilities can be entrusted also to aerial robots, enabling aerial object manipulation. This may have rather interesting applications in logistics, especially for last-mile delivery in the freight sector, allowing for a schedule not affected by the unpredictable traffic jam, as in the case of road transportation. Cooperative approaches to aerial object manipulation have been widely studied in the literature since they may increase manipulation capabilities and would allow overcoming payload limitations. However, communication among the robots, required for their coordination, typically increases the system complexity and represents a possible source of low performance and stability issues due to data loss, corruption, and delays.

This Thesis presents a method for the cooperative manipulation of cable-suspended objects not requiring any explicit communication among the robots. Instead, the coordination is enabled by an implicit form of communication that relies on contact-force sensing. The method exploits a leader-follower scheme on admittance-controlled multi-rotors.

First, two robots and a beam load are considered. The stability and passivity of the controlled system are discussed, as well as the effects of parametric uncertainties. The specific role of the internal force induced on the object by the robots through the cables is highlighted. An extension of the method to more than two robots is presented. Eventually, the theoretical analysis is validated through numerical simulations, and the results of preliminary experiments on two robots are presented as well.

Sommario

CHE la cedevolezza passiva, conferita dal design meccanico, e la cedevolezza attiva, ottenuta attraverso il controllo, stiano consentendo ai robot industriali di uscire dalle gabbie in cui erano tradizionalmente confinati è riconosciuto. Quali compiti i robot possano svolgere una volta liberati da quelle gabbie è una storia che si sta tuttora svolgendo ed è d'ispirazione per questa tesi. La robotica sta cercando di rispondere ai bisogni di un nuovo panorama industriale, come la necessità di una grande flessibilità negli odierni magazzini, soprattutto quelli legati all'e-commerce, la volontà di migliorare le dure condizioni di lavoro che talvolta gli alti standard di efficienza impongono ai lavoratori dell'ambito logistico, e quella di ridurre l'impatto ambientale delle nostre attività. Per raggiungere questi obiettivi, i robot devono agire in ambienti che cambiano e sono conosciuti in modo incerto, talvolta condividendoli con gli umani. Per questo, il tradizionale paradigma della robotica che prevedeva l'esecuzione di movimenti predefiniti, ad alta velocità e precisione, non è più applicabile. Ora il contatto fisico del robot con l'ambiente non è più da evitare, ma può essere anzi sfruttato per acquisire informazioni utili ad adattarsi ad un ambiente incerto, e quindi per aumentare le capacità del robot.

L'obiettivo di questa tesi è proprio lo studio del ruolo che le forze di interazione fisica con l'ambiente possono avere per consentire nuove applicazioni robotiche in logistica. Gli argomenti studiati spaziano dalla depallettizzazione e la presa di oggetti al loro trasporto.

In primo luogo, la tesi presenta una strategia per la rimozione automatica della plastica che avvolge gli oggetti sui pallet. Benché questa rappresenti una fase cruciale del flusso intralogistico, la sua automazione non ha ad oggi ricevuto grande attenzione. Infatti, la rimozione della plastica dai pallet viene svolta per lo più a mano dagli operatori addetti, anche a causa della complessità che caratterizza la pianificazione e il controllo del taglio. Per svolgere questa delicata operazione, nella tesi viene considerato un robot composto da un manipolatore Panda, prodotto dall'azienda FRANKA-EMIKA, equipaggiato con un organo terminale di taglio disegnato ad-hoc. La tesi presenta una strategia di pianificazione in grado di eseguire con successo l'operazione di taglio del film plastico anche nel caso in cui il suo profilo non sia noto con esattezza. Il metodo

sfrutta l'informazione derivante dal rilevamento e dall'interpretazione delle collisioni con l'ambiente. La sua efficacia è stata dimostrata attraverso test sperimentali.

Dopo aver rimosso la plastica dagli oggetti, questi diventano accessibili per la depallettizzazione. Questa tesi continua quindi concentrandosi su una pianificazione che consenta l'esecuzione di strategie di presa al robot depallettizzatore bi-manuale WRAPP-up. Detta strategia, sfruttando le informazioni derivanti dalle forze di contatto tra il robot e gli oggetti, permette a WRAPP-up di maneggiare oggetti molto diversi per forma, peso, e dimensioni, contentendo quindi una grande versatilità, anche nel caso in cui la conoscenza della posizione degli oggetti sul pallet sia affetta da incertezza. I risultati di esperimenti effettuati con oggetti forniti da una compagnia di distribuzione di generi alimentari sono riportati nella tesi.

Oltre alla depallettizzazione bimanuale già menzionata, anche la presa di oggetti più piccoli con un unico manipolatore è di interesse nella logistica e rappresenta un'altra operazione che WRAPP-up può eseguire. Pur essendo un argomento largamente studiato in letteratura sia da un punto di vista teorico che sperimentale, la presa robotica di oggetti non noti a priori è ancora un problema aperto per la ricerca. Per queste ragioni, la tesi studia la presa robotica di oggetti di cui non è noto alcun modello a priori, elaborando un metodo particolarmente adatto ad essere applicato a mani robotiche *soft*. Il maggior contributo della tesi in questo senso è un algoritmo di pianificazione della presa di tipo *data-driven*, basato però su un database di prese di esempio molto ridotto, generato da un operatore umano esperto nell'uso manuale della mano robotica. L'idea di fondo è quella di far afferrare all'operatore, usando la stessa mano del robot, non una grande serie di oggetti rappresentativi, bensì delle forme base, in questo caso scatole a facce rettangolari. Il metodo è poi generalizzato ad oggetti qualunque grazie alla decomposizione della loro *point-cloud* in scatole, effettuata basandosi su algoritmi dello stato dell'arte. L'approccio è stato testato usando la PISA/IIT SoftHand montata su un manipolatore Panda ed ha mostrato una percentuale di successo dell'87.6% su un totale di 105 prese effettuate su 21 oggetti diversi.

La capacità di interagire fisicamente con l'ambiente circostante può essere conferita anche ai robot aerei, consentendo così la manipolazione robotica aerea. Questo può avere conseguenze interessanti nella logistica, soprattutto nel settore delle spedizioni, al quale prometterebbe consegne che non siano influenzate negativamente ed imprevedibilmente dal traffico su strada. Un approccio *cooperativo* al trasporto aereo di oggetti ha attirato l'interesse dei ricercatori per la possibilità di superare la limitata capacità di carico dei singoli droni. Tuttavia, la comunicazione tra i robot necessaria al loro coordinamento aumenta tipicamente la complessità del sistema complessivo, oltre a rappresentare una possibile fonte di instabilità e di riduzione delle performance a causa di ritardi nella trasmissione dei pacchetti di dati, o della possibile corruzione dei dati stessi.

Questa tesi si concentra sul trasporto robotico aereo cooperativo di oggetti sospesi con cavi che non necessita di comunicazione esplicita tra i robot stessi. Invece, la coordinazione è ottenuta attraverso una modalità di comunicazione implicita, che sfrutta la misura delle forze di interazione tra i robot e l'oggetto trasportato. L'approccio è basato su un'architettura *leader-follower*. Inizialmente, vengono considerati due robot ed un oggetto snello. La stabilità e la passività del sistema vengono discusse nella tesi, così come gli effetti di eventuali incertezze che caratterizzino la conoscenza dei parametri

del sistema stesso. Lo studio evidenzia in particolar modo il ruolo della forza interna indotta dai robot sull'oggetto. I risultati vengono poi estesi ad un sistema composto da più robot. Infine, tutti i risultati teorici sono validati nella tesi attraverso simulazioni numeriche, mentre vengono mostrati anche i risultati di alcuni esperimenti preliminari condotti con due robot.

List of publications

International Journals

1. Tognon, M., Gabellieri, C., Pallottino, L., and Franchi, A. (2018). Aerial co-manipulation with cables: The role of internal force for equilibria, stability, and passivity. *IEEE Robotics and Automation Letters*, 3(3), 2577-2583. IEEE.
2. Gabellieri, C., Tognon, M., Sanalidro, D., Pallottino, L., and Franchi, A. (2020). A study on force-based collaboration in swarms. *Swarm Intelligence*, 14(1), 57-82. Springer.
3. Gabellieri, C., Palleschi, A., Mannucci, A., Pierallini, M., Stefanini, E., Catalano, M. G., Caporale, D., Settimi, A., Stoyanov, T., Magnusson, Garabini, M., and Pallottino, L. (2019). Towards an Autonomous Unwrapping System for Intralogistics. *IEEE Robotics and Automation Letters*, 4(4), 4603-4610. IEEE.
4. Gabellieri, C., Angelini, F., Arapi, V., Palleschi, A., Catalano, M. G., Grioli, G., Pallottino, L., Bicchi, A., Bianchi, M. and Garabini, M. (2020). Grasp It Like a Pro: Grasp of Unknown Objects With Robotic Hands Based on Skilled Human Expertise. *IEEE Robotics and Automation Letters*, 5(2), 2808-2815. IEEE.
5. Garabini, M., Caporale, D., Tincani, V., Palleschi, A., Gabellieri, C., Gugliotta, M., Settimi, A. Catalno, M. G., Grioli G., and Pallottino, L. WRAPP-Up: A Dual-Arm Robot for Intralogistics. *IEEE Robotics & Automation Magazine*, doi: 10.1109/MRA.2020.3015899.
6. Gabellieri, C., Palleschi, A., Garabini, M., and Pallottino, L. Autonomous Unwrapping of General Pallets: A Robotic Solution for Intralogistics. *IEEE Transactions on Automation Science and Engineering* **Submitted**.

International Conferences/Workshops with Peer Review

1. Gabellieri, C., Tognon, M., Pallottino, L., and Franchi, A. (2018, October). A study on force-based collaboration in flying swarms. In *International Conference on Swarm Intelligence* pp. 3-15. Springer, Cham.

-
2. Gabellieri, C., Sarkisov, Y. S., Coelho, L., Pallottino, A., Kondak, K., and Kim, M. J. Compliance Control of a Cable-Suspended Aerial Manipulator using Hierarchical Control Framework. *2020 IEEE/RSJ International Conference on Intelligent Robots and Systems*.
 3. Palleschi, A., Gugliotta, M., Gabellieri, C., Hoang, D.C., Stoyanov, T., Garabini, M., and Pallottino, L. Fully Autonomous Picking with a Dual-Arm Platform for Intralogistics. *I-RIM 3D Conference 2020* **Best Paper in Planning and Control of Robotic Systems**.
 4. Gabellieri, C., Palleschi, A., Catalano, M.G., Garabini, M., and Pallottino, L. Flexible Automated Depalletizing: an Unwrapping Robot to Remove Plastic from Palletized Goods. *I-RIM 3D Conference 2020*.
 5. Bettelani, G.C., Gabellieri, C., Mengacci, R., Massa, F., Mannucci, A., and Pallottino, L. Robotics Laboratory within the Italian School-Work Transition Program in High Schools: A Case Study. **Accepted** for publication in the *12th International Conference on Robotics in Education Proceedings (RIE 2021)* within the *Springer Series: Advances in Intelligent Systems and Computing*.
 6. Gabellieri, C., Palleschi, A., and Pallottino L. Force-based Formation Control of Omnidirectional Ground Vehicles. *2021 IEEE/RSJ International Conference on Intelligent Robots and Systems* **Submitted**.

Others

1. Pending Patent: Garabini, M., Caporale, D., Settimi, A., Pallottino, L., Bicchi, A., Gabellieri, C., Mannuci, A., Catalano, M.G., Grioli, G., Barbarossa, M.: DISPOSITIVO LOGISTICO. (2019)
2. Peer Reviewed Abstract: Dal Canto, M., Fortunato, G.M., De Acutis, A., Gabellieri, C., Palleschi, A., Garabini, M., Mendoza Buenrostro, C., Vozzi, G. & De Maria, C.: Collaborative robotic-arm based bioprinter for in-situ bioprinting, (2019) *International Conference on Biofabrication*.

Contents

1	Introduction	1
1.1	The four industrial revolutions	1
1.2	The Role of Compliant Robots	2
1.2.1	Compliant Robots inside Warehouses	3
1.2.2	Compliant Aerial Robot	5
1.2.3	Aerial Robots for Logistics	6
1.2.4	Revolution 5.0?	8
1.3	Contributions and Structure of the Thesis	9
2	Robotic Physical Interaction	11
2.1	Passive compliance	11
2.2	Active compliance	12
2.2.1	Impedance Control	13
2.2.2	Admittance Control	14
I	Robotics for Intralogistics: Force-based Depalletizing	16
3	An introduction to Robotics for Depalletizing: Unwrapping and Object Picking	18
3.1	Unwrapping—State of the Art	19
3.2	Object Picking for Logistics—State of the Art	22
3.2.1	Robotic Grasping	24
4	Depalletizing: Force-aided planning for an Unwrapping Robot to Work with Non-perfectly Known Pallets.	28
4.1	Introduction	28
4.2	Problem Statement	29
4.3	Proposed Solutions	32
4.3.1	Hardware Description	33
4.3.2	Contact-based Planning Strategy	35
4.3.3	Collision Classification and Reaction	38
4.3.4	Collision Detection and Isolation	40

Contents

4.3.5	Environment Categorization	42
4.3.6	Film Engagement	43
4.4	Experimental Validation	44
4.4.1	Validation of the Contact Isolation Procedure	44
4.4.2	Validation of the Environment Categorization	45
4.4.3	Validation of the Overall Method	46
4.5	Discussion	49
5	Depalletizing: Force-based Planning for WRAPP-up, a Dual-arm Depalletizer	52
5.1	Introduction	52
5.2	Problem statement	53
5.2.1	Objects	53
5.2.2	Object Configurations	54
5.2.3	Challenges	54
5.3	Human Manipulation Strategies	55
5.4	WRAPP-up: a Brief Hardware Description	56
5.4.1	End-Effectors	56
5.5	Robot working Principle	56
5.5.1	Robot Motion Primitives	56
5.5.2	Planner	58
5.6	Experimental Results	60
5.6.1	Without Perception	60
5.6.2	With Perception	63
5.7	Discussion	66
6	Object picking: Grasp Planning for Unknown Objects	69
6.1	Introduction	69
6.2	Proposed Solution	71
6.2.1	Candidate Box Selection	74
6.2.2	Exploitation of acquired human expertise	74
6.2.3	Candidate Grasp Selection	75
6.2.4	An Alternative Force-aided Candidate Grasp Selection Policy	76
6.2.5	To Support the Candidate Box Selection Policy	77
6.2.6	Acquisition of the Human expertise	77
6.3	Experimental Validation	78
6.4	Discussion	81
II	Robotics for Logistics: Force-based Object Delivery	83
7	An Introduction to Cooperative Manipulation with particular focus on cable-suspended loads	85
7.1	Related works	85
7.2	Dynamic Model	88
7.3	Control	91

8	Cooperative Manipulation of a Cable-suspended Beam Load by Two Aerial Robots	93
8.1	Introduction	93
8.2	Equilibrium Configurations	95
8.3	Stability	98
8.4	Passivity	101
8.5	Equilibrium Configurations in the case of Parametric Uncertainties and Force Measurement Errors	102
8.6	The Role of the Internal Force in the Load Error Caused by Parametric Uncertainties	108
8.6.1	Load Attitude Error	108
8.6.2	Load Position Error	110
8.7	Numerical Results	111
8.8	Experimental Results	119
8.9	Discussion	120
9	Cooperative Manipulation of a cable-suspended load by N Aerial Robots	122
9.1	Introduction	122
9.2	Equilibrium Configurations	122
9.2.1	Equilibrium Inverse Problem	122
9.2.2	Equilibrium Direct Problem	123
9.3	Stability	126
9.4	Numerical Results	127
9.4.1	Convergence	127
9.4.2	Robustness	134
9.5	A shift in the point of view: formation control	142
9.5.1	proposed solution	143
9.5.2	Numerical results	145
9.6	Discussion	149
10	Conclusions	150
	Bibliography	153

CHAPTER *1*

Introduction

Quoting [1],

"Revolutions have occurred throughout history when new technologies and novel ways of perceiving the world trigger a profound change in economic systems and social structures."

Right now, we find ourselves on the brick of the so-called fourth industrial revolution. The reason why it is called *the fourth* is that as many as three previous revolutions are considered to have shaped the world [2,3], as it is summarized in [4] and as I am going to briefly recall in the next paragraph. Fig. 1.1 conveys a schematic visualization of the time line.

1.1 The four industrial revolutions

The first revolution took place during the second half of the 18th century, when the steam engine revolutionized the perception of the world, allowing people and things to move fast from one point to another, and allowed mechanical production.

The second industrial revolution shaped the late 19th century and the early 20th century. Industrialization grew fast with standardization and mass production. Most of the people left the country to start living in the cities. The gasoline engine and the airplanes sped up the movements.

Digitalization is the cornerstone of what is considered the third industrial revolution. As a matter of fact, the advent of digital technologies initiated the Information Age in the middle of the 20th century. The world had changed again: more speed, more connections. Computers, cellular phones, and the internet are the main characters of this chapter.

Chapter 1. Introduction

Eventually, of the fourth industrial revolution, we are both witnesses and actors right now. The product of this revolution, Industry 4.0, is a world in which enormous amounts of data are collected and used to optimize processes and services. The new society is one in which objects, services, and people are going to be connected [5] and in which intelligent robots are likely to be more and more among us [6].

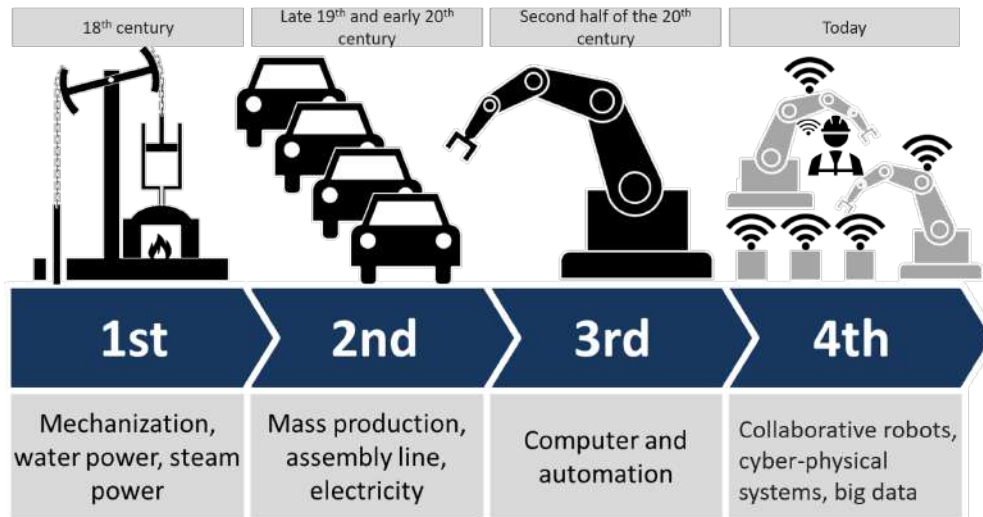


Figure 1.1: Time line and key-points of the four industrial revolutions.

1.2 The Role of Compliant Robots

As a matter of fact, robots represent a key feature of the fourth industrial revolution [6], and the one most related to this Thesis. Indeed, robots that can physically interact with humans have been changing the society we live in—they have found many applications in, e.g., assistive and companion robotics—as well as the factories [7] since they can autonomously complete tasks with enhanced safety, flexibility, versatility, and in a collaborative way [3]. These *collaborative robots* are also referred to as *cobots*. The patent "Cobots" [8], presented as a US patent application in 1997, later extended worldwide, and now expired, describes a cobot as "an apparatus and method for direct physical interaction between a person and a general-purpose manipulator controlled by a computer."

The history of industrial robots dates back to 1961 when a prototype of the Unimate industrial robot was successfully installed in a General Motors plant [9]. From that moment on, industrial robots have met a great fortune. Originally, they were bulky and heavy machines relegated into specific areas separated from humans due to safety issues and were deputed to execute repetitive operations in a structured environment [10]. On the contrary, today many industrial robots do not need to be confined in their working areas anymore, but they can be ubiquitous present in a human-shared environment [11]. From Fig. 1.2 the shift in industrial robots can be gathered.

Whereas, in general, many aspects might have contributed to the shift that we are witnessing, from robots towards cobots, it is fair to state that such a change may not have taken place without the robot compliance. In the 2016 edition of the Handbook of

Robotics [12], we can read:

"robots of the future will not resemble the bulky rigid machines found in today's factory floors but will be compliant and adaptable, and able to safely interact with humans – in other words, soft."

In general, we say that a robot is compliant when it responds to external forces (or torques) by modifying its motion in order to minimize the interaction forces (or torques)¹. Compliance can be either obtained by introducing flexible elements in the mechanical design of the robot (e.g., elastic actuators, elastic tendons, or soft materials), and this is called *passive compliance*, or *actively* produced through specific control laws [13], typically impedance and admittance control laws, as it will be further discussed in the next Chapter.



Figure 1.2: *Traditional industrial automation on the left. Modern collaborative robots that can work side-by-side with humans on the right. Source: <https://commons.wikimedia.org>.*

The physical interaction skills of these robots may enable new applications and better performance in uncertain scenarios. Interaction forces may represent a tool to gain knowledge of the uncertain environment surrounding the robots and to aid the development of suitable planning and control strategies. The common thread of this Thesis is leveraging the crucial information contained in the interaction forces to deploy autonomous robots in realistic scenarios characterized by uncertainties, noise, and limited communication and sensing. A key sector such as the movement of objects within the logistic flow serves as a common background. A special focus is put throughout the Thesis on analyzing the task outcome in the presence of uncertainties and on achieving a successful execution nevertheless. Typical considered uncertainties affect the pose of the manipulated objects and their geometric and dynamic parameters. The Thesis tackles interaction tasks with either ground or aerial robots showing how, in both cases, contact forces can be a valuable tool to develop awareness of the surrounding, non perfectly structure, environment.

1.2.1 Compliant Robots inside Warehouses

E-commerce, i.e., buying and selling physical goods via services over the internet, has reached his full development today. Led by Amazon, which accounted for more than 50% of the growth of the whole e-commerce market, and by Alibaba, in 2017 retail e-commerce sales amounted to more than 2 USD trillion with an annual growth rate

¹<https://www.motoman.com/en-us/about/company/robotics-glossary>

higher than 25% [14]. The expansion of e-commerce is affecting the way warehouses work, especially the intralogistics, i.e., the internal flow of goods within a distribution center [15, 16].

On one side, the market growth led to an increase in employment: data from the Census Bureau² show that in the U.S. there was an annual growth rate in the Warehousing and Storage (North American Industry Classification System - NAIC - 493) employment of the 28% (from 2015 to 2016) and that in 2016 the total workforce reached more than 600K units. On the other side, a strong effort is devoted to maximizing intralogistic efficiency by adopting automated solutions [17]. Moreover, the Western world is expected to experience labor shortage in the logistic sector [18], caused by the need for more logistic workers per item (due to e-commerce) combined to the shrinking in the Western population levels. Logistic robots may help to face these future challenges.

Not only are robotic solutions for intralogistics of particular interest in terms of time-efficiency and cost-efficiency, but they may also lift the human workers from executing repetitive, strenuous and even dangerous tasks. Consider, for instance, tasks involving the use of ladders or blades to unpack objects in a warehouse, or repetitive picking tasks, picking of heavy loads, or picking tasks to be executed in extreme conditions such as inside refrigerating rooms. Of course, in an era when e-commerce is leading toward the necessity of moving an enormous amount of *different* packages within the same warehouses [19], the challenges for robots in terms of versatility and flexibility have also increased. Figure 1.3 shows a picture of an Amazon plant where the reader can appreciate the difference in size and shapes of the stored items. A novel generation of intralogistic systems that are highly flexible and safe yet efficient in environments shared with humans is required. Contact detection and interpretation can represent useful information to execute logistic tasks in a very flexible way. The first part of this Thesis concerns contact-based planning methods to enable new applications of compliant robots inside warehouses. A thorough literature review of intralogistic robots is therefore presented in Chapter 3.



Figure 1.3: Amazon warehouse in Spain. E-commerce demands for a huge variety of items to be handled within the same premises. Source: <https://commons.wikimedia.org>.

²<https://www.census.gov/topics/employment/labor-force.html>

1.2.2 Compliant Aerial Robot

Indeed, besides industrial manipulators and other ground robots, aerial robots have been recently affected by the opportunities conferred by compliant and safe physical interactions. Everybody can easily observe that multi-rotors are already widely present in our society. Not only are aerial robots a popular product among general users [20], but they are also already quite commonly exploited in important applications that involve visual inspection of the environment. For instance, they are employed in precision agriculture [21], environment inspection in rescue missions [22], building inspection^{3,4}, and, eventually, the use of remotely operated aerial vehicles "for the visual and thermal inspection of onshore structures in refineries and chemical plants has become an established technique" [23].



(a) Source: <https://commons.wikimedia.org>



(b) Source: <https://www.flickr.com/photos/samchurchill/14586999783>



(c) Source: <https://pxhere.com/en/photo/1323677>



(d) Source: <https://vimeo.com/123248680>

Figure 1.4: Object transportation is one of the main missions aerial robots are envisioned for. First aid and medication delivery 1.4(a), packets delivery in the freight sector 1.4(b), 1.4(c), and food delivery 1.4(d) are typical use-cases.

Nowadays, the spectrum of applications of these robots has been widening from the mere observation of the environment towards the physical interaction with it [24]. This shift of paradigm in the use of aerial robots is not only the product of compliance but

³<https://abjdrones.com/drone-services/building-and-structure-inspections>

⁴<https://www.dslrpros.com/construction-inspection-drones.html>

comes as a result of multiple factors, e.g., new designs that allow for an omnidirectional thrust, and also passive compliant elements [25, 26].

While industrial robotic manipulators interacting with the environment have represented a classical field of robotics for decades, aerial manipulation [27] by autonomous robots is relatively new area. To give the reader an idea, as it is stated in [20], first works on aerial manipulation appeared in the robotic literature around the beginning of the past decade (e.g., [28] and [29]). Indeed, those years seem to be a cornerstone in the literature of autonomous aerial robot since pioneering papers on aerial manipulation, which inspired also a rich research thereafter, appeared (e.g., [30], [31], [32]). [30] concerns the statics and the kinematics of a load suspended by cables by a group of aerial robots. [31] and [32], and so does [33], study the transportation of a slung load by one or more unmanned aerial vehicles. [28] also tackles manipulation and transportation with aerial robots. It should not be too much surprising that the first papers

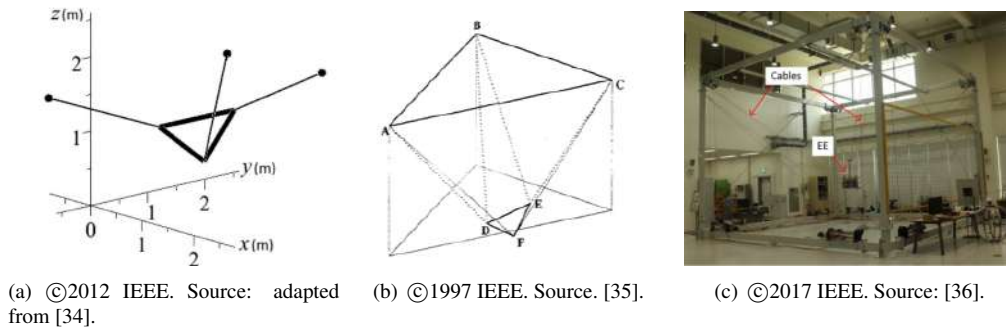


Figure 1.5: Fig. 1.5(a) shows the schematic representation of a cooperative aerial transportation system that considers three robots; three cables and a triangular object are also displayed. The reader can appreciate the similarity of this system with the model of a cable-driven robot shown in 1.5(b). Eventually, for the sake of clarity, Fig. 1.5(c) shows a picture of a real cable-driven robot.

on autonomous aerial manipulation address the *cooperative* transportation problem of *cable-suspended* loads: they take inspiration from the older field of cable-driven parallel manipulators (see Fig. 1.5(b) and 1.5(c)) and by the fact that cables and ropes had been used in rescue and military missions with manned helicopters, as it is explicitly stated in [30]. Indeed, the field of slung load transportation by a single manned helicopter has received considerable attention during the 1960s and 1970s [37].

Anyway, despite its recent birth, aerial manipulation is now a vast field studded with a large number of results. The graph in Fig. 1.6 shows a rough estimate of the number of research papers on aerial manipulation over the past years. An overview of the related literature can be found at the beginning of the second part of this Thesis, in Chapter 7.

1.2.3 Aerial Robots for Logistics

The missions in which the researchers have envisioned to employ aerial manipulators so far can be grouped, according to [20], in three main classes: load transportation, force/torque exertion, and structural construction. Among them, load transportation is of particular interest in logistics.

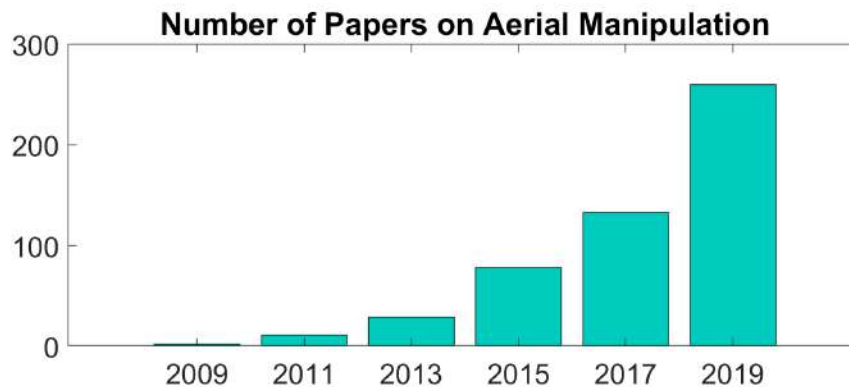


Figure 1.6: The bar plot shows an estimate of the number of papers on aerial manipulation in the past years. The data are based on the results found on Google Scholar when looking for all the papers that include "aerial manipulation" and "robot", "aerial manipulation" and "robots", "aerial manipulator", "aerial robotic manipulation", "UAV" and "manipulation", "UAVs" and "manipulation", "aerial grasping" in their titles. The results are of course only a rough estimate of the actual overall number of papers in the field. In fact, there might be other groups of relevant keywords that have not been included here, and sometimes, even if rarely, the same paper may have been counted more than once (if it includes in its title two or more groups of the aforementioned keywords). However, it is just interesting to see how the number of papers including those keywords in their title has been increasing lately.

Nowadays, the workers employed in the freight sector and last-mile services are sometimes overwhelmed by a high workload. Moreover, since the deliveries often rely on trucks and in general road transport [38], they are affected by the traffic jam in an unpredictable way. As a consequence, deliveries cannot be reliably scheduled. One of the of the main motivations behind the use of aerial manipulators is their large workspace, which easily allows operating at considerable heights.

Major companies, including Amazon⁵, UPS⁶, and Deutsche Post DHL⁷, have been interested in the development of an autonomous delivery system based on aerial robots (see Fig. 1.4(b), 1.4(c), 1.4(d)). It dates September 1st the news that "The US Federal Aviation Administration has given Amazon permission to make drone deliveries, certifying the company as an «air carrier» – basically like an airline company"⁸. Moreover, according to a recent study published in Nature Communications [38], the use of aerial drones could also produce a shift in energy use within the freight sector resulting in a positive environmental impact since it would potentially allow for reduced greenhouse gas emissions.

The need for decreasing person-to-person contact during the COVID-19 outbreak has posed new motivations for employing aerial robots in logistics. In fact, an autonomous delivery system would prevent the risk of exposure of the workers. Within this context, the Chinese e-commerce company JD.com has already deployed aerial

⁵<https://www.cbsnews.com/news/amazon-unveils-futuristic-plan-delivery-by-drone>

⁶<https://pressroom.ups.com/pressroom/ContentDetailsViewer.page?ConceptType=PressReleases&id=1487687844847-162>

⁷<https://www.dpdhl.com/en/media-relations/press-releases/2019/dhl-launches-its-first-regular-fully-automated-and-intelligent-urban-drone-delivery-service.html>

⁸<https://roboticsandautomationnews.com/2020/09/01/us-gives-amazon-permission-to-make-drone-deliveries/>

vehicles⁹ because the usual delivery modes were not suitable anymore due to the social distancing requirements. Moreover, during the Covid-19 recent pandemic, aerial drones have shown themselves useful in the management of hospital logistics (a representative image is in Fig. 1.4(a)). For instance, aerial robots have been used in China to reliably and quickly deploy medical samples and quarantine materials^{10,11}.

1.2.4 Revolution 5.0?

It has been postulated that we are on the verge of a new change that would bring to the so-called society 5.0. The new society would gravitate around the values of environmental sustainability and the creation of meaningful jobs, in order to reshape the results of industry 4.0 towards a more sustainable development [39–41], centered on Earth and human well-being.

Of course, the change towards the larger adoption of robots in logistics comes at the expense of partial substitution of human work. On one side, this may result in the lift of workers from sometimes harsh work conditions. On the other side, the ethical implications of human-work substitution have been clear since the very beginning of computer ethics. In [42], Robert Wiener, which is considered the father of computer ethics [43], thinking about the future society, writes that the creation of these "automata", as he refers to the robots, "gives the human race a new and most effective collection of mechanical slaves to perform its labor" but diminishes the value of human work since humans are compelled to compete with the more efficient machines. However, Wiener recognizes that the same scheme had already taken place in previous industrial revolutions. He claims that industrial revolutions are "two-edged swords" that can be either beneficial or destroying for human beings depending on how intelligently they are used. More recently, a new debate on *Roboethics* followed the first International Symposium on Roboethics in 2004. Roboethics is an applied ethics discipline that aims to provide answers to the new questions arising from the diffusion of robots in our societies, first identifying ethical issues and then formulating proper guidelines [44]. As a matter of fact, it is likely that in the near future a lot of effort will be put in creating proper regulations for robot employment in industries and multidisciplinary points of view will concur to shape robotics of the future [45].

The recent pandemic outbreak also changed our society in several unexpected ways and has risen new needs. Roboticists all over the world have worked hard to give some help providing on-purpose solutions. Consequently, it has been suggested that cobots will take a central role in society 5.0 [46].

Social distancing has now become crucial for preventing the spread of the contagion, both during the peak of the crises and in the phase of the reopening of city services. Home confinement has often made food and medicine delivery necessary. Understandably, e-commerce may be requested even more than before. Within this new context, the role of physically interacting robots may be of even greater importance.

As I have already mentioned, order delivery performed by robots shows its benefits in order to prevent human exposure to the contagion. For the same reason, the au-

⁹<https://asia.nikkei.com/Spotlight/Coronavirus/JD.com-makes-drone-deliveries-as-coronavirus-cuts-off-usual-modes>

¹⁰<https://www.terra-drone.net/global/2020/02/07/terra-drones-business-partner-antwork-helps-fighting-corona-virus-with-drones/>

¹¹https://www.youtube.com/watch?v=0KHaSK2qiIc&feature=emb_title

tomation of object picking in warehouses is now more important than ever, due to an increased need for automatic grasp and manipulation solutions that can ensure social distancing.

I would like to present here also a more concrete example related also to the content of this Thesis. As a matter of fact, one of the first topics addressed in the Thesis is a robotic autonomous solution for the unwrapping task, meaning the task of removing the plastic film wrapped around objects stacked on pallets. This task is usually accomplished by hand by a human operator. The actual investment in the automation of such an operation might be critical in terms of economical advantages since a limited number of operations per day are necessary and the human operator that normally performs them can be dedicated to other different tasks between the execution of one unwrapping task and the other. However, the reconfiguration of warehouse work in view of the promotion of social distancing may open room for such a technology. The automation of the unwrapping task, in fact, would lead towards completely autonomous warehouses.

Even after the pandemic major peak, the awareness about the need for these kinds of responses for the future will remain alive. Eventually, the emergency has probably boosted robot acceptance in our societies. Broad hostility about losing jobs to machines might in fact dissolve as people see the benefits of minimizing person-to-person interactions¹² [47].

1.3 Contributions and Structure of the Thesis

This section provides an outline of the Thesis contents. As I have already introduced, this Thesis studies the role of the interaction forces and the new possibilities that they may open in robotic logistic applications, ranging from ground manipulators to aerial robots. Indeed, the Thesis is divided into two main parts. Part I of the Thesis relates to intralogistics and, specifically, to those phases of the intralogistic flow that interest depalletizing and object picking, the main underlying motivations being already introduced in Sec. 1.2.1. Part II of the Thesis is focused on aerial object manipulation, the main motivations being already introduced in Sec. 1.2.3. The present chapter has been conceived as a general overview to introduce the context to the reader. However, other introductory sections are inserted in the text for each addressed topic, specifically, at the beginning of each part, in order to provide a more thorough review of the state of the art. The remainder of this Thesis is structured as follows.

First, Chapter 2 introduces the fundamentals of compliant control laws, which are useful to understand the rest of the Thesis.

Part I is divided into four chapters.

- Chapter 3 provides an overview of the state of the art of robotics in depalletizing and object picking.
- Chapter 4 presents a novel method for autonomous unwrapping. Unwrapping can be considered as the first step of the depalletizing task, since it consists of removing the plastic film that encloses the items staked on pallets, making them accessible for manipulation. This delicate operation is usually conducted by hand by human operators in the current industrial scenario. Instead, a novel solution

¹²<https://www.nytimes.com/2020/04/10/business/coronavirus-workplace-automation.html>

to autonomous unwrapping of even irregularly shaped heterogeneous pallets is conceived and described in Chapter 4. The adopted planning strategy is indented to accomplish the task in uncertain conditions due to inaccurate information of the environment provided by a perception system. It is based on collision detection enabled by external force and torque measurements. Experiments validating the proposed unwrapping strategy are conducted on a panda manipulator by FRANKA EMIKA equipped with a custom cutting end-effector.

- Chapter 5 presents a planning strategy for depalletizing, based on contact force measurements, aimed at picking different items from a pallet. A set of human-inspired picking strategies for WRAPP-up, a depalletizing dual-arm robot for intralogistics, are in fact introduced. The picking strategies are translated into trajectories for the robot thanks to the planner based on contact sensing. The planner allows the robot to handle items that differ in size, weight, and shape, showing great flexibility. The effectiveness of the method is shown experimentally on a set of objects provided by a food delivery company. Such goods are suitable for dual-arm manipulation due to their dimensions. A solution for picking smaller objects may be required, e.g., also in the considered food sector. Moreover, WRAPP-up, being equipped with a robotic hand, is capable of grasping also smaller objects with one single end-effector.
- Chapter 6, for the aforementioned reasons, presents a grasping method, particularly suited for soft hands, that WRAPP-up can exploit to grasp smaller, unknown objects. The major contribution of this chapter is a data-driven planner that generates suitable grasps by relying on a *reduced* database of grasps generated by a skilled operator manually using the robotic hand. The proposed method has been tested with the PISA/IIT SoftHand on 21 previously unseen objects.

Part II is divided into three chapters.

- Chapter 7 provides a literature overview of aerial object manipulation. It also introduces the dynamic model of the aerial cooperative manipulation system considered in this Thesis and describes the adopted control law. Specifically, a leader-follower scheme is exploited on admittance-controlled multi-rotors.
- Chapter 8 describes a method for the cooperative transportation of a *beam* load by *two* aerial vehicles. The proposed transportation method has the peculiarity, enabled by the adopted compliant control law and interaction force sensing, of not being based on any explicit exchange of information among the robots. The stability and passivity of the controlled system are discussed. The role of parametric uncertainties is also analyzed. Results of a thorough numerical study and preliminary experiments are presented.
- Chapter 9 contains an extension of the results of Chapter 8 to the $N > 2$ -robot case. The formal analysis of the equilibrium configurations and their stability is extended to this case, and results of numerical simulations validating the study are reported. Additional simulations show the behavior of the system subject to external disturbances and a different number of leader robots in the group.
- Chapter 10 contains the conclusions.

CHAPTER 2

Robotic Physical Interaction

Before presenting the results of the Thesis related to physical interaction tasks and the study of contact forces in advanced robotic applications, in this chapter I will briefly review the basic tools that confer compliance to the robots. Indeed, compliance is particularly useful to make the robots perform tasks in contact with the environment, especially in non-structured and uncertain environments, which is the background of the robotic applications analyzed in the Thesis.

The most traditional way of controlling robots is the control of motion, designed in order for the robot to follow a trajectory, or typically for its end-effector to follow a trajectory in $SE(3)$ —the space of rigid translations and rotations in the tridimensional space. If the robot is deputed to perform tasks in contact with the environment, such a control method requires very accurate knowledge of the robot model and of the environment, to achieve accurate position control and planning. In fact, slight errors in the knowledge of the environment position, e.g., may cause an undesirable loss of contact between the robot or the environment or the arising of contact forces and torques that would cause a deviation from the planned trajectory of the robot. On the other hand, motion control reacts to reduce such deviations. This leads, in the worst-case scenario, to a consequent increasing of the actuators torques up to saturation or to the breakage of the parts in contact. These problems can be solved by ensuring a compliant behavior to the robot [48]. Note, however, that an *ad hoc* control law is not the only way to confer compliance to the robots, as it will be briefly discussed in the following.

2.1 Passive compliance

An immediate way to confer compliance to the robots is embedding passive compliant elements in the robot structure. The structural compliance can be at a joint level, at a

link level, or can be due to a soft end-effector. Such robots are referred to as *soft robots*. The Encyclopedia of Robotics [49] states:

"Soft robots are robotic systems embedding in their mechanical structure purposefully designed compliant elements".

Soft robotics is a huge field currently very active, and providing a complete review is out of the scope of this Thesis. As a matter of fact, the results of this Thesis mostly concern active rather than passive compliance. To convey an overview, however, soft robots have been classified into two macro-categories: *continuum soft robots* and *articulated soft robots* [49]. The former contains continuously deformable parts and is basically inspired by the invertebrate animals, while the latter has elasticity only in the actuation and is inspired by the vertebrates.

About continuum soft robots, the interested reader can find several examples in [49–54]. Instead, in Chapters 5 and 6 we present results for robots equipped with compliant end-effectors characterized by compliant transmission elements, the Pisa/IIT SoftHand, which will be better described in Chapter 5.

Many articulated soft robots are based on flexible actuators—see, e.g., the anthropomorphic Baxter robot [55, 56] or the manipulator ANYpulator [57]. A flexible actuator overview can be found in [58]. The presence of such actuators poses new modeling and control challenges since the dynamics of the actuators cannot be neglected, and the elastic characteristics of the actuators are not always reliably known. The configuration variables of the robots are augmented to include the discrepancy between the actuator variables and the link variables [59].

2.2 Active compliance

While passive compliance can represent an effective way of achieving robot-environment physical interaction, it may present some drawbacks such as lack of versatility when the compliant behavior of the robot or its end-effector cannot be modified, or additional complexity in the planning and control. An alternative solution to passive compliance is active compliance, achieved by purposely designed control laws. Actually, the two can be, and in practice often are, combined (see [60]). Among several interaction control laws, here we will analyze indirect force control laws, namely *impedance* and *compliance* control laws. The interested reader can find further details in [48] and [60].

Consider a vector of configuration variables $\mathbf{q} \in \mathcal{R}^n$, typically, for a manipulator it is the vector of joint variables, and indicate time derivative with a dot, so that $\dot{\mathbf{q}}, \ddot{\mathbf{q}} \in \mathcal{R}^n$ are configuration velocity and acceleration vectors, respectively. Then, we can write the well known Lagrange dynamics equation of a robot as:

$$M(\mathbf{q})\ddot{\mathbf{q}} + C(\mathbf{q}, \dot{\mathbf{q}})\dot{\mathbf{q}} + \mathbf{g}(\mathbf{q}) = \boldsymbol{\tau} + \boldsymbol{\tau}_{ext} \quad (2.1)$$

where $M(\mathbf{q}) \in \mathcal{R}^{n \times n}$ is a symmetric positive-definite inertia matrix, $C(\mathbf{q}, \dot{\mathbf{q}}) \in \mathcal{R}^{n \times n}$ is a matrix containing the Coriolis and centrifugal terms, $\mathbf{g}(\mathbf{q}) \in \mathcal{R}^n$ is a vector containing the gravity terms, $\boldsymbol{\tau} \in \mathcal{R}^n$ is the vector of the control inputs, and $\boldsymbol{\tau}_{ext} \in \mathcal{R}^n$ models the effect of external forces and torques. We can write (2.1) in the operational space [61] to express the dynamic behavior of the robot end-effector. Consider the position of the end-effector $\mathbf{p}_e \in \mathcal{R}^3$ and its orientation expressed by a set of Euler angle $\boldsymbol{\phi}_e \in \mathcal{R}^3$ collected in a vector $\mathbf{x}_e \in \mathcal{R}^6$.

The operational space dynamics is then expressed by:

$$\Lambda(\mathbf{q})\ddot{\mathbf{x}}_e + \boldsymbol{\mu}(\mathbf{q}, \dot{\mathbf{q}}) + J^{-T}\mathbf{g}(\mathbf{q}) = \mathbf{f} + \mathbf{f}_{ext}, \quad (2.2)$$

where $\Lambda(\mathbf{q}) = (JM(\mathbf{q})^{-1}J^T)^{-1}$, J is the Jacobian matrix, $\bar{J} = M(\mathbf{q})^{-1}J^T\Lambda(\mathbf{q})$, $\boldsymbol{\nu}_e = J\dot{\mathbf{q}}$, $\mathbf{f} = \bar{J}^T\boldsymbol{\tau}$, $\mathbf{f}_{ext} = \bar{J}^T\boldsymbol{\tau}_{ext}$, and $\boldsymbol{\mu}(\mathbf{q}, \dot{\mathbf{q}}) = \bar{J}^T\mathbf{c}(\mathbf{q}, \dot{\mathbf{q}}) - \Lambda(\mathbf{q})J\dot{\mathbf{q}}$, where $\mathbf{c}(\mathbf{q}, \dot{\mathbf{q}}) = C(\mathbf{q}, \dot{\mathbf{q}})\dot{\mathbf{q}}$.

In the following, the dependencies will be sometimes omitted for the sake of brevity.

2.2.1 Impedance Control

The objective of the impedance control law is that of modulating the dynamic behavior of the system so that it reacts with a certain force to a displacement of its desired motion. The impedance control law has been introduced by Hogan in the '80s [62–64]. In this framework, the environment is regarded as a physical system capable of receiving force inputs and modifying its motion in accordance—the environment behaves as an admittance. To ensure physical compatibility with the environmental admittance, the manipulator must behave as an impedance. Hogan describes the impedance control as a control of the motion of the manipulator plus the assignment of "a «disturbance response» for deviations from that motion which has the form of an impedance" [62]. Choosing the control input [60]

$$\begin{aligned} \boldsymbol{\tau} = & \mathbf{g}(\mathbf{q}) + J^T(\boldsymbol{\mu}(\mathbf{q}, \dot{\mathbf{q}}) + \Lambda(\ddot{\mathbf{x}}_e^d + \Lambda_d^{-1}(D\tilde{\mathbf{x}}_e + \\ & + K\tilde{\mathbf{x}}_e) + (\Lambda\Lambda_d^{-1} - I_6))\mathbf{f}_{ext}, \end{aligned} \quad (2.3)$$

one obtains the following dynamic behavior of the closed-loop system:

$$\Lambda_d\ddot{\tilde{\mathbf{x}}}_e + D\dot{\tilde{\mathbf{x}}}_e + K\tilde{\mathbf{x}}_e = \mathbf{f}_e \quad (2.4)$$

in which Λ_d , D , and K are positive definite symmetric matrices defining the desired inertia, damping and stiffness of the closed-loop system as it were a mass-spring-damper connected to the desired frame. The tilde indicates the displacement w.r.t. the desired quantity, so that $\tilde{\mathbf{x}}_e = \mathbf{x}_e - \mathbf{x}_e^d$, and so on for the other quantities.

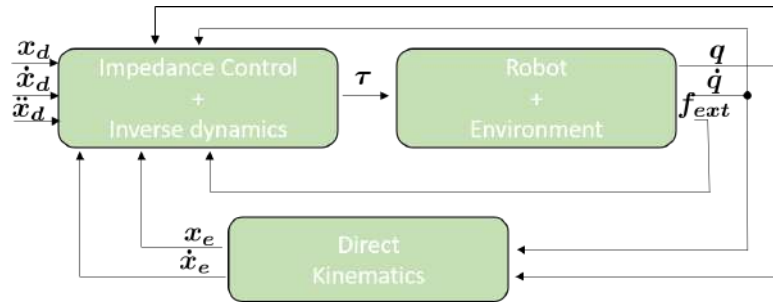


Figure 2.1: Block diagram of an Impedance controller.

Control law (2.3), which allows us to assign the desired dynamics (2.4) to the robot, requires the feedback of the external wrench acting on the end-effector, \mathbf{f}_{ext} . In practice, this might represent an implementation issue especially when external forces may be applied to different parts of the structure. A force-torque sensor is typically required, which measurements, still be affected by noise, do not provide measurements of forces

that do not directly act on the end-effector. The impedance in response to end-effector deviations due to such non collocated forces would not be shaped by the control in the desired manner. A simpler control law has been envisioned, called *compliance* control, which does not require the feedback of the external forces. This is obtained by imposing $\Lambda_d = \Lambda$ in (2.3), with the consequence that we cannot assign a desired inertia to the robot but we keep its natural inertia. The closed-loop dynamics is

$$\Lambda \tilde{\ddot{x}}_e + D \tilde{\dot{x}}_e + K \tilde{x}_e = f_e. \quad (2.5)$$

In [65, 66] a slightly different control is proposed, in which the Coriolis and centrifugal terms are only partially canceled out. This is done in order to confer passivity properties to the controlled system, particularly useful in case of imperfect knowledge of the robot dynamic model. In Fig. 2.1 is a control scheme of the impedance controller.

2.2.2 Admittance Control

The admittance control makes the robot behave as an admittance, which reacts changing its output motion in the presence of an external input force. The final result is similar to that of the impedance control and still consists of reshaping the dynamic response of the closed-loop system, but the implementation is different. In the admittance control, the robot is position controlled, namely it is controlled to follow a reference trajectory. That trajectory, on the other hand, is computed as the output motion of a desired dynamic system under the influence of the external action f_{ext} . The admittance control is hence realized as the cascade of two subsystems as depicted in Fig. 2.2. In order

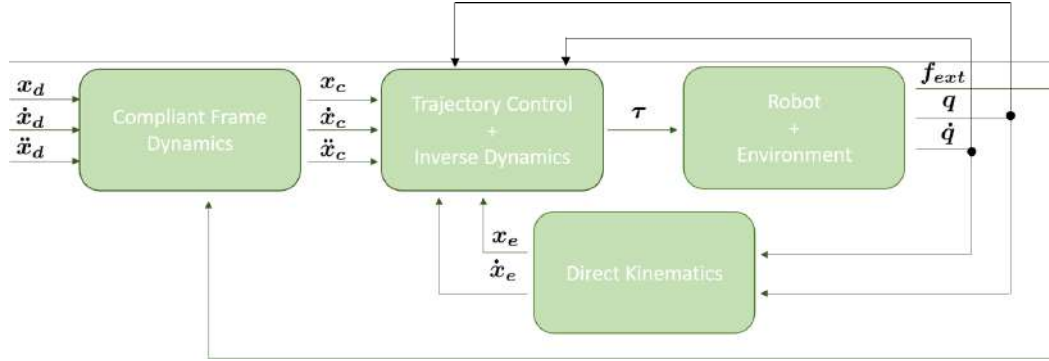


Figure 2.2: Block diagram of an Admittance controller.

to describe the admittance control implementation, we need to introduce an additional reference frame, sometimes called the *compliant frame* [67]. The pose of the compliant frame is described by $x_c = \begin{bmatrix} p_c \\ \phi_c \end{bmatrix} \in \mathcal{R}^6$, where, similarly as before, $p_c, \phi_c \in \mathcal{R}^3$ indicate, respectively, the position and the orientation expressed by three euler angles. The compliant frame is attached to a dynamic rigid body with dynamics given by:

$$\Gamma_d \tilde{\ddot{x}}_c + D \tilde{\dot{x}}_c + K \tilde{x}_c = f_{ext}. \quad (2.6)$$

\tilde{x}_c , and the quantities \tilde{x}_c and x_c obtained by the integration of dynamics (2.6), are the reference input of a trajectory controller, which can be represented, e.g., by a PD control law. Provided that the inner trajectory control loop is faster than the bandwidth

of the compliant frame dynamics, the result is that the closed-loop system is stable and the robot behaves as it had the same dynamics of the compliant frame [67].

Part I

Robotics for Intralogistics: Force-based Depalletizing

CHAPTER 3

An introduction to Robotics for Depalletizing: Unwrapping and Object Picking

While I have already mentioned *intralogistics* in Sec. 1, I provide here a more precise definition. The Intralogistics Forum of the Verband Deutscher Maschinen und Anlagenbau defines intralogistics as: “The organization, control, execution and optimization of in-plant material and information flows, and of goods transshipment in industry, distribution and public sector facilities.” [68]. Indeed, the first part of this Thesis concerns the *internal* movement of material, where internal indicates inside the factory premises.

The importance of robotic autonomous solutions in logistic applications has led to the ad-hoc word *Robotics-Logistics* defined in [15], where it is divided into four main phases: pallet unloading, depalletizing, palletizing, and pallet loading —thus, according to the previous definition, we could talk about *Robotics-Intralogistics*. Numerous are the past and current founded projects testifying the effort of the research community in order to design suitable intralogistic robotic solutions. The work contained in this Part of the Thesis has been carried out within the EU-funded research project IL-IAD¹ on Intra-Logistics with Integrated Automatic Deployment for safe and scalable fleets in shared spaces. The Roblog European project², concluded at the beginning of 2015, had the objective of overcoming perception and grasping challenges in shipping-container unloading, with a special focus on unloading deformable objects, i.e., coffee sacks [69]. The four-year European research project Safelog³ started in 2016 with the goal of achieving safe human-robot interaction in logistic applications, mostly related to heterogeneous fleet management [70]. REFILLS⁴ is an EU-funded project, which has

¹<https://iliad-project.eu/>

²<http://52367068.fn.freenet-hosting.de/project-plan/index.html>

³<http://safelog-project.eu/>

⁴<http://www.refills-project.eu/>

been concluded this year, aimed to deploy robotic solutions to improve grocery store management, with a focus on shelf refilling. Co4Robots⁵ is a three-year European research project that started in 2017 with the objective of deploying robots in industrial facilities to accomplish pick-up and delivery operations. The European research project SOPHIA⁶ started in 2020 with the aim of developing collaborative robotic solutions for workplace automation. Among the results of this project are studies on human-robot collaborative mixed-case palletizing [71] and autonomous pallet jack transportation using a mobile manipulator [72].

Among the different phases of Robotics-Logistics, this Thesis focuses on Depalletizing and, in general, on object picking, which may interest also objects that are not stuck on pallets but are, e.g., stored on shelves. Depalletizing is a crucial aspect of warehouse automation because the handling of materials within the logistic flow largely involves pallets, on which the items are stacked, wrapped, and easily moved. The importance of the depalletizing process can be testified by some figures that characterize the pallet market. Stacking objects onto pallets has been estimated as the most widely used method of bulk shipping, accounting for over 60% of the volume of goods shipped worldwide [73]. The global pallet market reached a volume of 6.87 Billion Units in 2018 and the leading market research company Imarc expects the market to reach 9.18 billion units by 2024⁷. Also, other recent data analysis⁸ confirms an increasing trend in the market of pallets, providing forecasts that cover a period up to 2029.

3.1 Unwrapping—State of the Art

When speaking of depalletizing, I do not refer solely to picking stacked items. Actually, the first action of depalletizing is the removal of the plastic film that usually tightly wraps the parcels to prevent them from falling and to protect them from the potentially damaging effects of adverse environmental conditions. The removal of the plastic film, which I refer to as *unwrapping*, is a preliminary and necessary operation to make the items accessible for manipulation. Despite the general trend towards the robotization of intralogistic processes, unwrapping, due also to the perception and control challenges that it poses (for a detailed discussion see Sec. 4.2), is particularly far from complete automation in the current industrial scenario. The very few examples of autonomous solutions are discussed in the following.

It is emblematic that even the most advanced integrated solutions for almost completely autonomous warehouses, i.e., systems of machines that accomplish all the intralogistic phases, require the presence of human operators to execute the unwrapping task. Examples of these autonomous systems for intralogistics are, e.g., the TATO-20R depalletizer by MAS PACK, in which "the presence of the operator is required only for the functions of removal of protection wrapping in the pallet unwrapping station"⁹, or Swisslog ACPaQ¹⁰.

⁵<http://www.co4robots.eu/>

⁶<https://project-sophia.eu/>

⁷<https://www.imarcgroup.com/pallet-market>

⁸<https://www.persistencemarketresearch.com/market-research/pallets-market.asp>

⁹<http://www.maspack.com/en/product/tato-r-400-bpm/>

¹⁰<https://www.swisslog.com/en-us/products-systems-solutions/picking-palletizing-order-fulfillment/robot-based-robotics-fully-automated/mixed-case-palletizing-acpaq>

Chapter 3. An introduction to Robotics for Depalletizing: Unwrapping and Object Picking

The challenges behind the execution of the unwrapping task are one of the reasons behind its manual execution, but, as already mentioned in Chapter 1, not the only one. In fact, the unwrapping is generally executed a limited number of times per working day in many industrial hubs. It is not a high-frequency repetitive task such as e.g., object picking in the depalletizing process. Once the human operator has unwrapped a pallet, he/she can be normally assigned to a different task that is carried out between an unwrapping-task execution and the following. Consequently, it should be clear that investing in the automation of pallet unwrapping has to be carefully considered in some warehouses especially from an economical-advantage point of view. On the other hand, unwrapping also constitutes nearly the last intralogistic operation yet to be automated in order to develop a fully-autonomous warehouse. With the recent pandemic outbreak, moreover, new room for task automation in warehouses has been created in the market in view of the importance of preventing person-to-person interactions. Thus, the necessity of automating the crucial task seems now more urgent. This additional motivation should be considered besides the improved safety and working conditions that could result from an automatic execution of the unwrapping task. According to BW Packaging System company¹¹, in fact, while of course reducing the physical strain, the automation of pallet unwrapping would avoid the need for ladders and prevent the risk of static electric shocks while manually handling the plastic film.

However, there are, indeed, some examples of complete automatic unwrapping machines available on the market. The MSK¹² fully automatic unwrapping machine is composed of a portal frame under which the palletized items are placed. A large metal structure cuts the wrapping film. Hence, a rolling cylinder connected to the portal moves around the pallet and winds the sheet. Eventually, the sheet is suctioned under the machine.

Another example is the BWContainer Systems automatic unwrapper¹³. The company distinguishes between the removal of stretch wraps and shrink wraps. The former is the most common for pallets, while the latter is used usually for packaging retail products one by one. For the BWContainer Systems automatic unwrapper, the wrap has to be uniform, single layered, and pre-stretched of at least 200% in order for the machine to succeed in melting the plastic through directed steam. Indeed, the unwrapper consists of a robotic arm of considerable size that melts the plastic with a hot air gun. No labels, tags, tapes, and the like are allowed in the working region. Eventually, a mechanism for removing the open plastic sheet is integrated into the station. The suitable items to be unwrapped are bulk glass or plastic bottles, and aluminum or steel cans. The hot air gun might be unsuitable for unwrapping, e.g., food items or carton box pallets and delicate materials in general. In the case of plastic straps are tied around the wrapped objects, a de-strapper machine is provided by the same company.

A de-bagging robot for removing the plastic case from boxed-shaped blocks of cheese is produced by H&C Automated Solutions¹⁴. In a fixed station, two robotic arms are used; one cuts the plastic bag, while the other removes it with a suction cup. The blocks of cheese are fed to the machine on a conveyor belt.

¹¹https://www.bwintegratedsystems.com/docs/default-source/literature/material-handling/robotic_unwrapper_hr.pdf?sfvrsn=d3f3e398_4

¹²<https://www.msk.de/loesungen/defoliersysteme/defolierer-paletten/>

¹³https://www.bwintegratedsystems.com/docs/default-source/literature/material-handling/robotic_unwrapper_hr.pdf?sfvrsn=d3f3e398_4

¹⁴https://www.youtube.com/watch?v=-UzWPUpTox4&t=54s&ab_channel=MHMAutomation

An interesting approach is represented by the VARO unwrapping machine¹⁵. The machine cuts the stretch film on the top and along the lateral surfaces of pallets of carton boxes and other stable objects. Two versions in which the removal of the film is either integrated or not are proposed. Another machine for handling unstable pallets of different objects is also available. In the case of stable objects, they may also be stacked in an irregular resulting shape.

Eventually, many examples apply solely to specific objects. Among these, the automatic unwrappers by Autorema¹⁶ and the CSW-Multifeeder series¹⁷ are designed for packets of end-cans, not for general pallets.

After having analyzed the state-of-the-art solutions to automatic unwrapping on the market, I conclude that, besides being usually non-relocatable and bulky, thus occupying a large surface of the warehouse, the available automatic machines usually work exclusively on properly shaped items of known dimensions. The material of the underlying objects can be subject to some constraints, too e.g., to ensure that the automatic blade does not damage the surface of the objects. The automation of the unwrapping task leaves space for further improvements and research.

Eventually, besides describing the current commercial solutions, I would like to present also related works in the robotic literature. Cutting tasks, especially in non-perfectly structured environments, are often critical due to the consequences of their failure, typical applications being surgical and nuclear robotics. In fact, in the literature, cutting robots are usually human-assisted and cutting tasks are executed under shared control paradigms [74]. Active force control has been proposed and validated with simulations in [75] for autonomous cutting tasks of uncertain profiles. The inclusion of force information in the control [76] is a classic solution to increase the robustness. However, force control may, in general, have stability issues and requires high bandwidth [77]. In [78] the problem of precision-cut of metallic industrial pieces is addressed. In that context, the position of the object is known exactly and the necessity of very accurate positioning of the cutting robot end-effector leads to exploiting measured forces at the level of the custom end-effector to online compensate the end-effector deviations caused by those forces due to the robot compliance. In [79] a method for cutting soft materials using two robotic manipulators, where one cuts and the other pulls the cut part to separate it from the rest of the object, is proposed. The method relies on a complex model of the soft object dynamics based on accurate knowledge of the target object, a beef shoulder in that case. The target application is the meat industry. In [80], a combination of visual servoing and force control is proposed to cut soft materials. A camera is used to control the orientation of the cutting tool avoiding to rely on noisy force measurements, while force control ensures that too high resistive forces are avoided by adjustments of the tool configuration. In [81], rough cutting is considered. A path planning algorithm based on sampling points on the point cloud of the object is exploited. The path has user-assigned initial and final points and is generated so as it maximizes the robot manipulability in between so that it can respond by modifying its trajectory in order, e.g., to comply with forces arising during the cut. The method restricts the target application to cutting tasks on smooth surfaces.

¹⁵<https://www.varomachinery.com/non-food/packaging/unwrapping-system/>

¹⁶<https://autorema.com/en/can-making-industry/>

¹⁷<https://www.youtube.com/watch?v=pnLEEi9ZY5I>

Chapter 3. An introduction to Robotics for Depalletizing: Unwrapping and Object Picking



(a) The velvet finger mounted on a KUKA LWR ©2014 IEEE. Source: adapted from [82] (b) A reproduction of the Boston Dynamics Handle. Source: <https://www.flickr.com/photos/87587140@N07/32549641707/>



(c) The DLR omniRob ©2015 IEEE. Source: [83]

(d) The Fetch robot by Fetch Robotics. Source: [84]

Figure 3.1: Some examples of robotic manipulator for logistics.

3.2 Object Picking for Logistics—State of the Art

Moving to the subsequent action of the depalletizing process, I provide an overview of object picking state-of-the-art. As a matter of fact, order picking —the process of retrieving products from storage (or buffer areas) in response to a specific customer request —is responsible for the 50-75% of the total costs of a conventional warehouse [85]. Hence, order picking can be considered one of the highest priority areas to improve in order to maximize the productivity of a warehouse.

The most widely adopted end effectors for robotic picking are vacuum grippers and mechanical grippers, either simple^{18,19} or complex/anthropomorphic [86].

To automate the picking of items that are located on a pallet, two main different solutions may be adopted: a manipulation provided with a mobile base or a ground manipulator in which the pallet is brought to the robot by mobile devices²⁰.

Among the prominent examples of autonomous mobile manipulation platforms for logistics are Little Helper III [87] and DLR OmniRob [88] (see Fig. 3.1(c)), which

¹⁸https://schunk.com/de_en/gripping-systems/category/gripping-systems/schunk-grippers

¹⁹<http://www.willowgarage.com/velo2g>

²⁰<https://www.greyorange.com>

are mainly devoted to picking objects from shelves. They consist of a robot arm with a two-fingered parallel gripper mounted on a stable mobile base. Handle²¹ is a commercial robot devoted to box-handling in warehouses. It has an unstable two-wheeled mobile base, which requires a more expensive control but may substantially reduce the footprint of the robot and is equipped with a vacuum gripper (see Fig. 3.1(b) for a reproduction). The MOBILE Collaborative robotic Assistant (MOCA) [89] is composed of a lightweight manipulator, an underactuated end-effector, and an omnidirectional mobile base. It is conceived for agile mobility and for accomplishing both autonomous [72] and collaborative tasks side-to-side with humans [71]. Bazar [90] is another example of a robot envisioned for the factory of the future that can both collaborate with humans and carry out heavy tasks such as transporting bulky loads thanks to its dual-arm configuration. Bazar is composed of two lightweight manipulators mounted on a mobile base and both equipped with an anthropomorphic, 20-actuated-Dofs hand. The robot Fetch [84], produced by Fetch Robotics²² and displayed in Fig 3.1(d), and TIAGo [91] by PAL Robotics²³ are two mobile manipulators that can pick small objects from standard warehouse shelves²⁴. Magazino²⁵ and InVia Robotics²⁶ sell two products, mainly devoted to box-picking and based on suction cups. Both the solutions exploit a picking strategy based on box sliding, which may not be suitable for boxes stacked one upon the other and in general not free to slide. TORU, the robot by Magazino is suitable for picking small boxes from shelves, especially shoe boxes. It has also been integrated with a different picking strategy, always based on objects sliding, and additionally requiring the accessibility of the rear surface of the box²⁷. The Velvet Finger [92, 93] is a mechanical gripper composed of two fingers with two phalanges each, actuated by two conveyor belts that also help collect the objects. The gripper can lift objects with a weight of up to 1 kg, and dimensions that fit the aperture and depth of the fingers. A picture is provided in Fig. 3.1(a). A bigger and more capable prototype would however imply a bigger and more performant manipulator. The survey [94] offers a literature review on the subject of industrial mobile manipulators. The Velvet Finger has been used to develop the APPLE research platform for robot commissioning [95]. An Autonomous Ground Vehicle (AGV) capable of detecting and transporting standard EUR pallets is equipped with a KUKA LBR iiwa manipulator mounting the Velvet Finger. The APPLE robot has been tested on different cans.

Dora Picker [96] is an example of a ground manipulator for warehouses. It comes with three grippers to grasp objects that differ in shape and weight, but always not very large in dimensions. It is more devoted to picking small single objects than to depalletize. [97] proposed a ground robotic system for flexible depalletizing in supermarkets and test it with simulations. The robot includes a vision module and a robotic manipulator equipped with a suction-based gripper [98] for box picking either from the top

²¹<https://www.bostondynamics.com/handle>

²²<https://fetchrobotics.com/>

²³<https://pal-robotics.com/robots/tiago/>

²⁴<http://iros18-mmh.pal-robotics.com/wp-content/uploads/2018/10/MMH-ROBOTICS.SG-VI-1024x574.png>

²⁵<https://www.youtube.com/watch?v=kj8NaHAoLJw>

²⁶<https://www.youtube.com/watch?v=sCE0a8625tE>

²⁷<https://www.youtube.com/watch?v=1j-RhPENu88>

Chapter 3. An introduction to Robotics for Depalletizing: Unwrapping and Object Picking

or from the lateral surface. There are also several commercial depalletizers^{28,29,30}. Often, they leverage suction cups or mechanical grippers designed according to certain object requirements. A commercial solution for unloading jute or plastic bags up to 100 kg is produced by Copal and consists of a performant manipulator equipped with the SpiderGripper, a complex gripper with several rotation and tilting points³¹. The dimensions of the object often represent a constraint for the range of applications of the robots. Swisslog³², for instance, propose a picking robot, ACPaQ, but also a different one suitable for bin-picking of smaller objects, ItemPiQ. Pick-it-Easy by Knapp³³ is an example of a similar robot that picks from above single items contained in bins using a suction-based gripper.

From the above overview, it emerges that the available solutions to depalletizing either work on very specific objects, for size, shape, and weight, or they need special surrounding conditions, such as the accessibility of certain portions of the object surface. On the other hand, besides the large variability of objects, especially in the e-commerce sector, real-world conditions normally include limited accessibility of object surface due to the presence of other objects or of the container, deformable materials, and pierced or porous objects that cannot be handled by suction-based mechanisms. All these are major challenges to the complete automation of picking operations in warehouses, which, in fact, still considerably relies on human work [99]. A suitable manipulation-planning strategy is required in order to handle the great variability of objects and configurations that may occur. Robotic object manipulation has been largely studied in the literature. The following section provides an overview of the state of the art of robotic grasping.

3.2.1 Robotic Grasping

The problem of grasping a single object with a given end-effector has been extensively studied from theoretical and experimental viewpoints. However, bin-picking still represents an open challenge, especially in unstructured environments. This is testified also by challenges aimed to enhance warehouse automation in picking operations, such as the Amazon Picking Challenge [100]. In the following, I provide an overview of the grasping-related literature.

Especially, grasping *previously unseen objects* represents an open and very challenging problem for robots [101]. Traditional grasp theory focused mostly on searching contact points on the (usually known) object in order to satisfy some constraints and typically guarantee force closure [102]. In [103] these methodologies have been defined as *analytic* to distinguish them from the *empirical* (or *data-driven* [101]) ones, which have gained a greater attention in the latest years.

However, the efficacy of the data-driven approaches depends on the quality of the grasp data sets. A prominent example is the Cornell Grasping Dataset, containing numerous objects and ground-truth labeled grasps specifically designed for parallel

²⁸<http://premium-robotics.com/index.php?id=6&L=1>

²⁹https://www.youtube.com/watch?time_continue=1&v=8Mbc9IaNVJM&feature=emb_logo

³⁰https://www.youtube.com/watch?v=_lH2snLVO7w

³¹<https://www.copalhandlingsystems.com/en/products/spidergripper/>

³²<https://www.swisslog.com/en-us/products-systems-solutions/picking-palletizing-order-fulfillment/robot-based-robotics-fully-automated>

³³<https://www.knapp.com/loesungen/technologien/robotik-und-handhabung/>

grippers. This data set allows the training of grasp-detection deep neural networks (e.g., [104], [105], and [106]). On the other hand, the adoption of such an approach for a different hand should rely on the creation of an extensive sample set, which is a time consuming and not trivial task—see, e.g., the data collection setup in [107].

On the other side, there are studies on vacuum grippers [108] and parallel grippers [109], [110] that use *synthetic* training data sets in order to reduce data collection time [109]. Such data sets rely on a model of the end-effector. Other examples of synthetic grasp datasets are the Jacquard dataset [111] and the Evolved Grasping Analysis Dataset [112]. The grasp simulator *GraspIt!* [113] has been used to generate the Columbia Grasp Database [114], for an anthropomorphic and a three-fingered hand.

Understandably, a reliable and computationally efficient simulator may not be available for all types of robotic hands, limiting the applicability of model-based approaches. This might be the case, e.g., for new robotic hands designed to structurally embody the *intelligence* of the human hand, through compliance and/or under-actuation [86]. An effort to model such robotic hands is the simulator described in [115]. However, in general, simulators for this kind of hands may suffer from not accurately modeled effects such as friction generated by the gloves that usually cover the hands, contacts between the objects and the hand, which can be many multiple in the case of adaptive hands and not necessarily on the tips of the fingers. Another issue is the computational cost of simulating a system with a large number of bodies (e.g., 20 in case of the Pisa/IIT SoftHand [116]) or continuously soft bodies [117].

A different approach to create a grasp dataset has been followed in [118], where the authors collect data by recording videos of humans grasping objects with their own hands. The observation of human grasps in order to plan robotic grasps has been exploited in the literature also by either direct human observation, such as in [119], where a taxonomy of manufacturing grasp poses has been derived, by sensorized gloves [120], or by motion capture, as in [121], where, after a set of force-closure grasps for a given object is generated by a simulator, the grasp with higher human-likeness is selected. This is done by defining a metric starting from data of human beings grasping several objects with their bare hands. Experiments are carried out using very simply shaped objects—a box and a cylinder. The underlying hypothesis of these methods is a certain analogy between the human hand and the interested robotic hand. Human grasping skills have also been transferred to robotic grasp planning through robot teleoperation [122, 123] and through human physical guidance of the robotic hand [124, 125].

In [126] and [127] the authors generate slim ground-truth grasp databases by associating each grasp of the training set to the *local* shape of the object instead than to the object itself. Then, the robot grasps previously unseen objects that *locally* resemble one of the shapes in the database. The success of these promising approaches still depends on the variability of the database.

In order to be independent of given models of the objects, namely in order to grasp unknown objects, the approximation of object point clouds with basic shapes has been exploited. The objective is to make the problem of grasping unknown objects more easily tractable. In [128] the authors localize graspable parts of object point clouds. In this way, even without additional information on the overall object, it is possible to envision a grasping strategy. However, the method exclusively recognizes parts that the robotic hand can completely wrap, thus limiting the applicability mostly to objects with

handles. A book, for instance, could not be grasped in this way. The method is tested on a parallel gripper generating grasps based on considerations on a suitable relative pose of the end-effector w.r.t. the graspable part. In [129] a method to grasp an object by representing it with one superquadric is presented. Superquadrics are a family of geometric surfaces which shape varies considerably based on the value of few parameters ranging, e.g., from being a sphere to resemble an octaedron or a cube [130]. However, the approximation of the entire object shape with a single superquadric is often not sufficiently accurate [131]. In [131] the authors state that, in order to grasp unknown objects, the MVBB (Minimum Volume Bounding Box) decomposition is an effective trade-off between good approximation and efficiency. MVBB algorithm has been tested in simulation as a tool for grasp planning in [132]: given the box decomposition of an object, a pose is heuristically computed based on user-defined geometric features, and random variations of the defined grasping pose are tested. MVBB has been used in [133] to plan 2D grasps based on the projection, on each face of the box, of the internal portion of the point cloud. Alternative object decomposition algorithms have been presented in the literature in order to plan the grasp accordingly. These methods exploit, e.g., inscribed spheres [134], different basic shapes such as boxes cylinders and cones [135], or several different superquadrics all together, such as in the decomposition tree proposed in [136].

Grasp planning in a cluttered or uncertain environment, typical, e.g., of depalletizing tasks, poses further challenges since many grasps predicted with standard data-driven methods would be discarded because colliding with the surroundings [95, 137]. In those works, a grasp planner that takes environmental constraints into account is proposed. The method builds a truncated grasping envelope around the object and then controls the robot to go to one grasping pose within that manifold of feasible grasping poses. The envelope is deliberately built by incorporating knowledge of the object, the environment, and the gripper. According to the same works, the inclusion of sensor feedback such as the information from a force/torque sensor at the manipulator wrist would be beneficial in terms of robustness since the motion of the robot could be corrected online, accordingly.

In general, a pre-planned robot trajectory can be reactively modified online to account for unpredicted changes in the environment or various sources of disturbance [138] —miscalibrations, noise, dynamic errors, etc. Sensor feedback has been envisioned also as a useful tool to robustify grasping, especially under uncertainties, in [118], where reflexes triggered by sensorized gloves for soft hands are used within a reactive grasp planner to detect collisions with the objects. Tactile information at the level of the fingers, referred to as *intrinsic tactile sensing* in [139], has been widely exploited in the literature [140]. A combination of tactile sensors on the fingers, and acceleration and force sensors at the wrist has been exploited in [141] in order to online adjust predefined grasp primitives to the physical object. Due to the limited sensitivity of the tactile sensors, while acquiring information by touching the object surface, the end-effector might move the object itself, with the possible consequence of compromising the grasp [142]. Hence, proximity sensors have been proposed for acquiring pre-touch information of the object and adjust the grasp accordingly [142–144]. In [145] a reactive trajectory planner is proposed and tested on a bin-picking use case. A nominal trajectory is planned in advance but extra flexibility is injected into the system by

3.2. Object Picking for Logistics—State of the Art

allowing online deviations of the generated trajectory based on the proximity with the environment, sensed thanks to an artificial skin on the robot.

Depalletizing: Force-aided planning for an Unwrapping Robot to Work with Non-perfectly Known Pallets.

4.1 Introduction

In recent years, robotics has been largely applied to improve the efficiency of logistic processes. Pallets cover a crucial role in the logistic flow since they represent the main way to store and ship items. When put onto pallets, the items are wrapped with plastic films to protect them and prevent them from falling. However, despite being the first and necessary operation for handling the stacked goods, unwrapping has not yet been satisfactorily automated. Autonomous solutions exist but, usually, they are designed for specific situations, require a large footprint, and are characterized by low flexibility. Consequently, unwrapping is mainly performed by human operators, due also to the complexity of its planning and control phases. Blade handling, ladders, and electrostatic shocks are sources of potential injury to the staff and further motivates the search for an automatic solution. This Chapter of the Thesis proposes a robotic solution to autonomous unwrapping applicable to generally shaped pallets, including both homogeneous and heterogeneous pallets. Partial results of the presented work have been published in [146, 147].

First, the problem is framed in Sec. 4.2. Then, a novel solution to automatic unwrapping (see Fig. 4.1), composed of a perception system, an impedance-controlled robot mounted on a mobile base, a custom cutting end-effector, and a suitable planning strategy is introduced in Sec. 4.3, where both the hardware (Sec. 4.3.1) and the control and planning strategies (Sec. 4.3.2-4.3.6) are described. Compared to the state of the art solutions, the proposed solution has a small footprint and can hence be easily

relocated to maximize the warehouse efficiency. The system is intended to cope with pallets having a wide variety of configurations. Experimental results are reported in Sec. 4.4 and final discussions drawn in Sec. 4.5.

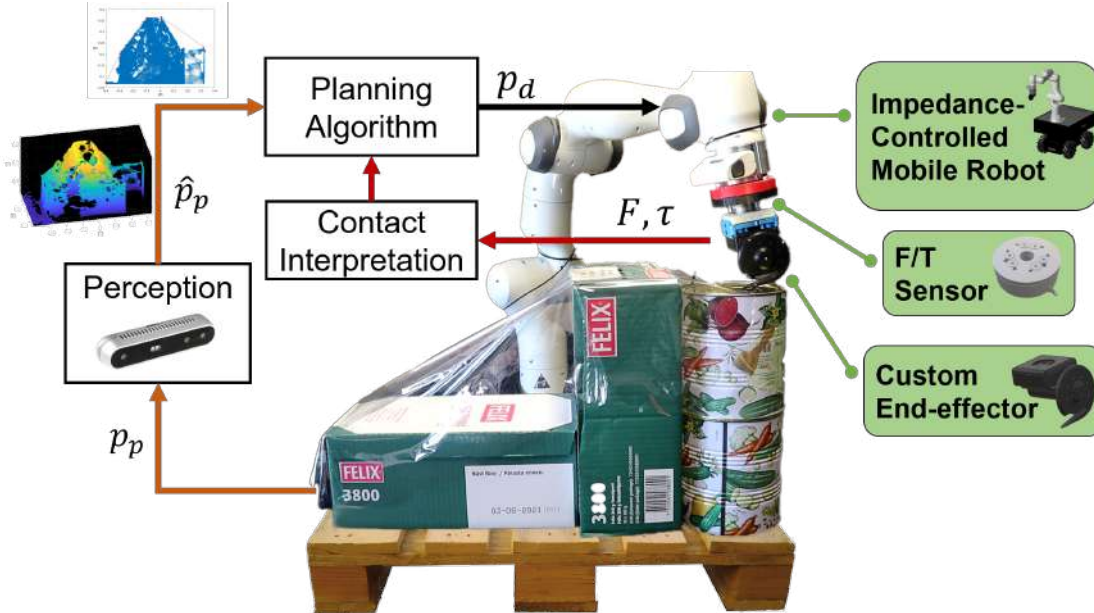


Figure 4.1: Architecture of the proposed autonomous unwrapping robot for intralogistics. The perception system acquires off-line some information of the pallet (p^p) and provides an estimate (\hat{p}^p) to the planning algorithm. Based on this, a rough desired trajectory (p_d) is planned for the custom cutting end-effector of the impedance-controlled manipulator. During the task execution, a force and torque (F/T) sensor continuously provides wrench measurements (F, τ) to the contact interpretation block, which detects contacts, computes the location of the contact point on the robot end-effector, and, relying on contextual knowledge, infers the contact nature (e.g., expected vs. unexpected). Hence, the planning module refines the reference trajectory accordingly on-the-fly.

4.2 Problem Statement

This section better frames the problem targeted in this Chapter, identifying the main challenges of the unwrapping tasks and the typical shapes assumed by the objects on the pallet and by the wrapping plastic film that are considered in this study.

Unwrapping Challenges The nwrapping task may be split into a sequence of sub-tasks, namely *pallet detection*, *film detection*, *film cutting*, and *film removal*, as represented in Fig. 4.2.

- *Pallet detection* has been already addressed in several works in the literature. In [148] the authors present ROBOLIFT: an autonomous forklift carrier able to perform pallet recognition and to estimate the pallet pose. In [149] an autonomous outdoor robotic forklift is able to safely engage unknown pallets, while in [150] the focus is put on the perception system for autonomous pallet detection to be applied in intralogistic operations. In [150] the reader can find references to pallet detection methods based on different working principles, such as laser scanners, vision-based, or relying on sensor fusion.

Chapter 4. Depalletizing: Force-aided planning for an Unwrapping Robot to Work with Non-perfectly Known Pallets.

- *Film detection* is, instead, more critical and cannot be considered completely solved yet. In this phase, the challenge is to reliably distinguish between the portions covered by the plastic and those uncovered, despite changes in the light conditions, object materials and colors, and the number of film layers. State-of-the-art methods for general surface reflectance characterisation ([151], [152]) require custom light and detector setups. Existing industrial sensors, such as the SICK OPR20G glare sensor, require close proximity to the material. None of these solutions are suitable for easy deployment on a mobile robot in a warehouse setting. Anyway, rough information about the plastic film distribution on the objects could be sufficient for the unwrapping execution. In the present work, this problem is not addressed; instead, the location of a region free of plastic from which the unwrapping task can start is supposed to be known.
- In the *film cutting* phase, the system executes the cutting task while preserving the integrity of the items. The autonomous and efficient execution of this phase is the focus of this chapter. In this phase, the pallet size and pose, together with the distribution of the wrapping film on the pallet itself, could be used to plan and control the system motion. Due to the variety of items (shape, size, colors, surfaces, etc.) that can be stacked in the pallets and the different environmental conditions, the information coming from the perception system will be affected by a certain degree of uncertainty. This poses two main challenges: from one side, successfully completing the cut of the plastic film anyway; from the other side, ensuring that when the robot comes in contact with the objects it does not damage them.
- The *film removal* phase can be addressed exploiting one of the solutions available in the state of the art of automatic unwrapping: the cut plastic might be collected and suctioned by a vacuum machine. However, one may also consider investigating possible solutions that exploit exploiting a manipulation system. This is left for future work and this last phase is not implemented in the Thesis.

Pallet Profile In this section, I identify the profile that the pallets considered in this work may assume. First, the pallets can be homogeneous, namely made of identical objects, or heterogeneous, namely made of objects of different sizes and/or shapes, stacked together. I shall tackle both cases, considering box-shaped items, which are the most commonly shipped [17, 153], and cylindrical bins. Two main different scenarios can occur.

From one side, there is the simplest and ideal scenario: the overall pallet shape is a cuboid. This is more likely to happen for homogeneous pallets. Fig. 4.3(a) shows a schematic representation of a cuboid profile made of homogeneous cylindrical objects stacked together.

From the other side, the overall pallet profile may not be a cuboid, but it may assume an irregular shape. We suppose that the objects are placed such that they lie on one of their faces so that the emerging profile is made of consecutive steps. Again, a stepped profile emerges when considering either box-shaped or cylindrical objects. This profile may occur with either homogeneous or heterogeneous pallets. First, identical items might be stacked so that they do not complete a cuboid. Second,

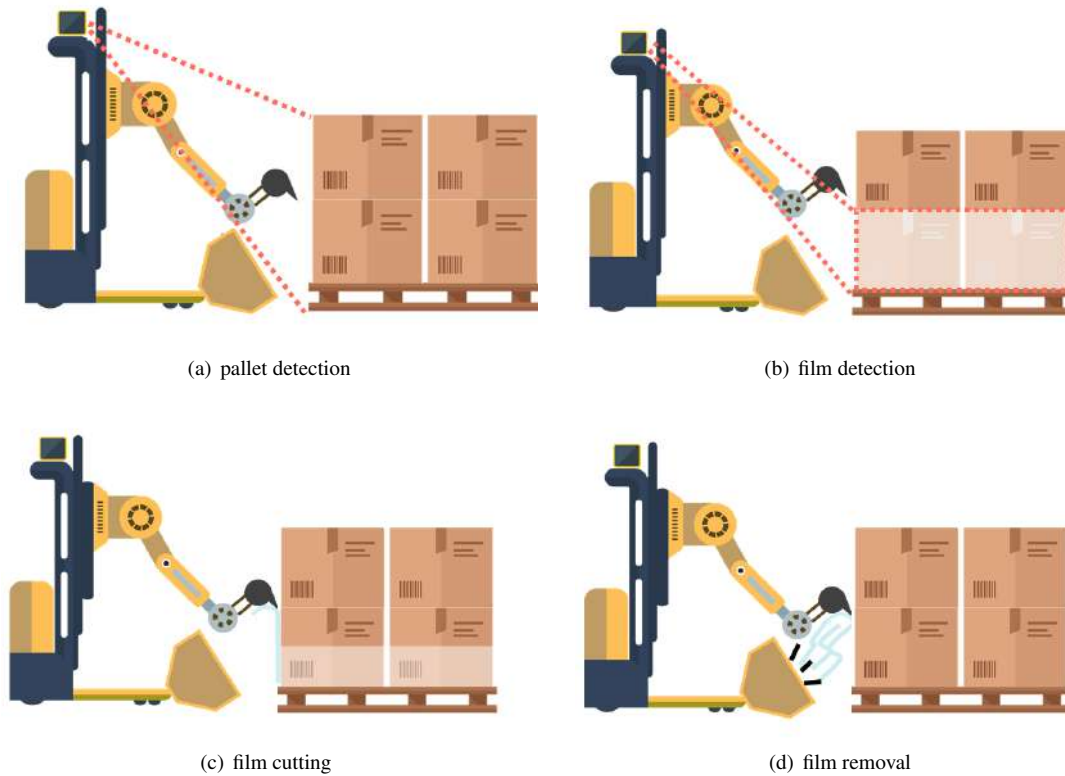


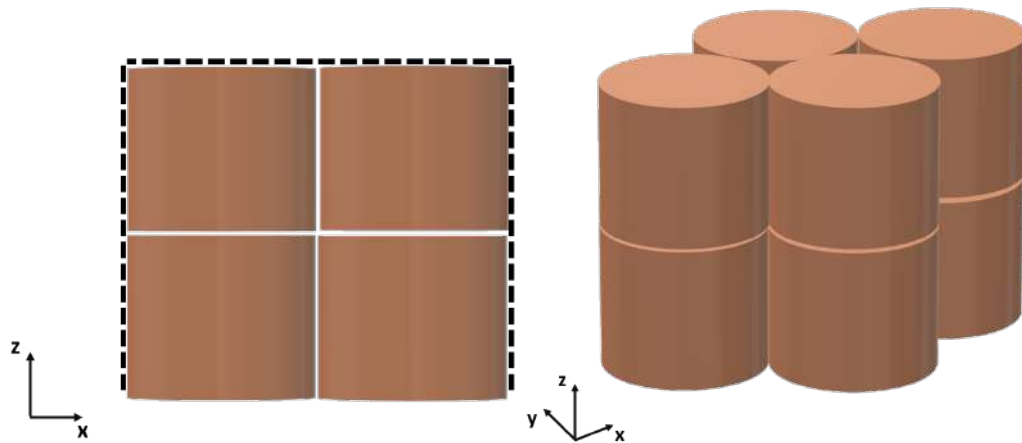
Figure 4.2: Four main phases of the unwrapping task. the pallet position and size (a) and the plastic film distribution (b) are acquired by a perception system; then, the plastic film is cut (c) and removed (d).

the stepped profile can be made of heterogeneous objects as in Fig. 4.3(b). Irregular profiles of the parcel units are quite common and can be due not only to the heterogeneity of single units—common in grocery, beverage distribution centers, and parcel services [154]—but also to the presence of defects in the underlying pallet [155]. In conclusion, we consider pallets with a cuboid profile or a stepped profile, which can be homogeneous or heterogeneous and composed of box-shaped and/or cylindrical items. Although other more irregular shapes may occur, the addressed cases cover a large part of real-case scenarios.

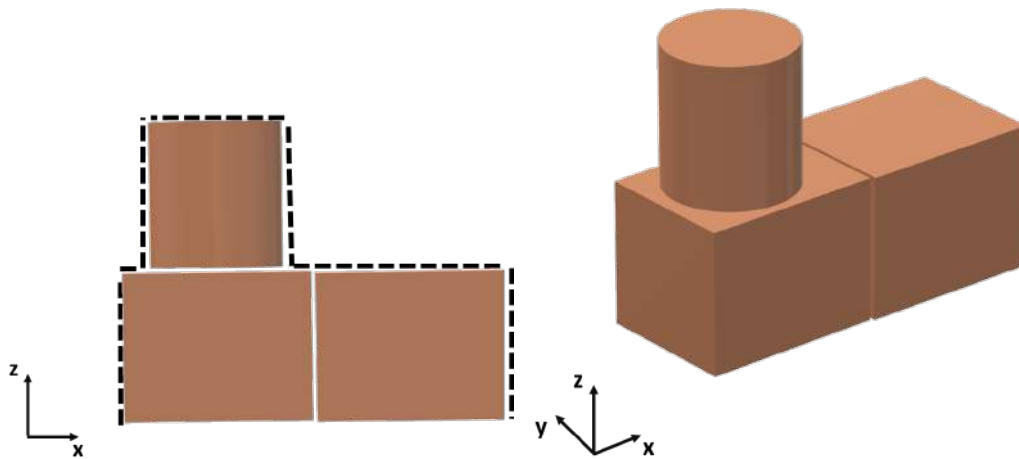
Film Profile Now that the profiles of the pallets have been outlined, the presence of the plastic film should be introduced in the problem. In fact, the film that wraps the pallet is the actual profile that we have to follow in order to accomplish the unwrapping task. Suppose that the plastic is wrapped only around the lateral surface of the pallet—*lateral wrapping*—or also *partially* around the top surface of the pallet—*incomplete top-wrapping*. There is actually another possibility, consisting of the pallet being completely covered in plastic. This case can be brought to the *incomplete top wrapping* provided that a hole is produced on the top surface. The problem of creating holes in the film is not tackled in this Thesis, so that the addressed problems fall into one of the two aforementioned cases.

Of course, the wrapping plastic film adapts its shape to that of the underlying objects.

Chapter 4. Depalletizing: Force-aided planning for an Unwrapping Robot to Work with Non-perfectly Known Pallets.



(a) 2D and 3D views of a homogeneous cuboid pallet made of cylindrical items. The cuboid profile is highlighted by a black dotted line.



(b) 2D and 3D views of a heterogeneous pallet with a stepped profile. The pallet is composed of box-shapes and cylindrical objects. The stepped profile is highlighted by a black dotted line.

Figure 4.3: Schematic representations of two different pallets.

Specifically, suppose that the profile of the plastic film distributes along consecutive segments of different slopes that constitute the convex hull of the pallet. See Fig. 4.4 for a schematic representation. As it will be clear in the following, this simplifying assumption facilitates the estimation of the film profile. Such a hypothesis may lead to a rough approximation of the actual profile of the film, especially if the shape of the stacked objects is irregular and the film is very much stretched or, e.g., belongs to the shrink type. In those cases, it is more likely that the plastic film generates curving lines between consecutive steps on the pallet. However, as it is explained in the following, the uncertainties introduced at this stage will be effectively managed during the execution of the unwrapping task by proper planning of the robot trajectory.

4.3 Proposed Solutions

This section describes a novel robotic automatic unwrapper for intralogistics.

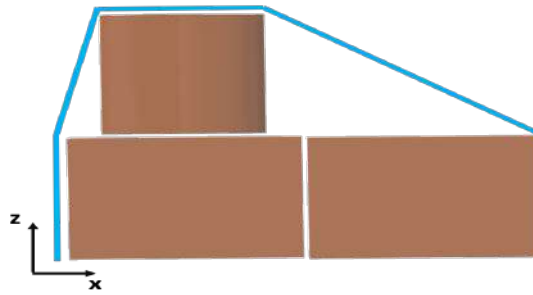


Figure 4.4: 2D view of a schematic representation of a wrapped heterogeneous pallet. The plastic film that wraps the objects is represented as a light blue line and is supposed to distribute along lines of different slopes along the convex hull of the objects.

4.3.1 Hardware Description

As for the hardware, the robot is composed of a 7-Dofs robotic manipulator, specifically a Panda robot by Franka Emika, equipped with a custom cutter as an end-effector. Due to its small size and weight, the robot is envisioned to be mounted on a mobile base characterized by a reduced footprint. This would make the platform relocatable while potentially enhancing its workspace during task execution. For the moment, the mobile base, which can be seen in Fig. 4.5, has been exploited only for bringing the robot close to the unwrapping site [146], but not to actively help during the cutting task execution. More general planning and control strategies that include also the motion of the mobile base are left for future work. As already mentioned, the manipulator is equipped



Figure 4.5: Picture of the system.

with a custom cutting end-effector. Two pictures of the cutter, one for manual use and one with the robot interface are provided in Fig. 4.6. The design of the cutter is the result of tests with existing manual tools, based on different working principles, to

Chapter 4. Depalletizing: Force-aided planning for an Unwrapping Robot to Work with Non-perfectly Known Pallets.

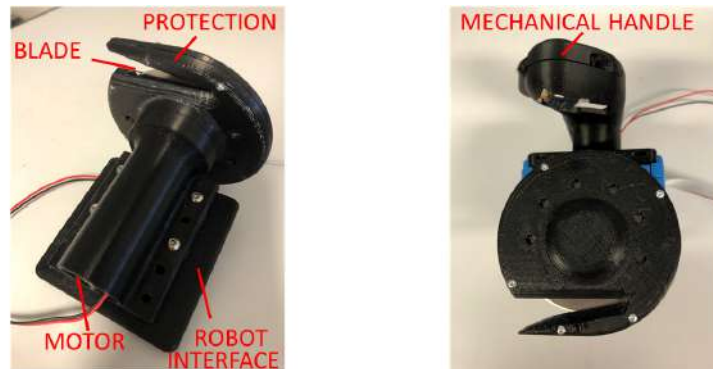


Figure 4.6: On the left, a picture of the cutter prototype; on the right, a version provided with a handle for the manual use.

evaluate their performance and problems. The list of objects on which the manual tools have been tested includes cardboard boxes of different sizes, plastic buckets, and metal cans. The manual tools that have been tested are a simple box-cutter, a circular blade cutter with an exposed blade, a linear but concealed blade cutter, and a hot-wire cutter. On the basis of the resulting performance, a concealed and circular but also actuated blade has been chosen. The protection has been sized for two purposes: preventing the contact between the objects and the blade, and facilitating the engagement between the cutter and the film. Furthermore, a protected blade is safer to be used in a human-robot shared environment. As it will be clear in the following, the plastic case that protects the blade has been leveraged to enable online refinement of the robot trajectory based on the contacts between the case itself and the environment. The actuation of the blade enables a more effective cut. The interested reader can find in [146] further details on the preliminary manual tests that brought to the design of the cutter, as well as more details on the single components of the device itself (i.e., blade model, motor, electronics).

Based on the analysis of the task challenges reported in Sec. 4.2, the goal of the robot to successfully engage the plastic film and complete the task without losing the engagement and without exerting an excessive force on the palletized items, despite the uncertainty affecting the knowledge of the pallet position and size and of the plastic film distribution. According to prior experience, especially acquired during the experiments conducted in [146, 147], it is crucially important to confer to the robot a certain awareness of the current task execution status. To do so, the robot is provided with a force and torque sensor at the wrist, as shown in Fig. 4.7. The measurements acquired by the torque and force sensor are used for contact detection, which, in turn, is exploited to augment the knowledge of the surrounding environment. This allows reacting by refining online the robot trajectory, thus enabling a robust task execution. This is particularly useful in realistic scenarios, in which the visual information of the environment are affected by uncertainty due to, e.g., noise and different light conditions. To handle the interaction forces between the cutter and the objects, a pure position control, making the robot stiff during the physical interaction, is not the most suitable solution, and would result in a very slow motion required to preserve the integrity of the goods. To overcome this issue, we choose to adopt a Cartesian impedance-controlled robot.

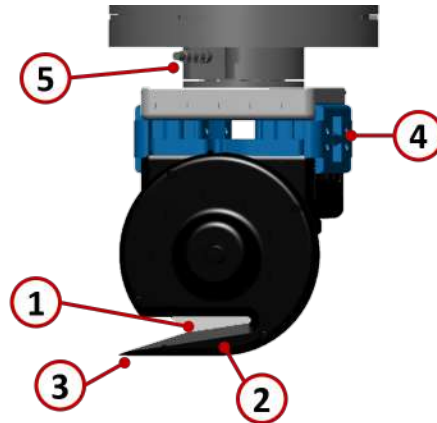


Figure 4.7: Custom cutting end-effector composed of a circular blade (1) encapsulated into a plastic case that has a tooth in its lower part (2) with a protruding tip (3). The end-effector is attached by means of a flange (4) to a force and torque sensor (5), in turn mounted on the last joint of a robotic arm.

4.3.2 Contact-based Planning Strategy

This Section provides a description of the overall planning architecture.

The first step is to plan the trajectory of the end-effector so that it follows the profile of the plastic film estimated, e.g., by a vision system. The vision system can provide an estimated profile of the pallet wrapped in plastic, which is affected by some uncertainty. Typically, for instance, RGB-D cameras do not perceive the transparent plastic layer in a reliable way. However, it is possible to process the point cloud and compute its convex hull. Thus, under the hypothesis introduced in Section 4.2 about the distribution of the plastic film along the convex hull of the objects, we can easily estimate the plastic film profile. Based on this estimation, the end-effector of the robot should move along segments with different slopes.

Whenever the slope of the plastic film changes and the end-effector proceeds forward, contacts against the plastic film occur and can be detected. Consequently, the cutter is rotated on the spot to align itself to the new slope of the plastic film. Eventually, it follows the new line, and so on. To better visualize this idea, a schematic representation is available in Fig. 4.8.

The importance of collision detection for modern physically interacting robots has been well highlighted in [156]. In that work, the fundamental steps of the collision management pipeline are divided into subsequent steps. In Fig. 4.9, the fundamental steps identified in [156] for managing collisions in physically interacting robots are schematically depicted. Specifically, the first step is collision *detection*, which returns a boolean output that informs whether a collision has occurred or not. This phase typically requires online signal monitoring, especially of force and torque measurements. Hence, whenever a collision is detected, the collision *isolation* phase takes place. This phase consists of the estimation of the exact contact location on the robot body. Hence, the exact contact wrench is estimated—collision *identification*—and the collision *classification* can take place. This is the phase in which the collision is interpreted, and hence classified into, e.g., intentional or undesired. This phase typically requires some knowledge of the context. The final step of the pipeline is the proper *reaction* to the

Chapter 4. Depalletizing: Force-aided planning for an Unwrapping Robot to Work with Non-perfectly Known Pallets.

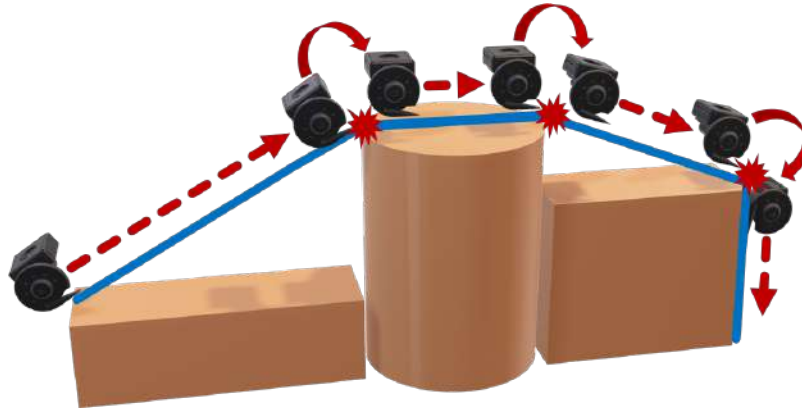


Figure 4.8: Schematic representation of the trajectory of the cutter during the unwrapping execution. The cutter is depicted in black, the boxes in the underlying pallet are brown and the plastic film is the light-blue line. From left to right, different instants of the task are displayed. Contacts on the tip of the cutter against the plastic film are visualized with a red symbol. Only intentional contacts are displayed. They inform the robot that it should rotate the end-effector according to the slope of the following film segment. Movements forward of the cutter are indicated with red dashed arrows, and cutter rotations are signaled by red arrows.

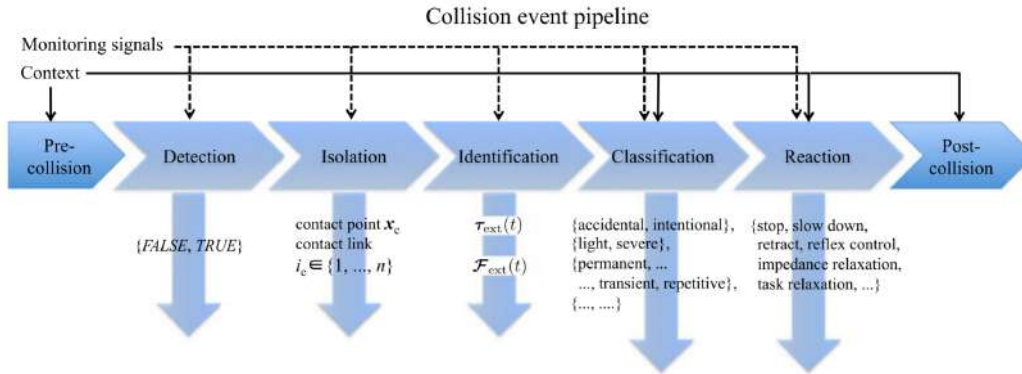
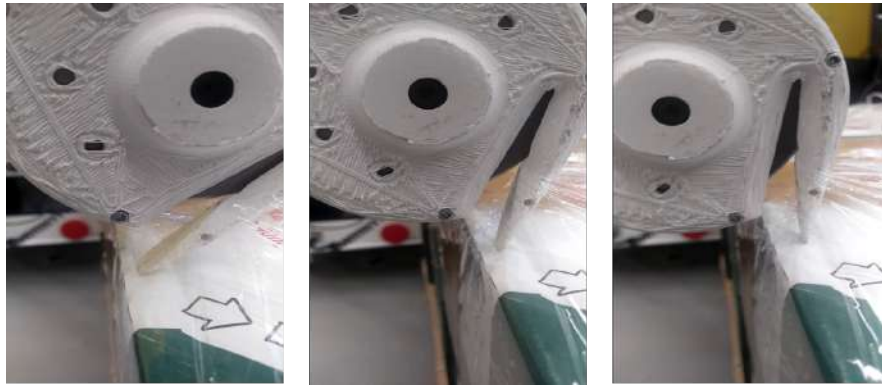


Figure 4.9: ©2017 IEEE. Pipeline of the collision management in physically interacting robots. Source: [156].

collision event. Following the classification of the collision management pipeline introduced in [156], in the remainder of this Section, I am going to explain how each step has been implemented in this work. It is worth highlighting how the exploitation of the contact information allows correcting the uncertainties that affect the knowledge of the environment provided by the perception system. In Fig. 4.10, we provide two different examples of pathological conditions that may take place under uncertain knowledge of the pallet edge position and that can be managed in an effective way through contact-based planning. Without proper planning, these conditions would result in task failure. Note that failure due to the wrong detection of the edge of the pallet constituted the greatest source of failure in the experiments shown in [146].

First, the skeleton of the proposed planner is composed of a finite-state machine, as schematically depicted in Fig. 4.11. As already mentioned, the starting point for defining the end-effector trajectory that is required to execute the cut is based on the plastic film estimated profile. More specifically, the trajectory is a broken line that



(a) The cutter rotates too early remaining stuck against the pallet surface while trying to cut downward.



(b) The cutter rotates too late causing the rupture of the film.

Figure 4.10: *Two pathological conditions that might take place in the case of a cuboid pallet characterized by an incomplete top wrapping.*

follows the plastic film profile. The different values of the slope and the points where the slope is expected to change (and hence a collision between the end-effector and the plastic to take place as in Fig. 4.8) can be stored. In order to achieve the sought robot behavior, the overall trajectory is hence decomposed into states of the finite-state machine.

Some states are defined to perform the initial engagement of the plastic film, better detailed Section 4.3.6, and labeled as FILM ENGAGEMENT in Fig. 4.11. After this initialization procedure, one fundamental state corresponds to a forward motion of the cutting end-effector—labeled as MOVE FORWARD in Fig. 4.11; the other basic state corresponds to a rotation of the end-effector on the spot aimed to align it to the slope of the subsequent film segment—this state is labeled as ROTATE in Fig. 4.11. Note that “forward”, as well as similar expressions that can be found in the following to refer to commanded end-effector movements, is expressed in a local frame fixed to the cutter. “Forwards” means in a direction aligned with the tooth of the cutter pointing to the tip; I shall write “backwards” to refer to the opposite movement. “Upwards” will refer to a movement in the direction orthogonal to the tooth of the cutter and pointing from the base of the cutter towards its center; an opposite motion will be referred to as “downwards”. Additional states—generally labeled as CORRECTIONS in Fig. 4.11—contain pieces of trajectory purposely designed as reactions to adjust the pre-planned

Chapter 4. Depalletizing: Force-aided planning for an Unwrapping Robot to Work with Non-perfectly Known Pallets.

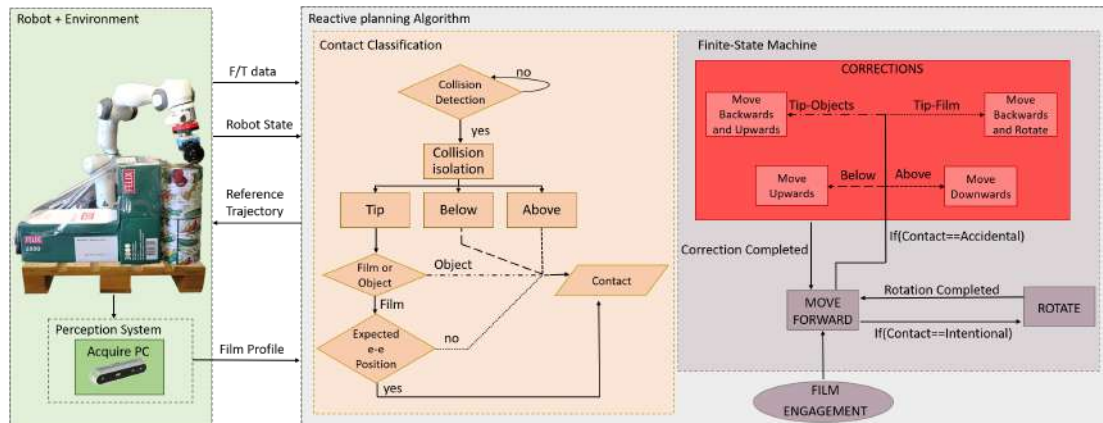


Figure 4.11: A schematic representation of the overall reactive planning strategy. The trajectory that the end-effector (e-e) must execute is first derived from the information provided by the perception block, which estimated the plastic film profile from the point cloud (PC) of the scene. The refined reference trajectory comes from the Finite-State Machine block, in which each state contains a piece of the trajectory. After an initialization phase (FILM ENGAGEMENT), the cutter moves forward (MOVE FORWARD state). The transition between the states is triggered by Contact Classification (enabled by the force and torque (F/T) data and by the knowledge of the robot state, especially the e-e position), or by the completion of a predefined movement, e.g., a rotation. If an intentional contact takes place the cutter rotates (ROTATE block) to align itself to the slope of the plastic film. If an accidental collision is detected, instead, a corrective action takes place (states contained into the CORRECTIONS block). In this way, the reference trajectory is planned on-the-fly and sent to the robot.

path to the environment.

The transitions between two states are triggered either by the *reaction* to a detected, isolated, identified, and classified collision (from MOVE FORWARD to ROTATE or to CORRECTIONS) or by the completion of a predefined movement (e.g., from ROTATE to MOVE FORWARD). The former is the reason why the planning strategy is sometimes referred to as *reactive*. The reactive behavior, in this case, refers to the activation of a state transition (the transition to a subsequent piece of trajectory), based on contacts with the environments. Note that, indeed, even for the same structured pallet, the final path followed by the end-effector cannot be foreseen but it depends, e.g., on the estimated film profile, or on the fact that, during the cut, the film profile may be unpredictably slightly altered by the cut itself, affecting the contacts that will arise between the end-effector and the plastic film. Anyway, the trajectory is not continuously re-planned but the final trajectory is composed of pre-defined pieces, the number and the order of which are determined online as a reaction to contacts with the environment. Note that a pre-defined piece of trajectory may be, for instance, moving in a certain direction until an event takes place. Consequently, in this case, the amount of displacement is also not set a priori.

4.3.3 Collision Classification and Reaction

The *classification* procedure discriminates between two main classes of collisions: *undesired* and *intentional*. The former is due to imperfect knowledge of the environment (typically, a wrong estimation of the slope of the plastic film segments); the latter is ex-

	ABOVE	BELOW	TIP	
OBJECT	N.D.	UNDESIRE	UNDESIRE	
FILM	UNDESIRE	N.D.	EXPECTED E-E POSITION	UNEXPECTED E-E POSITION
			INTENTIONAL	UNDESIRE

	ABOVE	BELOW	TIP	
OBJECT	N.D.	MOVE UPWARDS	MOVE BACKWARDS, THEN UPWARDS	
FILM	MOVE DOWNWARDS	N.D.	EXPECTED E-E POSITION	UNEXPECTED E-E POSITION
			GO TO THE «ROTATE» STATE	MOVE BACKWARDS, THEN ROTATE

Figure 4.12: The top table contains the output of the contact classification phase, and the bottom table contains the output of the contact reaction phase, where *N.D.* stands for not defined. The inputs of the tables are the result of the collision isolation phase and of the environment categorization phase. The bottom right part of the tables is further split based on an additional input, i.e., the position of the end-effector in the world. This is an expected position if it corresponds to a point in which, based on the estimated profile of the film, we expect the film to change its slope, or an unexpected position otherwise.

pected, in the sense that our planning strategy expects such a collision to take place in order to complete the task execution, (i.e., a collision between the tip of the cutter and the plastic film when this is supposed to change its slope, as represented in Fig. 4.8). The *classification* procedure takes as inputs the result of the previous *isolation* phase, the position of the robot end-effector in the world, and the information telling if the cutter collides against an item on the pallet or the plastic film. Let us call this last phase *environment categorization*. The *isolation* phase computes the location of the contact point on the surface of the end-effector, distinguishing among contacts *below* the tooth of the end-effector, *above* it, or on its *tip*. Contact *isolation* is detailed in Section 4.3.4. *Environment categorization* is explained in Section 4.3.5.

The outputs of contact *classification* and *reaction*, which determines the behavior of the robot end-effector, are summarized in Fig. 4.12 and explained in the following.

- Contacts **below** and contacts **above** the tooth of the cutter are regarded as undesired. In fact, ideally, the cutter would follow the profile of the plastic film exactly, without pulling the film upwards—generating contacts above the tooth—nor pushing against the underlying boxes—generating contacts below the tooth. The *reaction* to these collisions is a transition between the MOVE FORWARD state to one state of the CORRECTIONS block that makes the end-effector move downwards (if the collision is above) or upwards (if the collision is below) until the corresponding collision is not detected anymore.
- Contacts on the **tip** of the cutter **against the objects** stacked on the pallet are always classified as undesired collisions. The *reaction* is a transition between the MOVE FORWARD state to one state of the CORRECTIONS block that makes

Chapter 4. Depalletizing: Force-aided planning for an Unwrapping Robot to Work with Non-perfectly Known Pallets.

the end-effector move backward until the tip does not collide anymore, and then upwards. The upward motion stops when a contact above (against the plastic film) is detected. Hence, the robot can go back into the MOVE FORWARD state to keep executing the cutting task.

- A **tip-contact against the plastic film** may be classified either as undesired or intentional. If it takes place when the position of the end-effector in the world corresponds to the region in which we expect the plastic film to change its slope, the collision is classified as intentional. In fact, it informs the robot that the slope of the plastic film has changed and hence it should rotate accordingly. The *reaction* is a transition between the MOVE FORWARD state to the ROTATE state. The direction of the rotation is so that the cutter aligns itself with the following plastic film segment. The region in which the plastic film is expected to change its slope is based on the estimation of the film distribution provided by the vision module.
- On the other hand, **tip-contacts against the plastic film** that take place out of the expected regions are classified as undesired and are due to the wrong alignment between the end-effector and the current segment of the plastic film. In this case, the *reaction* is a transition between the MOVE FORWARD state to one state of the CORRECTIONS block that makes the end-effector move backward until the contact is not sensed anymore and then rotate so to move the tip downward. The amount of the rotation is to be picked by the user. Intuitively, to avoid over-correcting, this amount should be smaller than the error we expect in the estimation of the slope from the vision system.

Figure 4.8, actually represent a successful task execution in which contacts on the tip of the cutter against the plastic film are *intentional* and serve as a flag to inform the robot that the plastic film slope has changed and that it should adapt its orientation properly. In fact, the task execution is made of successive transitions between MOVE FORWARD and ROTATE states.

Remark: Every time a tip-contact against an object occurs, we command the cutter to move upward. This reaction is proper because we suppose that the objects lie below the cutter. However, the underlying assumption is also that the shape of the objects is regular (a box or a cylinder as detailed in Section 4.2). Otherwise, in the presence of an object showing concavities on its surface, the tip of the cutter could enter one of these holes and a movement upward would not be suitable to free it. It is to be expected that the collision classification and reaction phases are based on some knowledge of the context, as explained in [156]. Anyway, also to account for possible small irregularities on the surface of the objects, we also command a backward motion any time a tip-contact against an object occurs.

4.3.4 Collision Detection and Isolation

This section explains collision *detection* and successive *isolation*, which output is necessary to the *classification* and *reaction* procedure described in the previous Section.

In order to achieve collision *detection*, we constantly monitor the signals provided by the force and torque sensor at the wrist of the robot. Hence, a collision is detected whenever the intensity of the signal exceeds a certain threshold. Note that the force

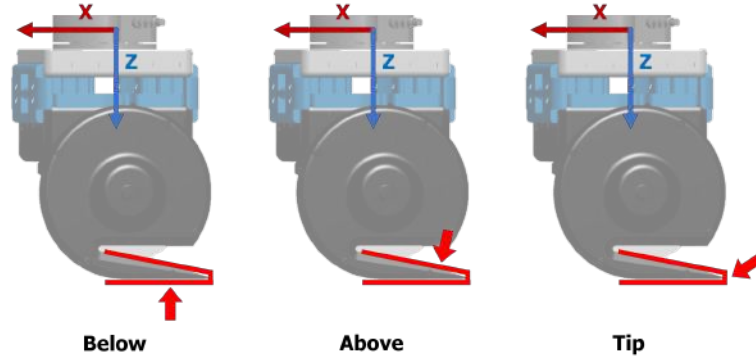


Figure 4.13: Planar representation of the three contact locations that we isolate. The portion of the cutter interested in the collisions (the tooth) is highlighted with a red line. The force and torque sensor is the grey cylinder on top of the flange of the cutter. Its local reference frame (sensor frame) is in black. A red arrow represents the contact force in each case. The contact can take place, from left to right, below the tooth of the cutter, above it, or on its tip.

exerted by the film on the blade during the cut is usually negligible during normal execution compared to the intensity of the forces that arise during significant contacts with the environment.

Whenever a contact is detected, contact-point location on the surface of the end-effector is estimated in the *isolation* phase. The inputs of the isolation phase are the force and torque sensor data and the end-effector geometry. The estimation of the contact-point location based on wrench measurements has been proposed already in [157]. Taking inspiration from [157], we adapt that idea to our case.

In our case, it is sufficient to consider the planar case, as depicted in Fig. 4.13. The estimated contact location is given in a reference frame fixed to the robot end-effector, referred to as the sensor frame (black frame in Fig.4.13). Let us consider that contacts take place on the tooth of the cutter, highlighted in red in Fig.4.13. The origin of the sensor frame is such that z_1 is the z-coordinate of the lower horizontal surface of the cutter tooth, z_2 is the z-coordinate of the upper cutter surface. Let us indicate with $F = [F_x \ F_y \ F_z]^T$, the force measured by the sensor, with $\tau = [\tau_x \ \tau_y \ \tau_z]^T$ the wrench measured by the sensor, and with $C = [C_x, C_y, C_z]^T$ the contact force. The contact point has a position $p_c = [x_c \ y_c \ z_c]^T$. All components are expressed in the sensor frame.

As in [157], we can write that

$$\begin{cases} F = C \\ \tau = p_c \wedge C, \end{cases} \quad (4.1)$$

where \wedge is the cross product operator, and we are assuming that no pure torques act at the contact. This means that the contact happens on a point and not on an extended surface. The force exerted by the film on the active blade during the cut is usually negligible. However, depending also on the type of plastic film and the number of layers, the intensity of such a force might be higher. In those cases, it is possible to suppose that the force exerted by the film on the blade is constant and, hence, compensate for it in the sensor measurements.

Chapter 4. Depalletizing: Force-aided planning for an Unwrapping Robot to Work with Non-perfectly Known Pallets.

Given the measured wrenches and the cutter geometry, and considering the planar case as in Fig. 4.13, we can write (4.1) as:

$$\begin{cases} F_x = C_x \\ F_z = C_z \\ \tau = z_c C_x - x_c C_z. \end{cases} \quad (4.2)$$

Hence, we have:

$$x_c = \frac{z_c F_x - \tau}{F_z}, \quad (4.3)$$

Referring to Figure 4.13, we distinguish among the three following contact cases:

1. **contact below:** $z_c = z_1$ in (4.3), $C_z < 0$, and $\underline{x}_c \leq x_c \leq \bar{x}_c$, where \underline{x}_c and \bar{x}_c are the ranges within which x_c can vary based on the geometry of the cutter. The cutter is pushed from below, typically due to the underlying objects;
2. **contact above:** $z_c = z_2$ in (4.3), $C_z > 0$, $\underline{x}_c \leq x_c \leq \bar{x}_c$. The cutter is pushed from upward, typically it tears the plastic film upwards;
3. **tip-contact:** $C_x > 0$, x_c exceeds \bar{x}_c . This contact type might be due either to a collision against the objects or against the plastic film.

The contact-point isolation procedure is summarized in algorithm 1.

Algorithm 1 Estimation of the contact location

```

1: function COLLISION ISOLATION ( $z_1, z_2, F, \tau$ )
2:   if  $F_z < 0$  then
3:      $z_c = z_1$ 
4:      $x_c \leftarrow Eq.(4.3)$ 
5:     switch  $x_c$ :
6:       case  $\in [\underline{x}_c, \bar{x}_c]$ 
7:         return Below
8:       case  $< \underline{x}_c$ 
9:         return Tip
10:      case  $> \bar{x}_c$ 
11:        return Error
12:   if  $F_z > 0$  then
13:      $z_c = z_2$ 
14:      $x_c \leftarrow Eq.(4.3)$ 
15:     switch  $x_c$ :
16:       case  $\in [\underline{x}_c, \bar{x}_c]$ 
17:         return Above
18:       case  $< \underline{x}_c$ 
19:         return Tip
20:       case  $> \bar{x}_c$ 
21:         return Error

```

4.3.5 Environment Categorization

Distinguishing between a tip-contact against the plastic film and a tip-contact against the underlying objects represents a key feature for planning the robot behavior correctly. We propose to distinguish between the two cases by looking at the variation of the

interaction force intensity w.r.t. the cutter displacement when the tip-contact occurred. In this way, we retrieve information about the stiffness of the environment. Hence, under the hypothesis that the objects are always stiffer than the plastic film, it is possible to distinguish between the two by looking at the estimated stiffness values and then classify the tip-contacts accordingly.

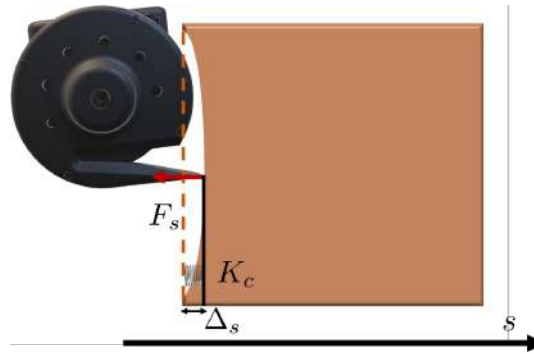


Figure 4.14: Schematic representation of a collision between the tip of the cutter and the environment. The environment (the brown shape in the picture) deforms after the contact, generating on the cutter a force F_s proportional to the deformation through the stiffness K_e .

More specifically, consider that the cutter moves along a direction s and that its tip makes contact with the environment. Moving forward, the cutter deforms the objects of a quantity Δ_s . Let us model the environment as a spring with stiffness K_e (see Fig. 4.14 for a schematic representation). Since the collision occurred, the robot end-effector senses a force in the s direction of intensity $F_s = K_e \Delta_s$. Eventually, we compute the value of K_e by differentiating F_s w.r.t. the motion of the end-effector along s since collision detection.

4.3.6 Film Engagement

The very first phase of the unwrapping task consists of the approaching phase and ends with the engagement of the plastic film. In this sort of initialization phase, indicated as FILM ENGAGEMENT in Fig. 4.11, the cutter moves perpendicular to the surface of the pallet until it touches it (a contact below is detected). This is the only time a contact below is intentional, and it triggers a forward motion until the cutter engages the plastic film. The force measurements allow establishing the film engagement. Indeed, when the plastic film is engaged, the blade is initially turned off, so that the film enters between the blade and the tooth of the cutter. By doing so, it exerts a force against the blade of the cutter that opposes to the forward motion of the cutter. Finally, after the film engagement is detected thanks to the force exerted by the film, the blade is activated. At this point, the cutter moves slightly upward not to unnecessarily slide further on the objects and possibly damage them. Then, the cut takes place. The robot enters the ROTATE state to align itself to the slope of the plastic film, then moves to the MOVE FORWARD state, and so on.

4.4 Experimental Validation

For the experiments, we used a Franka Emika Panda robotic manipulator equipped with an ATI mini45 force and torque sensor at the wrist. The robot is controlled via compliance control law¹, which does not require the feedback of the external wrench. The result is non-decoupled operational space dynamics with no possibility to reshape the inertia matrix. The control gives the possibility to tune the diagonal impedance K , and, chosen a critically damped behavior, automatically set the damping matrix D . As for the impedance values, they have been chosen as in [146] $K_x = 500\text{N/m}$, $K_y = 400\text{N/m}$, and $K_z = 200\text{N/m}$. These values allow for a reasonably precise position of the robot in free motion and for a sufficiently compliant behavior when it is in contact with the environment. While the impedance planning was more critical in [146] since it determined the maximum force exerted on the objects, the contact-based planner relax the need for precise impedance planning.

The reactive planner has been implemented in Matlab-Simulink. State Flow has been used to implement the finite-state machine. The Simulink scheme runs at a frequency of 50 Hz. Matlab-Simulink interfaces with ROS: from one side, it reads force and torque data from the sensor, and the end-effector pose from the robot; from the other side, it sends the reference trajectory commands to the robot controller.

4.4.1 Validation of the Contact Isolation Procedure

First, we present some results to validate algorithm 1. The geometric parameters of the cutter have been set as $z_1 = 0.105\text{m}$ and $z_2 = 0.1\text{m}$. The experiments consisted of touching the cutting end-effector in a series of points while recording the measurements of the force and torque sensor. Hence, the position of the contact point on the end-effector has been estimated thanks to algorithm 1 and compared with the position estimated through image processing leveraging the software Kinovea. The results of one of the collision isolation test is illustrated in Fig. 4.15, where both the estimate of x_c provided by algorithm 1 and by image processing are reported. The location of the contact point is computed only when a collision is detected. The collision detection threshold has been set equal to 3N. Only if the intensity of the measured forces exceeds the threshold a collision is positively detected.

Even though the estimation of the contact point is not extremely accurate, it allows to reliably distinguish between tip- and non-tip- contacts. The distinction between contacts above and below the cutter, in our case, can always rely upon evaluation of the reaction forces. In fact, a contact above always corresponds to a force (exerted by the plastic) that pushes the tooth downward ($F_z > 0$), while a contact below always corresponds to a force (exerted by the objects) that pushes the tooth upward, against the blade ($F_z < 0$). The sensor frame is depicted in Fig. 4.13. Based on the validation of the contact-point location as shown, e.g., in Fig. 4.15, lower and upper bounds of $\bar{x}_c = 0.07\text{m}$ and $\bar{x}_c = -0.07\text{m}$ has been set to reliably distinguish collisions below or above the tooth from those on the tip.

¹Code available at https://github.com/CentroEPIaggio/franka_softbots

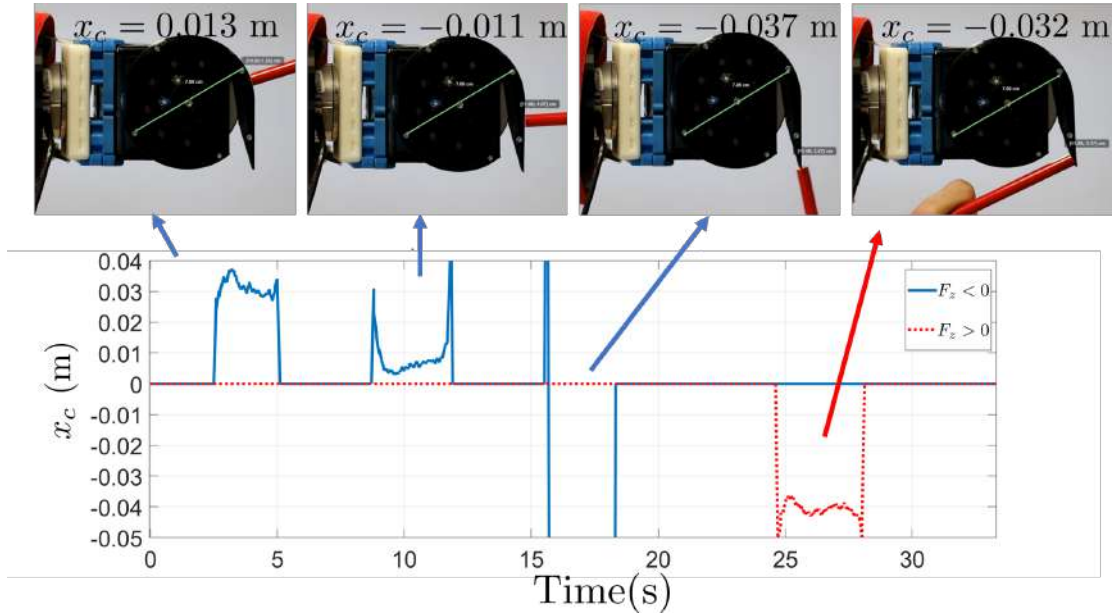


Figure 4.15: Validation of the contact-point estimation. The values on top of the screenshots are estimated using the software Kinovea, while the second graph is the result of the estimation algorithm 1. The estimation is affected by a little bias, but it is capable of distinguishing among the three cases in Fig. 4.13 in an effective way. Indeed, the tip contact produces an estimated value of x_c that is considerably out of the geometric parameters of the cutter. The signal is cut in correspondence of the tip-contact to fit the scale in order to appreciate the rest of the signal evolution. For the sake of completeness, we report that the minimum value reached by the signal suppressed in the plot is -0.36m .

4.4.2 Validation of the Environment Categorization

In this Section, I report the results of experiments that validate the procedure proposed in Section 4.3.5 to decide whether tip-contacts take place against the plastic film or the objects. Such a distinction is based on the estimation of the stiffness of the material with which the cutter makes contact. The underlying assumption is that the stiffness of the objects on the pallet is higher than that of the plastic film. From Fig. 4.16, it is possible to see that the estimated stiffness of a carton box and that of the plastic film are different, as expected. We report here experiments with a carton box as a worst-case scenario. In fact, other objects that we employ for the experiments, e.g., metal bins, are even stiffer, and thus distinguish them from the plastic film should result easier. In the experiments reported in the remainder of the paper, we reliably distinguish between objects and plastic film by defining a stiffness threshold equal to 1000N/m . A buffer is used so that at least 4 consecutive samples must be over/under the threshold for a tip-contact to be classified into object/plastic-film contact. In this way, the classification is more robust to noise that may generate outliers, at the expense of some reactivity. In fact, the result is that the classification of the tip-contacts between contacts against the plastic and against the object runs at 12.5 Hz .

Chapter 4. Depalletizing: Force-aided planning for an Unwrapping Robot to Work with Non-perfectly Known Pallets.

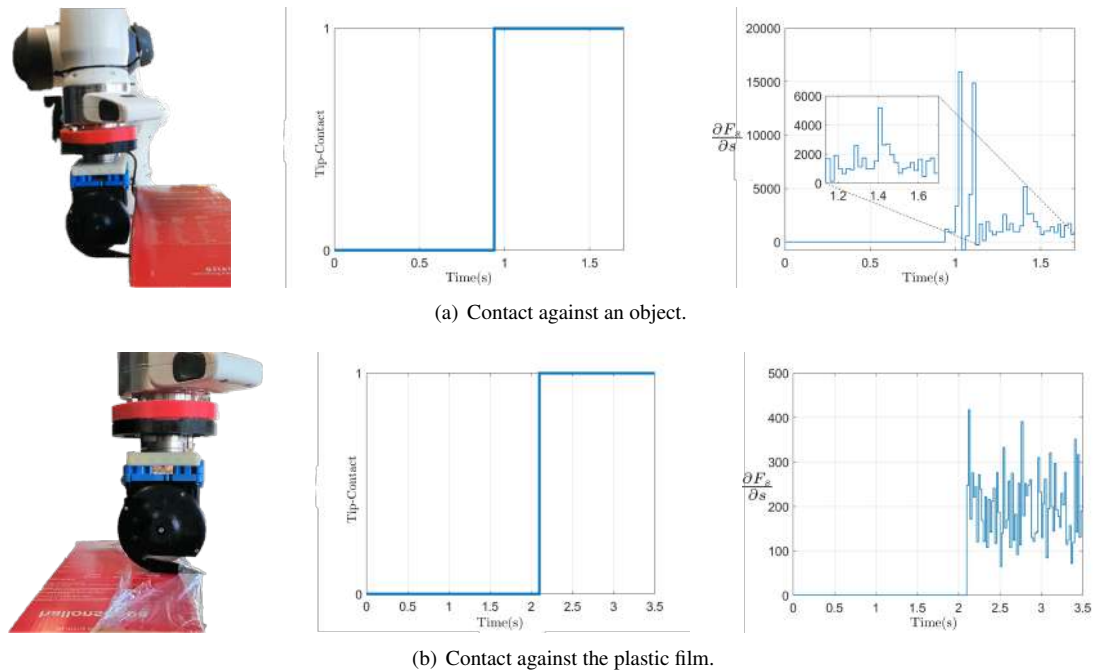


Figure 4.16: Validation of the environment categorization. On the top line, the cutter makes contact with the box; on the bottom line, with the plastic film. The first column shows a picture of the respective experimental setup. The second column contains the boolean value of the identification of a tip contact: 0 means that no tip-contact has been detected, and 1 that a tip contact has been detected. The third column shows the plot of the variation of the measured force in the direction of the motion, F_s , w.r.t. the cutter displacement, s , whenever the a tip-contact is isolated; it is possible to appreciate that its value is higher by up to two orders of magnitude when the contact is against the box than when it is against the film.

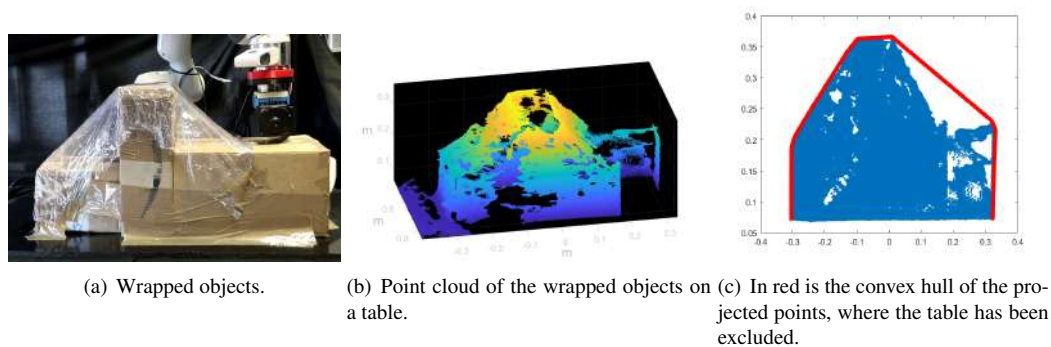


Figure 4.17: From left to right: some objects wrapped in a plastic film, their point cloud acquired by two RGB-D cameras, and the point cloud elaboration to estimate the profile of the film. The convex hull is highlighted in red in the picture on the right.

4.4.3 Validation of the Overall Method

After verifying that all the phases of the contact management pipeline work satisfactorily, we tested the overall unwrapping strategy. Every time an undesired collision with the plastic film is detected, the amount of rotation performed as a correction of the end-effector orientation is equal set to 10deg. After experimental evaluation, this

parameter has been found as a good trade-off. In fact, the amount of corrective rotation should not be too large, and hence greater than the end-effector alignment error, or too small, making a lot of subsequent corrections necessary and, thus, increasing the task execution time.

First, in Fig. 4.17(b) we provide the point cloud of the generally shaped pallet shown in Fig. 4.17(a). The point cloud of the wrapped items has been collected using two RealSense cameras. While the cameras perceive the objects, due to the transparency of the plastic film, depending on the environmental conditions, we cannot be sure to be able to collect the overall point cloud of the plastic itself. Hence, we estimate the profile of the film by supposing that it distributes along the convex hull of the objects. Should the transparent film be undetectable by the vision system due to adverse light conditions, the convex hull of the object point cloud would still return an estimation of the plastic film profile. Fig. 4.17(c), in particular, shows the convex hull (red points) of the point cloud, extracted using Matlab Computer Vision Toolbox. The red broken line that connects the points on the convex hull is a starting point for the trajectory of the robot end-effector. Even though it may constitute a rough approximation of the actual film profile and so of the path required to successfully unwrap the pallet, the contact-based planning strategy that we presented enables online autonomous correction of the end-effector trajectory to adapt to the actual film slope.

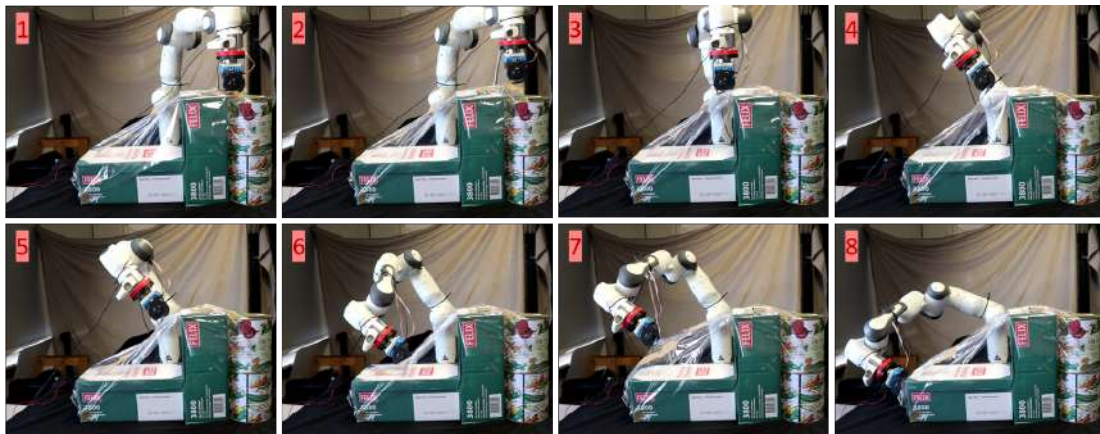
The proposed autonomous unwrapping method has been tested in many different conditions, obtaining positive results. We used the system on both cuboid and stepped pallets. The objects employed in the experiments include cuboid and cylindrical items of different materials and dimensions: specifically, metal bins and carton boxes. In this Chapter, I report the results of three experiments in total. The results are shown through photo sequences of significant instants of the task execution, plots of the end-effector pose, and plots of the detected, isolated, and classified contacts.

First, Fig. 4.18 and Fig. 4.19 show the unwrapping of two stepped pallets made by both metal bins and carton boxes of different sizes and with different configurations. Tape on the plastic film shows that the robot can manage the task in the presence of tags and labels. The pallet in Fig. 4.18 requires a shorter path to complete the unwrapping than that in Fig. 4.19. Moreover, in Fig. 4.19, the film is not always uniformly stretched. Our unwrapping method is successful in unwrapping both the complex irregular pallets

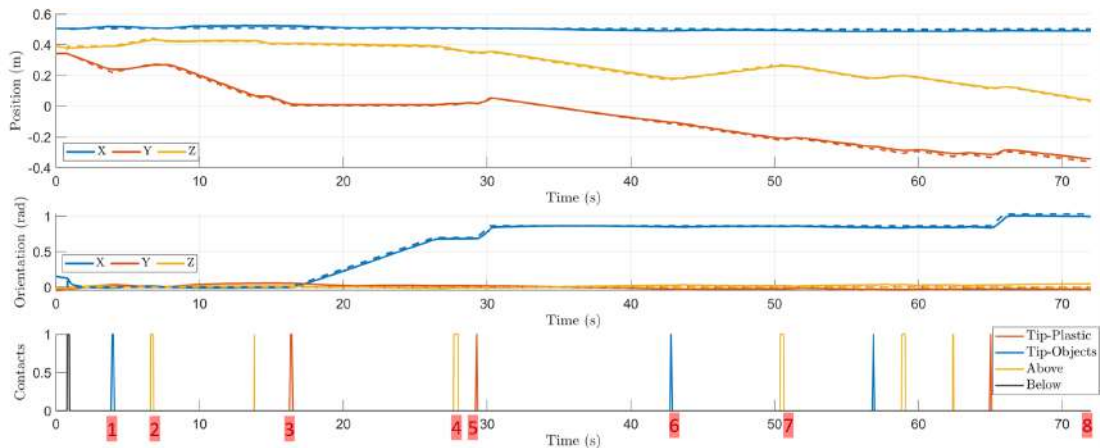
Fig.4.20 reports the results of an experiment in which our robot performs the unwrapping of a cuboid pallet. The metal bins that compose the cuboid pallet show some irregularities in their top surface, i.e., a ridge along the rim. The cutter collides with the rim during the task execution but, instead of remaining stuck, it carries out the cut successfully by detecting the contact and appropriately reacting to it. Moreover, the contact-based planner allows rotating at the right moment when the cutter arrives at the edge of the top surface of the pallet. Note that this point was the most critical one in the unwrapping of cuboid pallets carried out in previous work [146].

To better appreciate all the experimental results, the reader is referred to the video available at https://www.dropbox.com/s/tappl0we0gk40m0/Video_submission.mp4?dl=0, in which these and further results on different object configurations are shown. In the video, the reader can also appreciate the unwrapping of a pallet with a curved profile. Specifically, the end-effector moves along the side of a cylinder. This

Chapter 4. Depalletizing: Force-aided planning for an Unwrapping Robot to Work with Non-perfectly Known Pallets.



(a)



(b)

Figure 4.18: Fig. 4.18(a) shows some significant instants of the unwrapping of a heterogeneous pallet composed of metal bins and carton boxes, while Fig. 4.18(b) contains the corresponding identified contacts and the desired (dotted line) and actual (solid line) pose of the robot end-effector. The pose is expressed in a frame fixed to the base of the robot, with the x-axis pointing towards the reader, the z-axis pointing upwards, and the y-axis computed accordingly. Each frame in Fig. 4.18(a) is labeled with a colored number that puts it in relation with the corresponding event in Fig. 4.18(b). After the film engagement, in frame 1 a collision between the tip of the cutter and an object occur, hence the cutter reacts with a correction movement, moving upwards until it senses a contact above (frame 2); after proceeding forward, an undesired collision above is addressed; in frame 3 the tip makes contact with the plastic film, hence the cutter rotates to align itself to the new slope; in frame 4, after the rotation, contact above is detected, hence the cutter moves downward (see the Y and Z components of the robot position corresponding to frame 5); a collision between the tip and plastic is detected right after, and the robot rotates consequently; then, a collision with the objects is detected in frame 6, and the cutter moves upwards until it senses a contact above in frame 7; similar undesired contacts take place and are successfully managed until, eventually, the task is completed (frame 8).

case does not explicitly fall into our problem statement. However, the proposed approach shows its validity even in this scenario.

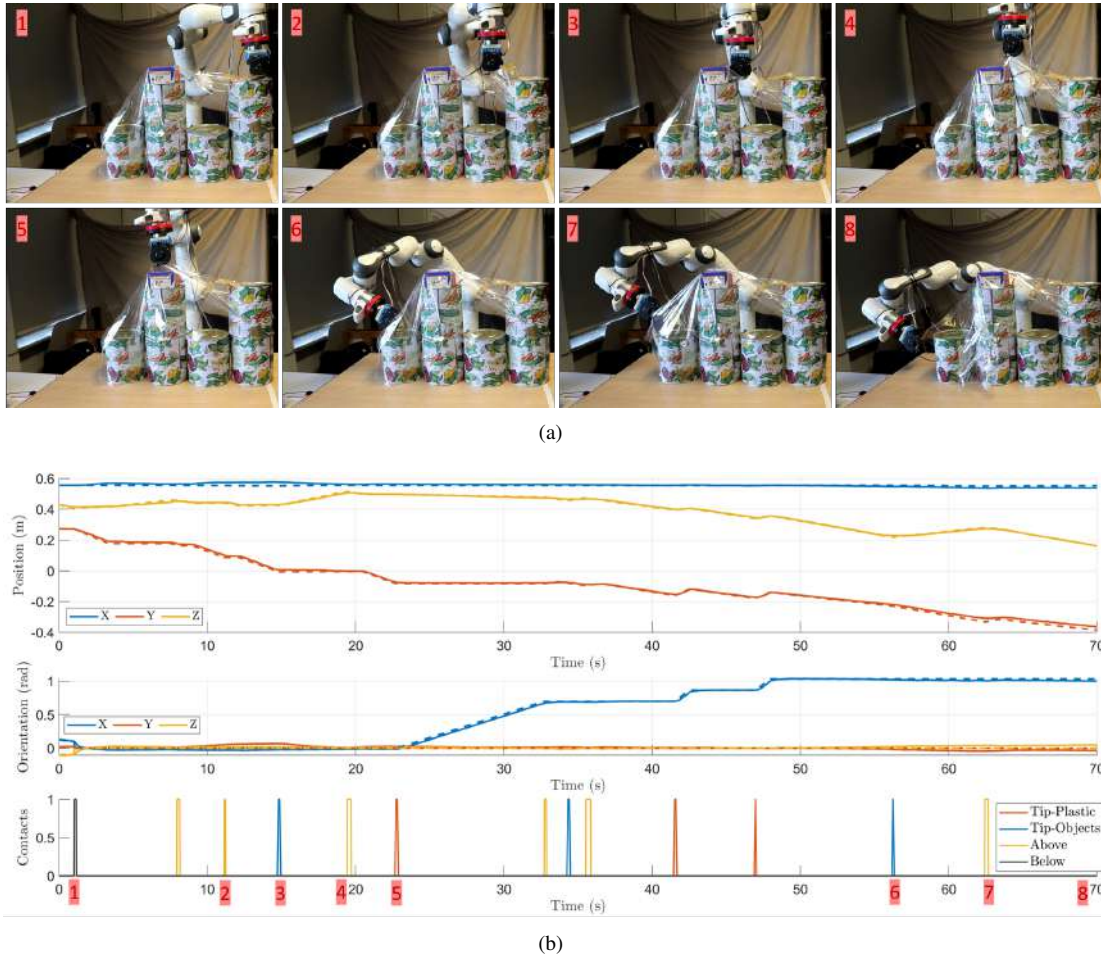
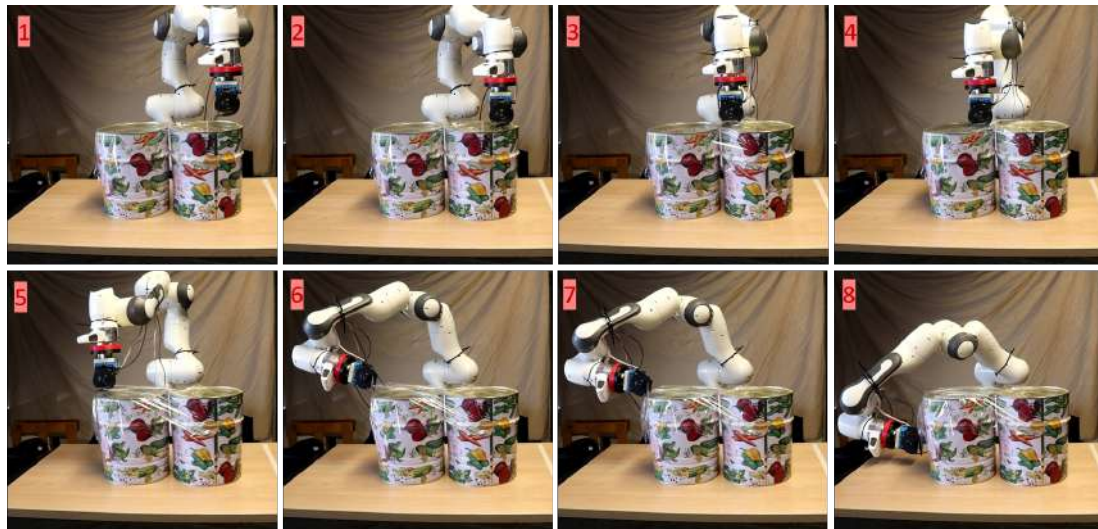


Figure 4.19: Fig. 4.19(a) shows some significant instants of the unwrapping of a heterogeneous pallet composed of metal bins and a carton box, while Fig. 4.19(b) contains the corresponding identified contacts and the desired (dotted line) and actual (solid line) pose of the robot end-effector. The pose is expressed in a frame fixed to the base of the robot, with the x-axis pointing towards the reader, the z-axis pointing upwards, and the y-axis computed accordingly. Each frame in Fig. 4.19(a) is labeled with a colored number that relates it to the corresponding event in Fig. 4.19(b). Frame 1 corresponds to the contact below the cutter against the top surface of the objects within the film engagement procedure; after the film is engaged and the cut started, some collisions above are detected (e.g., frame 2), and the cutter moves downward, consequently; in frame 3, the cutter tip makes contact with an object, hence the cutter, as a reaction, moves upward until a contact above is detected (frame 4); the robot comes back to the MOVE FORWARD state, and proceeds; a collision between the tip of the cutter and the plastic film is sensed (frame 5) and the cutter rotates to align itself to the new slope; some undesired collisions above and on the tip (both against the plastic and the objects) are detected and addressed: for instance, in frame 6, the cutter hurts the objects with its tip, and it moves upward until a contact above is detected in frame 7; eventually, the task is completed successfully (frame 8).

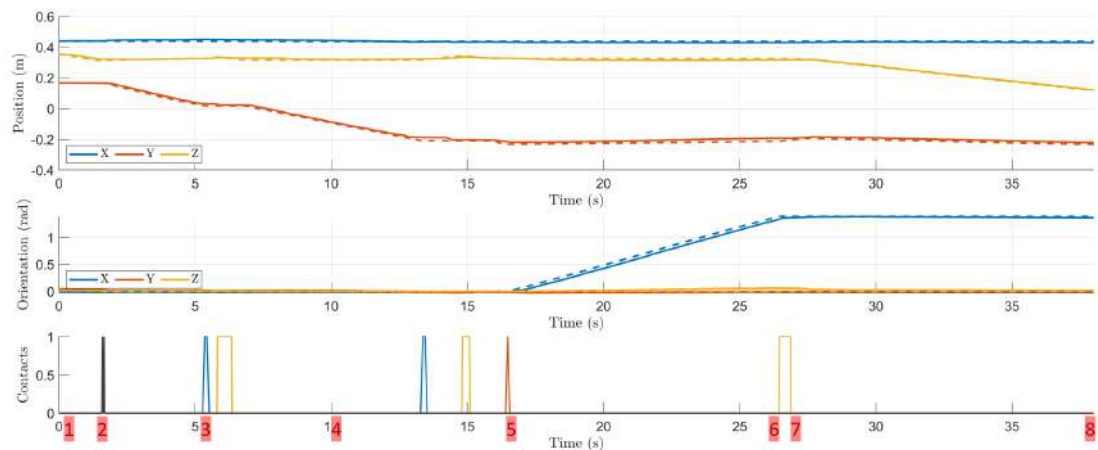
4.5 Discussion

This Chapter presented a practically working relocatable unwrapping robot, which is an important step towards a completely integrated solution to efficient automatic unwrapping. The solution proposed in this chapter consists of a robotic manipulator equipped with a custom cutting end-effector. The robot can be easily mounted on a small mobile

Chapter 4. Depalletizing: Force-aided planning for an Unwrapping Robot to Work with Non-perfectly Known Pallets.



(a)



(b)

Figure 4.20: Fig. 4.20(a) shows some significant instants of the unwrapping of a homogeneous cuboid pallet composed of metal bins, while Fig. 4.20(b) contains the corresponding identified contacts and the desired (dotted line) and actual (solid line) pose of the robot end-effector. The pose is expressed in a frame fixed to the base of the robot, with the x-axis pointing towards the reader, the z-axis pointing upwards, and the y-axis computed accordingly. Each frame in Fig. 4.20(a) is labeled with a colored number that relates it to the corresponding event in Fig. 4.20(b). The robots start the task in frame 1; hence, it moves downward to initiate the film engagement phase; in frame 2, it reaches the top surface of the objects and consequently senses a contact below; the film is engaged and the cutter moves forward until the robot detects an undesired collision between the tip of the cutter and an object in frame 3 (the metal bins have a ridge on the rim, and the robot end-effector collides with it); the robot reacts properly by moving upwards until a collision above is detected, so that the obstacle is overcome and the robot can go back to the MOVE FORWARD state (see, e.g., frame 4); an undesired contact against the rim happens again in correspondence to the second bin; after overcoming this obstacle, the cutter senses a tip-contact against the plastic film (frame 5), and rotates accordingly; after rotating, a contact above is detected (frame 6) so that the cutter moves downward (frame 7); eventually, the task is completed successfully (frame 8).

base. Consequently, the resulting relocatable platform has a reduced footprint not limit-

ing the efficiency of the warehouse, which is one of the main problems of the solutions available in the market nowadays. Integration of force and torque measurements have been exploited to develop a planning strategy based on contact detection, isolation, and classification. The strategy makes the task execution effective and robust to uncertainties while allowing also the unwrapping of heterogeneous, irregularly shaped pallets. The efficacy of the proposed method has been validated through experiments.

In the future, an additional degree of freedom, i.e., a prismatic joint at the base of the robot, will be integrated to augment the robot workspace in the vertical direction. In fact, real-world pallets may reach considerable heights. On the other hand, the workspace of the robot in the horizontal plane will be extended by suitable control of the mobile base. A perception system capable of distinguishing the regions covered in plastic from the uncovered ones will be investigated. Eventually, extensive testing in real-world scenarios should be carried out to assess both reliability and time-efficiency in more realistic working conditions. Unwrapping in the presence of typical plastic straps and different types of film, e.g., the shrink one, is to be evaluated.

Depalletizing: Force-based Planning for WRAPP-up, a Dual-arm Depalletizer

5.1 Introduction

As explained in the introduction to the first part of this Thesis, key features for a depalletizing robot are flexibility and versatility, generally lacking in the state-of-the-art solutions. These requirements are mostly set by the variability of the objects in terms of size, weight, shape, and material, and by their different possible configurations, that may result in non-accessible faces.

The main contribution of this chapter is a trajectory planner to execute picking strategies with WRAPP-up, a dual-arm depalletizer for intralogistics (see Fig. 5.1). The results contained in this Chapter have been presented in [158, 159]. Somewhat similar to the one adopted in Chapter 4, the planning strategy proposed in this Chapter is sometimes referred to as *reactive*. Again, it might be considered reactive only in the sense that the motion of the robots is split into a finite number of states, and the reactive behavior lies in the contact-based online triggering of transitions between states. Differently than before, however, the overall sequence of steps of the trajectory is defined a priori, both in terms of which states will be entered and in which order. As it will be clear, no unpredictable transitions to corrective states are conceived in this case.

The development of the picking strategies lies upon the observation of the techniques adopted by human pickers at work in warehouses. Following an approach similar to that adopted for instance in [119] for grasping taxonomy, the visual inspection of videos of expert operators at work has been exploited to identify four main maneuvers that they commonly adopt. In Sec. 5.2, the object variability that has been tackled in this work and the specific manipulation challenges are outlined. The observed human picking strategies have been encoded into parametric motion primitives, described in Sec. 5.3.

These serve as building blocks for planning the object picking. The final planner encodes force feedback to correct the robot motion on-the-fly. As also shown in Chapter 4, the online adjustment of pre-planned trajectories based on sensor feedback has been proved to be an effective way of boosting the flexibility and robustness of robotic systems. The design of the robot is briefly outlined in Sec. 5.4 and the trajectory planner to execute the picking strategies is explained in Sec. 5.5. An extensive experimental validation has been conducted and is presented in Sec. 5.6. With the proposed planner, the robot results to be capable of handling a large variety of objects in different configurations. Final discussions are drawn in Sec. 5.7. Indeed, besides performing dual-arm picking strategies, WRAPP-up may be also capable of grasping smaller objects without the need to change the hardware. The next chapter describes a grasp planning strategy that can be implemented on WRAPP-up to grasp previously unseen objects with one end-effector.

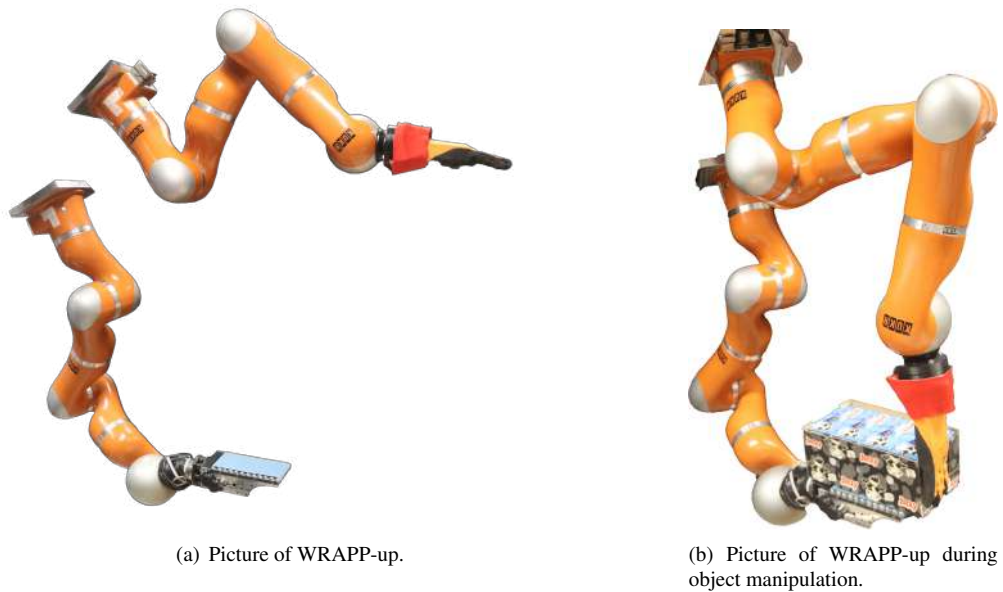


Figure 5.1: Pictures of the depalletizer robot WRAPP-up.

5.2 Problem statement

The task of interest consists in picking a number of different goods from a pallet, a shelf, or a conveyor belt with WRAPP-up [158]. The input to the picking system is the sequence of goods to be picked and their location, e.g., provided by a vision system.

5.2.1 Objects

This work focuses on the problem of picking objects that humans generally cannot pick with one hand. The objects have been provided by a food warehouse —note that the food & beverage is one of the market segments most affected by the e-commerce revolution that today allows customers to have their shopping bag directly delivered at home.

The concerned objects, shown in Fig. 5.2, can be grouped into two sets depending on their shape: boxes or cylinders. For the boxes, the values of the length (L), height (H), and width (W), expressed in centimeters, are reported, while for the cylinders the values of the diameter (D) and the height (H) are listed.

Regarding object shapes, cuboids constitute the vast majority of all the items stored in warehouses [160]. Among the shipped packages, according to [17], the shapes that occur more often are, indeed, cuboids and cylinders even if in a lower percentage. Thus, strategies to manipulate cylinders and cuboids in different configurations are able to handle a considerably large part of the goods in intralogistic processes.

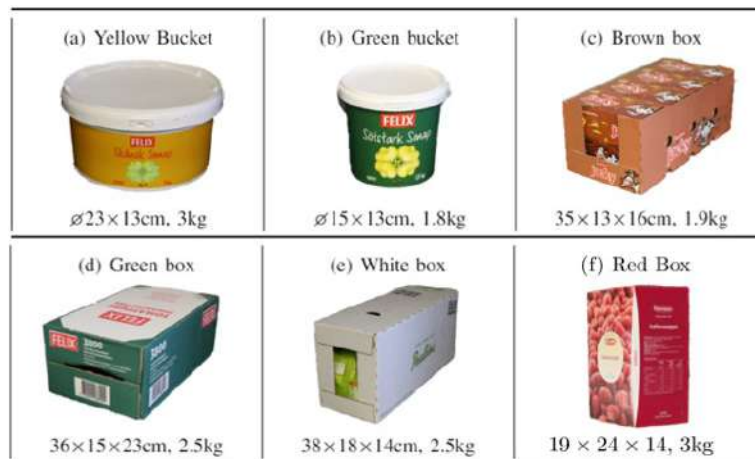


Figure 5.2: Objects used in this work.

5.2.2 Object Configurations

We may classify the different manipulation tasks that characterize the logistic scenario into three main categories, listed in order of increasing difficulty:

- A) Manipulation of single object;
- B) Manipulation of multiple loosely-packed objects;
- C) Manipulation of multiple tightly-packed objects.

Case C) is typical of picking operations from pallets and sometimes from shelves. Instead, cases A) and B) are typical of picking objects from, e.g., a conveyor belt. Examples of these three cases are shown in Fig. 5.3.

5.2.3 Challenges

The main challenges of the picking phase can be identified in the following 3 points:

- boxes are often very close to each other, with two opposite sides, which are the most desirable for a reliable and robust grasp, that are usually not easily accessible. This is, in general, the case for any object in configurations B) and especially C);
- some of the items do not have a top surface, or it may not be suitable to grasp the object. These objects cannot be grasped with vacuum grippers. This is the case for object c) in Fig. 5.2—the brown box;



Figure 5.3: *Examples of the three manipulation cases.*

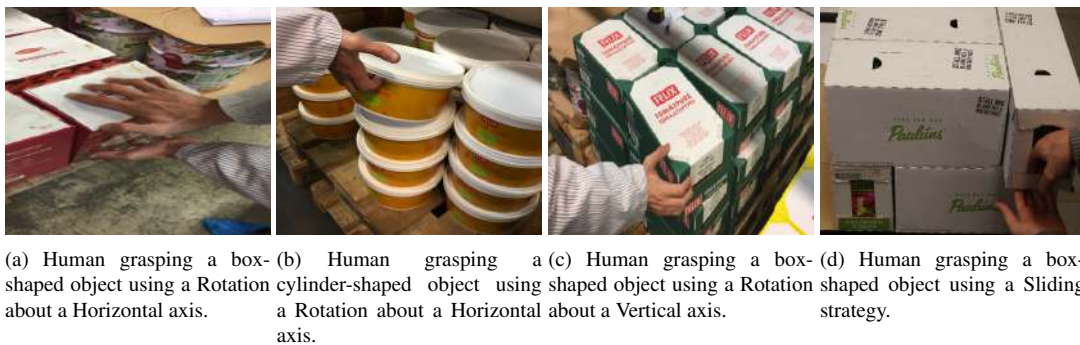


Figure 5.4: *Human workers handling differently shaped objects employing different picking strategies.*

- the bottom side of some objects is recessed in the upper side of the objects which lie beneath, or, more in general, they can not slide. This means that the objects can only translate along the vertical direction or rotate about a horizontal axis. This is the case for objects a) and b) in Fig. 5.2—the yellow and green buckets—when they are placed on top of another object of the same type.

5.3 Human Manipulation Strategies

Due to the variety of situations to be handled, picking operations largely rely on the flexibility of human work. Thus, we observed skilled human operators at a food warehouse during the execution of manipulation tasks. More in detail, two human operators from a food warehouse have been recorded while performing the picking actions. Each picking action has been repeated three times. These observations led to two lessons learned:

- bi-manual manipulation has a crucial role in picking operations since humans use both hands to manipulate and handle the objects. In the majority of the tasks, one hand is used to move the object and the other hand is used as a support;
- the human strategies to pick the items, shown in Fig. 5.4, are classifiable in three main classes.

These three classes depend on the object shape and form factor:

Chapter 5. Depalletizing: Force-based Planning for WRAPP-up, a Dual-arm Depalletizer

Rotation about Horizontal Axis In the case of thin boxes, i.e., $H > W, H > L$, cylindrical objects, and if the support surface of an object cannot slide, the operators use one hand to rotate the goods about a horizontal axis and to put the object on the supporting hand (see Fig. 5.4(a) and 5.4(b)).

Rotation about Vertical Axis In case of thick boxes ($H < W, H < L$) that do not have constraints at the base, the horizontal rotation is not convenient because of the less favorable lever arm, hence the operators decide to rotate the boxes about a vertical axis to have access to the back surface of the object, as in Fig. 5.4(c). This strategy can then evolve in two different picking continuations. In the first one, the box is picked up by two opposite surfaces while the operator uses his hands like the jaws of a parallel gripping device. In the second one, the box is first dragged towards the worker acting on the back surface and then supported by the other hand as the box sticks out the pallet or the underneath layer of goods.

Sliding In the case of thick boxes that have no constraints at the base, the operators push or pull the objects until they reach the support hand at the boundary of the pallet, as in Fig. 5.4(d).

5.4 WRAPP-up: a Brief Hardware Description

Since we observed that warehouse workers generally employ their hands in picking tasks so that one hand functions as a manipulation tool and the other one serves as a support tool, e.g., to sustain most of the weight of the objects, WRAPP-up is a dual-arm robot characterized by two different end effectors. The two arms that compose WRAPP-up are KUKA LightWeight robots. A 6-axis force/torque sensor is placed between the wrist of each arm and the corresponding end-effector. The sensors, as it will be clear in the following, can detect changes in the state of the end-effectors such as contacts with the objects to be manipulated in regular functioning but also undesired collisions, preventing the end-effector from damaging. Two pictures of WRAPP-up are provided in Fig. 5.1. For a more in-depth description of the robot design, the reader can refer to [158].

5.4.1 End-Effectors

To perform dexterous operations, one arm is featured with the Pisa/iit SoftHand: a human-like, adaptive, robust artificial hand the closure movement of which is easy to control since it is actuated by a single motor [161]. Please find a 3D model of the hand in Fig. 5.5. The second end-effector is the Velvet Tray, better described in Fig. 5.6, which works as a support tool. For a more detailed description of the Velvet Tray, the reader can refer to [158].

5.5 Robot working Principle

5.5.1 Robot Motion Primitives

We encoded the human manipulation strategies defined in Sec.5.3 into Motion Primitives of the robot. In a dual way, we define for the robot a Horizontal Rotation primitive,

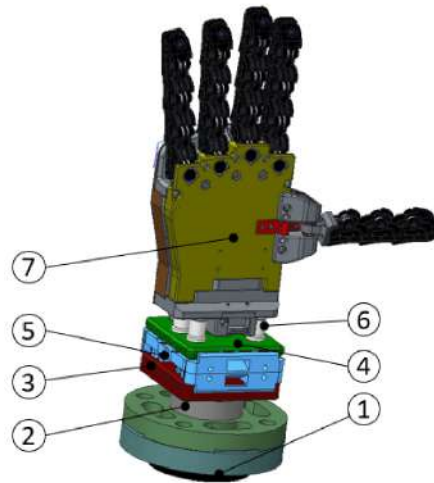


Figure 5.5: The Pisa/IIT SoftHand (7) is attached to the wrist flange of the robotic arm (1) through 6-axes Force/Torque ATI-Mini45 sensor (2) and four rubber beams (6). The rubber beams are located between the end-effector and the ATI-sensor and favor the slowdown of the external force loading rate in case of collision, increasing the time for a rapid emergency-stop response. Toothed flange (5) crimp plate (3) (fixed to the sensor) and plate (4) (fixed to the hand side) together.

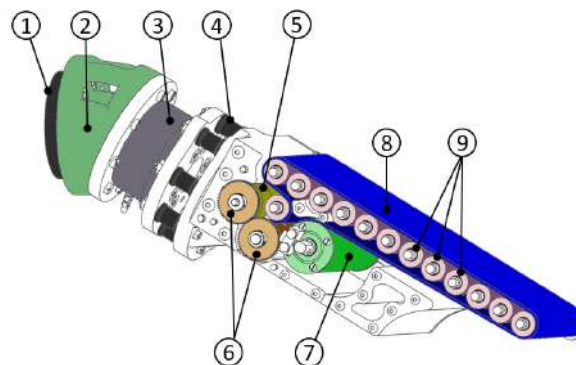


Figure 5.6: The Velvet Tray is equipped with an actuated belt (8) to ease the loading maneuvers of the goods. It is attached to the wrist flange (1) of the KUKA arm through flange (2). Between the KUKA arm and the Velvet Tray, a 6-axes Force/Torque ATI-Mini58 sensor (3) and rubber beams (4) are interposed. The elastic junction is here composed of 10 rubber beams (4) arranged in a circle that slows down the loading rate of the external forces in collision events. The belt is actuated by a Maxon motor DCX22 with gear-head GPX83 (5). The power transmission between the motor and the driver roll of the belt is due to gears (6). Tension roller (7) ensures proper tension in the belt. Finally, a set of idle rollers (9) sustain the objects and form an approximately flat surface under the belt.

namely a rotation about a horizontal axis, a Vertical Rotation primitive, namely a rotation about a vertical axis, and a Sliding primitive. The execution of such Motion Primitives by the robot is schematically represented in Fig. 5.7. For each object, a Picking Strategy is chosen that may involve multiple Motion Primitives in a sequence. In other words, the Motion Primitives serve as atomic blocks for the definition of a Picking Strategy for each object in a certain configuration. In fact, the Picking Strategy is based not only on the object shape but also on its configuration, e.g., the way it is

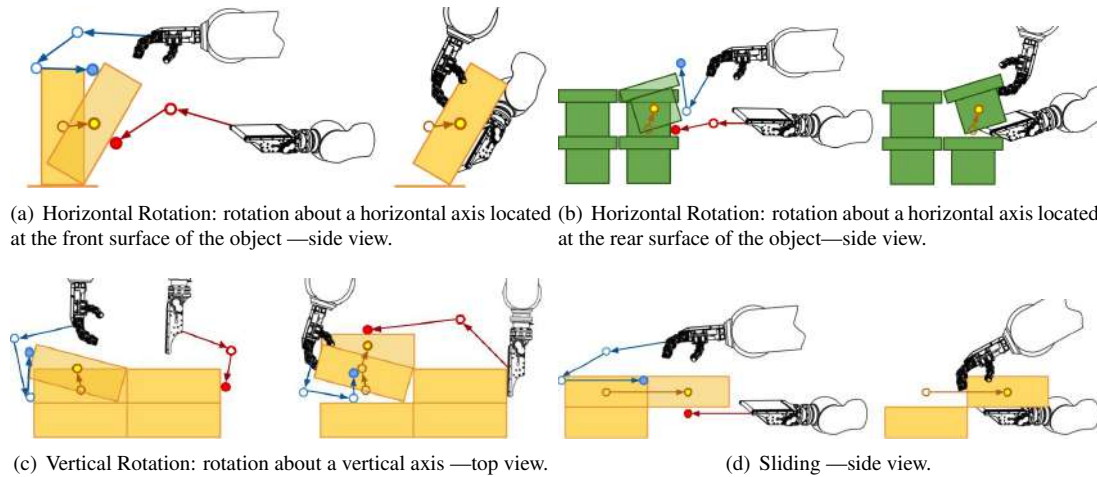


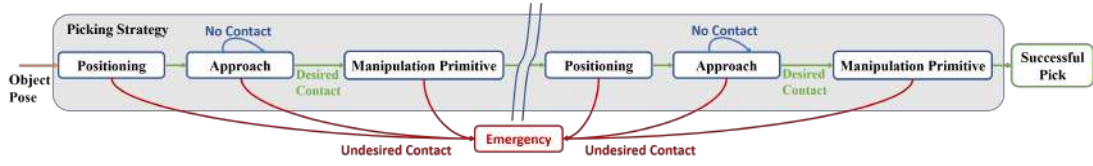
Figure 5.7: *Robot Manipulation Primitives.*

stacked on a pallet. In the next section, we describe the planning method that leverages the defined primitives of motion.

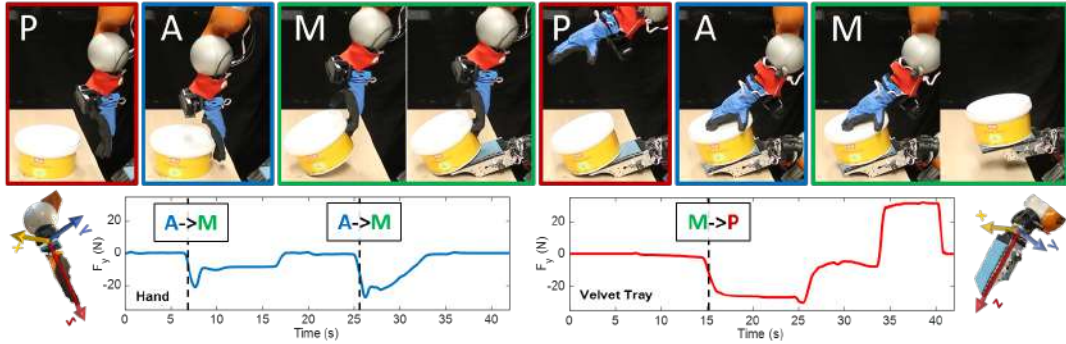
5.5.2 Planner

The planner executes a pre-defined Picking Strategy to correctly pick each object. In this work, a set of Picking Strategies is defined by the user based on the object type and its pose. Hence, the planner takes as an input the information about the object type and pose, e.g. provided by a perception system, and executes the corresponding Picking Strategy. Note that the Picking Strategies are expressed as a sequence of Cartesian waypoints for the end-effectors, relative to the pose of the object. An inverse kinematics stage, which exploits a Reverse Priority algorithm, is used to generate a joint path accounting for obstacles, and kinematic constraints [162].

The planning and the control of the robot have to take into consideration the errors that might affect the information provided by the perception system. A classic solution to increase the robustness is to include force information in the control [76]. However, force control may, in general, have stability issues and requires high bandwidth [77]. Instead of including force measurements at the control level, we use them at a planning stage. More in detail, the measured forces are used to detect a possible contact with an object whenever they exceed a user-defined threshold. The contact information is used as a trigger to plan online the motion of the robot in a reactive fashion, as envisioned, e.g., in [137]. The approach exploits the fact that we can decompose each picking strategy in a finite number of steps. The planner is then based on a finite state machine, in which each state represents a step of the strategy. Indeed, we are not planning the complete trajectory all at once, but we define a general Picking Strategy and then re-plan it step-by-step based on contact information. A somehow similar idea, here applied to bi-manual picking, has been proposed in [141] for grasping with a single end-effector. Furthermore, splitting the main task into sub-pieces embedded in the skeleton of a finite-state machine has shown its effectiveness in [163], where a peg-in-hole task has been performed in an environment affected by uncertainty due to the vision system estimation errors.



(a) General Scheme of the planning approach.



(b) Picking Strategy for a cylindrical object.

Figure 5.8: The figure shows the schematic approach used to implement the motion planner (a), and a practical implementation for a picking task (b). The conceptual scheme is used to represent the state machine approach, where the Picking Strategy is decomposed in a set of states. An example of this approach is represented in the bottom figure (b), where the Picking Strategy is decomposed in 6 states. When a contact between the hand and the bucket is detected (the force exceeds a given threshold), a transition from Approach (A) to Manipulation (M), ($A \rightarrow M$), is triggered.

The states of the state machines for each Picking Strategy are defined by the Manipulation Primitives and two other classes of actions to be executed before actually perform a primitive. These two actions have been defined as Positioning (P), in which one or both the end-effectors are placed near the target object, and Approach (A), which represents the state in which the end-effectors approach the object and establish a contact before starting the Manipulation Primitive (M).

As represented in Fig. 5.8(a), the pose of the target object is used to start the Positioning phase and plan a trajectory for the robot. Once one end-effector or both reach the desired position, they start approaching the object, i.e., they enter the Approach state. At this stage, the contact information is used to trigger the transition between the Approach state and the following state. If no contact is detected, the robot keeps moving toward the object. Instead, if an *unexpected* contact is detected, this could trigger the transition to an Emergency state. Once the *expected* contact is detected, the planner generates the set of way-points defined by the selected Manipulation Primitive and the manipulation action is performed. The transitions from the Manipulation Primitive state to the other states, Positioning or Emergency, are triggered by contact information and/or by the end-effectors reaching a specified position, depending on the strategy.

An example of this planning approach is displayed in Fig. 5.8(b) for the picking of a cylindrical object. The Picking Strategy is decomposed into 6 different states, and the contacts between the object and the hand are used to trigger the transition between the Approach states and the Manipulation Primitives, the lifting of the bucket using a Horizontal Rotation primitive and the Sliding primitive. On the other hand, a contact



Figure 5.9: WRAPP-up picks cylindrical objects.

between the Velvet Tray and the cylinder triggers the end of the first Manipulation Primitive and the transition to the successive Positioning state.

5.6 Experimental Results

In this section, we describe the experiments executed with WRAPP-up. First, we present the results of the experiments in which the pose of the objects is supposed to be known and no perception system is integrated within the system. Then, we also show the results obtained with the fully-integrated system, briefly describing the perception module.

5.6.1 Without Perception

In this part, I present the result of a set of experiments aimed at assessing the effectiveness of the Picking Strategy and the reactive planner designed for WRAPP-up. The pose of the objects is supposed to be known. As we shall see, in the case that a vision system is exploited to retrieve the object poses, the tightly-packed configuration may be problematic for the instance-recognition phase, while can be here considered without any problem. We tested different Picking Strategies that involve all the four defined Manipulation Primitives.

An example of the approach used to collect objects with a cylindrical shape that are recessed one upon the other is shown in Fig. 5.9. Three rows of objects placed on a pallet are considered. First, the hand is placed in front of the bucket and grasps its edge allowing to lift it and tilt it exploiting a Horizontal Rotation. This movement allows the tray to be placed beneath the object as support. Once the tray has been correctly positioned, the hand can release the object and a Sliding is performed so that the tray can be used to collect and deploy the bucket.

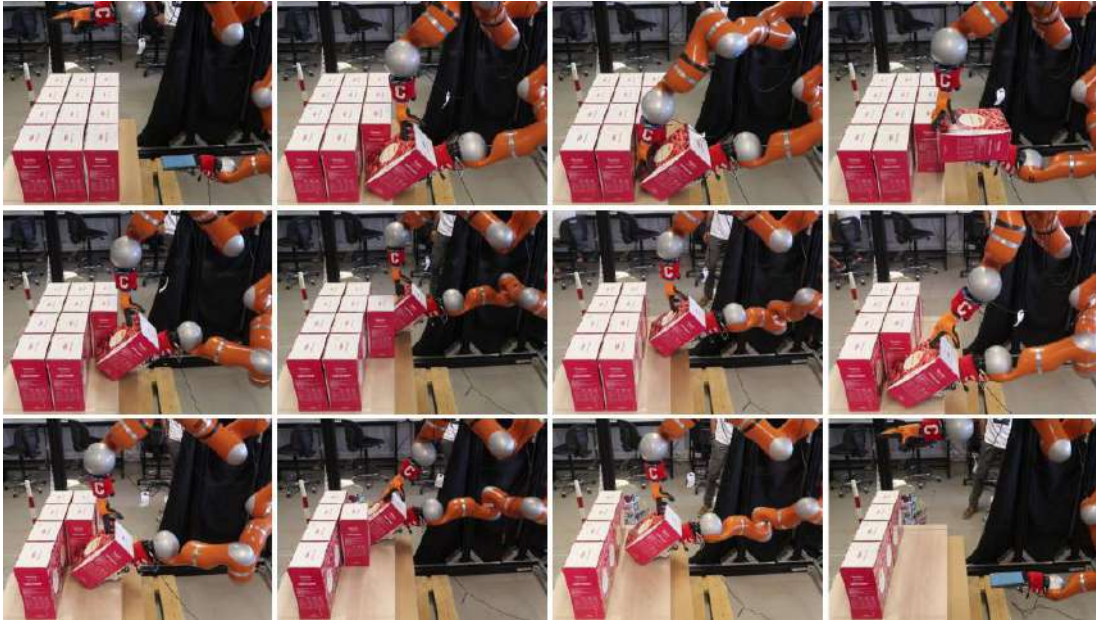


Figure 5.10: *WRAPP-up* picks two rows (8 pieces) of tall boxes.

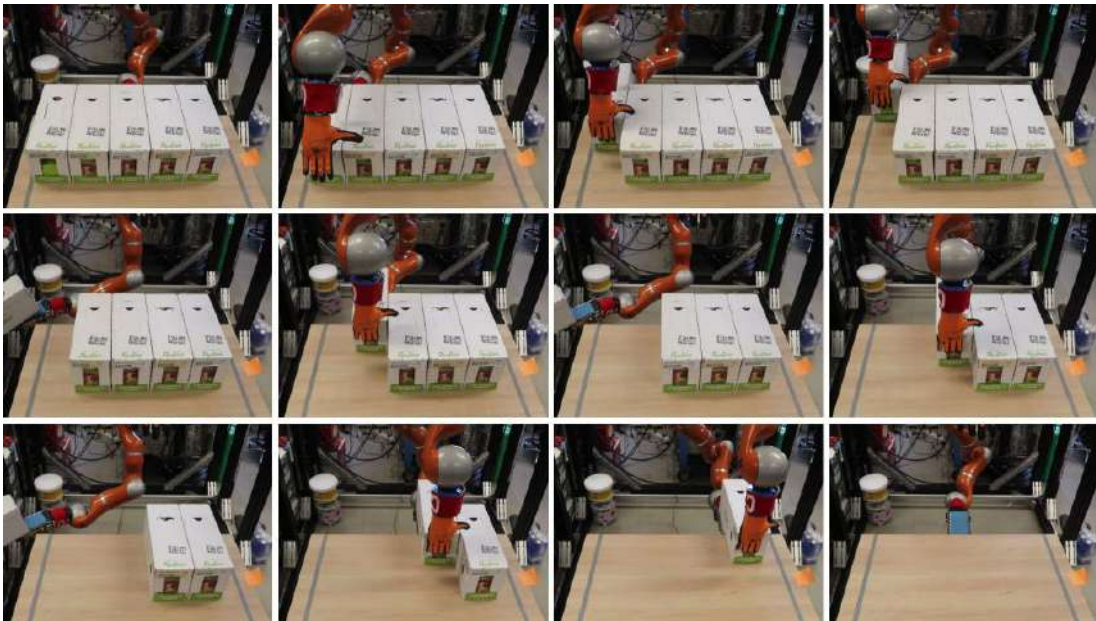


Figure 5.11: *WRAPP-up* picks flat boxes simply using the *Sliding Primitive*.

The strategy to pick tall, box-shaped objects is shown in Fig. 5.10. In this case, the hand is placed behind the box and tilts it until the box lays on the tray placed in front of the object with a proper inclination (Horizontal Rotation). Then, the hand performs a Sliding Primitive to ease the object picking. The former approach has been tested to successfully pick 8 boxes close to each other, showing the robustness of the designed strategy even in the presence of other objects behind the handled box (see Fig.5.10).

As said, the best Picking Strategy is not chosen solely on the basis of the object shape, but it also depends on the location of the object on the pallet and on the position

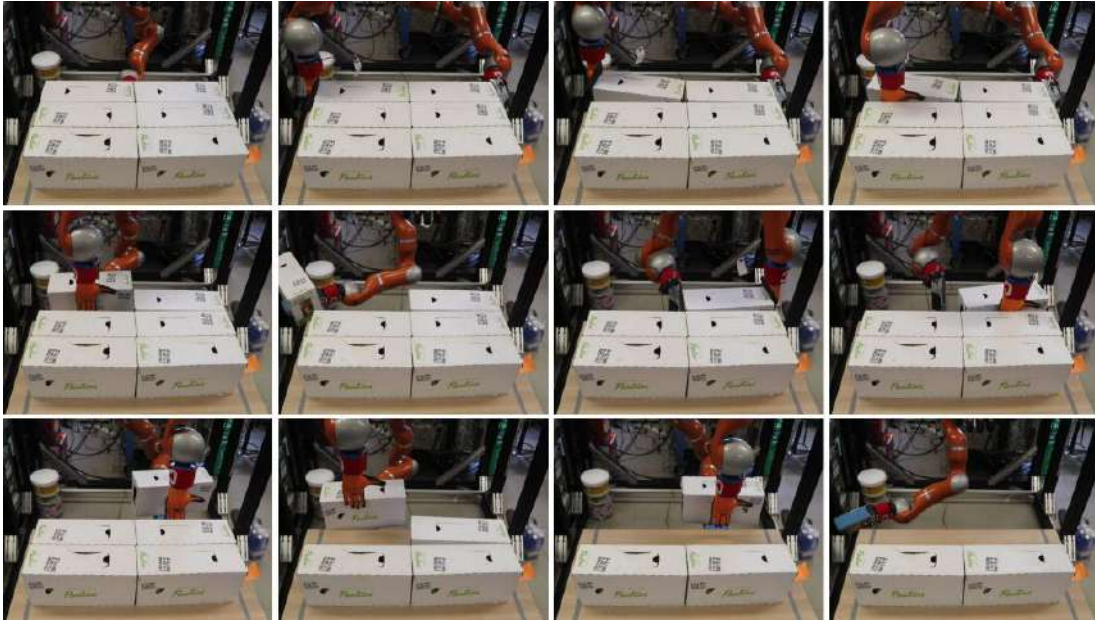


Figure 5.12: WRAPP-up picks flat boxes using the Vertical Rotation Primitive before Sliding.

of the other possible items. To show this concept, two different picking tests have been performed on the same object (white box e) in Fig. 5.2) depending on its different orientation, see Fig. 5.11 and Fig. 5.12. In the first test, due to their configuration, the boxes are easily picked using a Sliding Primitive, in which the hand is placed behind the box and used to pull the object towards the tray. On the other hand, a more complex strategy may be required if the boxes are in a different configuration, e.g., if they are rotated by 90 degrees around the vertical axis w.r.t. the previous case and they are tightly packed, as shown in Fig. 5.12. This condition requires the use of a Vertical Rotation primitive, where the hand approaches the box side and, eased by the tray, rotates it about a vertical axis located at one edge. Then, once the rear surface has been freed, the box can be collected with a Sliding primitive.

Table 5.1 shows the time for picking every single object during the performed experiments. Then, an estimation of the time to empty an entire pallet full of those objects is reported. To estimate the total number of boxes that are contained in the pallet, the

Object				
Picking time per object	55s	83s	16s	82.5s
Time to empty a pallet	176min	498min	47min	227min

Table 5.1: Picking performance indicators for the four scenarios.

Performance Area	Performance Indicator	Current	Unit
Productivity	Average time to empty a pallet	237	min
Reliability	Picking success	92.5	%

Table 5.2: Picking performance indicators

standard EU Pallet dimensions have been considered for the base of the pallet, and a full pallet has been considered to be 1.5 meters in height. To compute the number of objects that can be contained in such a pallet, the dimensions of the objects have been taken into account. A pallet of thin boxes contains thus 192 items, a pallet of cylinders 360 items, one of thick boxes 176 items in the first case (Fig. 5.11) and 165 items in the other (Fig. 5.12). Hence, the time to empty a pallet has been estimated multiplying the average time to pick an object for the number of objects in the full pallet. Table 5.2 reports the global performance indicators we obtained for the picking task. The time to empty a pallet has been computed as the average of the values reported in Tab. 5.1. 50 picking actions have been performed for each case in order to test the system and estimate the values of the performance indicators. The success rate is the average of the four cases.

5.6.2 With Perception

In this part of the section, I present the results of experiments conducted on the integrated systems containing also a vision module for object detection and 6D pose estimation. In this way, the object pose that is used by the robot planner as input is autonomously computed by the vision module. As in [82], integrating state-of-the-art perception algorithms with the picking robot is a useful testbed to assess the actual capability of the Picking Strategies to handle realistic pose estimation errors. As for the hardware, the integration has been realized thanks to an eye-in-hand setup, in which an Asus Xtion PRO¹ camera has been fixed on top of the Pisa/iit SoftHand through a custom case. The modified setup is visible in Fig. 5.13, which shows also the phases of the perception and highlights the overall working principle of the integrated system.

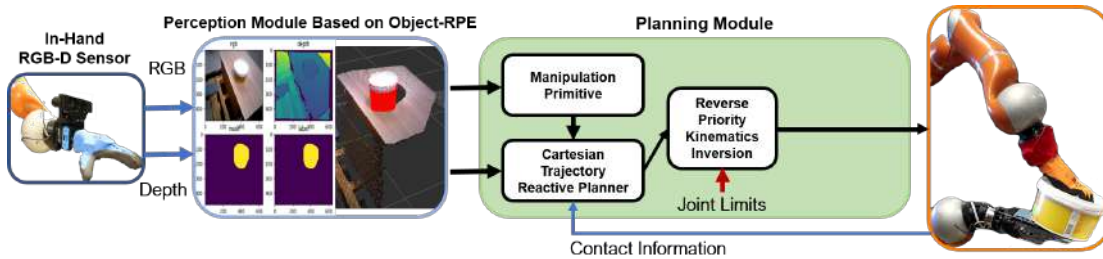


Figure 5.13: Block scheme of the integrated system. The pose of the object estimated by the perception system is the input of the planning module that generates a suitable Picking Strategy, according to pre-defined Manipulation Primitives taking into consideration the dimensions, the shape, and the pose of the target object.

More in detail, WRAPP-up integrates the Object-RPE framework proposed in [19], which couples Convolutional Neural Networks (CNNs) and a state-of-the-art dense Si-

¹<https://www.asus.com/3D-Sensor/XtionPRO>

Chapter 5. Depalletizing: Force-based Planning for WRAPP-up, a Dual-arm Depalletizer

multaneous Localization and Mapping (SLAM) system, ElasticFusion [22], to achieve both high-quality semantic reconstruction as well as robust 6D pose. The system consists of four main components: segmentation, registration, data fusion, and object pose estimation. The input RGB-D data are processed by a segmentation module and the

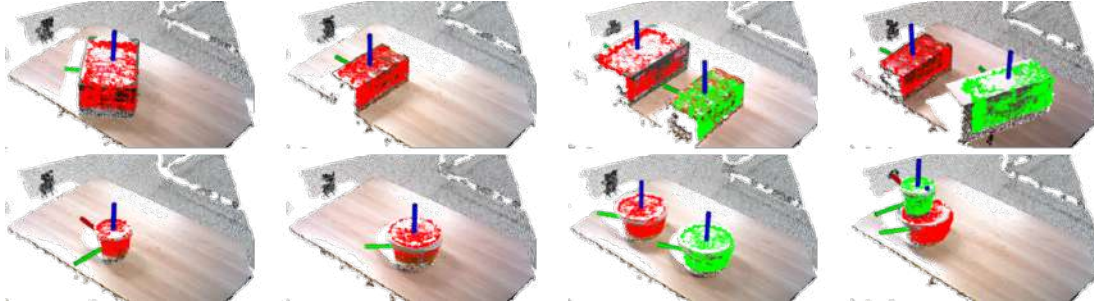


Figure 5.14: The output of the perception algorithm is shown overlaid on the point cloud of the scene. In the top row results for cuboid objects are displayed. From left to right: a single green box, a single brown box, a green box and a brown box in a loosely-packed configuration, a brown box and a white box in a loosely-packed configuration. At the bottom, results for the cylinders are displayed. From left to right: single green bucket, single yellow bucket, two yellow buckets in a loosely-packed configuration, green bucket stacked over a yellow bucket in a tightly-packed configuration.



Figure 5.15: Photo sequences of the experiments addressing the three manipulation cases: single object, loosely-packed objects, and tightly-packed objects.

object instance-detection is filtered and matched to the existing 3D reconstruction. Similar to ElasticFusion, the registration module utilizes both geometric and photometric cues for camera pose estimation. For every single frame, Object-RPE applies DenseFusion [17] to predict the position and orientation of objects in 3D space. The estimates obtained by DenseFusion and camera motions from the registration stage are used to compute the pose of each object instance with respect to a global coordinate system. The pose is then used as a measurement update in a Kalman filter to estimate an optimal 6D pose of the object. Object-RPE exploits the availability of multiple observations of

the scene acquired from different viewpoints. Compared to classic approaches that use a single view to estimate the pose of the objects, this approach allows performing a more robust estimation.

Experiments have been performed on the first 5 objects of Fig. 5.2, a representative set for what concerns the shape and the applied Manipulation Primitives. In fact, The objects include both boxes and cylinders, and the Picking Strategies applied to handle them involve Sliding, Vertical Rotations, and Horizontal Rotations. Specifically, Sliding Primitive is applied to flat boxes, Vertical Rotation *and* Sliding Primitives to flat boxes rotated in a different way, and Horizontal Rotation plus Sliding Primitives to the cylindrical buckets.

Several tests to address all the three possible object configurations presented in Sec. 5.2 have been carried out:

- 10 picking actions on each object for configuration A);
- 20 picking actions on combinations of multiple cuboid boxes and 20 on combinations of multiple cylinders for configuration B);
- 23 picking actions on multiple cylinders for configuration C).

Note that boxes in configuration C) have not been tested due to the difficulties of the instance recognition of tightly packed boxes by the vision module.

An example of the poses provided by the vision algorithm for some of the test cases is shown in Fig. 8, while in Fig. 9 are shown some of the picking actions performed during the tests.

We defined the following protocol for the experiments: i) the objects are placed on a flat surface with random position and orientation; ii) the scanning movement performed to detect the objects and retrieve the poses is always the same for each test; iii) the robot always starts the picking operation from a predefined joint configuration.

Single Object Picking - Object Configuration A) For each object, we performed 10 picking actions. A picking action is considered successful if the object is carried to the unloading position without falling during the task. Because two Picking Strategies have been defined for the cuboid boxes, depending on their orientation on the flat surface, we reported not only the success rate associated to each object, but also the success rate associated to each Picking Strategy in Tab. 5.3.

Multiple Objects Picking - Configurations B) and C) To address the other two object configurations, we performed a set of experiments with multiple objects. We performed 10 tests with two boxes placed in a loosely-packed configuration, for a total of 20 picking actions. More specifically, we picked 7 times the white box, 7 times the green box, and 6 times the brown box. Of the 20 picking actions, 11 were performed using a Sliding strategy, while 9 used the combination of Vertical Rotation and Sliding. Furthermore, we performed 10 tests with two buckets in a loosely-packed configuration, picking 10 times each the yellow and the green bucket.

Then, we performed 10 tests with two or three buckets in a tightly-packed configuration, e.g., very close to each other or stacked on top of each other. For this case, we performed a total of 23 picking actions, 12 for the green bucket, and 11 for the yellow

Chapter 5. Depalletizing: Force-based Planning for WRAPP-up, a Dual-arm Depalletizer

Object	# of picking actions	Picking rate
yellow bucket	10	100%
green bucket	10	80%
brown box	10	100%
green box	10	90%
white box	10	100%

Picking strategy	# of picking actions	Picking rate
Sliding	13	92.3%
Vertical Rotation + Sliding	17	100%
Horizontal Rotation + Sliding	20	90%

Top table: percentage of successful picking actions computed over 10 trials for each object. Bottom table: success rate of the three Picking Strategies.

Table 5.3: Performance of the manipulation system - single object

Object	# of picking actions	Picking rate
Loosely-packed boxes	20	95%
Loosely-packed cylinders	20	90%
Tightly-packed cylinders	23	91.3%

Table 5.4: Performance Results for multiple objects

one. The results of the tests addressing manipulation cases B) and C) are reported in Tab. 5.4 .

Eventually, note that picking action is defined as the robot starts a Picking Strategy *after an object has been correctly detected by the perception system*. In this way, the success of the picking action depends also on the goodness of the automatic estimation of the object pose. On the other hand, this analysis disregards the cases in which the vision system fails to detect the object. However, we also report in Tab. 5.5 a performance index for the system able to express the rate of success of both the detection and the picking action. 5.5.

5.7 Discussion

In this work, we addressed the problem of planning a Picking Strategy, for the depalletizer WAPP-up, that is flexible enough to manipulate a variety of goods relevant for the intralogistics of warehouses.

With the first set of experiments presented in this chapter, the effectiveness of the Picking Strategies on single-item pallets has been evaluated. A percentage of picking success equal to 92.5% allows claiming that the system shows promising results.

With the second set of experiments, we assessed the performance of the system in more realistic conditions. In fact, the pose of the object is, in this case, automatically computed through state-of-the-art perception techniques. With an average success of picking actions for single objects (configuration A)) equal to about 94 %, we can say that the success of the integrated system, in this case, is comparable to that of the system without perception, tested, however, on an entire pallet (configuration C)). This condition is challenging for the vision system and could not be tested on boxes.

Focusing on the single object case, it is worth noting that, for cuboid objects, the

Objects	Detection rate	Picking rate	Success rate
yellow bucket	100%	100%	100%
green bucket	90%	80%	72%
brown box	100%	100%	100%
green box	100%	90%	90%
white box	90%	100%	90%

Table 5.5: Performance of the integrated system for each object

combination of Vertical Rotation and Sliding corresponds to a 100% picking success for the integrated system, while a failure is present when the simple Sliding strategy is used. More specifically, the failure is on the picking of the green box. Even if the experimental validation is restricted to a limited number of trials, it is interesting to note that the influence of the pose estimation error for a sliding strategy seems to be lower for the white and brown boxes, that are thinner, while the error seems to affect more a larger box as the green one. A possible explanation of this fact is that the items contain moving objects, hence the mass distribution is not uniform (and not known). This may affect the position of the actual center of mass of the items in a more considerable way for boxes with a large base as the green ones, causing possible instability of the object on the narrow surface of the tray.

The picking performance for the cylinders is not strongly affected by their relative configuration on the pallet, sticking around 90 % in all the three configurations A), B), and C). The symmetry of the cylinders might be responsible for a small sensitivity to orientation estimation errors. The performance of the boxes, instead, slightly degrades when multiple objects are considered rather than single ones, and, in any case, no performance is shown for tightly-packed boxes due to problems of instance recognition. The buckets, due to their cylindrical shape, are easier to distinguish from each other in tight configurations, since there is space among their surfaces.

Considering the overall results contained in Tab. 5.5, the worst performance is obtained for the green bucket, which is the smallest object of the set. The adopted Picking Strategy, which is the same as that of the bigger, yellow buckets, turned out to be less effective for smaller objects. Indeed, we noted how the reduced footprint and weight of the green buckets makes it more likely for them to tip over while lifted by the hand, or during the Sliding action. Probably, for this kind of small objects, a different Picking Strategy should be investigated and developed to increase the performance.

As for the execution time, the average value reported in Tab. 5.2 is only an estimate and is relative to the case in which the pose of the object is known in advance. However, since efficiency is a crucial aspect for the adoption of these technologies in real warehouses, execution time should be improved. Moreover, the picking time in the experiments with the integrated vision module suffers from the additional time spent to detect the objects and to estimate their pose, accounting also for the time needed to perform the arm motion during the scene scanning procedure. At the current state, the time execution for the object recognition and pose estimation is 40 seconds, of which 12 seconds is the time of the scanning procedure, namely the motion of the robot in order to acquire different views of the objects. The remaining 28 seconds are required for data processing. The image processing currently works on a laptop PC running Ubuntu 16.04 Linux with an Intel COREi7-8750H 2.2GHz and a NVidia RTX 2080 Max-Q

Chapter 5. Depalletizing: Force-based Planning for WRAPP-up, a Dual-arm Depalletizer

8GBGPU. In order to assess the time to empty a pallet, one should carry out an analysis on tightly-packed objects, which showed to be problematic so far, especially for boxed-shape objects, and also evaluate whether the scanning procedure and estimation phase are necessary after every picking action, or it is accurate enough to be performed only once at the beginning of the manipulation phase, or once in a while during the manipulation. This could depend also on the amount of undesired motion caused by the movements of the robot while picking one object to the surrounding objects on the pallet. In case of a considerable disturbance of the previous object poses, more frequent scanning procedures might be required. This analysis is not ready at the moment and is left as an important future work.

In this work, the picking strategies have been deliberately designed based on the knowledge of the objects and the environment. Future works will also include providing the robot planner with a high-level decision tool that is able to automatically generate the right strategy to adopt on the basis of features of previously unseen objects that can be detected by a vision system, e.g. the shape and form factor, and the surrounding obstacles. Moreover, the average picking time will be minimized by adopting suitable optimization algorithms, and the robot will be provided with a mobile base.

Object picking: Grasp Planning for Unknown Objects

6.1 Introduction

As already mentioned, WRAPP-up could also grasp objects smaller than the ones presented in Chapter 5. In this chapter, a method to perform grasps of unknown single objects using robotic hands is presented. The results contained in this Chapter have been published in [164].

The major contribution is a data-driven planner that generates suitable grasps by relying on a *reduced* database of grasps performed by a skilled operator using the robotic hand.

Not only are humans efficacious at grasping with their own hands but are also capable of grasping objects using robotic hands—see e.g. [165, 166]. Therefore, we consider how the grasping skills of a human trained in robotic hand use can be transferred to a robot equipped with the same hand. As mentioned, a key aspect of this approach is a simple method for creating a very *slim* database. The idea is to exploit a skilled human performing experiments using the robotic hand to grasp only a set of *basic shapes* instead of general objects, dramatically reducing the number of trials. This approach is then generalized to grasp unknown objects by relying on state-of-the-art decomposition algorithms that allow approximating an object with such basic shapes—see Sec. 3.2.1.

Specifically, the human operator grasps cuboid boxes, and the MVBB decomposition algorithm proposed in [131] is used to decompose the object point clouds into bounding boxes. Hence, when a new object is presented to the robot, its point cloud is collected through RGB-D cameras and decomposed into bounding boxes; one of the boxes is selected as the suitable one, based on defined indexes. Given a candidate box, a Decision Tree Regression (DTR) algorithm trained on the human data predicts how

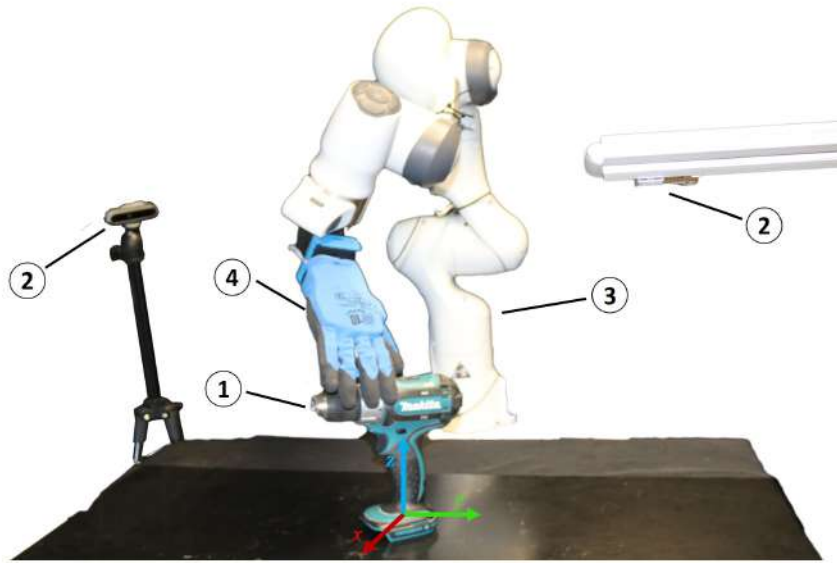


Figure 6.1: The Panda manipulator executing a grasp on a power drill. The experimental setup is composed of: (1) the object to be grasped and the reference frame. The object is placed at a random position in the xy plane with a random orientation along the z axis; (2) two Intel RealSense Depth Cameras D415 employed to sense the object; (3) a Panda manipulator by Franka EMIKA; (4) the employed end-effector, the Pisa/IIT SoftHand.

a professional user would grasp a generic cuboid with the robotic hand, thus providing a set of suitable grasps. The predicted grasps are successively ranked and checked for collision avoidance. Eventually, a robotic manipulator, equipped with the same robotic hand that the human operator used to generate the database, performs the first candidate grasp.

With this method, a general unknown object can be automatically grasped after a reduced training phase based only on sample boxes. We chose box approximation based on the availability of efficient state-of-the-art MVBB algorithms, purposefully designed in [131] as an aid for robotic grasping. Potentially, a different type of approximating shape could be used for the method implementation. Various shapes together might be used at the expense of increased complexity of human grasps acquisition and point cloud decomposition.

Employing a manipulator equipped with Pisa/IIT SoftHand (Fig. 6.1), we extensively tested the proposed approach on a set of 21 objects previously unseen by the regressor. We performed five tests of grasp for every single object, placed in a tabletop configuration, for a total of 105 grasps, obtaining an overall percentage of grasp success of 86.7%.

The Chapter is structured as follows: the proposed grasping planning is outlined in Sec. 6.2, specifically in Sec. 6.2.1 the policy to pick the candidate box is described, in Sec. 6.2.2 the exploitation of the human expertise, collected as described in Sec. 6.2.6, thanks to the DTR is clarified, and in Sec. 6.2.3 the policy to pick the candidate grasp among the ones associated with the candidate box is explained; Sec. 6.3 contains the experimental result and the description of the experimental setup; conclusive discussions are drawn in Sec. 6.4.

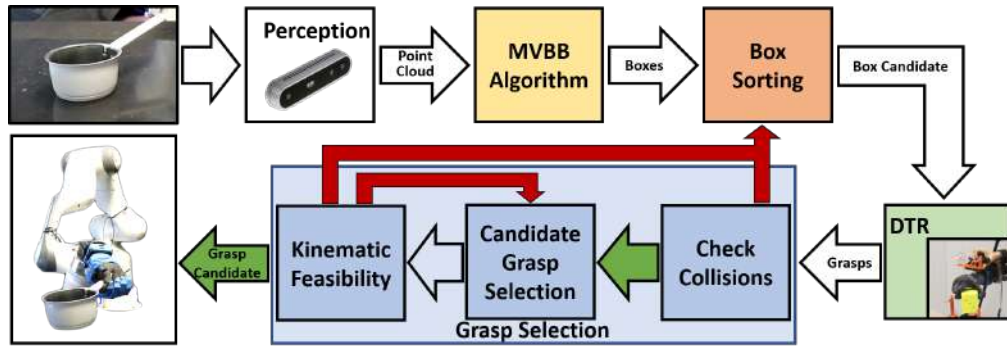


Figure 6.2: The diagram summarizes the basic steps of the procedure. First, the point cloud of a new object is acquired. Then, it is processed by a bounding box algorithm (MVBB) with approximating cuboid boxes. A candidate box is selected and a DTR algorithm, trained on data of a skilled human operator grasping boxes using the robotic hand manually, predicts the grasp poses to grasp the selected box. A collision avoidance algorithm discards the unfeasible grasps, and among the feasible ones, a candidate is selected. If none of the grasps is feasible for the candidate box, another box is selected. Inverse kinematics is used to check the kinematic feasibility of the pose based on the kinematic model of the robot used to perform the grasp. If the candidate grasp is not kinematically feasible, another grasp is selected. If none of the grasps is feasible, another box is selected. Eventually, the robot performs the grasp.

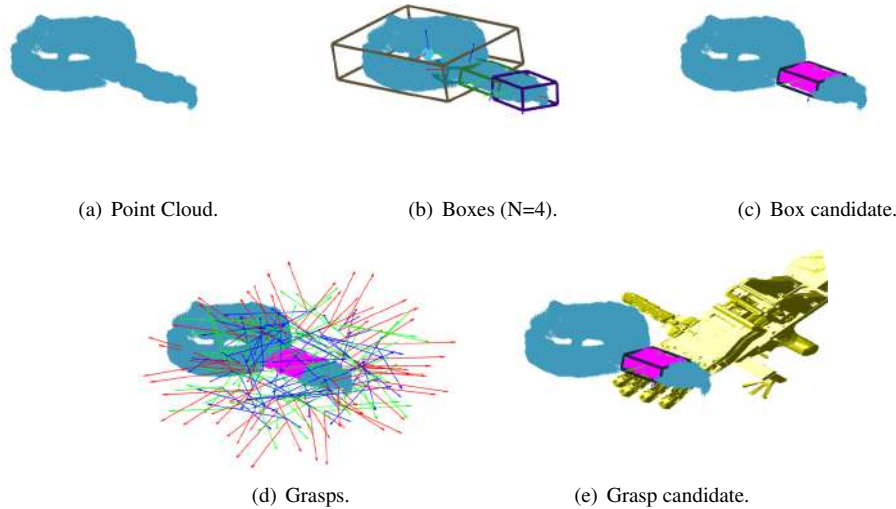


Figure 6.3: This sequence shows the outputs of the blocks in Fig. 6.2, labelled as the corresponding arrow in the diagram of in Fig. 6.2.

6.2 Proposed Solution

This section presents the method used to generate a grasping pose. The entire procedure is outlined in Algorithm 2 and explained in the following. The main steps of the algorithm and their outcomes are shown in Fig. 6.2 and Fig. 6.3, respectively.

The algorithm starts from the acquisition of the object point cloud (see Fig.6.3(a)), referred to as *PointCloud*. Once the point cloud is obtained (white block labeled “Perception” in Fig. 6.2), the function $MVBB()$ computes an approximation of the object

given by N cuboid boxes (see Fig. 6.3(b)), contained in the list *Boxes*. The user-defined parameter of the function, t , is related to the minimum volume of the bounding boxes, see [132] for more details. To obtain the bounding box decomposition from the object point cloud (yellow block labeled “MVBB Algorithm” in Fig. 6.2), we use the procedure described in Algorithm 1 and Algorithm 2 in [132] based on [131]. Each box contained in *Boxes* is described through 9 parameters: 3 for the dimensions, and 6 for the pose. The variable *SortedBoxes* contains the same data as *Boxes*, but ranked according to *BoxSorting()* function, detailed in Algorithm 3. The first item of *SortedBoxes* is the candidate box to be grasped (see Fig. 6.3(c)).

At this stage, the function *DTRPrediction()* predicts 48¹ possible poses to grasp the candidate box *BoxCand* (see Fig. 6.3(d)). The poses are stored in the variable *Grasps*. The function is based on a Decision Tree Regressor trained on the data registered from the skilled human operator (green block labeled “DTR” in Fig. 6.2), and it is better detailed in Sec. 6.2.2. Eventually, the function *GraspSelection()* selects a candidate grasp pose, namely *GraspCand*, among the ones stored in *Grasps* (see Fig. 6.3(e)). It is possible that no feasible grasp can be selected among the ones in *Grasps*, e.g. because all the grasps would result in the hand colliding with the environment or with the object. In this case, the procedure is repeated from the point in which *DTRPrediction()* is called, assigning to *BoxCand* the second box contained in *SortedBoxes*, and so on until a feasible grasp is selected or until all the boxes are considered. The proposed grasp selection algorithm follows a greedy approach, which consists of selecting one single box and evaluating the quality of the grasps for that box. Such a sub-optimal approach has the advantage of a low computational cost also with numerous boxes.

Eventually, *GraspCand* is assigned as desired pose for the robotic manipulator by the function *SendToRobot()*. If no feasible grasp has been found for any box, then the procedure fails. This occurs in the unlikely eventuality that none of the boxes is graspable by none of the 48 grasps associated with it. However, a possible recovery policy is to restart from line 2 of Algorithm 2 with a different value of the parameter t . This leads to a different box decomposition, which may result in a non-null feasible grasps set.

Algorithm 2 Object grasping procedure

```

1: Get PointCloud;
2: Boxes = MVBB(PointCloud,  $t$ );
3: SortedBoxes = BoxSorting(PointCloud, Boxes);
4: GraspCand = [];
5:  $i = 1$ ;
6: while (GraspCand == [] &&  $i \leq N$ ) do
7:   BoxCand = SortedBoxes[ $i$ ];
8:   Grasps = DTRPrediction(BoxCand)
9:   GraspCand = GraspSelection(PointCloud, Grasps, BoxCand);
10:   $i = i + 1$ ;
11: SendToRobot(GraspCand);

```

¹For each face, two grasps are predicted along the short side and two along the other side. Due to the symmetry of the boxes, each grasp is then rotated by 180 deg around the axis normal to the box face to consider the other approaching directions.

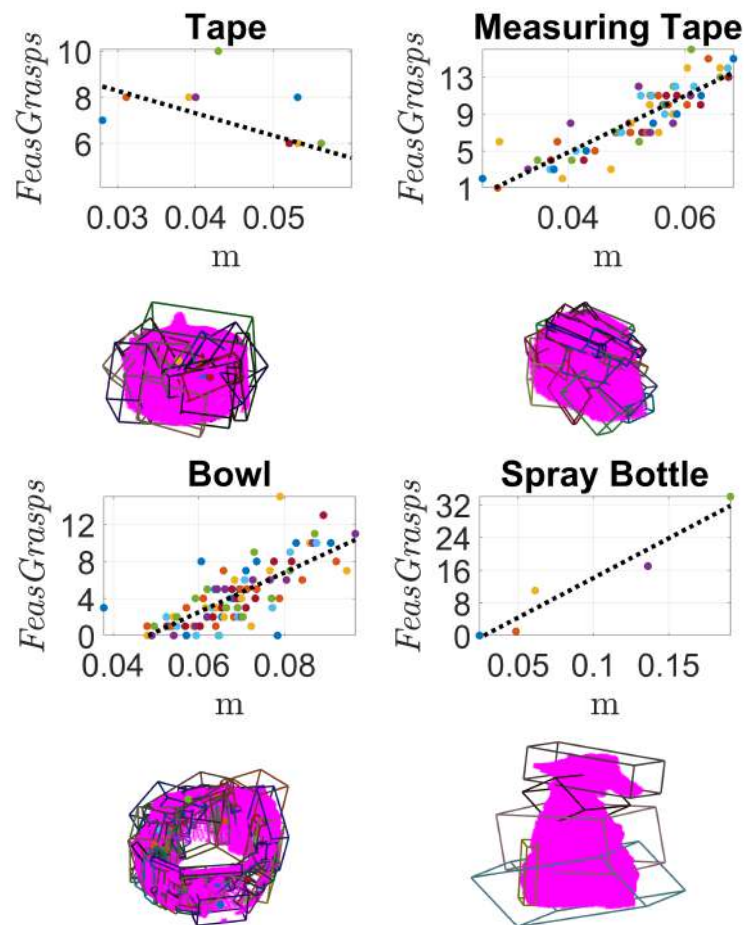


Figure 6.4: Number of feasible grasps versus distance from the centroid of the point cloud (non-normalized, expressed in meters) for four objects from Tab. 6.1. A linear fitting of the data is shown by a black dotted line. Below each plot there is the box decomposition of the corresponding object.

6.2.1 Candidate Box Selection

Algorithm 3 outlines the steps of the candidate box selection, namely the content of the orange block labeled “Box Sorting” in Fig. 6.2. The boxes contained in *Boxes* are

Algorithm 3 Box Sorting

```

1: function BOXSORTING(PointCloud,Boxes)
2:   Centroid ← CompCentroid(PointCloud);
3:   for ( $i = 1, i \leq N, i++$ ) do
4:     Volume[ $i$ ] = GetBoxVolume(Boxes[ $i$ ]);
5:     Points[ $i$ ] = PointsInside(Boxes[ $i$ ], PointCloud);
6:     Density[ $i$ ] = Points[ $i$ ]/Volume[ $i$ ];
7:     Distance[ $i$ ] = CompDist(Centroid, Boxes[ $i$ ]);
8:   for ( $i = 1, i \leq N, i++$ ) do
9:     NormDens[ $i$ ] = Density[ $i$ ]/Max(Density);
10:    NormDist[ $i$ ] = Distance[ $i$ ]/Max(Distance);
11:     $P[i] = \frac{1}{2}(\text{NormDens}[i]^2 + \text{NormDist}[i]^2)$ ;
12:   SortedBoxes = Sort(Boxes, P);
13:   return SortedBoxes;
    
```

ranked by decreasing values of the performance index, P , and stored in *SortedBoxes*.

In this Chapter, a box ranking policy that favors the outermost box has been adopted, as done in [132]. Additionally, noise can introduce scattered points in the point cloud leading to bounding boxes with a low density of points. If grasped, such boxes may result in a grasp that does not have a grip on many actual points of the real object. To address this issue, our policy also favors the boxes with a higher density of points. The i -th element of *Density*, indicated with *Density*[i], contains the ratio between number of points of the point cloud *PointCloud* contained inside the i -th box, *Boxes*[i] and *Volume*[i], namely the volume of *Boxes*[i]. *NormDens*[i] is the *Density*[i] normalized by the maximum value of the vector *Density* (computed by *Max()* function). The volume of a box, given its dimensions, is returned by *GetBoxVolume()*. The number of points contained in a box, stored in *Points*, are computed by *PointsInside()*. The function *CompDist()* computes the distance between the center of the i -th box and the centroid, *Centroid*, of the point cloud. The centroid is the arithmetic mean of all the positions of the points and is computed by *CompCentroid()*. *NormDist*[i] contains the value of *Distance*[i] normalized by the maximum value of the vector *Distance*.

6.2.2 Exploitation of acquired human expertise

This section explains the content of the green block labeled “DTR” in Fig. 6.2, and of the function *DTRPrediction()* in Algorithm 2, which associates to *BoxCand* the grasp poses of the hand. This is done by learning a model $\mathbf{y} = f(\mathbf{x})$ capable of predicting a human-like hand pose $\mathbf{y} = [y_1, \dots, y_6]^T \in \mathbb{R}^6$, given the box dimensions $\mathbf{x} = [x_1, x_2, x_3]^T \in \mathbb{R}^3$. To this end, we employ a Decision Tree Regressor (DTR). DTR methods are indeed particularly suited for reduced-dimension training sets, as it is our case. The representation of the Regression Tree model is a binary tree, where each node represents a single input variable x_j , with $j = \{1, \dots, 3\}$ and a split point on that variable. The leaf nodes of the tree contain an output variable \mathbf{y} which is used to make a prediction. Creating a binary decision tree is actually a process of dividing up the input space.

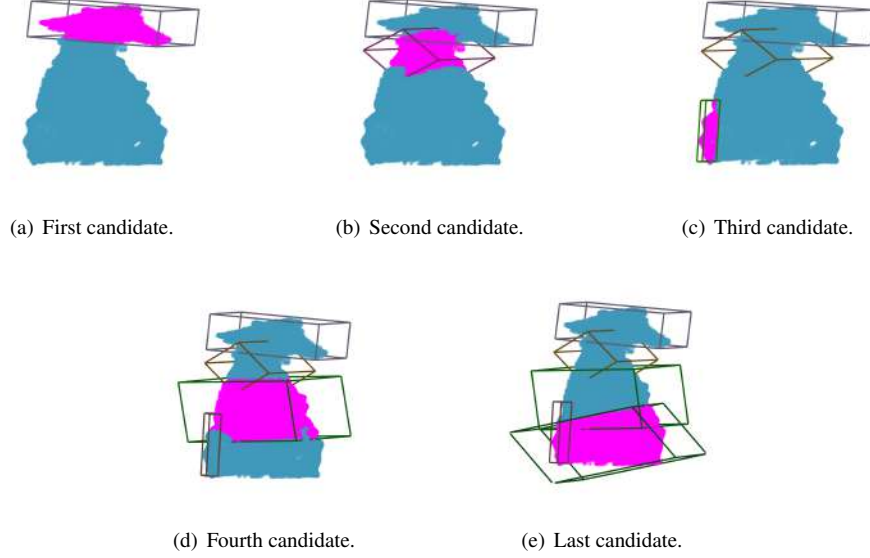


Figure 6.5: Box ranking obtained from Algorithm 3 applied to a point cloud decomposition for the Spray Bottle.

A greedy approach is used to divide the space called *recursive binary splitting*. Given an observation $(\mathbf{x}_i, \mathbf{y}_i)$ for $i = 1, 2, \dots, n$, the regression tree construction is explained by the following steps: i) select a splitting variable j and a split point s ; ii) define 2 regions R_1 and R_2 : $R_1(j, s) = \{\mathbf{x} | x_j \leq s\}$, $R_2(j, s) = \{\mathbf{x} | x_j > s\}$; iii) for each $k \in \{1, \dots, 6\}$ seek the splitting variable j and the split point s that solve

$$\min_{j,s} [\min_{c_{1,k}} \sum_{\mathbf{x}_i \in R_1(j,s)} (y_{i,k} - c_{1,k})^2 + \min_{c_{2,k}} \sum_{\mathbf{x}_i \in R_2(j,s)} (y_{i,k} - c_{2,k})^2],$$

where $c_{1,k}, c_{2,k} \in \mathbb{R}$ are two constant decision variables that describe the model response. Given j and s , the solution of the minimization is

$$\hat{c}_{1,k} = \text{ave}(y_{i,k} | \mathbf{x}_i \in R_1(j, s)), \hat{c}_{2,k} = \text{ave}(y_{i,k} | \mathbf{x}_i \in R_2(j, s)),$$

where ave is the average of $y_{i,k}$ in region R_1 or R_2 , and we define $\hat{c}_1 = [\hat{c}_{1,1}, \hat{c}_{1,2}, \dots, \hat{c}_{1,6}]^T$ and $\hat{c}_2 = [\hat{c}_{2,1}, \hat{c}_{2,2}, \dots, \hat{c}_{2,6}]^T$. iv) after finding the best split for each splitting variable, split the data into the 2 regions and repeat the splitting process recursively on each of the two regions. The maximum tree depth is empirically set equal to 8 as a trade-off between model complexity and minimization of overfitting risk. We used *SciKit-Learn* to train the algorithm, using as a labeled dataset the one described in Sec. 6.2.6. Hold out validation has been used to verify the generalization and robustness of pose prediction. We trained different model configurations to adjust the model parameters using the mean square error (MSE) between the predicted poses and the true-labeled poses in the validation dataset.

6.2.3 Candidate Grasp Selection

This section provides details about the content of the blue blocks collectively labeled as “Grasp Selection” in Fig. 6.2. This procedure, detailed in Algorithm 4, selects a candi-

Algorithm 4 Grasp Selection

```

1: function GRASPSELECTION(PointCloud, Grasps, BoxCand)
2:   FeasGrasps = CheckCollisions(PointCloud, Grasps, EnvCloud);
3:   if FeasGrasps == [] then
4:     GraspCand = [];
5:   else
6:     GraspCand = CandGraspSelection(FeasGrasps, BoxCand);
7:     while (KinFeasibility(GraspCand))==false do
8:       FeasGrasps = FeasGrasps \ GraspCand;
9:       GraspCand = CandGraspSelection(FeasGrasps, BoxCand);
10:  return GraspCand;

```

date grasp once all grasps of *BoxCand* are generated by the *DTRPrediction()* function. First, the function *CheckCollisions()* (right-hand side blue block in Fig. 2) discards all the grasps that would result in the hand colliding with the object and/or the environment. This is done approximating the hand by a virtual cuboid box. The function *PointsInside()* is called in order to compute how many points lie inside the hand box. If the number of such points is greater than a threshold, then the corresponding grasp pose is discarded. Similarly, the collisions between the hand and the environment point cloud, *EnvCloud*, are checked. The remaining grasps are stored in *FeasGrasps*; if no grasp is collision-free, then *FeasGrasps* is an empty variable. Eventually, among the remaining grasps, if any, the function *CandGraspSelection()* (central blue block in Fig. 6.2) selects the one with the thumb aligned with the longest side of *BoxCand*, according to what has been already explored in [132]. The boolean function *KinFeasibility()* (corresponding to the left-hand side blue block in Fig. 6.2), checks if *GraspCand* is kinematically feasible for the robot. If *GraspCand* is not kinematically feasible, then it is removed (through the operator \backslash) from the list *FeasGrasps*, and another grasp pose is selected as *GraspCand*.

6.2.4 An Alternative Force-aided Candidate Grasp Selection Policy

Note that the adopted policy tends to discard those grasps that would close around the longest side of the box, privileging those that close around a thin box in the most intuitive way. The second type of grasps is likely more stable and able to produce a greater hold on the object. Consequently, a possible way for selecting the candidate grasp could be that of picking the grasps associated with a greater force applied to the object. In practice, this could be implemented by registering not only the pose of the hand manually operated by the human. Instead, the human could be asked to try and exert some forces and torques on the box once grasped and these wrenches would be registered. Hence, a second DTR could be trained to associate to each grasp an output expected force, e.g. taking as labels in the training data set the maximum intensity of the force that the human user was able to exert with each grasp on each box. In Sec. 6.2.6 the reader will see that the described experimental setup already includes a possible way to register the forces exerted by the humans during the grasps using the robotic hand. The implementation of this alternative policy is not ready at the moment but represents an interesting future work.

Note that this alternative policy for selecting the candidate grasp could also be beneficial in terms of generalizing the method to different robotic hands. In fact, choosing

the grasp with the thumb aligned with the longest side of a box assumes an anthropomorphic gripper. Instead, selecting the grasp capable of exerting greater forces may represent a more generally applicable criterion.

6.2.5 To Support the Candidate Box Selection Policy

To support the choice of our box selection policy, we used the number of collision-free grasps contained in *FeasGrasps* to show that the boxes more distant from the centroid of the point cloud are more accessible by the hand. For each object in Tab. 6.1, we plotted the number of collision-free grasps for each box (random values of t were used) as a function of the distance of the box from the centroid of the point cloud (containing also a portion of the table on which the object lies). Linear fittings of the data for all objects show an average slope of 15.45, which means that the number of feasible grasps associated with a box increases with the distance from the centroid. A negative slope has been obtained only for two objects: the Tape (-6.57), probably due to its symmetry and flatness, and the Courgette (-0.04), lying on the table. The highest values of slope have been obtained for the tallest objects: the Drill (28.35) and the Spray Bottle (37.05). See Fig. 6.4 for some examples. Figure 6.5 shows the results of our box ranking on one decomposition of the point cloud of the Spray Bottle. The first ranked box according to our policy is the farthest from the table (Fig. 6.5(a)). This solution is a reasonably desirable one since it likely leads to hand poses distant from the obstacle represented by the table. In the case of objects with handles or protrusions, these elements are also likely selected (see, e.g., Fig. 6.3(c)), which is another favorable choice in many cases. Note also that the third candidate box (Fig. 6.5(c)) is closer to the centroid of the point cloud than the fourth box (Fig. 6.5(d)). However, it has a better rank because it provides a better local approximation of the object point cloud (higher density of points).

6.2.6 Acquisition of the Human expertise

This section describes the first set of experiments, aimed to collect the data of the pose of the robotic hand used by a skilled human operator for grasping a set of sample boxes. The following setup has been employed:

- a Pisa/IIT SoftHand [116] provided with a handle and a battery to be used manually by the human operator;
- a commercial Phase Space Motion Capture System for 3D motion tracking with active LED markers, the Phase Space², to record kinematic data: ten stereo cameras working at 480 Hz tracked the 3D positions of 8 markers put on the handle of the Pisa/IIT SoftHand and of 8 world-fixed markers. The LED frequency is in the visible red;
- a fixed station made of two supports on which the 8 world-fixed LED markers are put, as shown in Fig. 6.6, equipped with a force-torque sensor ATI mini45, placed as in Fig. 6.6;
- a set of 56 cuboid sample boxes to be grasped (Fig. 6.6(b)), whose dimensions vary within the discrete interval $\{15, 30, 45, 60, 75, 90\}$ mm. The smallest box is a

²<http://phasespace.com/>

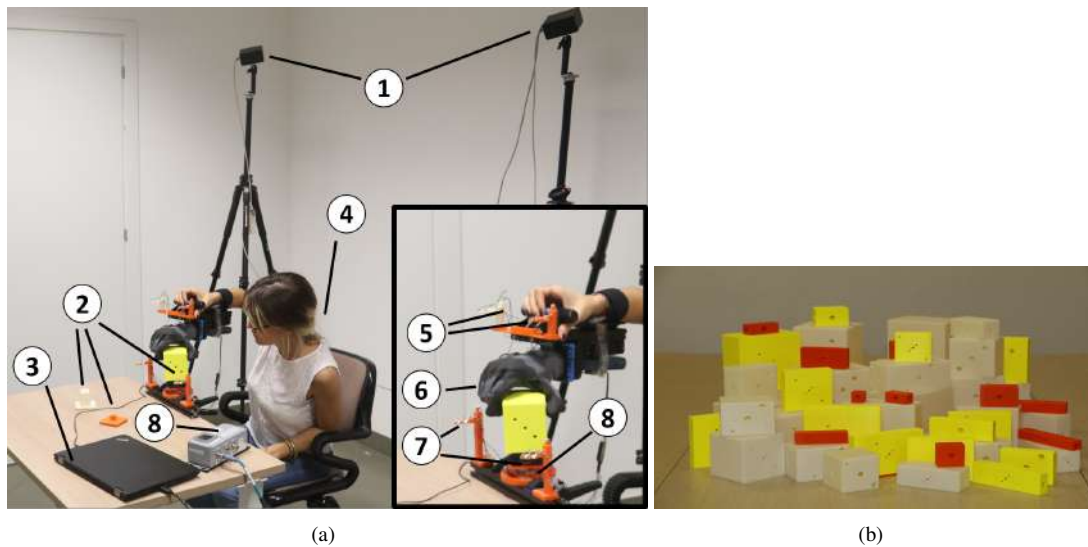


Figure 6.6: *Experimental setup during the first phase of the study. In 6.6(a), the acquisition of the data from an expert human user (4). The PhaseSpace cameras (1) record the position of the LED markers, eight world-fixed markers (7) and eight hand-fixed ones (5). A set of boxes (e.g. 2) are grasped with a Pisa/IIT SoftHand (6). The interaction forces during the grasp are measured with a torque-force sensor for future use (8). All the data are recorded on a pc (3). In 6.6(b), the complete set of sample boxes.*

cube of edge 15 mm, and the largest one is a cube of edge 90 mm. These bounds are dictated by the Pisa/IIT SoftHand design and are provided by the supplier³.

Fig.6.6 shows the above-described experimental setup. The real experiments have been conducted in dark conditions. Each box has been rigidly fixed to the sensorized platform before being grasped. This allows measuring the interaction forces between the environment and the box itself (left for future use). The 8 world-fixed markers placed on their supports are used to robustly define a fixed reference frame. The 8 hand-fixed markers are placed on two supports on the handle, as shown in Fig. 6.6(5). They are used to define a reference frame placed on the palm of the Pisa/IIT SoftHand, which is fixed relative to the handle. A custom application developed in C++ enabled the synchronization between Phase Space data and force/torque sensor, and the Phase Space OWL library was used to get the optical tracking data.

Two different grasps, each repeated three times so as to have multiple acquisitions, were performed on the different faces of each box, both along the short side and the other side, for a total of 648 trials.

6.3 Experimental Validation



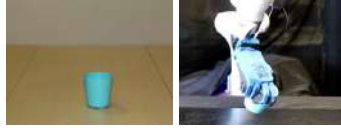







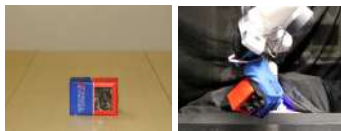

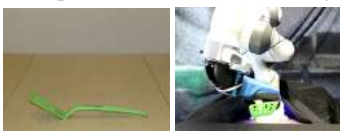
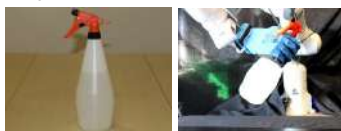

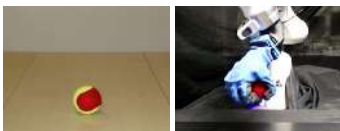


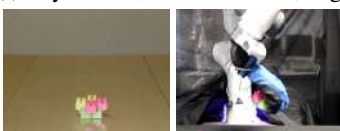
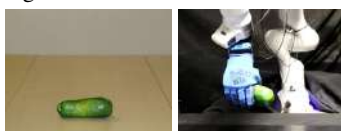
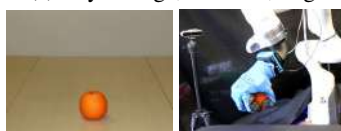
The experimental setup is depicted in Fig. 6.1. The object to be grasped (1) is placed by an operator on the table. Both the object position along the xy plane and its orientation along the z -axis are randomly chosen by the operator. Two Intel RealSense Depth Cameras D415⁴ (2) capture the point cloud of the object. Then the outcome of the

³https://qbrobotics.com/wp-content/uploads/2016/03/QBsofthand_datasheet_general.pdf

⁴<https://www.intelrealsense.com/depth-camera-d415/>

6.3. Experimental Validation

Table 6.1: Set of tested objects. Each cell reports a picture of the object, its size, weight and a successful grasp.

<p>(a) Bowl, $\varnothing 140 \times 65$mm, 55g.</p> 	<p>(b) Container, $\varnothing 115 \times 48$mm, 35g.</p> 	<p>(c) Cup, $\varnothing 74 \times 84$mm, 35g.</p> 
<p>(d) Foam Brick, $92 \times 44 \times 44$mm, 6g.</p> 	<p>(e) Juice Box, $60 \times 38 \times 80$mm, 221g.</p> 	<p>(f) Measuring Tape, $75 \times 35 \times 65$mm, 189g.</p> 
<p>(g) Mug, $135 \times 95 \times 100$mm, 345g.</p> 	<p>(h) Pot, $280 \times 133 \times 74$mm, 374g.</p> 	<p>(i) Power Drill, $200 \times 95 \times 195$mm, 1190g.</p> 
<p>(j) Skillet, $380 \times 230 \times 40$mm, 316g.</p> 	<p>(k) Screws Box, $125 \times 55 \times 90$mm, 444g.</p> 	<p>(l) Small Cup, $80 \times 50 \times 60$mm, 107g.</p> 
<p>(m) Spatula, $310 \times 80 \times 60$mm, 45g.</p> 	<p>(n) Spray Bottle, $120 \times 95 \times 290$mm, 927g.</p> 	<p>(o) Tape, $\varnothing 89 \times 53$mm, 62g.</p> 
<p>(p) Tennis Ball, $\varnothing 71$mm, 46g.</p> 	<p>(q) Torch, $185 \times \varnothing 78$mm, 466g.</p> 	<p>(r) Toy Apple, $\varnothing 73 \times 64$mm, 140g.</p> 
<p>(s) Toy Blocks, $87 \times 87 \times 47$mm, 34g.</p> 	<p>(t) Toy Courgette, $145 \times \varnothing 49$mm, 15g.</p> 	<p>(u) Toy Orange, $\varnothing 73$mm, 18g.</p> 

proposed algorithm is used to grasp the object with an impedance controlled Panda

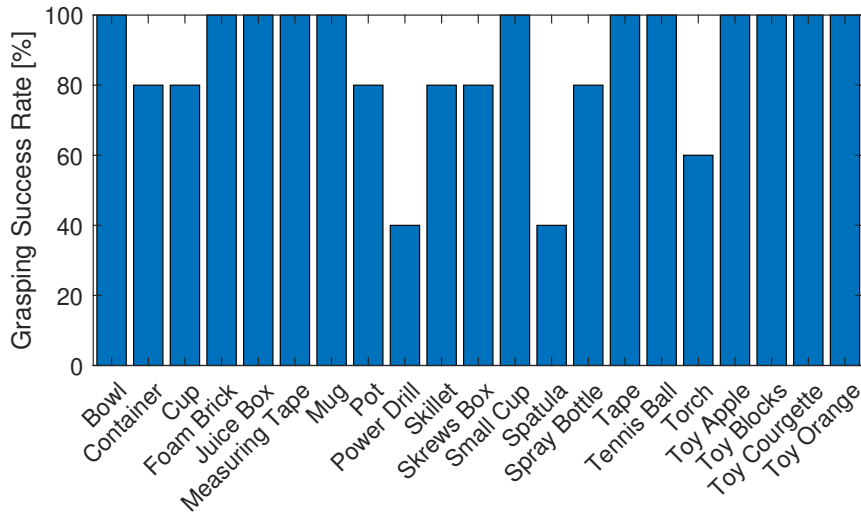


Figure 6.7: Grasping success rate for each of the 21 objects, the total average is 86.7%. Each item has been tested 5 times.

arm by Franka EMIKA⁵ (3). The manipulator is equipped with the same end-effector employed to acquire the human expertise (Sec. 6.2.6), i.e., the Pisa/IIT SoftHand (4) and it is controlled using ROS.

To validate the method, we tested 21 objects. Tab. 6.1 shows the objects and reports their geometrical and physical properties. The objects were chosen to span a wide variety of size, weight, texture, and stiffness. Most of the objects present similar characteristics to the ones of the benchmark set proposed in [167], and none of them was used to train the DTR. Each object is tested 5 times with different random positions and orientations. This means that a total of 105 grasps have been tested. After closing the fingers, the end-effector of the robot is lifted of 150mm in 5.5s. If the object does not fall during this interval, the grasp is considered successful. The parameter of the bounding box algorithm [132] is fixed and equal to $t = 5 \cdot 10^{-5}$. This value is a trade-off between performance and computational time. The results are reported in Fig. 6.7. The average grasping success rate, among all the 105 trials is equal to 86.7%. The objects more challenging to grasp resulted to be the Spatula and the Power Drill. The difficulty of the former object is linked to its geometrical properties. Indeed, it is a flat object lying on the table, thus it may occur that the hand fingers remain stuck against the table while closing. On the other hand, the power drill is the heaviest object in the set (1190g). Heavy objects require more solid grasps to be lifted.

Finally, we compare the proposed method with the one developed in [132], where MVBB decomposition is used as well, but the grasping poses are generated based on geometric considerations, and multiple variations of the generated grasps are tested in simulation. In [132], the efficacy of the method is tested in simulation with 4 objects perfectly reproduced by the point cloud. The average grasping success rate in [132] is 77.61%. In order to compare the two methods, we tested our approach on the object in [132] with the worst and best performance, i.e., the Mug (52.5%) and the Pot (97.5%).

⁵<https://frankaemika.github.io/docs/>

For the single item, we obtain 100% of success for the Mug and 80% success for the Pot (one failure over five trials was due to the poor quality of the point cloud and consequently of the box decomposition). The average for these two objects is 75% for [132] versus the 90% obtained by the novel approach.

6.4 Discussion

We proposed and validated a planning algorithm for grasping with robotic hands that encodes the expertise of a skilled user, trained in robotic hand use. The method starts with the acquisition of the point cloud of the object to be grasped that is approximated via cuboid bounding boxes. Then one box is selected and a DTR algorithm, based on grasps performed by the skilled human user on elementary boxes, generates a set of suitable hand poses to grasp this box. The grasps are ranked and checked for collision avoidance and kinematic feasibility. Finally, a candidate grasp is executed by the robot.

We tested the proposed approach using the Pisa/IIT SoftHand achieving a percentage of grasp success of 86.7% over 105 grasps on 21 previously unseen objects. First of all, it is worth mentioning that the efficacy of the proposed method relies on the accuracy of the captured point cloud. If the object is only partially captured, or if the point cloud is noisy, then also the approximation of the object in minimum volume bounding boxes will be poor, resulting in a failure. The adaptability of Pisa/IIT SoftHand to the shape of the grasped object may play a role in determining the success of a grasp in the presence of a rough approximation of the object. Validation with different types of robotic hands will be carried out in the future to explore the generality of the proposed method. If different hands were used, it might be necessary to modify the human pose acquisition procedure, e.g., registering also the position of the fingers.

Furthermore, at the moment we are considering a fixed parameter t for the MVBB algorithm. Its value has been chosen empirically, after a preliminary visual inspection of the results of the box decomposition applied to the test objects. The automatic tuning of the parameter depending on the point cloud may be beneficial to the method, although its definition is not straightforward. Indeed, different objects with different dimensions and shape complexity can be better approximated with a larger number of boxes. A better approximation of the point cloud resulting from an automatic parameter tuning may be advantageous also for the application of the method to rigid hands. The automatic selection of parameter t based on point cloud and hand parameters will be studied.

Another aspect worth noticing is that the proposed method evaluates only the feasibility of the final candidate pose and not of the approaching trajectory. A collision avoidance algorithm may be integrated to improve effectiveness. Segmentation algorithms could make the method suitable also for grasping grouped objects. Future work will further focus on the integration of force measurements as possible indicators of the grasp quality.

Something has not been considered in the presented work is that grasping is highly related to the reason behind the grasp itself. The specific intention of the task, i.e., handing-over, lifting, showing, moving the object, and so on, influences the way in which the object should be grasped [168, 169]. The target position of the object in pick and place tasks may also influence the way a grasp is performed, i.e., the height of

human grasps on a vertical cylinder has been shown to be inversely related to the target height [170]. MVBB algorithm has been considered for planning task-oriented grasp in [171]. Including task-dependent constraints in our grasp planning pipeline may be an interesting development. Task-based constraints could be embedded either in the policy to select the candidate box, based, e.g., on box location or in the grasp selection policy, e.g., hand orientation in order to leave enough space on the object for handing-over.



Part II

Robotics for Logistics: Force-based Object Delivery

CHAPTER 7

An Introduction to Cooperative Manipulation with particular focus on cable-suspended loads

While the first part of this Thesis focuses on robotic solutions to intralogistic tasks, especially to depalletizing, this second part of the Thesis can be of great interest to those parts of the logistic flow that take place out of the industrial premises and concerns, e.g., order delivery. In fact, this part is centered on robotic applications for object transportation, specifically, *aerial* object transportation. We have already seen how the development of e-commerce is setting new challenges to logistics. The large volume of orders to be delivered and the short delivery-time that is expected are pushing the research towards innovative approaches. For these reasons and in view of limiting the emission of truck-based systems [38], autonomous delivery solutions attract great attention. Moreover, as stated in the introduction of this Thesis, deliveries accomplished through autonomous robots are beneficial for reducing the exposure of human workers to dangerous/contaminated parcels (medical samples, etc.) and for limiting human contact. These goals have risen only recently due to the pandemic outbreak. Eventually, aerial robots would bring the additional advantage of not being subject to traffic-related delays, so that complying with a schedule in a more reliable way would be possible

7.1 Related works

A very recent and popular research topic in aerial robotics is aerial physical interaction [172]. Target applications are many, especially, as they have been classified in [20], force/torque exertion—see, e.g., contact-based inspection and maintenance tasks [173] as they have been developed within the AEROARMS project [174], the AEROWORKS

Chapter 7. An Introduction to Cooperative Manipulation with particular focus on cable-suspended loads

project¹, the AIRobots project², the AEROBI project³ aimed to the development of an aerial robot for in-depth bridge inspection by contacts, and also the HYFLIERS project⁴ [175]—, assembly and structural construction — [176–179], and in general the work produced within of the ARCAS project—, and load manipulation and transportation [180].

In order to manipulate objects, aerial platforms have been endowed with different physical interaction tools, such as cables [31, 181, 182], more complex robotic manipulators [179, 183–191], or rigid tools [192] and grippers directly attached to the robot body [29, 193]. This part of the Thesis will focus on aerial robots that exploit cables in order to manipulate objects.

Load transportation often takes advantage of the *cooperation* between multiple robots to enhance the overall payload [194] and thus to allow lifting heavy loads. Many approaches have been proposed to the interesting problem of aerial multi-robot manipulation. Even collaboration between aerial and ground robots for the purpose of object manipulation has been proposed [195, 196].

Also in cooperative approaches, different manipulation tools have been envisioned. [197] and [198] treat cooperative aerial transportation of rigid and elastic objects, respectively, using passive tools attached to the robots. On the other hand, multiple flying arms are considered, e.g., by [199]. Cables, however, have attracted great attention. Not only is the use of cables advantageous in terms of lightweight and low cost, but it also mitigates the coupling between the load and the robots attitude and can hence simplify the control problem, especially when using under-actuated aerial platforms —think of a cable attached to the CoM of the robot.

Cooperative aerial manipulation of cable-suspended load has been studied, e.g., in [28, 200–203]. [204] proposes a method for the transportation of a cable-suspended beam load by two aerial vehicles based on a PD control law with an additional integral term in the vertical direction. The reason is that a feedforward force term is given to each robot in addition to the feedback on its own trajectory. The addition of a feedforward term in such a trajectory control law, besides being redundant since the pose of the commonly transported bar would be already univocally determined by the positions of the two robots, is disadvantageous if the mass of the system is not exactly known, since it generated an error in the two robots vertical position, and hence in the vertical position and pitch angle of the bar. Anyway, since both the robots have a reference trajectory, the two trajectories must be coordinated throughout the whole manipulation task. [205] exploits a similar control approach in which a centralized trajectory-planner communicates the coordinated way-points to the robots. If no feedback on the state of the other robot is provided, then the closed-loop system could lack robustness in the presence of uncertainties or external disturbances. The focus of [205], however, is on trajectory planning to optimize the energy consumption based on battery level information. In [206] a planner computes the trajectories of both the two robots transporting a cable-suspended bar but can receive online re-planning requests by the robots.

Decentralized algorithms such as [193, 207–209] can be advantageous in terms of fault-tolerance and scalability. However, explicit communication may still represent an

¹<http://www.aeroworks2020.eu>

²<http://airobots.dei.unibo.it/>

³<https://www.aerobi.eu/>

⁴<https://www.oulu.fi/hyflinders/>

issue, being it subject to delays and packet corruption and losses. These phenomena can potentially undermine the performance and efficacy of these control laws. Furthermore, the hardware and software complexity of the system can be reduced by confining the explicit communication.

Notably, coordination through implicit communication, made possible mostly by physical interactions, has been observed in insects a long time ago and the term *Stigmergy* has been coined to refer to it by the entomologist Grasse' in 1959 [210]. With the progress of mobile robotics, such behaviors observed especially in groups of ants have inspired the robotic research concerning swarms of miniaturized robots [211–213]. A typically addressed problem is box-pushing and the involved robots have limited on-board resources and sensing capabilities. For instance, the robots can generally recognize the target position of the object because it is illuminated in a more intense way than the surrounding environment.

Communication-less object transportation with more complex mobile manipulators has also been developed. Note, however, that in the case of manipulators endowed with grippers rigidly attached to the object, knowing the pose of its own end-effector is equivalent, for each robot, to knowing the pose of the object, considering a simple kinematic relationship [214, 215]. This fact is exploited, e.g., in communication-less cooperative transportation schemes for ground manipulators in [216]. Instead, in the case of cable-suspended objects, knowledge of the pose of the object requires direct sensing or estimation using information coming also from the neighbors since the contact model allows for an arbitrary orientation between the robot end-effector and the object. A decentralized algorithm for object transportation that does not rely on explicit communication is the leader-follower algorithm presented [217] for a group of mobile *ground* robots. There, the robots cooperate for regulating the object translation, while the attitude of the object is controlled solely by the leader, which, unlike the other robots, can apply pure torque to the object. *Aerial* cooperative transportation by two [218, 219] or more [220] robots attached to the object either through cables or passive spherical joints can be found in the literature. While the approach in [218] is vision-based, [219, 220] use a force-based control law. [219, 220] accomplish the cooperative transportation leveraging a leader/follower scheme. The leader robot is assigned a reference trajectory, while the slave robot is not. Instead, through an admittance control law, it follows the leader motion in the horizontal plane, while trying to keep its own cable vertical. Both the robots have a reference fixed position in the vertical direction, which limits the workspace of the manipulation task. However, since no squeezing of the object is induced by the robots, the reference vertical position of the two robots become necessary, as it will be also more clear in the following. To change the constant altitude at which the manipulation task takes place, explicit communication becomes necessary. [221] focuses on the collaborative communication-less transportation of a flexible load by a group of aerial robots equipped with arms to manipulate the load. The control is based on force regulation, is at a kinematic level, and does not rely on explicit communication. The case in which the mass of the load is unknown is considered. An adaptive approach is proposed, in which an integral term is added to the velocity control. The control of the linear velocity of the system is addressed, while the attitude control of the load is not treated. None of these three communication-less methods focuses on the control of the entire pose of the manipulated object. More

Chapter 7. An Introduction to Cooperative Manipulation with particular focus on cable-suspended loads

recently, [222] proposes a passivity-based communication-less control method for the cooperative manipulation of a slung beam-load by two PVTOLs (*Planar Vertical Take-Off and Landing* aircrafts). In other words, the study constrains its analysis to the vertical plane.

In this part of the Thesis, a method for the cooperative manipulation of cable-suspended loads by means of aerial robots is presented. The proposed method leverages a leader-follower scheme and does not rely on explicit communication among the agents. Instead, a sort of *physical communication* takes place among the robots through the load and the cables. Thanks to this force-based form of communication, the robots retrieve the information to coordinate themselves in a decentralized fashion. Partial results of the presented work have been published in [223], [224], and [225].

The remainder of this part is structured as follows. Sec. 7.2 contains the general dynamic model of the considered system and Sec. 7.3 gives details about the adopted control law. In Chapter 8 we restrict the analysis to the interesting case of manipulation of a *cable-suspended beam* load by means of *two* aerial vehicles. Chapter 9 extends the results of the previous chapter to a more general load manipulated by $N \geq 2$ robots.

7.2 Dynamic Model

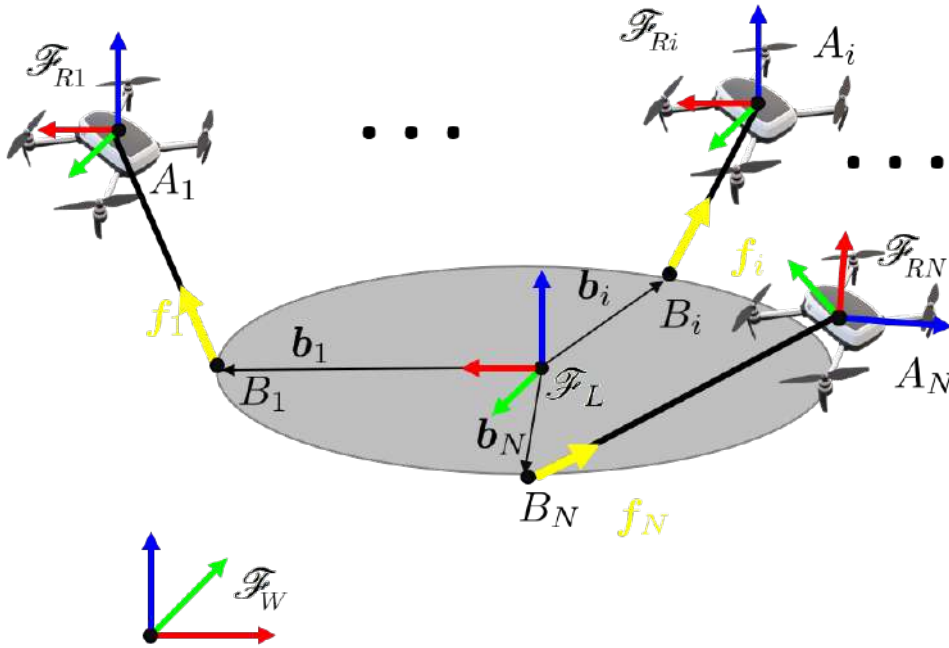


Figure 7.1: Schematic representation of the system and its main variables. The aerial vehicles do not necessarily need to be quadrotors since the analysis and control design is valid for general aerial vehicles.

In this section, the dynamic equations that describe the motion of the system are derived. A schematic representation of the considered system with its major variables is shown in Fig. 7.1. The manipulated load is modeled as a rigid body with mass $m_L \in \mathbb{R}_{>0}$ and a positive definite inertia matrix $\mathbf{J}_L \in \mathbb{R}^{3 \times 3}$. We define the frame

$\mathcal{F}_L = \{O_L, \mathbf{x}_L, \mathbf{y}_L, \mathbf{z}_L\}$ rigidly attached to it, where O_L is the the load CoM. Then, we define an inertial frame $\mathcal{F}_W = \{O_W, \mathbf{x}_W, \mathbf{y}_W, \mathbf{z}_W\}$ with \mathbf{z}_W oriented in the opposite direction to the gravity vector. The configuration of the load is then described by the position of O_L and orientation of \mathcal{F}_L with respect to \mathcal{F}_W , i.e., by the vector $\mathbf{p}_L \in \mathbb{R}^3$ and the rotation matrix $\mathbf{R}_L \in SO(3)$, respectively⁵. To express the load attitude, we also define the three Euler angles load roll, pitch, and yaw, as ϕ , θ , and ψ , respectively,

and the vector $\text{vect}\phi = \begin{bmatrix} \phi \\ \theta \\ \psi \end{bmatrix}^\top \in \mathbb{R}^3$. The load dynamics is given by the Newton-Euler equations

$$\begin{aligned} m_L \ddot{\mathbf{p}}_L &= -m_L g \mathbf{e}_3 + \mathbf{f}_e \\ \dot{\mathbf{R}}_L &= \mathbf{S}(\boldsymbol{\omega}_L) \mathbf{R}_L \\ \mathbf{J}_L \dot{\boldsymbol{\omega}}_L &= -\mathbf{S}(\boldsymbol{\omega}_L) \mathbf{J}_L \boldsymbol{\omega}_L + \boldsymbol{\tau}_e - \mathbf{B}_L \boldsymbol{\omega}_L, \end{aligned} \quad (7.1)$$

where, $\boldsymbol{\omega}_L \in \mathbb{R}^3$ is the angular velocity of \mathcal{F}_L w.r.t. \mathcal{F}_W expressed in \mathcal{F}_L , $\mathbf{S}(\star)$ is the operator such that $\mathbf{S}(\mathbf{x})\mathbf{y} = \mathbf{x} \times \mathbf{y}$, g is the gravitational constant, \mathbf{e}_i is the canonical unit vector with a 1 in the i -th entry, \mathbf{f}_e and $\boldsymbol{\tau}_e \in \mathbb{R}^3$ are the sum of external forces and moments acting on the load, respectively. The positive definite matrix $\mathbf{B}_L \in \mathbb{R}^{3 \times 3}$ is a damping factor modeling the energy dissipation phenomena. This damping action has been added to the rotational dynamics of the load because, otherwise, in a two-robot case as the one addressed in Chapter 8, any rotation of the load around the axes that lie between the two cable anchoring points would be persistent. Indeed, the two robots are not able to apply, through the cable forces, any torque in this direction. No dissipative action has been added, instead, to the translational dynamics in (7.1). This is because a dissipative action would facilitate the load pose stabilization but is not necessary in this case. As shown in the following, the damping injected into the systems by the controlled robots stabilizes the load configuration even without considering any dissipation phenomenon acting on the load translational dynamics.

The load is transported by N aerial robots by means of cables, one for each robot. We denote with A_i the attachment point of the i -th cable to the i -th robot, with $i = 1, \dots, N$, and we define the frame $\mathcal{F}_{Ri} = \{A_i, \mathbf{x}_{Ri}, \mathbf{y}_{Ri}, \mathbf{z}_{Ri}\}$ rigidly attached to the robot and centered in the attachment point, which coincided with the CoM of the robot. As a consequence, the rotational dynamics of the robots is decoupled from the tension in the cables, as in [226]. We consider the special case in which the robots are attached to the load in an evenly distributed way along a circle centered on O_L with radius $b \in \mathbb{R}_{>0}$. This also means, similarly to [28], that we suppose the object CoM lies in the same plane of the cables anchoring points B_i . In particular, we assume without loss of generality that:

$${}^L \mathbf{b}_i = b[\cos \theta_i \ \sin \theta_i \ 0]^\top =: [x_i \ y_i \ 0]^\top, \quad (7.2)$$

where $\theta_i = (i-1)2\pi/N$. The i -th robot configuration is described by the position of A_i and orientation of \mathcal{F}_{Ri} w.r.t. \mathcal{F}_W , denoted by the vector $\mathbf{p}_{Ri} \in \mathbb{R}^3$, and the rotation matrix $\mathbf{R}_{Ri} \in SO(3)$, respectively. Being the cable attached to the CoM of the

⁵The left superscript indicates the reference frame. \mathcal{F}_W is considered as the reference frame when the superscript is omitted.

Chapter 7. An Introduction to Cooperative Manipulation with particular focus on cable-suspended loads

robot, it exerts only forces but no torques on the robot. We assume that a position controller is applied to each aerial robot, able to track any C^2 trajectory with negligible error in the domain of interest, independently from external disturbances. Indeed, with the recent robust controllers (as the one in [227] for both unidirectional-thrust and multidirectional-thrust vehicles) and disturbance observers for aerial vehicles, one can obtain very precise motions, even in the presence of external disturbances. Anyway, the control method proposed in this part results particularly robust to non-idealities (see Sec. 8.6).

The closed-loop translational dynamics of the robot subject to the position controller is then assumed as the one of a double integrator: $\ddot{\mathbf{p}}_{Ri} = \mathbf{u}_{Ri}$, where \mathbf{u}_{Ri} is a virtual input to be designed. If we consider aerial platforms capable of controlling both the position and orientation independently [228–232], the double integrator can be considered an exact model of the closed-loop system apart from modeling errors. In the case of under-actuated vehicles, the double integrator is still a good approximation. A similar assumption can be found also in [233]. Indeed, the rotational dynamics is decoupled from the translational one and it is typically faster than the latter [197, 234], allowing to apply the time-scale separation principle.

The other end of the i -th cable is attached to the load at the anchoring point B_i described by the vector ${}^L\mathbf{b}_i \in \mathbb{R}^3$ denoting its position with respect to \mathcal{F}_L . The position of B_i w.r.t. \mathcal{F}_W is then given by $\mathbf{b}_i = \mathbf{p}_L + \mathbf{R}_L {}^L\mathbf{b}_i$.

We model the i -th cable as a unilateral spring along its principal direction, characterized by a constant elastic coefficient $k_i \in \mathbb{R}_{>0}$, a constant nominal length denoted by l_{0i} and a negligible mass and inertia w.r.t. the ones of the robots and of the load. The attitude of the cable is described by the normalized vector, $\mathbf{n}_i = \mathbf{l}_i / \|\mathbf{l}_i\|$, where $\mathbf{l}_i = \mathbf{p}_{Ri} - \mathbf{b}_i$. Given a certain elongation $\|\mathbf{l}_i\|$ of the cable, the latter produces a force acting on the load at B_i equal to:

$$\mathbf{f}_i = t_i \mathbf{n}_i, \quad t_i = \begin{cases} k_i(\|\mathbf{l}_i\| - l_{0i}) & \text{if } \|\mathbf{l}_i\| - l_{0i} > 0 \\ 0 & \text{otherwise} \end{cases}. \quad (7.3)$$

$t_i \in \mathbb{R}_{\geq 0}$ denotes the tension along the cable and it is given by Hooke's law. As usually done in the related literature ([202, 204, 218, 235]), we assume that the controller and the gravity force always maintain the cables taut, at least in the domain of interest⁶. The force produced at the other end of the cable, namely on the i -th robot at A_i , is equal to $-\mathbf{f}_i$.

Considering the forces that robots and load exchange by means of the cables, the dynamics of the full system is:

$$\begin{aligned} \dot{\mathbf{v}}_R &= \mathbf{u}_R \\ \dot{\mathbf{v}}_L &= \mathbf{M}_L^{-1} (-\mathbf{c}_L(\mathbf{v}_L) - \mathbf{g}_L + \mathbf{G}(\mathbf{q}_L) \mathbf{f}), \end{aligned} \quad (7.4)$$

where $\mathbf{q}_R = [\mathbf{p}_{R1}^\top \dots \mathbf{p}_{RN}^\top]^\top$, $\mathbf{q}_L = (\mathbf{p}_L, \mathbf{R}_L)$, $\mathbf{v}_R = [\dot{\mathbf{p}}_{R1}^\top \dots \dot{\mathbf{p}}_{RN}^\top]^\top$, $\mathbf{v}_L = [\dot{\mathbf{p}}_L^\top \ \boldsymbol{\omega}_L^\top]^\top$, $\mathbf{u}_R = [\mathbf{u}_{R1}^\top \dots \mathbf{u}_{RN}^\top]^\top$, $\mathbf{f} = [\mathbf{f}_1^\top \dots \mathbf{f}_N^\top]^\top$ where \mathbf{f}_i is given in (7.3), and is a function of the state, $\mathbf{M}_L = \text{diag}(m_L \mathbf{I}_3, \mathbf{J}_L)$ and $\mathbf{I}_3 \in \mathbb{R}^{3 \times 3}$ the identity matrix, $\mathbf{g}_L = [-m_L g \mathbf{e}_3^\top \ \mathbf{0}^\top]^\top$,

⁶This assumption makes the analysis likely unsuitable for agile, acrobatic motions of the load but is reasonable for a control law that can be employed in realistic transportation scenarios.

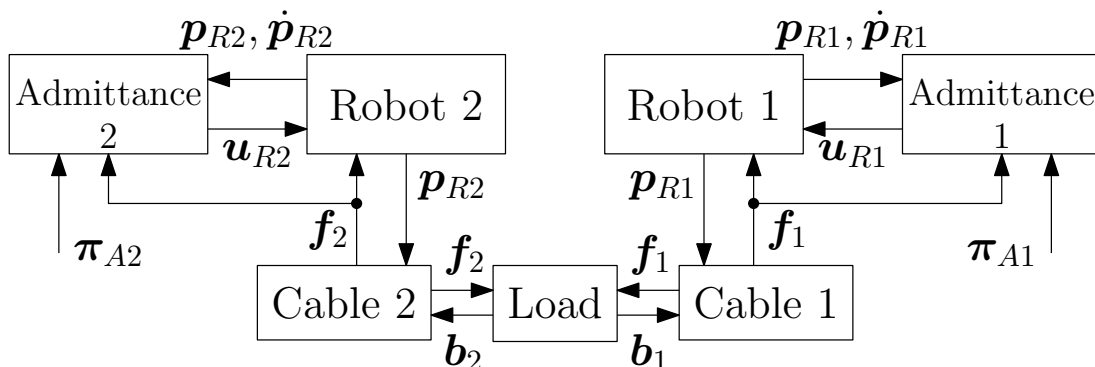


Figure 7.2: Schematic representation of the overall system including both physical and control blocks. Only two robots are considered for the sake of clarity.

$c_L = [0 \ S(\omega_L)J_L\omega_L - \omega_L^\top B_L\omega_L]^\top$ and

$$\mathbf{G} = \begin{bmatrix} \mathbf{I}_3 & \dots & \mathbf{I}_3 \\ \mathbf{S}({}^L\mathbf{b}_1)\mathbf{R}_L^\top & \dots & \mathbf{S}({}^L\mathbf{b}_N)\mathbf{R}_L^\top \end{bmatrix}. \quad (7.5)$$

We remark that the two dynamics in (7.4) are coupled together by the cable forces in (7.3).

As we shall see, a key role in all the following analyses is played by the *load internal force*. Given an equilibrium load configuration $(\bar{\mathbf{p}}_L, \bar{\mathbf{R}}_L)$ and resolving the equilibrium equations for \mathbf{f} , we can obtain the forces that the robots should apply:

$$\mathbf{f} = \mathbf{G}(\bar{\mathbf{R}}_L)^\dagger [m_L \mathbf{g} \mathbf{z}_W^\top \ 0_{1 \times 3}]^\top + t_L \mathbf{r}_L, \quad (7.6)$$

where † indicates the pseudo-inverse, $t_L \in \mathbb{R}$ is referred to as the *load internal force* and $\mathbf{r}_L \in \text{null}(\mathbf{G}(\bar{\mathbf{R}}_L)) \subset \mathbb{R}^{3N}$ is a vector containing the robot forces that produce internal forces on the object.

7.3 Control

The goal of our work is to i) stabilize the load at a desired configuration, $\bar{\mathbf{q}}_L = (\bar{\mathbf{p}}_L, \bar{\mathbf{R}}_L)$; ii) preserve the stability of the load during its transportation. For the reasons already introduced, we are interested in solving the mentioned objectives using a decentralized approach without explicit communication among the robots. To achieve the previous control objectives, we propose the use of an admittance filter for *all* the robots:

$$\mathbf{u}_{Ri} = \mathbf{M}_{Ai}^{-1} (-\mathbf{B}_{Ai}\dot{\mathbf{p}}_{Ri} - \mathbf{K}_{Ai}\mathbf{p}_{Ri} - \mathbf{f}_i + \boldsymbol{\pi}_{Ai}), \quad (7.7)$$

where the three positive definite symmetric matrices $\mathbf{M}_{Ai}, \mathbf{B}_{Ai}, \mathbf{K}_{Ai} \in \mathbb{R}^{3 \times 3}$ are the virtual inertia of the robot and the damping and stiffness of a virtual damper-spring system attached to the robot and connecting it to a reference trajectory yet to be defined; $\boldsymbol{\pi}_{Ai} \in \mathbb{R}^3$ is an additional input (see Fig. 7.2 for a schematic representation). Additional details about the admittance control law can be found in Chapter 2 of this Thesis. Basically, thanks to the aforementioned assumptions on the robot dynamics and on the presence of a perfect trajectory tracking, the robot translational dynamics in this analysis coincides with that of the compliant reference system described in Chapter 2.

Chapter 7. An Introduction to Cooperative Manipulation with particular focus on cable-suspended loads

The control approach that we propose in this section is similar to the one proposed in [219] for a two-robot case. However, we propose to have an admittance controller on all the robots, leader robot included. This confers to it some awareness of the rest of the system through the feedback of the contact forces. Moreover, in our approach, the follower robots are not assigned any reference trajectory, not even in the vertical direction. This, compared to [219], enlarges the workspace of the robots that now can move the object also along the vertical direction.

Notice that (7.7) does not require explicit communication between the robots. Indeed it requires only local information, i.e., the state of the robot $(\mathbf{p}_{Ri}, \dot{\mathbf{p}}_{Ri})$, and the force applied by the cable \mathbf{f}_i . The first can be retrieved with standard onboard sensors, while the second can be directly measured by an onboard force sensor or estimated by a sufficiently precise model-based observer as done in [192, 219]. There is a sort of implicit, *physical* communication taking place thanks to the interaction forces exchanged by means of the cables between the robots and the load. Combining equations (7.4) and (7.7) we can write the closed-loop system dynamics as $\dot{\mathbf{v}} = \mathbf{m}(\mathbf{q}, \mathbf{v}, \boldsymbol{\pi}_A)$ where

$$\mathbf{m}(\mathbf{q}, \mathbf{v}, \boldsymbol{\pi}_A) = \begin{bmatrix} \mathbf{M}_A^{-1} (-\mathbf{B}_A \dot{\mathbf{p}}_R - \mathbf{K}_A \mathbf{p}_R - \mathbf{f} + \boldsymbol{\pi}_A) \\ \mathbf{M}_L^{-1} (-\mathbf{c}_L(\mathbf{v}_L) - \mathbf{g}_L + \mathbf{G}\mathbf{f}) \end{bmatrix}, \quad (7.8)$$

with $\mathbf{q} = (\mathbf{q}_R, \mathbf{q}_L)$, $\mathbf{v} = [\mathbf{v}_R^\top \ \mathbf{v}_L^\top]^\top$ and $\boldsymbol{\pi}_A = [\boldsymbol{\pi}_{A1}^\top \ \dots \ \boldsymbol{\pi}_{AN}^\top]^\top$. Furthermore,

$\mathbf{M}_A = \text{diag}(\mathbf{M}_{A1}, \mathbf{M}_{A2})$, $\mathbf{B}_A = \text{diag}(\mathbf{B}_{A1}, \dots, \mathbf{B}_{AN})$, and $\mathbf{K}_A = \text{diag}(\mathbf{K}_{A1}, \dots, \mathbf{K}_{AN})$. In order to coordinate the motions of the robots in a decentralized way, we propose a leader-follower approach. Only one robot, namely the designated leader, will have active control of the system. Choosing robot 1 as leader, we set $\mathbf{K}_{A1} \neq \mathbf{0}$, $\mathbf{K}_{Ai} = \mathbf{0} \ \forall i \neq 1$ to obtain the sought leader-follower paradigm.

Intuitively, the behavior of the controlled system can be explained as it follows: the leader robot is the only one attracted to a position in the space. When it moves to follow a reference trajectory, it also drags the object. The follower robots, sensing the change in their own cable force, moves to actively restore the force reference value, thus following the force changes and hence the motion of the leader robot while also performing a damping action.

Cooperative Manipulation of a Cable-suspended Beam Load by Two Aerial Robots

8.1 Introduction

This chapter considers the case of $N=2$ robots transporting a cable-suspended beam-like load. Beam-like load transportation has received a considerable attention in the literature of aerial manipulation so far ([204, 205, 208, 218, 219]). As a matter of fact, it is of interest for several real-world applications, especially in the construction field, where we find columns, wooden pillars, iron beams for cement walls, scaffolds, pipes piece of the roofs and other beam-like building elements. The choice of considering two robots is based on the fact that two is the minimum number of robots that allows to control both the position and attitude of a cable-suspended beam-like load [204]. While three aerial robots allow controlling the entire pose of a generic rigid body [28], using more than two robots for a beam-like load might not be the best choice since it would increase the complexity of the system without being necessary for the control of the load. First, we carry out a study of the system equilibrium configurations and of their stability in Sec. 8.2 and 8.3. By doing so, we highlight the role played by a squeezing of the object induced by the robots —namely an internal force generated thanks to appropriate values of the reference forces given to the robots. Not only an internal force on the object determines the number of the equilibrium configurations of the system, but its value also influences their stability. Intuitively, we will see that an equilibrium in which the object is compressed is unstable while one in which the robot is under tension is stable. The passivity of the system is discussed in Sec. 8.4. These results have been previously published in [223] as well as the corresponding numerical validation.

Secondly, in Sec. 8.5 we study the effect of parametric uncertainty and force

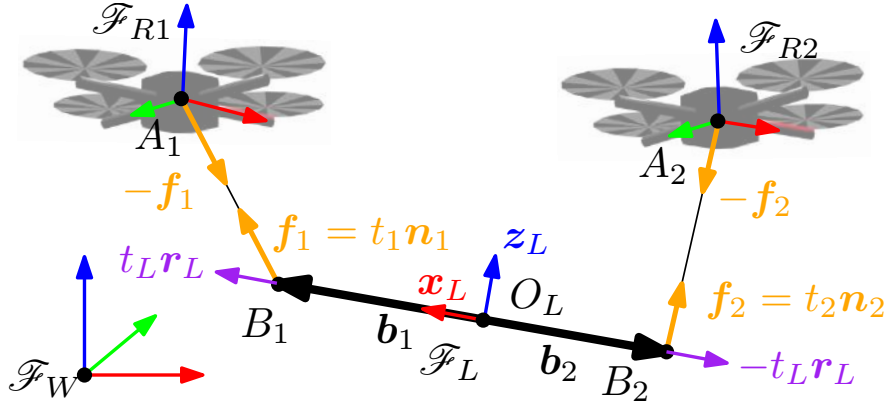


Figure 8.1: Representation of the two-robot system and its major variables. In this case, \mathbf{b}_1 and \mathbf{b}_2 are two opposite vectors aligned with the beam load.

measurement errors on the system equilibrium configurations. This is particularly important in order to assess the behavior of the system in non-ideal conditions—more realistic ones. Notably, some effort has been put in the literature to robustly handle the uncertainties about the parameters of the object to manipulate [203, 204]. While in [236] the unknown parameters of the object are estimated thanks to a centralized approach during preliminary maneuvers, in [220] the gains of the robot admittance controllers are tuned in order to minimize the effect of the uncertainties. In our analysis, we try to understand the effect of the uncertainties in the system equilibrium configurations and limit their effects.

After a formal analysis of the system new equilibrium configurations, we provide useful suggestions on how to perform the manipulation task in these non-ideal conditions. The role of the load internal force in the robustness of the system against the effect of the uncertainties emerges from the computations—see Sec. 8.6. On one side, we show the beneficial effect of a load internal force in the load *attitude* error and, on the other side, we also show how the internal force diminishes the sensitivity of the error to uncertainty variations.

The study of the error sensitivity to parametric and measurement uncertainty variations can be of particular practical interest, e.g., in the case in which the load to be transported contains moving masses (containers of liquids, boxes with moving objects inside). In these cases, in fact, the position of CoM of the load varies, and this can be interpreted as a variation over the uncertainty we have on that parameter. The significance of such a problem has been highlighted in [237], where the CoM of the load has been modeled as a mass-spring-damper system with its own dynamics that is supposed to be known. In our framework, instead, the movements of the CoM are regarded as disturbances. Another interesting example in this respect is the consecutive transportation of objects that are slightly different from each other, e.g. for what concerns the mass and length. One may want to transport the objects without changing the controller parameters every time, thus putting oneself in a situation characterized by varying parametric uncertainties. We also consider how to act on the load *position* error in the occurrence of parametric uncertainties.

Results of numerical simulations and experiments are shown in Sec. 8.7 and 8.8, respectively. Final discussions are drawn in Sec. 8.9.

8.2 Equilibrium Configurations

In this section the equilibrium configurations of the two-robot system are obtained. We say that \mathbf{q} is an *equilibrium configuration* if $\exists \pi_A$ s.t. $\mathbf{0} = m(\mathbf{q}, \mathbf{0}, \pi_A)$, i.e, if the corresponding zero-velocity state $(\mathbf{q}, \mathbf{0})$ is a forced equilibrium for the system (7.8) for a certain forcing input π_A . We say that an equilibrium configuration \mathbf{q} is stable, unstable, or asymptotically stable if $(\mathbf{q}, \mathbf{0})$ is stable, unstable, or asymptotically stable, respectively.

In the following, we shall prove that for any desired load configuration $\bar{\mathbf{q}}_L$ there exists a set $\Pi_A(\bar{\mathbf{q}}_L) \subset \mathbb{R}^6$ such that for any $\pi_A \in \Pi_A(\bar{\mathbf{q}}_L)$ one can compute a $\bar{\mathbf{q}}_R$, depending on $\bar{\mathbf{q}}_L$ and π_A , that makes $\bar{\mathbf{q}} = (\bar{\mathbf{q}}_L, \bar{\mathbf{q}}_R)$ an asymptotically stable equilibrium with π_A as forcing input. It will also emerge that, in order to stabilize the load at $\bar{\mathbf{q}}_L$, both the robots must know $\bar{\mathbf{R}}_L$ and only the leader robot needs to know $\bar{\mathbf{p}}_L$. Such one-time information is provided to the robot a priori, while no feedback on the actual load configuration will be required for any of the robots. In particular, we shall study:

- i) *equilibrium inverse problem*: the set of inputs (and corresponding robot positions) that originates equilibrium configurations in which $\mathbf{q}_L = \bar{\mathbf{q}}_L$ (Theorem 1);
- ii) *equilibrium direct problem*: which is the set of equilibrium configurations if π_A , chosen in the aforementioned set, is applied to the system (Theorem 2).

Theorem 1 (equilibrium inverse problem). *Consider the closed loop system (7.8) and assume that the load is at a given desired configuration $\mathbf{q}_L = \bar{\mathbf{q}}_L = (\bar{\mathbf{p}}_L, \bar{\mathbf{R}}_L)$. For each internal force $t_L \in \mathbb{R}$, there exists a unique constant value for the forcing input $\pi_A = \bar{\pi}_A$ (and a unique position of the robots $\mathbf{q}_R = \bar{\mathbf{q}}_R$) such that $\bar{\mathbf{q}} = (\bar{\mathbf{q}}_L, \bar{\mathbf{q}}_R)$ is an equilibrium of the system.*

In particular $\bar{\pi}_A$ and $\bar{\mathbf{q}}_R = [\bar{\mathbf{p}}_{R1}^\top \bar{\mathbf{p}}_{R2}^\top]^\top$ are given by

$$\bar{\pi}_A(\bar{\mathbf{q}}_L, t_L) = \mathbf{K}_A \bar{\mathbf{q}}_R + \bar{\mathbf{f}}(\bar{\mathbf{q}}_L, t_L) \quad (8.1)$$

$$\bar{\mathbf{p}}_{Ri}(\bar{\mathbf{q}}_L, t_L) = \bar{\mathbf{p}}_L + \bar{\mathbf{R}}_L {}^L \mathbf{b}_i + \left(\frac{\|\bar{\mathbf{f}}_i\|}{k_i} + l_{0i} \right) \frac{\bar{\mathbf{f}}_i}{\|\bar{\mathbf{f}}_i\|}, \quad (8.2)$$

for $i = 1, 2$, where

$$\bar{\mathbf{f}}(\bar{\mathbf{q}}_L, t_L) = \begin{bmatrix} \bar{\mathbf{f}}_1 \\ \bar{\mathbf{f}}_2 \end{bmatrix} = \begin{bmatrix} \frac{m_L g b_2 \mathbf{e}_3}{L} \\ \frac{m_L g b_1 \mathbf{e}_3}{L} \end{bmatrix} + t_L \begin{bmatrix} \mathbf{I}_3 \\ -\mathbf{I}_3 \end{bmatrix} \bar{\mathbf{R}}_L \mathbf{e}_1. \quad (8.3)$$

Proof. The desired load configuration $\bar{\mathbf{q}}_L$ can be equilibrated if there exists at least a $\bar{\mathbf{q}}_R$ and a π_A such that:

$$m(\bar{\mathbf{q}}, \mathbf{0}, \pi_A) = \mathbf{0}. \quad (8.4)$$

Consider the last six rows of (8.4). We must find the \mathbf{f} solving

$$\mathbf{G} \mathbf{f} = \mathbf{g}_L. \quad (8.5)$$

\mathbf{G} is not invertible since $\text{rank}(\mathbf{G}) = 5$, thus we have to verify that a solution for (8.5) exists. Expanding (8.5) we obtain

$$\mathbf{f}_1 + \mathbf{f}_2 = m_L g \mathbf{e}_3 \quad (8.6)$$

$$\mathbf{S}({}^L \mathbf{b}_1) \bar{\mathbf{R}}_L^\top \mathbf{f}_1 + \mathbf{S}({}^L \mathbf{b}_2) \bar{\mathbf{R}}_L^\top \mathbf{f}_2 = \mathbf{0}. \quad (8.7)$$

Chapter 8. Cooperative Manipulation of a Cable-suspended Beam Load by Two Aerial Robots

Then, substituting in (8.7) the \mathbf{f}_1 obtained from (8.6) we have $LS(\mathbf{e}_1)\bar{\mathbf{R}}_L^\top \mathbf{f}_2 = b_1 S(\nu E1)\bar{\mathbf{R}}_L^\top m_L g \mathbf{e}_3$, for which $\mathbf{f}_2 = \frac{m_L b_1 g \mathbf{e}_3}{L}$ is always a solution. Therefore, all the solutions of (8.5) can be written as

$$\bar{\mathbf{f}} = \mathbf{G}^\dagger \mathbf{g}_L + \mathbf{r}_L t_L, \quad (8.8)$$

where $\mathbf{G}^\dagger = [\frac{b_2}{L} \mathbf{I}_3 \quad \frac{b_1}{L} \mathbf{I}_3]^\top$ is the pseudo inverse of \mathbf{G} , $\mathbf{r}_L \in \mathbb{R}^6$ is a vector in $\text{Null}(\mathbf{G})$, and $t_L \in \mathbb{R}$ is an arbitrary number. We computed $\mathbf{r}_L = [\mathbf{f}_1^\top \quad \mathbf{f}_2^\top]^\top$ from (8.6) and (8.7) imposing the right hand side equal to zero. From (8.6) $\mathbf{f}_2 = -\mathbf{f}_1$, and replacing it into (8.7) we obtain $S(\mathbf{e}_1)\bar{\mathbf{R}}_L^\top \mathbf{f}_1 = \mathbf{0}$ which is verified if $\mathbf{f}_1 = t_L \bar{\mathbf{R}}_L \mathbf{e}_1$ with $t_L \in \mathbb{R}$. Finally, we obtain $\mathbf{r}_L = [\mathbf{I}_3 \quad -\mathbf{I}_3]^\top \bar{\mathbf{R}}_L \mathbf{e}_1$. Equation (8.8) can be then rewritten as (8.3). The expression of $\bar{\mathbf{p}}_{Ri}$ in (8.2) is computed using (7.3) and the kinematics of the system. Notice that (8.2) is singular when $\bar{\mathbf{f}}_i = \mathbf{0}$ for some i , which is, however, of no practical relevance. Lastly, from the first six rows of (8.4) we have that $\bar{\mathbf{q}}_L$ is equilibrated if $\boldsymbol{\pi}_A = \bar{\boldsymbol{\pi}}_A$, where $\bar{\boldsymbol{\pi}}_A$ is defined as in (8.1). \square

Remark 1. Based on Theorem 1 we can define a set

$$\Pi_A(\bar{\mathbf{q}}_L) = \{\boldsymbol{\pi}_A \in \mathbb{R}^6 : \boldsymbol{\pi}_A = \bar{\boldsymbol{\pi}}_A(\bar{\mathbf{q}}_L, t_L) \text{ for } t_L \in \mathbb{R}\} \text{ parametrized by the scalar } t_L \in \mathbb{R}.$$

Remark 2. Given a desired load configuration $\bar{\mathbf{q}}_L$ to equilibrate, Theorem 1 and its constructive proof give an intuitive method for choosing the forcing input $\boldsymbol{\pi}_A$.

Specifically, the only free parameter that the user has to choose is the value of the internal force t_L . We shall show that is always preferable to pick $t_L > 0$.

Once t_L is chosen and the input $\boldsymbol{\pi}_A = \bar{\boldsymbol{\pi}}_A(t_L, \bar{\mathbf{q}}_L)$ is applied to the system, it is not in general granted that $(\bar{\mathbf{q}}_L, \bar{\mathbf{q}}_R)$ is the only equilibrium of (7.8), i.e., the equilibrium direct problem may have multiple solutions.

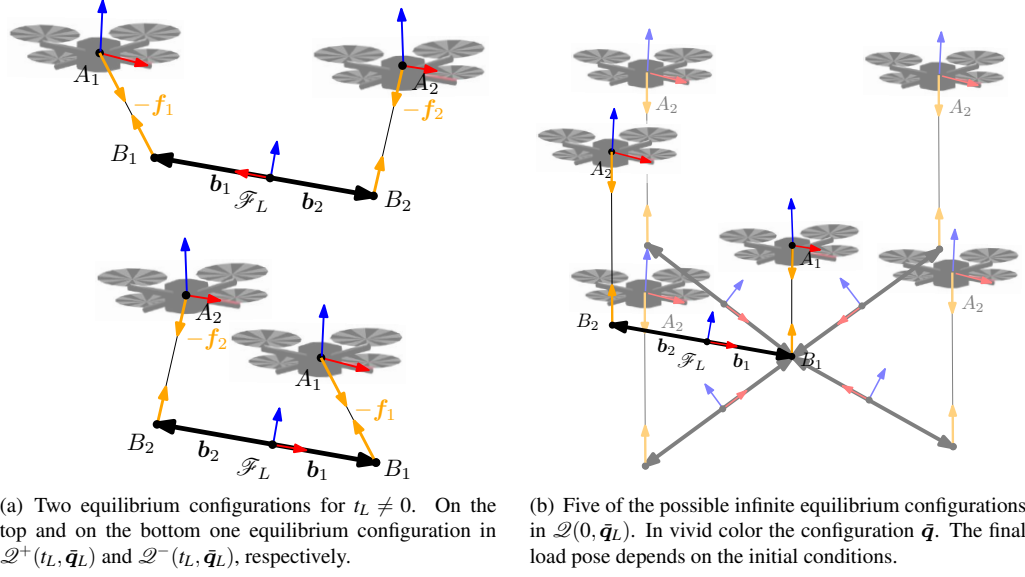
Theorem 2 (equilibrium direct problem). Given $t_L \in \mathbb{R}$, the equilibrium configurations of the system (7.8) when the input $\boldsymbol{\pi}_A = \bar{\boldsymbol{\pi}}_A(t_L, \bar{\mathbf{q}}_L)$ —computed as in (8.1)—is applied are all, and only, the ones described by the following conditions:

$$\begin{aligned} \mathbf{R}_L \mathbf{e}_1 \times t_L \bar{\mathbf{R}}_L \mathbf{e}_1 &= \mathbf{0} \\ \mathbf{p}_{R1} &= \bar{\mathbf{p}}_{R1} \\ \mathbf{p}_L &= \mathbf{p}_{R1} - \mathbf{R}_L^L \mathbf{b}_1 - \left(\frac{\|\bar{\mathbf{f}}_1\|}{k_1} + l_{01} \right) \frac{\bar{\mathbf{f}}_1}{\|\bar{\mathbf{f}}_1\|} = \\ &= \bar{\mathbf{p}}_L + (\bar{\mathbf{R}}_L - \mathbf{R}_L)^L \mathbf{b}_1 \\ \mathbf{p}_{R2} &= \mathbf{p}_L + \mathbf{R}_L^L \mathbf{b}_2 + \left(\frac{\|\bar{\mathbf{f}}_2\|}{k_2} + l_{02} \right) \frac{\bar{\mathbf{f}}_2}{\|\bar{\mathbf{f}}_2\|}. \end{aligned} \quad (8.9)$$

$\mathcal{Q}(t_L, \bar{\mathbf{q}}_L)$ denotes the set of configurations respecting (8.9).

Proof. Given $t_L \in \mathbb{R}$, and $\bar{\boldsymbol{\pi}}_A \in \Pi_A(\bar{\mathbf{q}}_L)$, a configuration \mathbf{q} is an equilibrium if $m(\mathbf{q}, \mathbf{0}, \bar{\boldsymbol{\pi}}_A) = \mathbf{0}$. The first six rows are $\mathbf{K}_A \mathbf{q}_R + \mathbf{f} - \bar{\boldsymbol{\pi}}_A = \mathbf{0}$. Then, using (8.1) we have that

$$\mathbf{f} = \mathbf{K}_A(\bar{\mathbf{q}}_R - \mathbf{q}_R) + \bar{\mathbf{f}}. \quad (8.10)$$



(a) Two equilibrium configurations for $t_L \neq 0$. On the top and on the bottom one equilibrium configuration in $\mathcal{Q}^+(t_L, \bar{q}_L)$ and $\mathcal{Q}^-(t_L, \bar{q}_L)$, respectively.

(b) Five of the possible infinite equilibrium configurations in $\mathcal{Q}(0, \bar{q}_L)$. In vibrant color the configuration \bar{q} . The final load pose depends on the initial conditions.

Figure 8.2: 2D representation of the equilibrium configurations for different values of t_L .

At this point, recalling that $\mathbf{K}_{A2} = \mathbf{0}$ and the expression of $\bar{\mathbf{f}}$ in (8.3), we get

$$\mathbf{f}_2 = \bar{\mathbf{f}}_2. \quad (8.11)$$

Substituting (8.11) into the load translational equilibrium (8.6), one finds that

$$\mathbf{f}_1 = \bar{\mathbf{f}}_1, \quad (8.12)$$

which implies, from (8.10), that $\mathbf{e}_R = (\bar{\mathbf{p}}_{R1} - \mathbf{p}_{R1}) = \mathbf{0}$ and hence $\mathbf{p}_{R1} = \bar{\mathbf{p}}_{R1}$.

Replacing (8.11) and (8.12) into the last three rows of (8.4), we obtain the first condition in (8.9). We can retrieve \mathbf{p}_L and \mathbf{p}_{R2} , using (7.3) and the kinematics. \square

If $t_L = 0$, the conditions in (8.9) hold for all the possible load attitudes $\mathbf{R}_L \in SO(3)$. This means, using the notation introduced in Theorem 2, that $\mathcal{Q}(0, \bar{q}_L)$ contains all $\mathbf{R}_L \in SO(3)$ and, consequently, the corresponding \mathbf{p}_{R2} and \mathbf{p}_L computed using (8.9). Figure 8.2(b) illustrates some of these equilibrium configurations. Basically, $\mathbf{p}_{R1} = \bar{\mathbf{p}}_{R1}$, as well as (8.11) and (8.12), always hold. However, the attitude of the load is arbitrary, as well as \mathbf{p}_{R2} and \mathbf{p}_L that can be computed accordingly.

For $t_L \neq 0$, it is required that $\mathbf{R}_L \mathbf{e}_1$ is parallel to $\bar{\mathbf{R}}_L \mathbf{e}_1$. This can be obtained with $\mathbf{R}_L = \mathbf{R}_L(k, \phi) = \bar{\mathbf{R}}_L \mathbf{R}_{z_L}(k\pi) \mathbf{R}_{x_L}(\phi)$, where $k = 0, 1$, $\phi \in [0, 2\pi]$, and $\mathbf{R}_{z_L}(\cdot)$ and $\mathbf{R}_{x_L}(\cdot)$ are the rotations about z_L and x_L , respectively. Considering that ${}^L \mathbf{b}_1$ is parallel to x_L we have that $\mathbf{R}_{z_L}(k\pi) \mathbf{R}_{x_L}(\phi) {}^L \mathbf{b}_1$ is either equal to ${}^L \mathbf{b}_1$ if $k = 0$ or to $-{}^L \mathbf{b}_1$ if $k = 1$. Therefore, using (8.9), we obtain either $\mathbf{p}_L = \bar{\mathbf{p}}_L$ if $k = 0$ or $\mathbf{p}_L = \bar{\mathbf{p}}_L + 2\mathbf{b}_1$ if $k = 1$. Fig. 8.2(a) provides a simplified representations of the two different sets of equilibrium configurations for $k = 0$ and $k = 1$, formally defined as follows:

- $\mathcal{Q}^+(t_L, \bar{q}_L) = \{\mathbf{q} \in \mathcal{Q}(t_L, \bar{q}_L) | \mathbf{R}_L = \mathbf{R}_L(0, \phi) \forall \phi\}$,
- $\mathcal{Q}^-(t_L, \bar{q}_L) = \{\mathbf{q} \in \mathcal{Q}(t_L, \bar{q}_L) | \mathbf{R}_L = \mathbf{R}_L(1, \phi) \forall \phi\}$.

Notice that $\mathcal{Q}(0, \bar{q}_L)$ is parametrized by an element in $SO(3)$ (any $\mathbf{R}_L \in SO(3)$ is allowed), while $\mathcal{Q}^+(t_L, \bar{q}_L)$ and $\mathcal{Q}^-(t_L, \bar{q}_L)$, for $t_L \neq 0$, are parametrized by an element

Chapter 8. Cooperative Manipulation of a Cable-suspended Beam Load by Two Aerial Robots

in $SO(1)$ ($\mathbf{R}_L(0, \phi)$ and $\mathbf{R}_L(1, \phi)$, for any $\phi \in [0, 2\pi]$, respectively). For all t_L , the load rotation about x_L is arbitrary because the robots can not apply any torque along x_L , so the corresponding rotation results uncontrollable.

8.3 Stability

In this section, we shall analyze the stability of the equilibrium configurations discovered in Sec. 8.2. First, we define $\mathbf{x} = (\mathbf{q}, \mathbf{v})$ as the state of the system, $\bar{\mathbf{x}} = (\bar{\mathbf{q}}, \mathbf{0})$ the desired equilibrium state, and the following sets (subspaces of the state space):

- $\mathcal{X}(t_L, \bar{\mathbf{q}}_L) = \{\mathbf{x} : \mathbf{q} \in \mathcal{Q}(t_L, \bar{\mathbf{q}}_L), \mathbf{v} = \mathbf{0}\}$,
- $\mathcal{X}(0, \bar{\mathbf{q}}_L) = \{\mathbf{x} : \mathbf{q} \in \mathcal{Q}(0, \bar{\mathbf{q}}_L), \mathbf{v} = \mathbf{0}\}$,
- $\mathcal{X}^+(t_L, \bar{\mathbf{q}}_L) = \{\mathbf{x} : \mathbf{q} \in \mathcal{Q}^+(t_L, \bar{\mathbf{q}}_L), \mathbf{v} = \mathbf{0}\}$,
- $\mathcal{X}^-(t_L, \bar{\mathbf{q}}_L) = \{\mathbf{x} : \mathbf{q} \in \mathcal{Q}^-(t_L, \bar{\mathbf{q}}_L), \mathbf{v} = \mathbf{0}\}$.

Theorem 3. *Let us consider a desired load configuration $\bar{\mathbf{q}}_L$. For the system (7.8) let the constant forcing input π_A be chosen in $\Pi_A(\bar{\mathbf{q}}_L)$ corresponding to a certain internal force t_L . Then \mathbf{x} belonging to:*

- $\mathcal{X}^+(t_L, \bar{\mathbf{q}}_L)$ is asymptotically stable if $t_L > 0$;
- $\mathcal{X}^-(t_L, \bar{\mathbf{q}}_L)$ is unstable if $t_L > 0$;
- $\mathcal{X}(0, \bar{\mathbf{q}}_L)$ is asymptotically stable;
- $\mathcal{X}^+(t_L, \bar{\mathbf{q}}_L)$ is unstable if $t_L < 0$;
- $\mathcal{X}^-(t_L, \bar{\mathbf{q}}_L)$ is asymptotically stable if $t_L < 0$.

Proof. Let us consider the following Lyapunov candidate:

$$V(\mathbf{x}) = \frac{1}{2}(\mathbf{v}_R^\top \mathbf{M}_A \mathbf{v}_R + \mathbf{e}_R^\top \mathbf{K}_A \mathbf{e}_R + \mathbf{v}_L^\top \mathbf{M}_L \mathbf{v}_L + \boldsymbol{\omega}_L^\top \mathbf{J}_L \boldsymbol{\omega}_L + k_1(\|\mathbf{l}_1\| - l_{01})^2 + k_2(\|\mathbf{l}_2\| - l_{02})^2) - \mathbf{l}_1^\top \bar{\mathbf{f}}_1 - \mathbf{l}_2^\top \bar{\mathbf{f}}_2 + t_L(1 - (\bar{\mathbf{R}}_L \mathbf{e}_1)^\top \mathbf{R}_L \mathbf{e}_1) + V_0, \quad (8.13)$$

where $V_0 \in \mathbb{R}_{\geq 0}$. First, we want to show that

- i) $\mathbf{x}_{\min} = \operatorname{argmin}_{\mathbf{x}} V(\mathbf{x})$ is such that $\mathbf{x}_{\min} \in \mathcal{X}(0, \bar{\mathbf{q}}_L)$ and $\mathbf{x}_{\min} \in \mathcal{X}^+(t_L, \bar{\mathbf{q}}_L)$ for $t_L > 0$;
- ii) $V(\mathbf{x})$ is positive definite for an opportune choice of V_0 .

We divide (8.13) into three parts such that

$$V(\mathbf{x}) = \bar{V}(\mathbf{x}) + V_1(\mathbf{x}) + V_2(\mathbf{x}), \quad (8.14)$$

where

$$\begin{aligned} \bar{V}(\mathbf{x}) &= \frac{1}{2}(\mathbf{v}_R^\top \mathbf{M}_A \mathbf{v}_R + \mathbf{e}_R^\top \mathbf{K}_A \mathbf{e}_R + \mathbf{v}_L^\top \mathbf{M}_L \mathbf{v}_L + \boldsymbol{\omega}_L^\top \mathbf{J}_L \boldsymbol{\omega}_L + t_L(1 - (\bar{\mathbf{R}}_L \mathbf{e}_1)^\top \mathbf{R}_L \mathbf{e}_1) + V_0 \\ V_i(\mathbf{x}) &= \frac{1}{2}k_i(\|\mathbf{l}_i\| - l_{0i})^2 - \mathbf{l}_i^\top \bar{\mathbf{f}}_i, \end{aligned} \quad (8.15)$$

for $i = 1, 2$.

We first show that the Lyapunov function is *radially unbounded* (also called *coercive*), i.e., $\lim_{\|\mathbf{x}\| \rightarrow \infty} V(\mathbf{x}) = \infty$. Indeed, we have that clearly $\lim_{\|\mathbf{x}\| \rightarrow \infty} \bar{V}(\mathbf{x}) = \infty$, while

$$\begin{aligned}
 & \lim_{\|\mathbf{x}\| \rightarrow \infty} V_i(\mathbf{x}) \\
 & \lim_{\|\mathbf{x}\| \rightarrow \infty} \frac{1}{2} k_i (\|\mathbf{l}_i\| - l_{0i})^2 - \mathbf{l}_i^\top \bar{\mathbf{f}}_i = \\
 & \lim_{\|\mathbf{x}\| \rightarrow \infty} \frac{1}{2} k_i (\|\mathbf{l}_i\|^2 + l_{0i}^2) - k_i \|\mathbf{l}_i\| l_{0i} - \mathbf{l}_i^\top \bar{\mathbf{f}}_i \geq \\
 & \lim_{\|\mathbf{x}\| \rightarrow \infty} \frac{1}{2} k_i (\|\mathbf{l}_i\|^2 + l_{0i}^2) - k_i \|\mathbf{l}_i\| l_{0i} - \|\mathbf{l}_i\| \|\bar{\mathbf{f}}_i\| = \\
 & \lim_{\|\mathbf{x}\| \rightarrow \infty} \|\mathbf{l}_i\|^2 \left(\frac{k_i}{2} + \frac{k_i l_{0i}^2}{2 \|\mathbf{l}_i\|^2} - \frac{k_i l_{0i}}{\|\mathbf{l}_i\|} - \frac{\|\bar{\mathbf{f}}_i\|}{\|\mathbf{l}_i\|} \right) = +\infty.
 \end{aligned} \tag{8.16}$$

Based on this results and on Theorem 1.15 of [238], we can say that function (8.15) has a global minimum. Now we can look for this minimum among the stationary points, i.e., where the gradient $\nabla V(\mathbf{x}) = \mathbf{0}$, and among the points where (8.13) is not differentiable [239].

It is clear that $\nabla \bar{V}(\mathbf{x}) = \mathbf{0}$ only if $\mathbf{v} = \mathbf{0}$, $\mathbf{p}_{R1} = \bar{\mathbf{p}}_{R1}$ and $t_L \mathbf{R}_L \mathbf{e}_1 \times \bar{\mathbf{R}}_L \mathbf{e}_1 = \mathbf{0}$.

Regarding $V_i(\mathbf{x})$, let us consider its gradient with respect to the cable configuration \mathbf{l}_i :

$$\nabla_{\mathbf{l}_i} V_i(\mathbf{x}) = \frac{\partial V_i(\mathbf{x})}{\partial \mathbf{l}_i} = k_i (\|\mathbf{l}_i\| - l_{0i}) \frac{\mathbf{l}_i^\top}{\|\mathbf{l}_i\|} - \bar{\mathbf{f}}_i^\top. \tag{8.17}$$

Then, $\nabla_{\mathbf{l}_i} V_i(\mathbf{x}) = \mathbf{0}$ if and only if

$$k_i (\|\mathbf{l}_i\| - l_{0i}) \frac{\mathbf{l}_i^\top}{\|\mathbf{l}_i\|} = \bar{\mathbf{f}}_i. \tag{8.18}$$

Condition (8.18) holds in two different cases:

- a) $k_i (\|\mathbf{l}_i\| - l_{0i}) = \|\bar{\mathbf{f}}_i\|$ and $\frac{\mathbf{l}_i}{\|\mathbf{l}_i\|} = \frac{\bar{\mathbf{f}}_i}{\|\bar{\mathbf{f}}_i\|}$, for which $\|\mathbf{l}_i\| > l_{0i}$ and $\mathbf{l}_i^\top \bar{\mathbf{f}}_i > 0$;
- b) $\frac{k_i (\|\mathbf{l}_i\| - l_{0i})}{\|\mathbf{l}_i\|} = -\|\bar{\mathbf{f}}_i\|$ and $\frac{\mathbf{l}_i}{\|\mathbf{l}_i\|} = -\frac{\bar{\mathbf{f}}_i}{\|\bar{\mathbf{f}}_i\|}$, for which $\|\mathbf{l}_i\| < l_{0i}$ and $\mathbf{l}_i^\top \bar{\mathbf{f}}_i < 0$.

The previous two cases have a straightforward physical interpretation. Since the cables are modeled as a spring, they can produce a force at a certain point both being stretched in the same direction of the force itself, as in case a), or being compressed in the opposite direction, as in case b). However, in this work, we consider only case a) because case b) is not practicably feasible for cables, thus out of our region of interest. Therefore, $\nabla V(\mathbf{x}) = \mathbf{0}$ if $\mathbf{x} \in \mathcal{X}_{\mathbf{v}\mathbf{0}}^a \cup \mathcal{X}_{\mathbf{v}\mathbf{0}}^b$ where

- a) $\mathcal{X}_{\mathbf{v}\mathbf{0}}^a = \{ \mathbf{x} \mid \mathbf{v} = \mathbf{0}, \mathbf{p}_{R1} = \bar{\mathbf{p}}_{R1}, t_L \mathbf{R}_L \mathbf{e}_1 \times \bar{\mathbf{R}}_L \mathbf{e}_1 = \mathbf{0}, k_i (\|\mathbf{l}_i\| - l_{0i}) = \|\bar{\mathbf{f}}_i\|, \frac{\mathbf{l}_i}{\|\mathbf{l}_i\|} = \frac{\bar{\mathbf{f}}_i}{\|\bar{\mathbf{f}}_i\|} \}$
- b) $\mathcal{X}_{\mathbf{v}\mathbf{0}}^b = \{ \mathbf{x} \mid \mathbf{v} = \mathbf{0}, \mathbf{p}_{R1} = \bar{\mathbf{p}}_{R1}, t_L \mathbf{R}_L \mathbf{e}_1 \times \bar{\mathbf{R}}_L \mathbf{e}_1 = \mathbf{0}, k_i (\|\mathbf{l}_i\| - l_{0i}) = -\|\bar{\mathbf{f}}_i\|, \frac{\mathbf{l}_i}{\|\mathbf{l}_i\|} = -\frac{\bar{\mathbf{f}}_i}{\|\bar{\mathbf{f}}_i\|} \}$

Chapter 8. Cooperative Manipulation of a Cable-suspended Beam Load by Two Aerial Robots

However, $\mathbf{x} \in \mathcal{X}_{\nabla 0}^b$ can not be the global minima since we can show that $V(\mathbf{x}_a) < V(\mathbf{x}_b)$ with $\mathbf{x}_a \in \mathcal{X}_{\nabla 0}^a$ and $\mathbf{x}_b \in \mathcal{X}_{\nabla 0}^b$. This comes from the fact that in (8.13), $-\mathbf{l}_i^\top \bar{\mathbf{f}}_i < 0$ and $-\mathbf{l}_i^\top \bar{\mathbf{f}}_i > 0$ for $\mathbf{x} \in \mathcal{X}_{\nabla 0}^a$ and $\mathbf{x} \in \mathcal{X}_{\nabla 0}^b$, respectively. Finally, we have to check the non-differentiable points of (8.13), namely the state $\mathbf{x} \in \mathcal{X}_{\mathbf{l},0} = \{\mathbf{x} \mid \|\mathbf{l}_i\| = 0 \text{ for } i = 1, 2\}$. Notice that this condition is out of our domain of interest. Nevertheless, also in this case we can show that $V(\mathbf{x}_a) < V(\mathbf{x}_{\mathbf{l},0})$. Indeed, $\bar{V}(\mathbf{x}_a) = \bar{V}(\mathbf{x}_{\mathbf{l},0})$ and

$$\begin{aligned} V_i(\mathbf{x}_{\mathbf{l},0}) &= \frac{1}{2}k_i l_{0i}^2 \\ V_i(\mathbf{x}_a) &= \frac{1}{2}k_i(\|\mathbf{l}_i\|^2 + l_{0i}^2 - 2\|\mathbf{l}_i\|l_{0i}) - \mathbf{l}_i^\top k_i(\|\mathbf{l}_i\| - l_{0i}) \frac{\mathbf{l}_i}{\|\mathbf{l}_i\|} \\ &= \frac{1}{2}k_i\|\mathbf{l}_i\|^2 + \frac{1}{2}k_i l_{0i}^2 - k_i\|\mathbf{l}_i\|l_{0i} - k_i\|\mathbf{l}_i\|^2 + k_i\|\mathbf{l}_i\|l_{0i} \\ &= \frac{1}{2}k_i l_{0i}^2 - \frac{1}{2}k_i\|\mathbf{l}_i\|^2. \end{aligned}$$

Thus $V_i(\mathbf{x}_a) < V_i(\mathbf{x}_{\mathbf{l},0})$.

We can finally conclude that $\mathbf{x} \in \mathcal{X}_{\nabla 0}^a$ is the global minimum of (8.13). Furthermore, with a similar reasoning we can show that $\mathcal{X}_{\nabla 0}^a = \mathcal{X}(0, \bar{\mathbf{q}}_L)$ for $t_L = 0$ and $\mathcal{X}_{\nabla 0}^a = \mathcal{X}^+(t_L, \bar{\mathbf{q}}_L)$ for $t_L > 0$, proving point i).

Concerning point ii), let us define the function $V'(\mathbf{x})$ as in (8.13) but without V_0 . We can simply set

$$V_0 = \min_{\mathbf{x}}(V'(\mathbf{x})) = V'(\mathbf{x}_a)$$

with $\mathbf{x}_a \in \mathcal{X}_{\nabla 0}^a$. With this choice, we have that $V(\mathbf{x}) \geq 0$ and $V(\bar{\mathbf{x}}) = 0$.

To conclude the proof, we need now to study the sign of the time derivative of (8.13).

Using (7.8), (7.3) and (8.3) we obtain $\dot{V} = -\mathbf{v}_R^\top \mathbf{B}_A \mathbf{v}_R - \boldsymbol{\omega}_L^\top \mathbf{B}_L \boldsymbol{\omega}_L$ that is clearly negative semidefinite. In particular $\dot{V}(\mathbf{x}) = 0$ for all $\mathbf{x} \in \mathcal{E} = \{\mathbf{x} : \mathbf{v}_R = \mathbf{0}, \boldsymbol{\omega}_L = \mathbf{0}\}$

Since \dot{V} is only negative semidefinite, we rely on *LaSalle's invariance principle*. Let

us define a positively invariant set $\Omega_\alpha = \{\mathbf{x} : V(\mathbf{x}) \leq \alpha \text{ with } \alpha \in \mathbb{R}_{>0}\}$. By

construction, Ω_α is compact since (8.13) is radially unbounded and Ω_0 is compact

($\Omega_0 = \mathcal{X}(0, \bar{\mathbf{q}}_L)$ and $\Omega_0 = \mathcal{X}^+(t_L, \bar{\mathbf{q}}_L)$ for $t_L = 0$ and $t_L > 0$, respectively, are both

compact sets). Then, we need to find the largest invariant set \mathcal{M} in

$\mathcal{E} = \{\mathbf{x} \in \Omega_\alpha \mid \dot{V}(\mathbf{x}) = 0\}$. A trajectory $\mathbf{x}(t)$ belongs identically to \mathcal{E} if

$\dot{V}(\mathbf{x}(t)) \equiv 0 \Leftrightarrow \mathbf{v}_R(t) \equiv \mathbf{0}$ and $\boldsymbol{\omega}_L(t) \equiv \mathbf{0} \Leftrightarrow m(\mathbf{q}(t), \mathbf{0}, \boldsymbol{\pi}_A) = \mathbf{0}$ for all $t \in \mathbb{R}_{>0}$.

Therefore, \mathbf{x} has to be an equilibrium, and from Theorem 2 we have that

$\dot{V}(\mathbf{x}(t)) \equiv 0 \Leftrightarrow \mathbf{x}(t) \in \mathcal{X}(t_L, \bar{\mathbf{q}}_L)$. Thus, we obtain $\mathcal{M} = \Omega_\alpha \cap \mathcal{X}(t_L, \bar{\mathbf{q}}_L)$.

For $t_L > 0$, it is easy to see that for a sufficiently small α , $\mathcal{X}^+(t_L, \bar{\mathbf{q}}_L) \subseteq \Omega_\alpha$ but

$\mathcal{X}^-(t_L, \bar{\mathbf{q}}_L) \cap \Omega_\alpha = \emptyset$. This holds because $V(\mathbf{x}) = 0$ for $\mathbf{x} \in \mathcal{X}^+(t_L, \bar{\mathbf{q}}_L)$, while

$V(\mathbf{x}) > 0$ for $\mathbf{x} \in \mathcal{X}^-(t_L, \bar{\mathbf{q}}_L)$. Indeed, in (8.13), for $\mathbf{x} \in \mathcal{X}^-(t_L, \bar{\mathbf{q}}_L)$,

we have $t_L(1 - (\bar{\mathbf{R}}_L \mathbf{e}_1)^\top \mathbf{R}_L \mathbf{e}_1) = 2t_L > 0$. Therefore, $\mathcal{M} = \mathcal{X}^+(t_L, \bar{\mathbf{q}}_L)$. All

conditions of LaSalle's principle are satisfied and $\mathcal{X}^+(t_L, \bar{\mathbf{q}}_L)$ is locally asymptotically stable.

On the other hand, for $t_L = 0$ we have that $\mathcal{X}(t_L, \bar{\mathbf{q}}_L) \subseteq \Omega_\alpha$ for every sufficiently small

α . Therefore, $\mathcal{M} = \mathcal{X}(t_L, \bar{\mathbf{q}}_L)$ and, as before, we can conclude that $\mathcal{X}(t_L, \bar{\mathbf{q}}_L)$ is

locally asymptotically stable for the LaSalle's invariance principle.

Now, let us investigate the stability for $t_L < 0$. As before, with an opportune choice of V_0 , we have that $V(\mathbf{x}) = 0$ for $\mathbf{x} \in \mathcal{X}^+(t_L, \bar{\mathbf{q}}_L)$. However, $\mathcal{X}^+(t_L, \bar{\mathbf{q}}_L)$ is a set of accumulation for the points where $V(\mathbf{x}) < 0$. Indeed, consider $\mathbf{v} = \mathbf{0}$, $\mathbf{p}_{R1} = \bar{\mathbf{p}}_{R1}$, \mathbf{R}_L such that $(\bar{\mathbf{R}}_L \mathbf{e}_1)^\top \mathbf{R}_L \mathbf{e}_1 = 1 - \varepsilon$, with $\varepsilon > 0$ arbitrarily small, \mathbf{p}_L and \mathbf{p}_{R2} as in (8.9). Under this conditions, we have that $V(\mathbf{x}) = t_L(1 - (\bar{\mathbf{R}}_L \mathbf{e}_1)^\top \mathbf{R}_L \mathbf{e}_1) = t_L \varepsilon < 0$. Then, $\dot{V}(\mathbf{x}) < 0$ in a neighborhood of $\mathcal{X}^+(t_L, \bar{\mathbf{q}}_L)$. All conditions of *Chetaev's theorem* (the formulation of both this and La Salle's invariance principle can be found, e.g., in [240]) are satisfied, and we can conclude that $\mathcal{X}^+(t_L, \bar{\mathbf{q}}_L)$ is an unstable set. Finally, to study the stability of $\mathcal{X}^-(t_L, \bar{\mathbf{q}}_L)$ for $t_L \neq 0$, let us consider a desired load configuration $\bar{\mathbf{q}}'_L = (\bar{\mathbf{p}}'_L, \bar{\mathbf{R}}'_L)$ such that $\bar{\mathbf{p}}'_L = \mathbf{p}'_L + 2\bar{\mathbf{R}}_L \mathbf{e}_1$ and $\bar{\mathbf{R}}'_L = \mathbf{R}_L(1, \phi)$ for a certain ϕ . We choose $\pi'_A \in \Pi_A(\bar{\mathbf{q}}'_L)$ with $t'_L = -t_L$. For the reasoning in Sec. 8.2, note that $\mathcal{X}^+(t'_L, \bar{\mathbf{q}}'_L) = \mathcal{X}^-(t_L, \bar{\mathbf{q}}_L)$. Furthermore, for the previous results, if $t_L > 0$, and thus $t'_L < 0$, $\mathcal{X}^+(t'_L, \bar{\mathbf{q}}'_L)$ is unstable. Therefore, $\mathcal{X}^-(t_L, \bar{\mathbf{q}}_L)$ is unstable, too. A similar reasoning can be done to prove that $\mathcal{X}^-(t_L, \bar{\mathbf{q}}_L)$ is locally asymptotically stable for $t_L < 0$. This ends the proof. \square

To summarize the content of this section, we have shown that it is advisable to choose $t_L > 0$. From one side, because $t_L = 0$ generates an asymptotically stable set of equilibrium points (thus, being non-isolated none of them is attractive) in which the attitude of the load is arbitrary. This prevents us from being able to control the pose of the load. On the other side, $t_L < 0$ originates an unstable equilibrium so that, again but for different reasons, we are not able to effectively control the pose of the object. Choosing $t_L > 0$ and $\pi_A \in \Pi_A(\bar{\mathbf{q}}_L)$ bring the system to asymptotically converge to the desired load configuration.

8.4 Passivity

Theorem 3 characterizes the stability of the static equilibrium configurations given a certain constant forcing input. In this section, we focus instead on the dynamic part of the object manipulation. Let us now show how one can exploit the input π_{A1} in order to move the load between two distinct positions. From (8.1)–(8.3) and from the fact that $\mathbf{K}_{A2} = \mathbf{0}$, it descends that only $\bar{\pi}_{A1}$, in $\bar{\pi}_A = [\bar{\pi}_{A1}^\top \bar{\pi}_{A2}^\top]^\top$, actually depends on the desired load position $\bar{\mathbf{p}}_L$. This makes robot 1 able to steer alone the load position without communicating with robot 2. This is done by first plugging a new desired position $\bar{\mathbf{p}}'_L$ in (8.1) thus computing a new $\bar{\mathbf{p}}'_{R1}$, and then plugging $\bar{\mathbf{p}}'_{R1}$ in (8.2) in order to compute the new constant forcing input $\bar{\pi}'_{A1}$. However, one may want to minimize the transient phases generated by a piecewise constant forcing input. It is sufficient to design π_{A1} as

$$\pi_{A1}(t) = \bar{\pi}_{A1} + \mathbf{u}_{A1}(t), \quad (8.19)$$

where $\mathbf{u}_{A1}(t)$ is a smooth function such that $\pi_{A1}(0) = \bar{\pi}_{A1}$ and $\pi_{A1}(t_f) = \bar{\pi}'_{A1}$ for $t_f \in \mathbb{R}_{>0}$. To ensure that the system remains stable when the input is time-varying, we shall prove that the system is output-strictly passive w.r.t. the input-output pair $(\mathbf{u}, \mathbf{y}) = (\mathbf{u}_A, \mathbf{v}_R)$.

Theorem 4. *If π_A is defined as in (8.19) for a certain $\bar{\mathbf{q}}$ and $\bar{\mathbf{q}}'$ with $t_L \geq 0$, then system (7.8) is output-strictly passive w.r.t. the storage function (8.13) and the input-output pair $(\mathbf{u}, \mathbf{y}) = (\mathbf{u}_A, \mathbf{v}_R)$.*

Chapter 8. Cooperative Manipulation of a Cable-suspended Beam Load by Two Aerial Robots

Proof. In the proof of Theorem 3 we already shown that (8.13) is a continuously differentiable positive definite function for $t_L \geq 0$, properly choosing V_0 . Furthermore, replacing (8.19) into (7.7), and differentiating (8.13) we obtain

$$\begin{aligned}\dot{V} &= -\mathbf{v}_R^\top \mathbf{B}_A \mathbf{v}_R + \mathbf{v}_R^\top \mathbf{u}_A - \boldsymbol{\omega}_L^\top \mathbf{B}_L \boldsymbol{\omega}_L \\ &\leq \mathbf{u}^\top \mathbf{y} - \mathbf{y}^\top \mathbf{B}_A \mathbf{y} = \mathbf{u}^\top \mathbf{y} - \mathbf{y}^\top \Phi(\mathbf{y}),\end{aligned}\tag{8.20}$$

with $\mathbf{y}^\top \Phi(\mathbf{y}) > 0 \forall \mathbf{y} \neq \mathbf{0}$. Therefore, system (7.8) is *output-strictly passive* [240] \square

Thanks to the passivity of the system we can say that for a bounded input provided to the leader, the energy of the system remains bounded, too. This means that while moving the leader, the overall state of the system will remain bounded, and will converge to another specific equilibrium configuration when the input of the leader becomes constant.

8.5 Equilibrium Configurations in the case of Parametric Uncertainties and Force Measurement Errors

In the previous sections, we have studied the behavior of the system in ideal conditions. In this section, on the other hand, model uncertainties and measurement errors are introduced to consider the behavior of the system in a more realistic scenario. More specifically, we consider the scenarios in which:

- m_L is not known, but only its nominal value \hat{m}_L is available for the control design. We define the uncertainty as $\Delta_m = m_L - \hat{m}_L$;
- b_1 is not known, but only its nominal value \hat{b}_1 is available for the control design. This corresponds to some uncertainty on the position of the load CoM $\Delta_b = b_1 - \hat{b}_1$;
- L is not known, but only its nominal value \hat{L} is available. In this case the distance between the points B_1 and B_2 is affected by uncertainty, and we define $\Delta_\ell = \frac{1}{L} - \frac{1}{\hat{L}} = \ell - \hat{\ell}$;
- \mathbf{f}_1 and \mathbf{f}_2 are not exactly known, because the measured or estimated values are affected by errors. Thus robot i -th only knows the quantity $\hat{\mathbf{f}}_i = \mathbf{f}_i + \boldsymbol{\delta}_i$.
- the model of the cable i -th is not exact, so that the nominal length l_{0i} and the stiffness k_i are not known, but only their nominal values \hat{l}_{0i} and \hat{k}_i are available for the control design. We define the uncertainties $\Delta_{ki} = k_i - \hat{k}_i$, $\Delta_{l0i} = l_{0i} - \hat{l}_{0i}$.

In the following, the hat symbol will be used over a reference quantity also to indicate the corresponding quantity but computed using the uncertain parameters.

Given the desired $\bar{\mathbf{q}}_L$, we choose a value of t_L and compute the corresponding forcing input $\hat{\boldsymbol{\pi}}_A$ according to the results of Theorem 1. We are interested in understanding the actual equilibrium configuration of the system provided that $\hat{\boldsymbol{\pi}}_A \neq \bar{\boldsymbol{\pi}}_A$ due to the parametric uncertainties listed above.

8.5. Equilibrium Configurations in the case of Parametric Uncertainties and Force Measurement Errors

Theorem 5. *For uncertain parameters as described before, at the equilibrium, the following conditions hold:*

$$\mathbf{p}_{R1} = \hat{\mathbf{p}}_{R1} - \mathbf{K}_{A1}^{-1}(\Delta_m g \mathbf{e}_3 + (\boldsymbol{\delta}_1 + \boldsymbol{\delta}_2)) \quad (8.21)$$

$$\mathbf{S}(\mathbf{e}_1) \mathbf{R}_L^\top \left[\left(b_1 m_L - \frac{\hat{b}_1 \hat{m}_L L}{\hat{L}} \right) g \mathbf{e}_3 + t_L \bar{\mathbf{R}}_L \mathbf{e}_1 + L \boldsymbol{\delta}_2 \right] = \mathbf{0} \quad (8.22)$$

$$\mathbf{f}_1 = m_L g \mathbf{e}_3 - \frac{\hat{m}_L \hat{b}_1 g}{\hat{L}} \mathbf{e}_3 + t_L \bar{\mathbf{R}}_L \mathbf{e}_1 + \boldsymbol{\delta}_2 \quad (8.23)$$

$$\mathbf{f}_2 = \frac{\hat{b}_1 \hat{m}_L g}{\hat{L}} \mathbf{e}_3 - t_L \bar{\mathbf{R}}_L \mathbf{e}_1 - \boldsymbol{\delta}_2 \quad (8.24)$$

$$\mathbf{p}_L = \mathbf{p}_{R1} - \mathbf{R}_L^L \mathbf{b}_1 - \left(\frac{\|\mathbf{f}_1\|}{k_1} + l_{01} \right) \frac{\mathbf{f}_1}{\|\mathbf{f}_1\|}, \quad (8.25)$$

where $\hat{\mathbf{p}}_{R1}$ indicates the reference position of the leader robot computed as in (8.2), namely starting from $\bar{\mathbf{p}}_L, \bar{\mathbf{R}}_L$, but using the uncertain parameters.

Proof. In this situation, the control input (7.7) would contain a term $\hat{\boldsymbol{\pi}}_A$ defined according to (8.1), where (8.3) becomes:

$$\hat{\mathbf{f}}(\bar{\mathbf{q}}_L, t_L) = \begin{bmatrix} \hat{\mathbf{f}}_1 \\ \hat{\mathbf{f}}_2 \end{bmatrix} = \begin{bmatrix} \frac{(\hat{L} - \hat{b}_1) \hat{m}_L g}{\hat{L}} \\ \frac{\hat{b}_1 \hat{m}_L g}{\hat{L}} \end{bmatrix} \begin{bmatrix} \mathbf{I}_3 \\ \mathbf{I}_3 \end{bmatrix} \mathbf{e}_3 + t_L \begin{bmatrix} \mathbf{I}_3 \\ -\mathbf{I}_3 \end{bmatrix} \bar{\mathbf{R}}_L \mathbf{e}_1. \quad (8.26)$$

and the control (7.7) becomes:

$$\mathbf{u}_{Ri} = \mathbf{M}_{Ai}^{-1} \left(-\mathbf{B}_{Ai} \dot{\mathbf{p}}_{Ri} - \mathbf{K}_{Ai} \mathbf{p}_{Ri} \right) - (\mathbf{f}_i + \boldsymbol{\delta}_i) + \hat{\boldsymbol{\pi}}_{Ai}$$

Consider the equilibrium condition (8.4), then (8.24) is obtained solving the equilibrium conditions for the follower robot, namely solving lines 4, 5, and 6 of (8.4) where the last three lines of (8.26) have been substituted. This allows computing the force that the follower robot sense or measure, and the actual force in the cable can be found simply subtracting $\boldsymbol{\delta}_2$, which leads to (8.24). Then, (8.24) can be substituted into the load translational equilibrium, namely into lines 7, 8, and 9 of (8.4) to retrieve (8.23). (8.27) results from solving the first three lines of (8.4) using (8.23). Finally, (8.22) can be obtained using (8.23) and (8.24) into the last three lines of (8.4). Equation (8.25) is obtained from the previous and exploiting the system kinematics, as in (8.9). \square

Note that the system reaches an equilibrium only if $\boldsymbol{\delta}_i$ is a *constant* bias, as it emerges from Theorem 5. In the following, we will consider $\boldsymbol{\delta}_i$ to be constant, since we are interested here in the study of the equilibrium configurations of the system.

In the remainder of this section, we analyze the system equilibrium when each one of the uncertainties is considered individually since the effect of each uncertain parameter on the final equilibrium is different and characterized by interesting aspects that it is worth noting.

Uncertainty affecting the load mass m_L In this subsection, we consider solely uncertainty on the mass of the load. Consequently, the hat symbol indicates here the value of the

Chapter 8. Cooperative Manipulation of a Cable-suspended Beam Load by Two Aerial Robots

corresponding quantity computed considering that only the load mass is not exactly known, while the other parameters are. In this situation, eq. (8.21)-(8.24) become:

$$\mathbf{p}_{R1} = \hat{\mathbf{p}}_{R1} - \mathbf{K}_{A1}^{-1} \Delta_m g \mathbf{e}_3 \quad (8.27)$$

$$b_1 \mathbf{S}(\mathbf{e}_1) \mathbf{R}_L^\top g \Delta_m \mathbf{e}_3 + t_L L \mathbf{S}(\mathbf{e}_1) \mathbf{R}_L^\top \bar{\mathbf{R}}_L \mathbf{e}_1 = \mathbf{0} \quad (8.28)$$

$$\mathbf{f}_1 = m_L g \mathbf{e}_3 - \frac{\|\mathbf{b}_1\| \hat{m}_L g}{L} \mathbf{e}_3 + t_L \bar{\mathbf{R}}_L \mathbf{e}_1 = \hat{\mathbf{f}}_1 + \Delta_m g \mathbf{e}_3 \quad (8.29)$$

$$\mathbf{f}_2 = \frac{\|\mathbf{b}_1\| \hat{m}_L g}{L} \mathbf{e}_3 - t_L \bar{\mathbf{R}}_L \mathbf{e}_1 = \hat{\mathbf{f}}_2, \quad (8.30)$$

where $\hat{\mathbf{p}}_{R1} = \bar{\mathbf{p}}_{R1} + \frac{\Delta_m}{L} g \mathbf{e}_3 + l_{01} \left(\frac{\hat{\mathbf{f}}_1}{\|\hat{\mathbf{f}}_1\|} - \frac{\bar{\mathbf{f}}_1}{\|\bar{\mathbf{f}}_1\|} \right)$ and it differs from $\hat{\mathbf{p}}_{R1}$ only because of the uncertain parameter \hat{m}_L .

Remark 3. Under the hypothesis that $\bar{\theta} \neq \pi/2 + k\pi$, with $k \in \mathbb{N}$, and $t_L \neq 0$, (8.28) leads to:

$$\psi = \bar{\psi} + k\pi \quad (8.31)$$

$$\theta = \text{atan2} \left(\frac{(L t_L \sin \bar{\theta} - b_1 g (\Delta_m))}{L t_L \cos \bar{\theta}} \right) + k\pi. \quad (8.32)$$

In other words, the yaw angle at the equilibrium is not affected by some uncertainty on the mass of the load. ψ may differ from $\bar{\psi}$ by π because, as already discussed, both $\mathcal{Q}^+(t_L, \bar{\mathbf{q}}_L)$ and $\mathcal{Q}^-(t_L, \bar{\mathbf{q}}_L)$ are equilibrium configurations. The value of \mathbf{p}_L at the equilibrium is easily computed by the third equation of (8.25) where only the mass is affected by uncertainty.

Remark 4. If $t_L = 0$ and $\Delta_m \neq 0$, then (8.28) leads to:

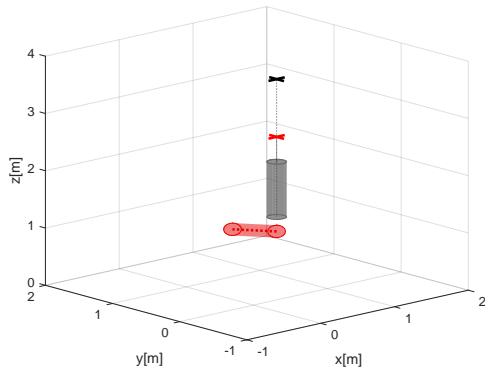
$$b_1 \mathbf{S}(\mathbf{e}_1) \mathbf{R}_L^\top g (\Delta_m) \mathbf{e}_3 = \mathbf{0}, \quad (8.33)$$

thus:

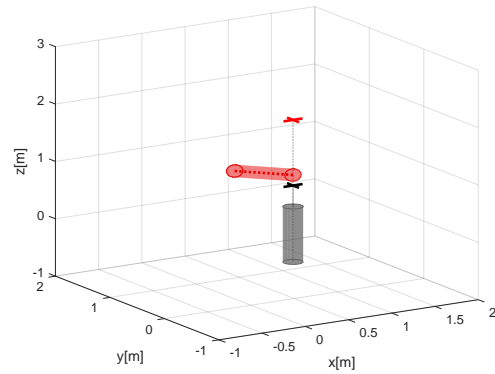
$$\mathbf{e}_1 \times \mathbf{R}_L^\top \mathbf{e}_3 = \mathbf{0}, \quad (8.34)$$

which means, by definition of \mathcal{F}_L , that the load at the equilibrium is aligned with the vertical direction. Furthermore, the two cables at the equilibrium would be vertical, too (substitute $t_L = 0$ into (8.29) and (8.30) to see it). In conclusion, we have found that with no internal forces in the load and for any value of the load mass uncertainty, the equilibrium configuration would be of poor practical realization, since all the bodies would be aligned along the vertical direction, similarly to what is schematically represented in Fig. 8.3(a) and Fig. 8.3(b). As we shall see, a similar result is obtained for uncertainties on the load CoM position or on the load length. Basically, we can say that the presence of such uncertainty, at least with small values, always occur. Consequently, due to their effect on the load attitude in the case of unbiased estimation or measurements of the force (we have not included the force measurement bias here), this could explain the choice made in [219] of assigning a reference altitude to the follower robot, too. In addition to that, an interesting aspect worth noticing is that the equilibrium attitude of the load when $t_L = 0$ does not depend on the mass uncertainty. In other words, if $t_L = 0$ the load attitude error is not sensitive to the parametric uncertainty affecting the load mass.

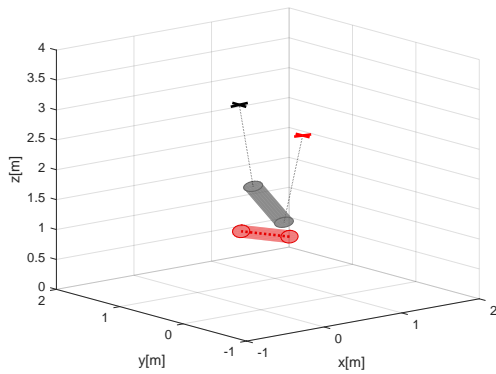
8.5. Equilibrium Configurations in the case of Parametric Uncertainties and Force Measurement Errors



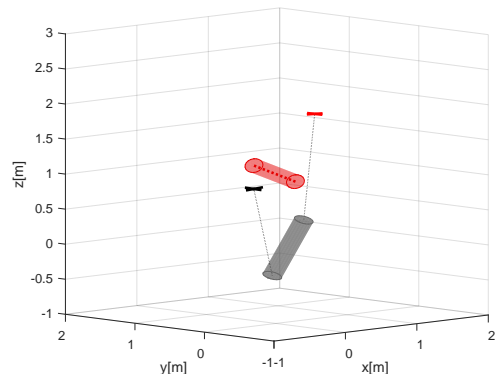
(a) $m_L < \hat{m}_L, t_L = 0$



(b) $m_L > \hat{m}_L, t_L = 0$



(c) $m_L < \hat{m}_L, t_L \neq 0$



(d) $m_L > \hat{m}_L, t_L \neq 0$

Figure 8.3: Equilibrium configurations of the system with $\hat{m}_L \neq m_L$. The grey cylinder is the load, the black lines the cables, the red cross the leader robot and the black cross is the follower one. The red cylinder correspond to teh desired pose of the load.

Chapter 8. Cooperative Manipulation of a Cable-suspended Beam Load by Two Aerial Robots

Note that also the position of the load CoM at the equilibrium is different from \bar{p}_L , and it is equal to $p_L = \hat{p}_{R1} - \mathbf{R}_L^L \mathbf{b}_1 - \left(\frac{\hat{f}_1 + \Delta_m g e_3}{k_1} + l_{01} \frac{\hat{f}_1 + \Delta_m g e_3}{\|\hat{f}_1 + \Delta_m g e_3\|} \right)$.

We would like to highlight that the leader robot, knowing \hat{f}_1 and measuring its actual value f_1 at steady state, corresponding to (8.29), can recognize a discrepancy between the two. We know from (8.29) that such an error in the leader robot cable force depends only on Δ_m . Thus, the leader robot, knowing \hat{m}_L , may be programmed to retrieve the value of the actual load mass m_L and use it to correct its reference force and position. On the other hand, the follower robot should correct its own force reference, too. This might be achieved allowing a one-time data communication between the robots so that the information about m_L is transferred to the follower robot. At this point, thanks to the analysis presented in the previous section, provided that $t_L \neq 0$ we ensure that the load is at its desired equilibrium.

Uncertainty affecting the Load CoM Position or Length These two types of uncertainties have similar effects so that we analyze them in the same section. In one case we have $\|\hat{\mathbf{b}}_1\| \neq b_1$, namely the load CoM is aligned to the cables attachment points on the load at an uncertain position, such that the real distance between the leader robot cable attachment point on the load and the load CoM is not exactly known, but L is known exactly. In the other case, $\|{}^L \mathbf{b}_1\|$ is known exactly, but L is not. In both cases, at the equilibrium, the following conditions hold:

$$p_{R1} = \hat{p}_{R1} \quad (8.35)$$

$$\mathbf{S}(e_1) \mathbf{R}_L^\top (L t_L \bar{\mathbf{R}}_L e_1 + y m_L g e_3) = \mathbf{0} \quad (8.36)$$

$$f_1 = \hat{f}_1 \quad (8.37)$$

$$f_2 = \hat{f}_2, \quad (8.38)$$

where $y = \Delta_b$ in one case, and $y = b_1 L \Delta_\ell$ in the other; \hat{p}_{R1} , \hat{f}_1 , and \hat{f}_2 are computed from (8.2) and (8.3), where the corresponding uncertain parameter is used in place of the real one.

Remarks 3 and 4 have their analog counterparts for these cases. In other words, *the yaw angle at the equilibrium is not affected by some uncertainty on the position of the load CoM or on the load length; if $t_L = 0$, the load attitude error is not influenced by these parametric uncertainties and, at the equilibrium, the load is aligned with the vertical.*

The load position at the equilibrium is different from the desired one and it is equal to $p_L = \hat{p}_{R1} - \mathbf{R}_L^L \mathbf{b}_1 - \left(\frac{\hat{f}_1}{k_1} + l_{01} \frac{\hat{f}_1}{\|\hat{f}_1\|} \right)$. On the other hand, in this case the leader robot position and cable force and the follower robot cable force at the equilibrium coincide with the reference values \hat{p}_{R1} , \hat{f}_1 , and \hat{f}_2 , respectively. Consequently, *it is not possible in this case for the robots to estimate the uncertain parameter at the equilibrium based on their own state.*

Uncertainty on the estimated or measured forces The external control loop given by (7.7) uses the estimated or the measured values of the cable force f_i . Here we consider the

8.5. Equilibrium Configurations in the case of Parametric Uncertainties and Force Measurement Errors

case in which the only uncertainty in the system is on the measured or estimated cable force $\hat{f}_i = f_i + \delta_i$. Then, at the equilibrium, the following conditions hold:

$$p_{R1} = \bar{p}_{R1} - K_{A1}^{-1}(\delta_2 + \delta_1) \quad (8.39)$$

$$S(e_1)R_L^\top(t_L\bar{R}_Le_1 + \delta_2) = 0 \quad (8.40)$$

$$f_1 = \frac{L-b_1}{L}mge_3 + t_L\bar{R}_Le_1 - \delta_2 = \bar{f}_1 + \delta_2 \quad (8.41)$$

$$f_2 = \frac{b_1}{L}mge_3 - t_L\bar{R}_Le_1 - \delta_2 = \bar{f}_2 - \delta_2 \quad (8.42)$$

Remark 5. *In order to study the equilibrium, we have to assume that the error on the measured or estimated forces is constant. Otherwise, there would exist no equilibrium, since the leader robot position and the load attitude would follow the variation of the error vectors (see for instance (8.39) and (8.43)).*

From (8.40) one can compute the value of the yaw and pitch angle of the load at the equilibrium. Specifically, the second line of (8.40) contains only ψ as unknown quantity, thus one can retrieve:

$$\psi = \text{atan2} \left(\frac{t_L \cos \bar{\theta} \sin \bar{\psi} + e_2^\top \delta_2}{t_L \cos \bar{\theta} \cos \bar{\psi} - e_1^\top \delta_2} \right) + k\pi. \quad (8.43)$$

From the third line of (8.40), substituting (8.43), one can compute the value of the pitch angle at the equilibrium, which is different from the desired one. Note that the attitude of the robot at the equilibrium this time is different from the desired one also for the yaw angle. Furthermore, the difference between the equilibrium attitude and the desired one depends solely on the uncertainty on the follower robot measured or estimated force, δ_2 . *The attitude of the load at the equilibrium and the forces in the cables are not affected by δ_1 ; only the leader robot position and, consequently, the load com position are.*

Note that in this case the reference input π_A is not affected by any uncertainty (neither \bar{p}_{R1} nor \bar{f} are). At steady state, the leader robot could estimate δ_2 from (8.41), and also δ_1 from (8.39) and the follower robot could estimate δ_2 from (8.42). In this way, the robots could correct their references accordingly and thus bring the system to the desired equilibrium configuration.

Uncertainty on the Cable Stiffness or Length Consider some uncertainty on the parameters of the i^{th} cable such that the rest length is $\hat{l}_{0i} \neq l_{0i}$ and the stiffness is $\hat{k}_i \neq k_i$. At the equilibrium it holds that $f_i = \bar{f}_i$, $R_L = \bar{R}_L$, and $p_{R1} = \hat{p}_{R1}$, where

$$\hat{p}_{R1} = \bar{p}_L + \bar{R}_L^L b_1 + \left(\frac{\|\bar{f}_1\|}{\hat{k}_1} + \hat{l}_{01} \right) \frac{\bar{f}_1}{\|\bar{f}_1\|} \quad (8.44)$$

The value of p_L at the equilibrium is:

$$p_L = \hat{p}_{R1} - \bar{R}_L^L b_1 - \left(\frac{\|\bar{f}_1\|}{k_1} + l_{01} \right) \frac{\bar{f}_1}{\|\bar{f}_1\|} \neq \bar{p}_L. \quad (8.45)$$

Basically, the only step in which the knowledge of the cable characteristics is required is when computing the reference position for the leader robot according to (8.2).

Chapter 8. Cooperative Manipulation of a Cable-suspended Beam Load by Two Aerial Robots

Actually, only the information about k_1 and l_{01} are required. We conclude that the knowledge of the characteristics of the cable attached to the follower robot, specifically of l_{02} and k_2 , is not necessary to stabilize the load at a desired pose. Moreover, the value of the load attitude at the equilibrium is not affected by l_{01} and k_1 while the value of the load position at the equilibrium is.

8.6 The Role of the Internal Force in the Load Error Caused by Parametric Uncertainties

In this section, we provide a formal analysis of the role that the internal force plays in determining the load pose at the equilibrium in the presence of parametric uncertainties. We shall consider the simultaneous presence of all the uncertainties listed in Sec 8.5. We start considering the load attitude.

8.6.1 Load Attitude Error

Theorem 6. Given the definition of the load attitude error, $e_{\mathbf{R}_L}$ as:

$$e_{\mathbf{R}_L} = \|\mathbf{R}_L e_1 \times \bar{\mathbf{R}}_L e_1\|^2, \quad (8.46)$$

$e_{\mathbf{R}_L}$ is inversely proportional to the intensity of the internal force, t_L . Furthermore, the error sensitivity w.r.t Δ_m , Δ_b , $\|\delta_i\|$, Δ_{ki} , Δ_{l0i} , and Δ_ℓ , defined as $\frac{\partial e_{\mathbf{R}_L}}{\partial \Delta_m}$, $\frac{\partial e_{\mathbf{R}_L}}{\partial \Delta_b}$, $\frac{\partial e_{\mathbf{R}_L}}{\partial \|\delta_2\|}$, $\frac{\partial e_{\mathbf{R}_L}}{\partial \Delta_{ki}}$, $\frac{\partial e_{\mathbf{R}_L}}{\partial \Delta_{l0i}}$ and $\frac{\partial e_{\mathbf{R}_L}}{\partial \Delta_\ell}$, are given by:

$$\frac{\partial e_{\mathbf{R}_L}}{\partial \Delta_m} = 2 \left[\frac{-\hat{b}_1 \hat{\ell} g^2 \alpha \cos \theta^2}{t_L^2 L^2} + \frac{\hat{b}_1 \hat{\ell} \gamma}{t_L^2 L} \right]. \quad (8.47)$$

$$\frac{\partial e_{\mathbf{R}_L}}{\partial \Delta_b} = 2 \left[\frac{-\hat{m}_L \hat{\ell} g^2 \alpha \cos \theta^2}{t_L^2 L^2} + \frac{\hat{m}_L \hat{\ell} \gamma}{t_L^2 L} \right], \quad (8.48)$$

$$\frac{\partial e_{\mathbf{R}_L}}{\partial \|\delta_2\|} = 2 \left[\frac{g \alpha (-\sin \theta \cos \beta_1 - \cos \beta_2)}{L t_L^2} - \frac{\|\delta_2\| \cos \beta_1^2}{t_L^2} \right], \quad (8.49)$$

$$\frac{\partial e_{\mathbf{R}_L}}{\partial \|\delta_1\|} = \frac{\partial e_{\mathbf{R}_L}}{\partial \Delta_{ki}} = \frac{\partial e_{\mathbf{R}_L}}{\partial \Delta_{l0i}} = 0 \quad (8.50)$$

$$\frac{\partial e_{\mathbf{R}_L}}{\partial \Delta_\ell} = 2 \left[\frac{-\hat{b}_1 \hat{m}_L g^2 \alpha \cos \theta^2}{t_L^2 L^2} + \frac{\hat{b}_1 \hat{m}_L \gamma}{t_L^2 L} \right]. \quad (8.51)$$

$$(8.52)$$

where

$$\alpha := (b_1 - \Delta b)(m_L - \Delta m)(\ell - \Delta_\ell) - m_L b_1$$

and

$$\gamma := \|\delta_2\| g (\cos \beta_2 - \cos \beta_1 \sin \theta),$$

with β_1 the angle between $\mathbf{R}_L e_1$ and δ_2 , and β_2 the angle between e_3 and δ_2 .

8.6. The Role of the Internal Force in the Load Error Caused by Parametric Uncertainties

proof

Rewrite (8.22) in \mathcal{F}_W as:

$$\mathbf{R}_L \mathbf{e}_1 \times [(b_1 m_L - \hat{b}_1 \hat{m}_L) g \mathbf{e}_3 + L t_L \bar{\mathbf{R}}_L \mathbf{e}_1 + L \delta_2] = \mathbf{0}. \quad (8.53)$$

Define also:

$$\begin{aligned} & \frac{(b_1 - \Delta b)(m_L - \Delta m) - b_1 m_L}{t_L L} (\mathbf{R}_L \mathbf{e}_1 \times g \mathbf{e}_3) + \\ & - \frac{1}{t_L} (\mathbf{R}_L \mathbf{e}_1 \times \delta_2) = \frac{\alpha}{t_L L} (\mathbf{R}_L \mathbf{e}_1 \times g \mathbf{e}_3) + - \frac{1}{t_L} (\mathbf{R}_L \mathbf{e}_1 \times \delta_2) := \mathbf{x}. \end{aligned}$$

Thus, from (8.53) we have that $\mathbf{R}_L \mathbf{e}_1 \times \bar{\mathbf{R}}_L \mathbf{e}_1 = \mathbf{x}$ and, from (8.46), that $e_{\mathbf{R}_L} = \mathbf{x}^\top \mathbf{x}$. From these it is clear that $e_{\mathbf{R}_L}$ is inversely proportional to t_L . Regarding the sensitivity, we show the proof for (8.51) only, since the other cases follow the exact same analysis. We can write the sensitivity as:

$$\begin{aligned} \frac{\partial e_{\mathbf{R}_L}}{\partial \Delta_m} &= 2 \mathbf{x}^\top \frac{\partial \mathbf{x}}{\partial \Delta_m} = \\ &= 2 \left[\frac{1}{t_L L} \mathbf{R}_L \mathbf{e}_1 \times (\alpha) g \mathbf{e}_3 \right]^\top \left[\frac{1}{t_L L} \mathbf{R}_L \mathbf{e}_1 \times (\Delta b - b_1) g \mathbf{e}_3 \right] + \\ & - 2 \left(\frac{\bar{\mathbf{R}}_L \mathbf{e}_1}{t_L} \times \delta_2 \right)^\top \left(\frac{1}{t_L} \bar{\mathbf{R}}_L \mathbf{e}_1 \times \frac{\Delta b - b_1}{L} g \mathbf{e}_3 \right) \end{aligned} \quad (8.54)$$

Eventually, (8.54) can be rewritten as (8.51), remembering that, given three vectors \mathbf{a} , \mathbf{b} , and \mathbf{c} :

$$(\mathbf{a} \times \mathbf{b})^\top (\mathbf{a} \times \mathbf{c}) = |\mathbf{a}|^2 (\mathbf{b}^\top \mathbf{c}) - (\mathbf{a}^\top \mathbf{b})(\mathbf{a}^\top \mathbf{c}).$$

Remark 6. We wish that the error is zero when $\mathbf{R}_L = \bar{\mathbf{R}}_L$. Indeed, in such a case we have $\|\mathbf{R}_L \mathbf{e}_1 \times \bar{\mathbf{R}}_L \mathbf{e}_1\|^2 = 0$, and this quantities increases with the displacement between the two vectors, at least locally (for displacements smaller than $\pi/2$ radians). For these reasons and because the unit vector $\mathbf{R}_L \mathbf{e}_1$ is enough to describe the entire attitude of the beam-like load, the definition in (8.46) is a suitable metric for the attitude error.

Note that, if $t_L = 0$ (8.51) is not defined. Theorem 6 shows that the sensitivity of the attitude error w.r.t. the considered parametric uncertainties is inversely proportional to the internal force intensity raised to the second power. In other words, *not only does the internal force t_L make the attitude error smaller in the presence of parametric uncertainties, but it also makes the error more robust to variations of such uncertainties.*

This may be interesting for practical applications. As a matter of fact, parametric uncertainty variations take place every time the actual physical parameters of the system change, e.g. because we transport slightly different objects without changing the controller parameters. Especially interesting is the variation affecting the center of mass position. In fact, this uncertainty changes every time we transport a load containing moving masses, i.e. containers of liquids, or boxes containing smaller objects free to move inside it. The previous analysis suggests that in all these cases having a larger value of t_L is even more beneficial, resulting in an error that is less sensitive to the aforementioned parametric variations.

8.6.2 Load Position Error

In this section, we will study the load position error at the equilibrium in the presence of all the uncertainties listed at the beginning of Sec. 8.5. Differently from what happens for the load attitude error, the load position error at the equilibrium does not necessarily decrease for higher values of t_L . What happens, instead, is that depending on the specific values and type of uncertainties, it may decrease, increase, or have a non-monotonic evolution. Thus, we propose a different method for correcting the load position error at the equilibrium.

We substitute (8.21) into (8.25) recalling that

$$\bar{\mathbf{p}}_{R1} = \bar{\mathbf{p}}_L + \bar{\mathbf{R}}_L^L \hat{\mathbf{b}}_1 + \left(\frac{\hat{\mathbf{f}}_1}{\hat{k}_1} + l_{01} \right) \frac{\hat{\mathbf{f}}_1}{\|\hat{\mathbf{f}}_1\|}. \quad (8.55)$$

What we obtain is that the load position at the equilibrium is given by

$$\begin{aligned} \mathbf{p}_L &= \mathbf{p}_{R1} - \left(\frac{\mathbf{f}_1}{k_1} + l_{01} \right) \frac{\mathbf{f}_1}{\|\mathbf{f}_1\|} - \mathbf{R}_L \mathbf{b}_1 = \\ &= \bar{\mathbf{p}}_L + \bar{\mathbf{R}}_L \hat{\mathbf{b}}_1 + \left(\frac{\hat{\mathbf{f}}_1}{\hat{k}_1} + l_{01} \right) \frac{\hat{\mathbf{f}}_1}{\|\hat{\mathbf{f}}_1\|} - K_A^{-1} (\Delta_m + \delta_1 + \delta_2) + \\ &\quad - \left(\frac{\mathbf{f}_1}{k_1} + l_{01} \right) \frac{\mathbf{f}_1}{\|\mathbf{f}_1\|} - \mathbf{R}_L \mathbf{b}_1 \end{aligned} \quad (8.56)$$

with the corresponding equilibrium values of \mathbf{f}_1 and \mathbf{R}_L . From (8.56) we have an expression of $\mathbf{p}_L - \bar{\mathbf{p}}_L := \tilde{\mathbf{p}}_L$. Now, *if the leader robot knows of the load position*, it can recognize that at steady state it holds $\tilde{\mathbf{p}}_L \neq 0$ and adjust its previous position reference $\bar{\mathbf{p}}_{R1}$ such that the new reference, call it ${}^2\bar{\mathbf{p}}_{R1}$, is:

$${}^2\bar{\mathbf{p}}_{R1} = \bar{\mathbf{p}}_{R1} - \tilde{\mathbf{p}}_L. \quad (8.57)$$

In this way, there will be a new equilibrium in which the leader robot position is:

$$\mathbf{p}_{R1} = {}^2\bar{\mathbf{p}}_{R1} - K_A^{-1} (\Delta_m + \delta_1 + \delta_2) \quad (8.58)$$

and thus (8.56) becomes:

$$\mathbf{p}_L = \bar{\mathbf{p}}_L \quad (8.59)$$

The load desired position is exploited only for computing the position reference of the leader robot, and it is important to highlight that the leader robot position does not influence the attitude of the load at the equilibrium, which is determined by the cable reference forces. Hence, the leader robot can correct the position error of the load, while the internal force acts decreasing the attitude error. In order to apply this strategy, the leader robot must be able to collect some feedback on the load position. In the setup that we have described this is not envisioned, hence additional sensors would be probably required. The fact that the position of the load can be steered relying only on the leader robot is beneficial to maintain the distributed character of the control method. In fact, only the leader robot needs additional information to correct the position error. Moreover, it might be exploited also in the case that the user wishes to manually command the leader robot itself. The reference forces generated

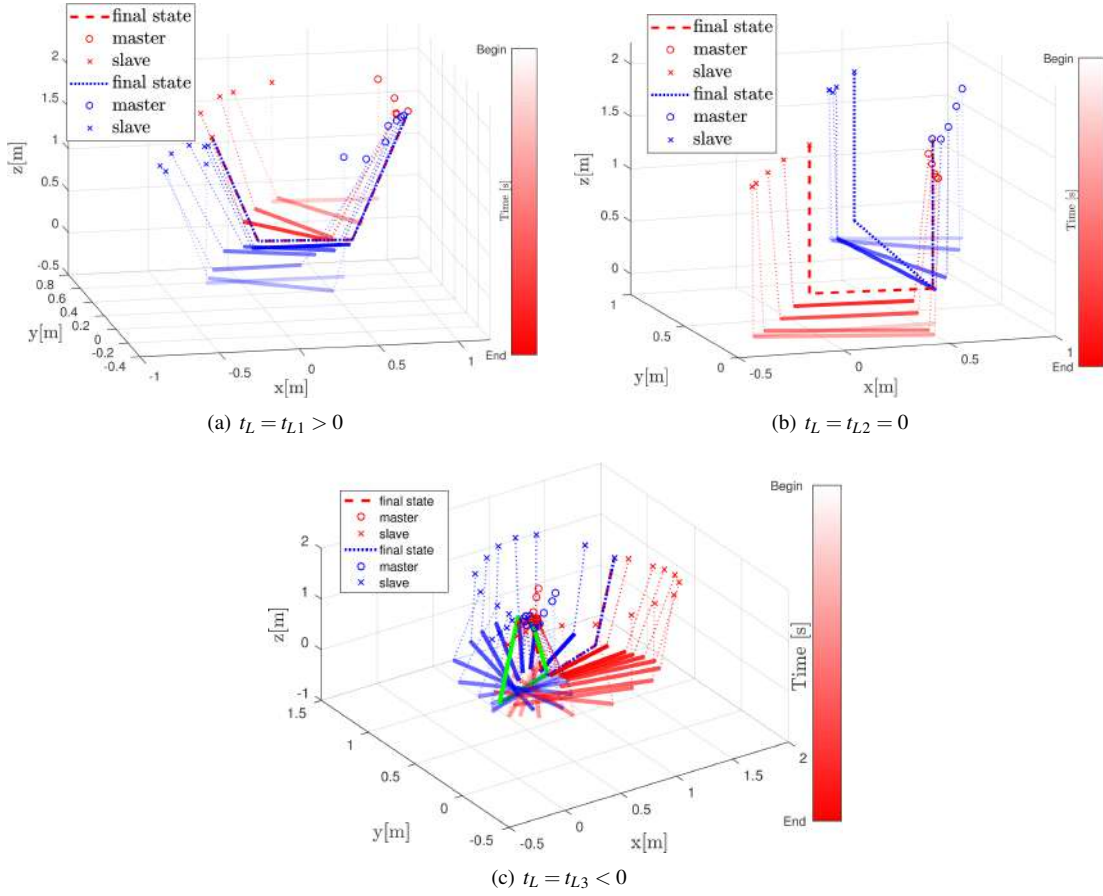


Figure 8.4: Each figure shows the evolution of the system from two different initial conditions (one is shown in red and the other in blue). The two evolutions are represented as a sequence of images discriminated by the brightness of the color that represents the time (from bright/start to dark/end). The load is represented as a thick solid line, the cables as thin dashed lines, the leader robot as a circle, and the follower robot as a cross.

by the combined action of leader and follower robots will take care of correcting the load final attitude, while the user has control over the load position through the control of the sole leader robot position.

8.7 Numerical Results

In this section, we shall describe the results of several numerical simulations validating the proposed method and all the presented theoretical concepts and results. For the simulation, we considered a quadrotor-like vehicle with its proper nonlinear dynamics together with a geometric position controller, even though, our method can be applied to more general flying vehicles. System and control parameters are reported in Tab. 8.1. Notice the smaller apparent inertia of the follower, chosen to make it more sensitive to external forces. Let us consider the desired equilibrium $\bar{\mathbf{q}} = (\bar{\mathbf{p}}_L, \bar{\mathbf{R}}_L)$, whose value are in Tab. 8.1, where $(\bar{\phi}, \bar{\theta}, \bar{\psi})$ are the Euler angles that parametrize $\bar{\mathbf{R}}_L$. We performed several simulations with $\pi_A \in \Pi_A(\bar{\mathbf{q}}_L)$ computed as in (8.1) for the cases: 1. $t_{L1} = 1.5$ [N] > 0 , 2. $t_{L2} = 0$ [N], 3. $t_{L3} = -1$ [N] < 0 . To test the stability of

Chapter 8. Cooperative Manipulation of a Cable-suspended Beam Load by Two Aerial Robots

System Parameters			Controller Gains		
	$i = 1$	$i = 2$		$i = 1$	$i = 2$
m_{Ri} [Kg]	1.02	0.993	M_{Ai}	$3I_3$	$0.5I_3$
J_{Ri} [Kg·m ²]	$0.015I_3$	$0.015I_3$	B_{Ai}	$18I_3$	$1.3I_3$
l_{0i} [m]	1	1	K_{Ai}	$15I_3$	$\mathbf{0}$
k_i [N/m]	20	20	Desired Load Pose		
${}^L\mathbf{b}_i$ [m]	[0.433 0 0]	[-0.433 0 0]	$\bar{\mathbf{p}}_L = [0.3 \ 0.3 \ 0.2]^T$ [m]		
$m_L = 0.900$ [Kg], $J_{Lx} = 0.112$ [Kg·m ²]			$\bar{\boldsymbol{\phi}} = \mathbf{0}$, $\bar{\boldsymbol{\theta}} = \pi/8$ [rad]		
$J_{Ly} = 5.681$, $J_{Lz} = 5.681$ [Kg·m ²]			$\bar{\boldsymbol{\psi}} = \pi/7$ [rad]		

Table 8.1: Parameters used in the simulations.

the equilibria, we initialized the system in different initial configurations and we let it evolve. Figure 8.5 shows the position and orientation error for the three t_L and several different initial conditions. 1) For $t_L = t_{L1}$, the system always converges to a state belonging to $\mathcal{X}^+(t_L, \bar{\mathbf{q}}_L)$, independently from the initial state, validating the asymptotic stability of $\mathcal{X}^+(t_L, \bar{\mathbf{q}}_L)$ when $t_L > 0$. 2) For t_{L2} , the system final state belongs to $\mathcal{X}(0, \bar{\mathbf{q}}_L)$. The particular final attitude of the load depends on the initial state. 3) For t_{L3} , the system never converges to $\mathcal{X}^+(t_L, \bar{\mathbf{q}}_L)$ even with a very close initial configuration. This is due to the instability of $\mathcal{X}^+(t_L, \bar{\mathbf{q}}_L)$ when $t_L < 0$. Fig. 8.4 shows the evolution of the system starting from two different initial states for the three cases.

The results of further simulations of transportation tasks in which the leader input $\pi_{A1}(t)$ is chosen as in (8.19) so that the leader robot follows a fifth-order polynomial trajectory to bring the load in the desired configuration, as well as further simulation results considering also non-ideal conditions due to the inclusion of noise in the system state can be found in the published technical report attached to [223].

I also show here the results of some simulations conducted in the presence of parametric uncertainties, aimed to validate the theoretical results presented in Sec. 8.5 and 8.6. All of them are carried out with a desired value of internal force $t_L > 0$.

First, Fig. 8.6, obtained in the presence of uncertainty on the mass equal to 20% of the actual value, confirms what is stated by (8.30) and (8.29), namely that \mathbf{f}_2 goes to the reference value while \mathbf{f}_1 does not, as well as \mathbf{p}_{R1} —see (8.27). Moreover, as stated in Remark 3, the convergence of the yaw angle of the load to its desired value is not disturbed by the uncertain mass. Figures 8.7 and 8.8 are conducted in the presence of uncertainties of about 25% on b_1 and 13% on L , respectively. Both the sets of results confirm what is stated in (8.35), (8.37), and (8.38), namely that the cable forces converge to their desired values as well as the position of the leader robot. On the the hand, since the pitch of the load, as stated in (8.36), does not converge to its desired value, neither does the load position.

Figures 8.9 and 8.10 shows what happens when the rest length of cable 1 and cable 2 is affected by uncertainty equal to 25% of its actual value, respectively. One can appreciate how the position of the load at the equilibrium is the only quantity affected by the uncertainty on cable 1, while an uncertain length of the second cable (the one attached to the follower robot) does not perturb the system equilibrium. Eventually, Fig. 8.11 and Fig. 8.12 shows the numerical results in the presence of a constant measurement bias on the measured force equal to 1N in each of the three orthogonal

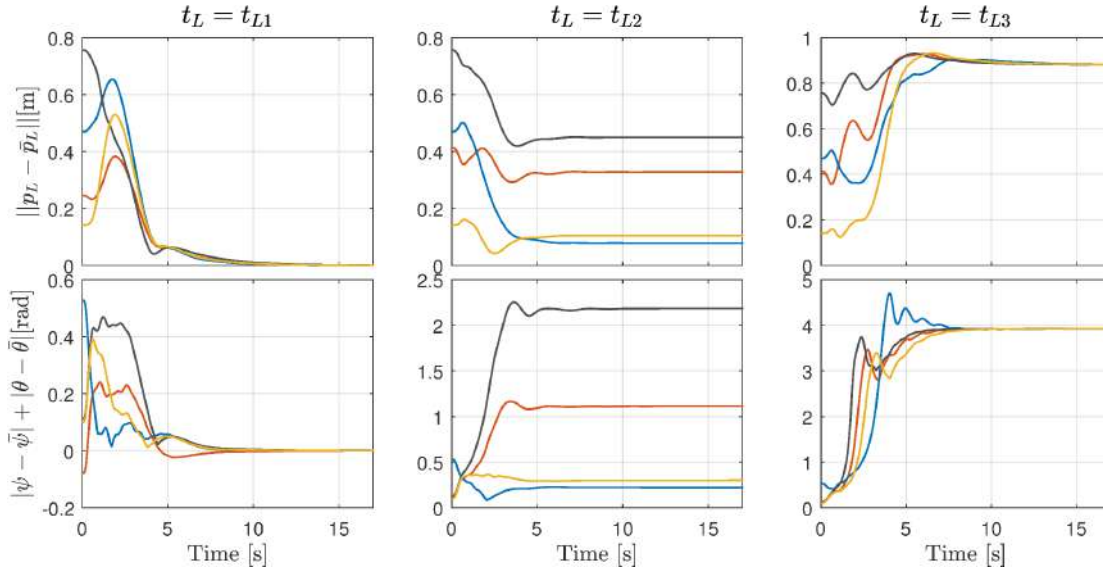


Figure 8.5: Convergence to the desired load configuration for cases 1) 2) and 3). In particular, the first and second rows show the position and the attitude errors, respectively, for four different initial conditions (different colors) and for the three different internal force values (columns). The attitude error is computed as the sum of pitch and yaw errors. The roll error is not considered since it is not controllable.

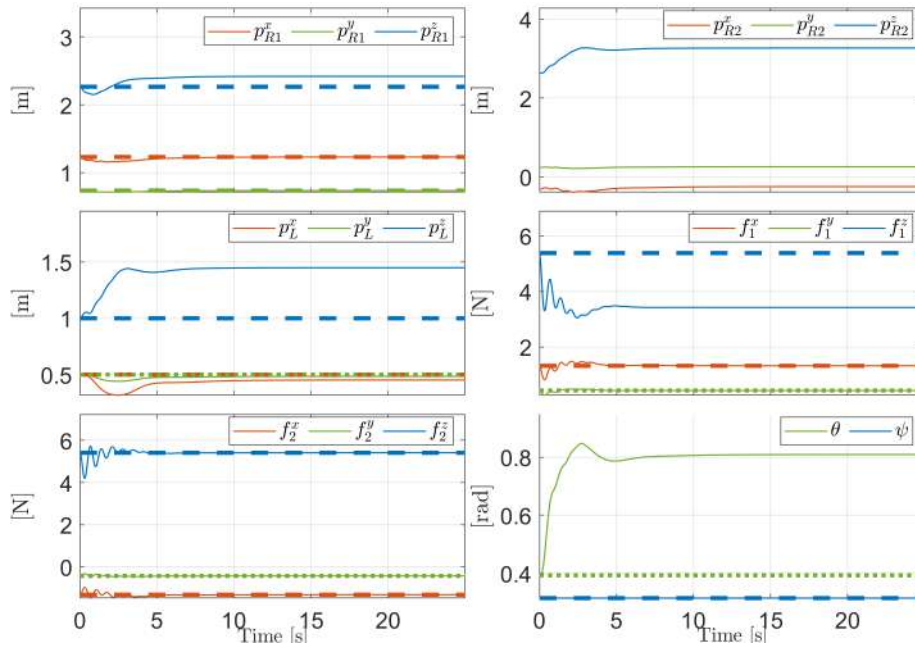


Figure 8.6: Numerical results in the presence of mass uncertainty. The dashed lines indicate the desired value of the solid line signal with corresponding color.

directions. Specifically, it emerges how, according to (8.40), (8.41), and (8.42), the forces and the load attitude are not disturbed by the error on the leader measured force, but only its position and consequently the load position are.

In Fig. 8.13 the load attitude error, as defined also in Fig. 8.5, is depicted for

Chapter 8. Cooperative Manipulation of a Cable-suspended Beam Load by Two Aerial Robots

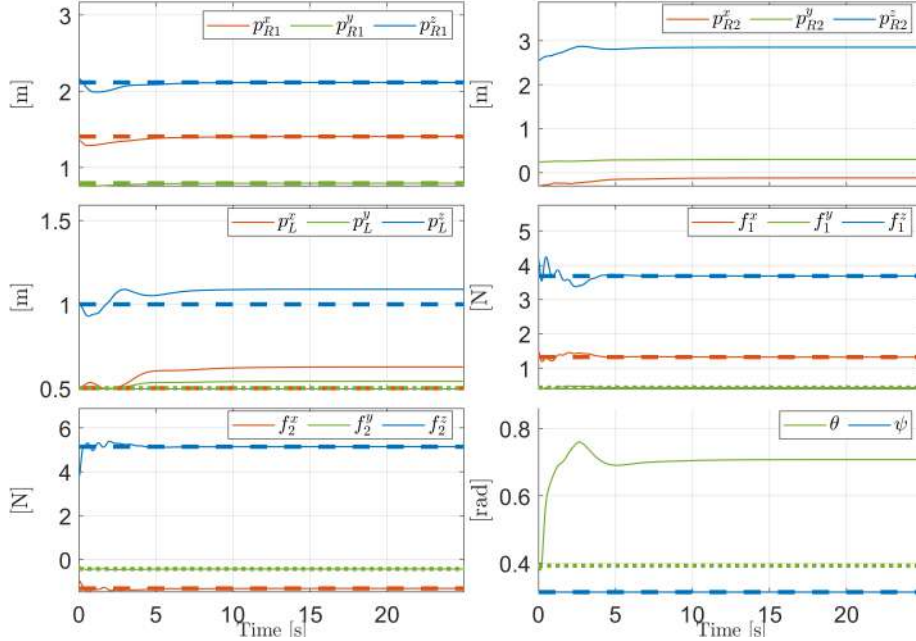


Figure 8.7: Numerical results in the presence of uncertainties on b_1 . The dashed lines indicate the desired value of the solid line signal with corresponding color.

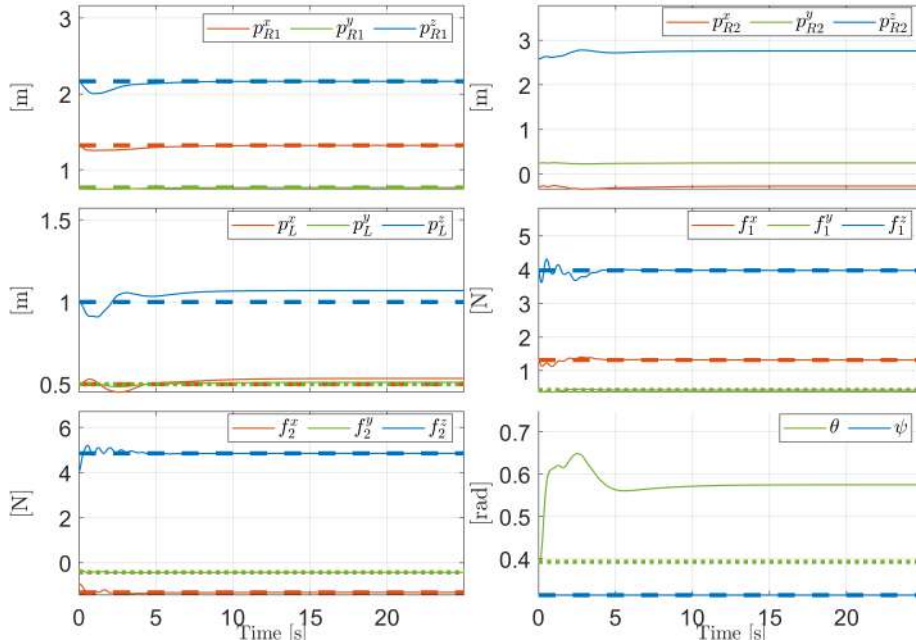


Figure 8.8: Numerical results in the presence of the uncertainty on L , but not on b_1 . The dashed lines indicate the desired value of the solid line signal with corresponding color.

increasing values of $t_L < 0$ and the combination of all the aforementioned uncertainties. The plot validates the claim of Sec. 8.6 since it shows that the attitude error is inversely proportional to the value of the load internal force.

For what concerns the position error, since it is not in general diminished by an increased value of the reference internal force, in Sec. 8.6 a method for bringing the

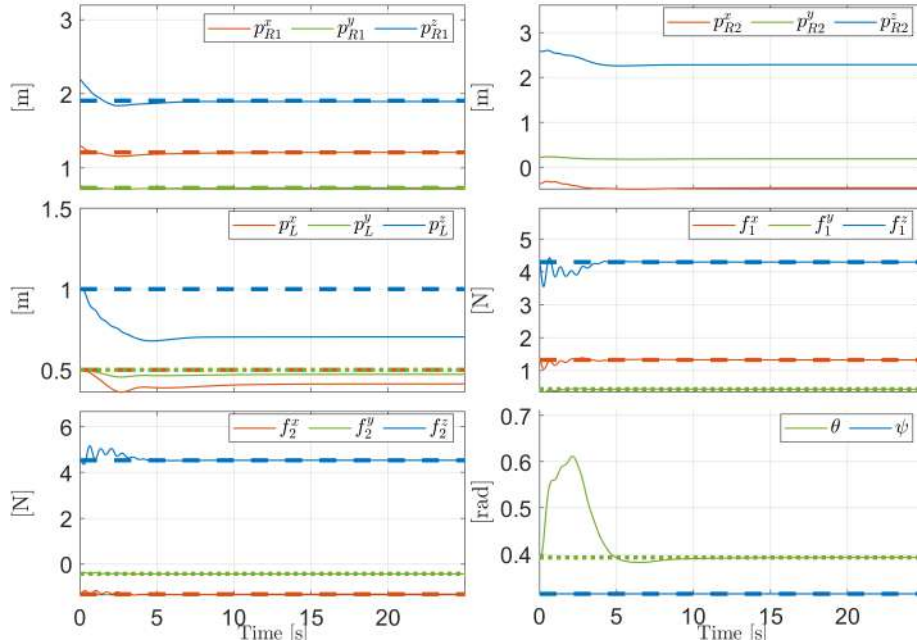


Figure 8.9: Numerical results in the presence of an uncertain value of l_{01} . The dashed lines indicate the desired value of the solid line signal with corresponding color.

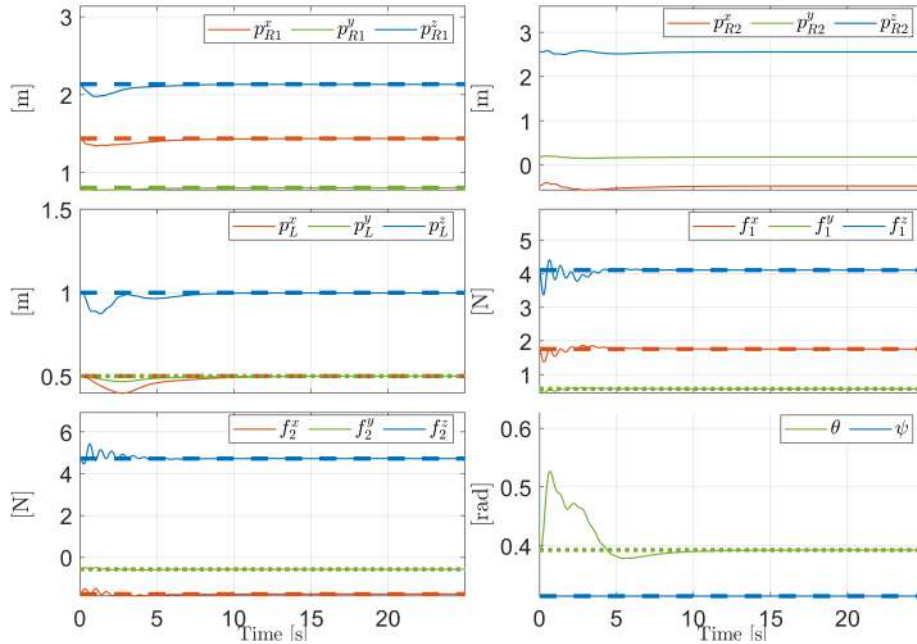


Figure 8.10: Numerical results in the presence of an uncertain value of l_{02} . The dashed lines indicate the desired value of the solid line signal with corresponding color.

error to zero in the presence of the uncertainties has been proposed. It consists of changing the reference of the leader robot after the system has reached its steady state and requires feedback of the load position on the leader robot. This method is validated by the simulation shown in Fig. 8.14, in which at $t = 100s$ the reference position of the leader robot is updated by taking into account the load position error at

Chapter 8. Cooperative Manipulation of a Cable-suspended Beam Load by Two Aerial Robots

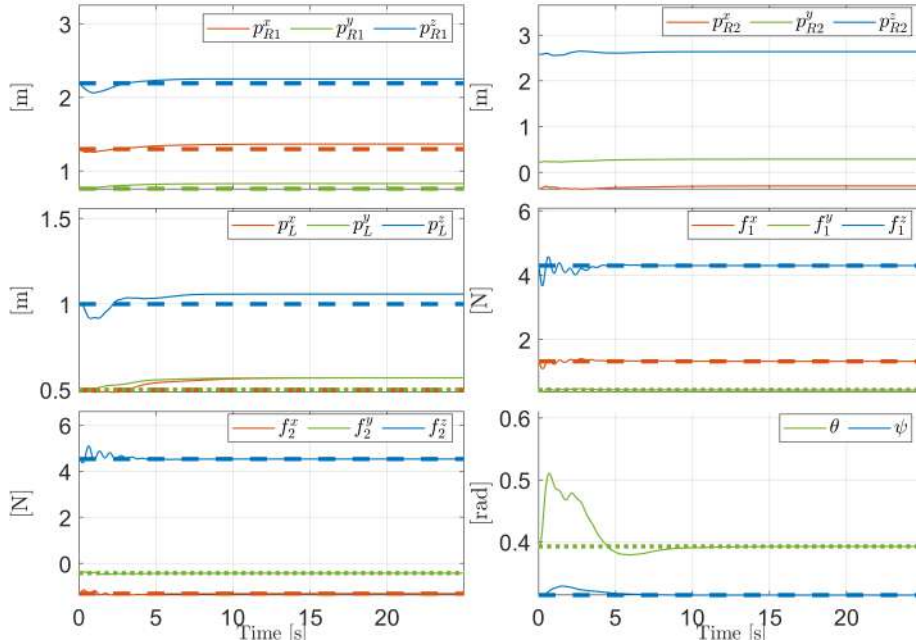


Figure 8.11: Numerical results in the presence of $\delta_1 = [1 \ 1 \ 1]^T N$. The dashed lines indicate the desired value of the solid line signal with corresponding color.

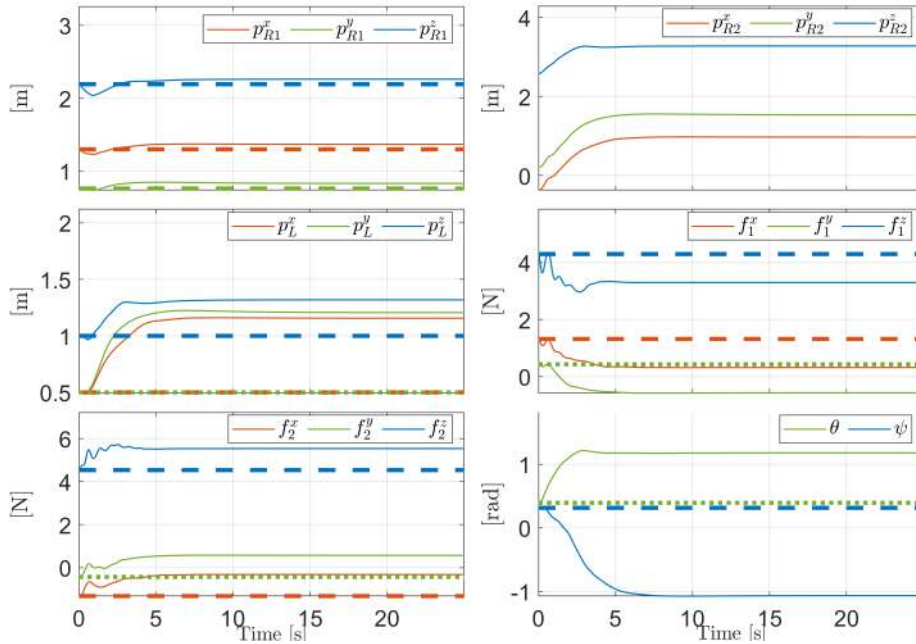


Figure 8.12: Numerical results in the presence of $\delta_2 = [1 \ 1 \ 1]^T N$. The dashed lines indicate the desired value of the solid line signal with corresponding color.

that instant. As a consequence, the load position error is brought to zero, while the attitude of the load is not perturbed at steady state. Note that the attitude of the load is slightly perturbed in a transitory way but then it comes back to the previous steady-state value. Finally, I show simulation results that validate the findings about the sensitivity of the attitude error in the presence of uncertainties. Specifically, I show

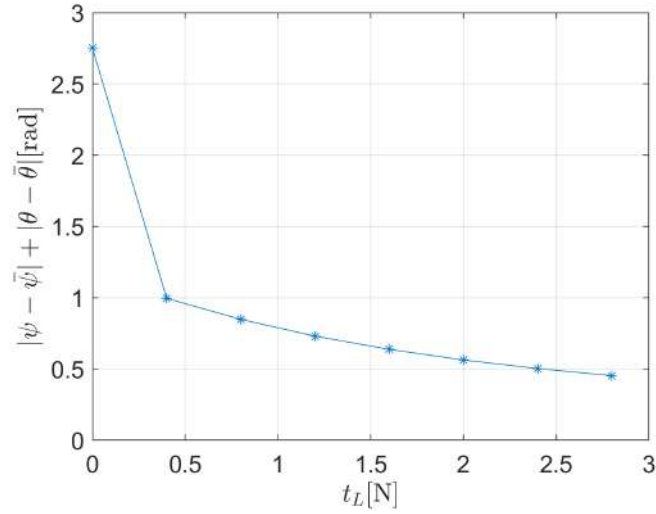


Figure 8.13: Values of the load attitude error for increasing values of internalTension > 0 and in the presence of measurement bias and parametric uncertainties. The plot shows how the attitude error is inversely proportional to the internal force intensity.

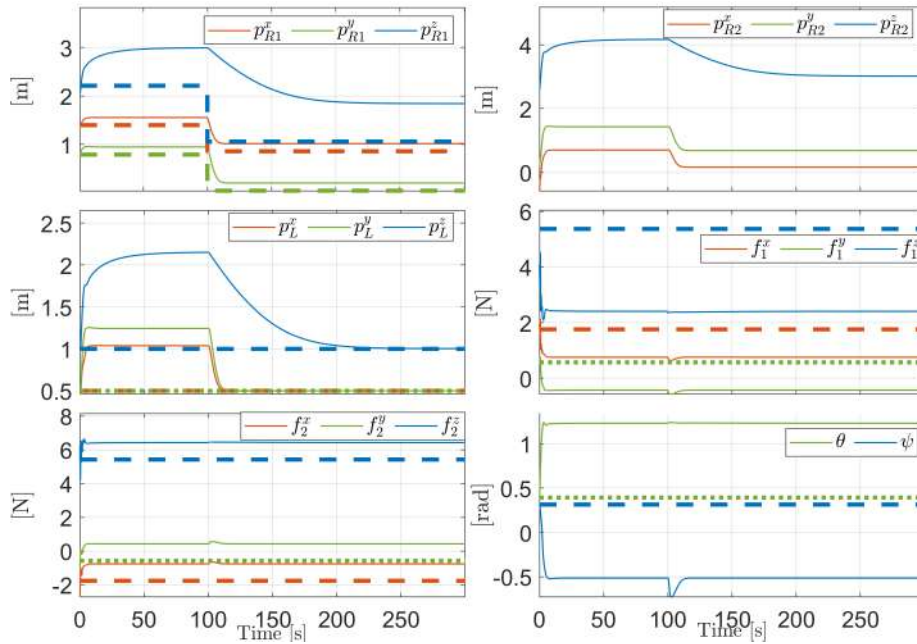


Figure 8.14: Numerical results in the presence of measurement and parametric uncertainties with a correction in the position reference of the leader robot at $t = 100s$, as described in (8.57). As a consequence, the load position error is brought to zero. The dashed lines indicate the desired value of the solid line signal with the corresponding color.

the results for two cases that are, in my opinion, of particular practical interest when transporting objects with different masses or containing moving parts. The results of several sets of simulations carried out considering different values of the uncertainty on the mass and on the load CoM position for different values of t_L are reported in Figure 8.15. These plots show that, as suggested in Sec. 8.6.1, for higher values of the

Chapter 8. Cooperative Manipulation of a Cable-suspended Beam Load by Two Aerial Robots

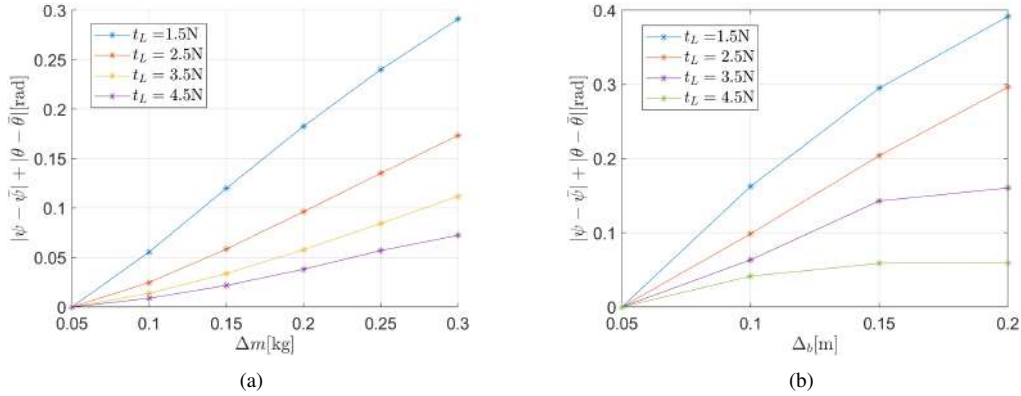


Figure 8.15: Attitude error of the load for different values of Δm and of Δb and for different values of t_L . Greater values of t_L makes the attitude variations smaller when the uncertainty on the parameters varies.

internal force, the attitude error of the load is less sensitive to variations of the parametric uncertainties. Variations of the mass and CoM location uncertainties are of particular practical interests when transporting objects with different masses or containing moving parts.

Error in the Estimated Robots' CoM As I have already introduced, the proposed method relies on the fact that the cables are attached at the CoM of the aerial robots, so that, ideally, their attitude dynamics is not perturbed by any external torque. On the contrary, when the cables are attached at a point that is different from the CoM of the robot, the cable force exerts a torque on the robot CoM perturbing the robot attitude. The intensity of the disturbance exerted by the cable force depends on the magnitude of the error between the actual robot's CoM location and the cable anchoring point and on the intensity of the force in the cable. The latter increases when the weight of the transported load, or the reference internal force, increases. Indeed, in real scenarios, it is likely that the robot CoM is estimated with some uncertainty and that, even when the CoM is known, it is physically impossible to attach the cable at that exact location. To account for this scenario in the numerical validation, I ran a set of simulations in which, for each robot, the cables are attached at a point different from the robot CoM but with position defined by a constant vector in \mathcal{F}_{R_i} . All other uncertainties have not been considered here. The robots are required to bring the load for about 3.5m in 5s to a target pose characterized by $\bar{\psi} = \pi/10$ and $\bar{\theta} = \pi/8$. By comparing these results with the ones in which the cables are attached exactly at the robot CoM, I observed that, up to a certain value of t_L , the behavior of the system in terms of pose control of the object is unaffected by the uncertain parameter. This shows some robustness of the controlled system. However, starting from a certain value of t_L , the system becomes unstable. The control inputs of the robots are saturated, as in the real case, so that the control effort of the robots is not enough to also reject the disturbance. For the same value of t_L , the system with no uncertainty is stable. Specifically, for instance, when the cables are attached to a point with position $[0.04 \ 0.04 \ 0.03]$ m in \mathcal{F}_{R_i} , the system state diverges (with the control inputs that begin to saturate and chatter) for a reference

internal force of 1.6N. On the other hand, if the mass of the transported load is decreased to 0.5kg, the system is still stable for a reference internal force of 2N. I also verified that for smaller, and probably more realistic, errors, the system is still stable for higher values of the reference internal force. When the cables are attached to a point with position $[0.02 \ 0.02 \ 0.02]$ m in \mathcal{F}_{Ri} for each robot and $m_L = 0.9$ kg, the system state diverges for $t_L = 3.1$ N but is still stable for lower values of t_L . When the cables are attached at a point with position $[0.01 \ 0.01 \ 0.01]$ m in \mathcal{F}_{Ri} , the system, as expected, tolerates higher values of t_L than before. However, for $t_L = 4.7$ N the system state starts oscillating (Fig. 8.16 shows the load state in this condition). The observed behavior is still not unstable but of course undesirable in practice.

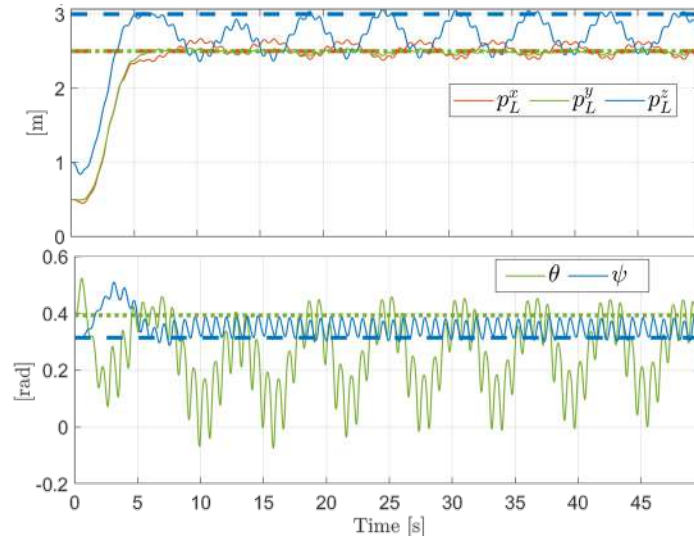


Figure 8.16: Evolution of the pose of the object transported for about 3.5m in 5s. $t_L = 4.7$ N and the position of each cable anchoring point on the corresponding robot is $[0.01 \ 0.01 \ 0.01]^T$ m in \mathcal{F}_{Ri} . The system state oscillates undesirably due to the disturbance torques that the cable forces apply to the robots.

My conclusions are that, if the cables are not attached exactly at the CoM of each robot, the greater is the reference internal force t_L the greater is the disturbance on the robots and hence the control effort they must spend to reject it. Consequently, the internal force cannot be increased arbitrarily. Of course, that a higher value of the reference internal force implies an increased control effort for the robots is clear since they need to exert such a force. However, an error in the estimated CoM of the robots further restricts the possibility to increase the reference internal force. The value of t_L should be chosen as a compromise between a small load attitude error in the presence of parametric uncertainties and a reduced control effort.

8.8 Experimental Results

The vehicles used in the experiments are two MikroKopter quadrotors weighing about 1.03 Kg and having a maximum thrust for each propeller of 6 N. They are equipped with two light cables attached from one side as close as possible to their CoM and from the other side directly to a bar. The cable has a length of 1 m and a mass negligible w.r.t. the vehicle one. The control law is implemented in Matlab-Simulink

Chapter 8. Cooperative Manipulation of a Cable-suspended Beam Load by Two Aerial Robots

and runs on a desktop PC sending the commanded propeller velocities at 500 Hz through serial communication. A motion capture system is used to measure the position and the yaw angle of the vehicle with a frequency of 120 Hz. The velocity is computed by the numerical derivation. An onboard IMU is used to estimate the remaining attitude and measure the angular rate. An onboard momentum-based wrench observer [241] for determining the forces experienced by both robots has been implemented, as well as an admittance filter on both robots.

Preliminary experiments on the convergence of the system to the desired equilibrium for $t_L > 0$ have been carried out so far. In the future, a more extensive experimental campaign will be conducted. In Fig. 8.17 and 8.18 the position and attitude of the load, estimated with the motion capture system, are displayed. A reference internal force of 4 N has been set in order to be robust against the noise in the force estimation. A mean error of about 0.1 m for the position and 4 deg for the orientation has been obtained. A force sensor might improve the performance of the load positioning.

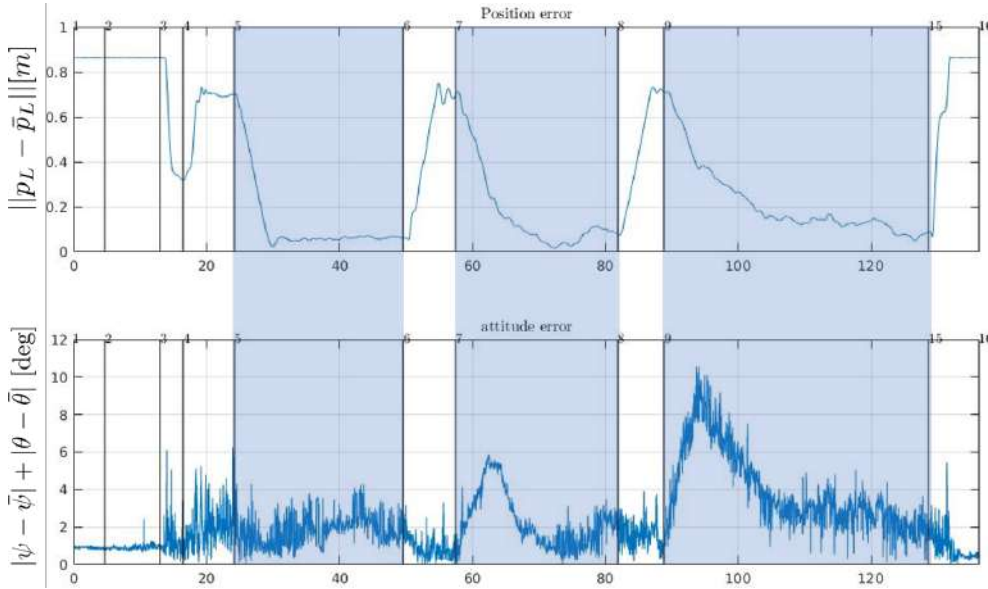


Figure 8.17: Evolution of the load position and attitude errors. Our controller is activated in the blue regions, while the robots are position-controlled elsewhere. During the white intervals 5-6, 7-8, and 9-15, the robots are controlled so that an error of 0.7 m is induced in each of the components of the load position. Hence, when our controller is activated, thanks to $t_L = 4$ N, the load position and attitude errors go towards zero.

8.9 Discussion

This chapter presented a decentralized cooperative manipulation framework for a cable-suspended load manipulated by two aerial vehicles. The proposed leader-follower architecture exploits an admittance controller in order to coordinate the robots with implicit communication only, using the cable forces. The passivity of the system has been proven, and the stability of the static equilibria has been studied highlighting the crucial role of the internal force. A numerical validation and a preliminary experimental validation have been presented. The presence of several

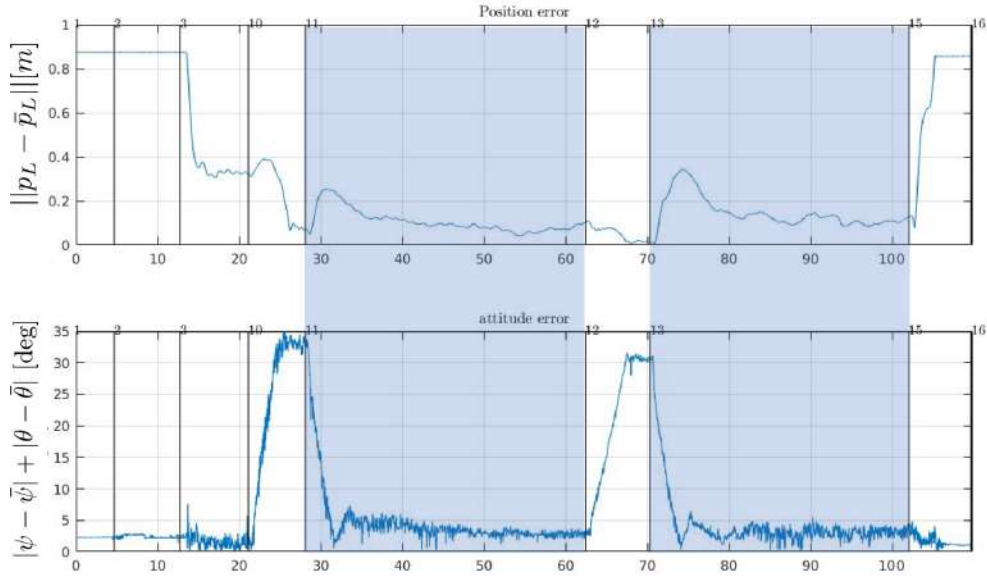


Figure 8.18: Evolution of the load position attitude errors. Our controller is activated in the blue regions, while the robots are position-controlled elsewhere. During the white intervals 11-12 and 13-15, the robots are controlled so that an error of 30 deg is induced in each of the components of the load attitude (only yaw and pitch as already explained). Hence, when our controller is activated, thanks to $t_L = 4$ N, the load position and attitude errors go towards zero.

parametric uncertainties has been studied from a theoretical point of view and the results have been numerically validated. In conclusion, a positive reference internal force is beneficial for the convergence of the pose of the manipulated object to the desired configuration. In the presence of uncertainties, higher values of the reference internal force decrease the load attitude error at the equilibrium and its sensitivity to changes of the parametric uncertainties (or, in a dual way, of the system parameters). However, increasing the reference internal force means demanding a greater control effort to the robots and, if the cables are not attached exactly to the CoM of each robot, this also means producing higher disturbance torques on the robots. In the next chapter, some of the previous results are extended to $N > 2$ robots and a more general manipulated object.

Cooperative Manipulation of a cable-suspended load by N Aerial Robots

9.1 Introduction

This Chapter extends the results of Chapter 8 towards a more general scenario in which the number of robots is $N \geq 2$ and the assumption of a beam-like load is relaxed. If not differently stated, robot 1 is always the leader and the remainder of the robots are the followers. A schematic representation of the considered system is in Fig. 7.1. In Sec. 9.2 the equilibria of the system are studied and their stability discussed in Sec. 9.3. Numerical validation results are presented in Sec. 9.4.1, while in Sec. 9.4.2 additional sets of simulations in the presence of non-ideal conditions such as external disturbances are carried out, together with simulations considering different numbers of leader robots. Final discussions are drawn in Sec. 9.6. The results contained in this chapter have been partially published in [224] and [225] for what concerns $\bar{\mathbf{R}}_L = \mathbf{I}_3$, while in this chapter I present them extended to consider a generic desired attitude of the load.

9.2 Equilibrium Configurations

9.2.1 Equilibrium Inverse Problem

Theorem 7. *Consider the closed loop system (7.8) and assume that the load is at a given desired configuration $\mathbf{q}_L = \bar{\mathbf{q}}_L = (\bar{\mathbf{p}}_L, \bar{\mathbf{R}}_L)$. For each internal force $t_L \in \mathbb{R}$, there exists an unique constant value for the forcing input $\boldsymbol{\pi}_A = \bar{\boldsymbol{\pi}}_A$ (and a unique position of the robots $\mathbf{q}_R = \bar{\mathbf{q}}_R$) such that $\bar{\mathbf{q}} = (\bar{\mathbf{q}}_L, \bar{\mathbf{q}}_R)$ is an equilibrium of the system.*

In particular $\bar{\pi}_A$ and $\bar{q}_R = [\bar{p}_{R1}^\top \bar{p}_{R2}^\top]^\top$ are given by

$$\bar{\pi}_A(\bar{q}_L, t_L) = \mathbf{K}_A \bar{q}_R + \bar{\mathbf{f}}(\bar{q}_L, t_L) \quad (9.1)$$

$$\bar{p}_{Ri}(\bar{q}_L, t_L) = \bar{p}_L + \bar{\mathbf{R}}_L^L \mathbf{b}_i + \left(\frac{\|\bar{\mathbf{f}}_i\|}{k_i} + l_{0i} \right) \frac{\bar{\mathbf{f}}_i}{\|\bar{\mathbf{f}}_i\|}, \quad (9.2)$$

for $i = 1, \dots, N$, where $\bar{\mathbf{f}}$ is given by (7.6)

The proof is omitted since it is the same as in theorem 1. In the following, we will consider a particular solution of (7.6), in which the robots equally share the effort:

$$\mathbf{f}_i = \bar{\mathbf{f}}_i(\bar{q}_L, t_L) := \frac{m_L g}{N} z_W + t_L \bar{\mathbf{R}}_L^L \frac{\mathbf{b}_i}{b}, \quad (9.3)$$

In general, $\mathbf{G} \in \mathbb{R}^{6 \times 3N}$, thus there are also multiple internal force distributions (parametrized by $3N-6$ scalars if \mathbf{G} has full row rank) for the same equilibrium configuration of the object, see e.g. [30] for an example with three robots. However, we consider here the particular solution in (9.3), which is the one in which the robots contribute equally to the internal force. This particular choice of the internal force is a reasonable choice in practice since all the followers share the same control, and it is also the one that always corresponds to an asymptotically stable equilibrium, as it will be more clear in the following.

As in the two-robot case, we have that if $t_L > 0$ the internal force is a *tension* while if $t_L < 0$ the internal force is a *compression*.

9.2.2 Equilibrium Direct Problem

Once t_L is chosen and the input $\pi_A = \bar{\pi}_A(t_L, \bar{q}_L)$ is applied to the system, it is not in general granted that (\bar{q}_L, \bar{q}_R) is the only equilibrium of (7.8), i.e., the equilibrium direct problem may have multiple solutions.

Theorem 8. *Given $t_L \in \mathbb{R}$, the equilibrium configurations of the system (7.8) when the input $\pi_A = \bar{\pi}_A(t_L, \bar{q}_L)$ —computed as in (7) using (9.3)—is applied are all and only the ones described by the following conditions:*

$$\begin{aligned} t_L \sum_{i=1}^N \mathbf{S}({}^L \mathbf{b}_i) \mathbf{R}_L^\top {}^L \mathbf{b}_i &= \mathbf{0} \\ \mathbf{p}_{R1} &= \bar{\mathbf{p}}_{R1} \\ \mathbf{p}_L &= \mathbf{p}_{R1} - \mathbf{R}_L^L \mathbf{b}_1 - \left(\frac{\|\bar{\mathbf{f}}_1\|}{k_1} + l_{01} \right) \frac{\bar{\mathbf{f}}_1}{\|\bar{\mathbf{f}}_1\|} \\ &= \bar{\mathbf{p}}_L + (\bar{\mathbf{R}}_L - \mathbf{R}_L)^L \mathbf{b}_1 \\ \mathbf{p}_{Ri} &= \mathbf{p}_L + \mathbf{R}_L^L \mathbf{b}_i + \left(\frac{\|\bar{\mathbf{f}}_i\|}{k_i} + l_{0i} \right) \frac{\bar{\mathbf{f}}_i}{\|\bar{\mathbf{f}}_i\|}. \end{aligned} \quad (9.4)$$

Proof. Given $t_L \in \mathbb{R}$, and $\bar{\pi}_A \in \Pi_A(\bar{q}_L)$, a configuration \mathbf{q} is an equilibrium if $m(\mathbf{q}, \mathbf{0}, \bar{\pi}_A) = \mathbf{0}$. The first rows are $\mathbf{K}_A \mathbf{q}_R + \mathbf{f} - \bar{\pi}_A = \mathbf{0}$. Then, using (8.1) we have that

$$\mathbf{f} = \mathbf{K}_A(\bar{q}_R - \mathbf{q}_R) + \bar{\mathbf{f}}. \quad (9.5)$$

At this point, recalling that $\mathbf{K}_{A_i} = \mathbf{0} \forall i \neq 1$ and the expression of $\bar{\mathbf{f}}$ in (8.3), we get, for $i = 2, \dots, N$, that

$$\mathbf{f}_i = \bar{\mathbf{f}}_i. \quad (9.6)$$

Substituting (8.11) into the load translational equilibrium (8.6), one finds that

$$\mathbf{f}_1 = \bar{\mathbf{f}}_1, \quad (9.7)$$

which implies, from (9.5), that $\mathbf{e}_R = (\bar{\mathbf{p}}_{R1} - \mathbf{p}_{R1}) = \mathbf{0}$ and hence $\mathbf{p}_{R1} = \bar{\mathbf{p}}_{R1}$. Replacing (9.6) and (9.7) into the last three rows of (8.4), we obtain

$$t_L \sum_{i=1}^N \mathcal{S}({}^L \mathbf{b}_i) \mathbf{R}_L^\top \bar{\mathbf{R}}_L \frac{{}^L \mathbf{b}_i}{b_i} + \left(\sum_{i=1}^N {}^L \mathbf{b}_i \right) \times \mathbf{R}_L^\top \frac{m_L g \mathbf{e}_3}{N} = \mathbf{0}. \quad (9.8)$$

Remembering that

$$\sum_{i=1}^N {}^L \mathbf{b}_i = \mathbf{0} \quad (9.9)$$

for the symmetry imposed by definition (7.2) (see, e.g., [200] or notice that the left side of (9.9) is the sum of $N > 1$ roots of unity and thus is equal to zero), we obtain the first condition in (9.4). We can retrieve \mathbf{p}_L and \mathbf{p}_{Ri} , using (7.3) and the kinematics. \square

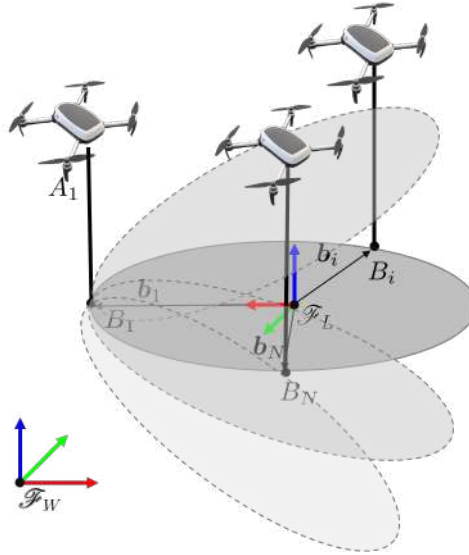


Figure 9.1: Five of the infinite possible equilibrium configurations of the system with N robots and $t_L = 0$. For the sake of clarity, only 3 robots are depicted and only for one configuration. The desired configuration of the load in which $\mathbf{R}_L = \bar{\mathbf{R}}_L$ is in solid line, other 4 possible configurations in dashed lines. Note that the leader robot is always in the same position, the cables would always be vertical, and each of them exerts the same force in all equilibrium configurations.

In a specular way compared to the two-robot case in Chapter 8, if $t_L = 0$, the conditions in (9.4) hold for all the possible load attitudes $\mathbf{R}_L \in SO(3)$. This means, using the notation introduced in Theorem 8, that $\mathcal{Q}(0, \bar{\mathbf{q}}_L)$ contains all $\mathbf{R}_L \in SO(3)$

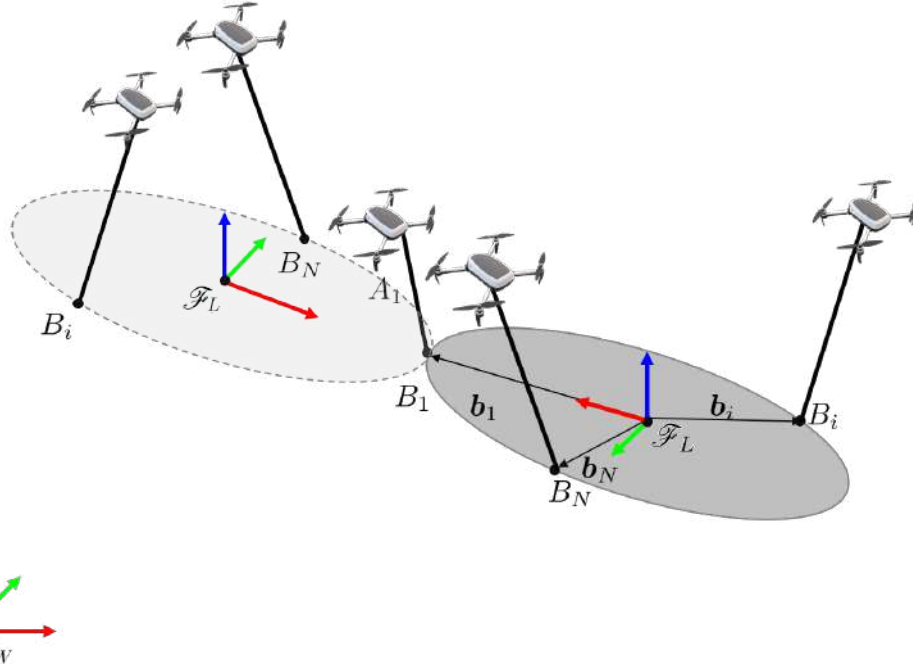


Figure 9.2: Two different equilibrium configurations for $t_L \neq 0$. The desired configuration of the load in which $\mathbf{R}_L = \bar{\mathbf{R}}_L$ is in solid line, the other is in dashed line. For the sake of clarity, only 3 robots are depicted. The master robot is always at the same position, and the force in each cable is the same in the two configurations.

and, consequently, the corresponding \mathbf{p}_{R2} and \mathbf{p}_L computed using (9.4). Figure 9.1 is a graphical representation of the infinite possible equilibrium configurations for $t_L = 0$. For $t_L \neq 0$, it is required that $\mathbf{R}_L \bar{\mathbf{R}}_L^\top \mathbf{b}_i$ is parallel (or anti-parallel) to ${}^L \mathbf{b}_i \forall i$. This is of course verified for $\mathbf{R}_L = \bar{\mathbf{R}}_L$, but also for $\mathbf{R}_L^\top \bar{\mathbf{R}}_L = \text{diag}(-1, -1, 1)$, i.e., $\mathbf{R}_L = \mathbf{R}_{z_L}(\bar{\psi} \pm \pi) \mathbf{R}_{y_L}(-\bar{\theta}) \mathbf{R}_{x_L}(-\bar{\phi})$. Let us call this matrix $\bar{\mathbf{R}}_L^-$. Note that in the different possible equilibrium configurations of the load, as for the two-robot system, the internal forces stretch the object in one case, and compress it in the other case. Furthermore, for the same load configuration, multiple robot configurations that respect (9.6) and (9.7) and the condition of the leader robot position are possible. However, we are also not considering the cases in which the cables are under compression due to condition (7.3). In this way, we restrict our analysis to the practically feasible poses. Figure 9.2 is a graphical representation of the two different equilibrium configurations for $t_L \neq 0$. Similarly to the definitions in the previous Chapter, we define here

- $\mathcal{Q}^+(t_L, \bar{\mathbf{q}}_L) = \{\mathbf{q} \in \mathcal{Q}(t_L, \bar{\mathbf{q}}_L) | \mathbf{R}_L = \bar{\mathbf{R}}_L\}$,
- $\mathcal{Q}^-(t_L, \bar{\mathbf{q}}_L) = \{\mathbf{q} \in \mathcal{Q}(t_L, \bar{\mathbf{q}}_L) | \mathbf{R}_L = \bar{\mathbf{R}}_L^-\}$.

In conclusion, theorem 8 implies that for $t_L = 0$ there is a continuum of equilibrium points, while the equilibrium points for $t_L \neq 0$ are isolated. This already let us know that $t_L = 0$ may not be a good choice also in this case, since in any case the corresponding equilibrium points cannot be asymptotically stable because

non-isolated. Hence, the robots will not be able to univocally control the pose of the object to its desired value, which represent our final goal.

9.3 Stability

In this section, we shall analyze the stability of the equilibrium configurations discovered in Sec. 9.2. First, we define the following sets (subspaces of the state space):

- $\mathcal{X}(0, \bar{\mathbf{q}}_L) = \{\mathbf{x} : \mathbf{q} \in \mathcal{Q}(0, \bar{\mathbf{q}}_L), \mathbf{v} = \mathbf{0}\},$
- $\mathcal{X}^+(t_L, \bar{\mathbf{q}}_L) = \{\mathbf{x} : \mathbf{q} \in \mathcal{Q}^+(t_L, \bar{\mathbf{q}}_L), \mathbf{v} = \mathbf{0}\},$
- $\mathcal{X}^-(t_L, \bar{\mathbf{q}}_L) = \{\mathbf{x} : \mathbf{q} \in \mathcal{Q}^-(t_L, \bar{\mathbf{q}}_L), \mathbf{v} = \mathbf{0}\}.$

Theorem 9. *Let us consider a desired load configuration $\bar{\mathbf{q}}_L$. For the system (7.8) let the constant forcing input π_A be chosen in $\Pi_A(\bar{\mathbf{q}}_L)$ corresponding to a certain internal force t_L . Then \mathbf{x} belonging to:*

- $\mathcal{X}^+(t_L, \bar{\mathbf{q}}_L)$ is asymptotically stable if $t_L > 0$;
- $\mathcal{X}^-(t_L, \bar{\mathbf{q}}_L)$ is unstable if $t_L > 0$;
- $\mathcal{X}(0, \bar{\mathbf{q}}_L)$ is stable;
- $\mathcal{X}^+(t_L, \bar{\mathbf{q}}_L)$ is unstable if $t_L < 0$;
- $\mathcal{X}^-(t_L, \bar{\mathbf{q}}_L)$ is asymptotically stable if $t_L < 0$.

Proof. The proof is based on Lyapunov's direct method. Let us consider the following Lyapunov's candidate function:

$$V(\mathbf{x}) = \frac{1}{2} \left(\sum_{i=1}^N \dot{\mathbf{p}}_{Ri}^\top \mathbf{M}_{Ai} \dot{\mathbf{p}}_{Ri} + \mathbf{e}_{Ri}^\top \mathbf{K}_{Ai} \mathbf{e}_{Ri} + k_i (\|\mathbf{l}_i\| - l_{0i})^2 - 2\mathbf{l}_i^\top \bar{\mathbf{f}}_i \right) + \quad (9.10)$$

$$+ (Nt_L b - \sum_{i=1}^N \bar{\mathbf{f}}_i^\top \mathbf{R}_L^L \mathbf{b}_i) + m_L \dot{\mathbf{p}}_L^\top \dot{\mathbf{p}}_L + \boldsymbol{\omega}_L^\top \mathbf{J}_L \boldsymbol{\omega}_L + V_0,$$

where $V_0 \in \mathbb{R}_{\geq 0}$ and $\mathbf{e}_{Ri} = \bar{\mathbf{p}}_{Ri} - \mathbf{p}_{Ri}$. Note that for $i \neq 1$ one can set \mathbf{e}_{Ri} arbitrarily, since the terms multiply $\mathbf{K}_{Ai} = \mathbf{0}$. Note that, using (9.3) and (9.9),

$(Nt_L b - \sum_{i=1}^N \bar{\mathbf{f}}_i^\top \mathbf{R}_L^L \mathbf{b}_i) = t_L (Nb - \sum_{i=1}^N \frac{L \mathbf{b}_i^\top}{b} \bar{\mathbf{R}}_L^\top \mathbf{R}_L^L \mathbf{b}_i)$, which is equal to zero for $\mathbf{x} = \mathcal{X}^+(t_L, \bar{\mathbf{q}}_L)$, positive elsewhere if $t_L > 0$, and negative elsewhere if $internalTension < 0$. For an opportune choice of V_0 , $V(\mathbf{x})$ is a positive definite, continuously differentiable function in the domain of interest for which we have that \mathbf{x}_{\min} ($\mathbf{x}_{\min} = \operatorname{argmin}_{\mathbf{x}} V(\mathbf{x})$) is such that $\mathbf{x}_{\min} \in \mathcal{X}(0, \bar{\mathbf{q}}_L)$ and $\mathbf{x}_{\min} \in \mathcal{X}^+(t_L, \bar{\mathbf{q}}_L)$ for $t_L > 0$. The proof of this result has been derived following similar reasoning done in the proof of theorem 3, and here it is omitted for the sake of brevity.

Let us now compute the time derivative of (9.10):

$$\dot{V}(\mathbf{x}) = \sum_{i=1}^N \left(\dot{\mathbf{p}}_{Ri}^\top \mathbf{M}_{Ai} \dot{\mathbf{p}}_{Ri} + \mathbf{e}_{Ri}^\top \mathbf{K}_{Ai} \dot{\mathbf{e}}_{Ri} + \dot{\mathbf{l}}_i^\top \mathbf{f}_i - \dot{\mathbf{l}}_i^\top \bar{\mathbf{f}}_i - \bar{\mathbf{f}}_i^\top \mathbf{S}(\boldsymbol{\omega}_L) \mathbf{R}_L^L \mathbf{b}_i \right) \quad (9.11)$$

$$+ m_L \dot{\mathbf{p}}_L^\top \ddot{\mathbf{p}}_L + \boldsymbol{\omega}_L^\top \mathbf{J}_L \dot{\boldsymbol{\omega}}_L,$$

where we used the fact that $\frac{d}{dt} \left(\frac{1}{2} k_i (\|l_i\| - l_{0i})^2 \right) = \dot{l}_i^\top f_i$. Replacing (7.1), we obtain:

$$\begin{aligned} \dot{V}(\boldsymbol{x}) = & \sum_{i=1}^N \left(\dot{\boldsymbol{p}}_{Ri}^\top (-\boldsymbol{f}_i - \boldsymbol{B}_{Ai} \dot{\boldsymbol{p}}_{Ri} - \boldsymbol{K}_{Ai} \boldsymbol{e}_{Ri} + \bar{\boldsymbol{f}}_i) + \dot{\boldsymbol{p}}_{Ri}^\top \boldsymbol{K}_{Ai} \boldsymbol{e}_{Ri} + \dot{l}_i^\top (\boldsymbol{f}_i - \bar{\boldsymbol{f}}_i) + \right. \\ & \left. - \bar{\boldsymbol{f}}_i^\top \boldsymbol{S}(\boldsymbol{\omega}_L) \boldsymbol{R}_L^L \boldsymbol{b}_i \right) + \dot{\boldsymbol{p}}_L^\top \left(-m_L \boldsymbol{g} \boldsymbol{z}_W + \sum_{i=1}^N \boldsymbol{f}_i \right) + \\ & + \boldsymbol{\omega}_L^\top \left(-\boldsymbol{S}(\boldsymbol{\omega}_L) \boldsymbol{J}_L \boldsymbol{\omega}_L - \boldsymbol{B}_L \boldsymbol{\omega}_L + \sum_{i=1}^N \boldsymbol{S}(\boldsymbol{b}_i) \boldsymbol{R}_L^\top \boldsymbol{f}_i \right), \end{aligned} \quad (9.12)$$

Noticing that $\dot{l}_i = \dot{\boldsymbol{p}}_{Ri} - \dot{\boldsymbol{p}}_L - \boldsymbol{S}(\boldsymbol{\omega}_L) \boldsymbol{R}_L^L \boldsymbol{b}_i$ and $\sum_{i=1}^N \bar{\boldsymbol{f}}_i = -m_L \boldsymbol{g} \boldsymbol{z}_W$, after few algebraic computations we get:

$$\dot{V}(\boldsymbol{x}) = \sum_{i=1}^N -\dot{\boldsymbol{p}}_{Ri}^\top \boldsymbol{B}_{Ai} \dot{\boldsymbol{p}}_{Ri} - \boldsymbol{\omega}_L^\top \boldsymbol{B}_L \boldsymbol{\omega}_L, \quad (9.13)$$

that is clearly negative semidefinite. In particular $\dot{V}(\boldsymbol{x}) = 0$ for all $\boldsymbol{x} \in \mathcal{E} = \{\boldsymbol{x} \in \mathbb{X} \mid \dot{\boldsymbol{p}}_{Ri} = \mathbf{0} \forall i, \dot{\boldsymbol{p}}_L = \mathbf{0}, \boldsymbol{\omega}_L = \mathbf{0}\}$. Based on the *LaSalle's invariance principle* and the *Chetaev's theorem*, similarly to what previously done in the proof of theorem 3, the stability nature of the equilibria according to t_L can be proved. \square

9.4 Numerical Results

The content of this section is the validation of the theoretical results through numerical simulations as well as the investigation of different system properties, such as its behavior under the effect of multiple leader robots. The simulations are carried out both in nominal and far-from-ideal conditions, as it will be clear in the following. The role of the internal force in all situations is highlighted.

The simulated system has the following characteristics. The load is a rigid body with mass $m_L = 5$ kg and inertia matrix $\boldsymbol{J}_L = \boldsymbol{I}_3$ kg m². The leader robots gains are: $\boldsymbol{M}_A = 0.5 \boldsymbol{I}_3$ kg, $\boldsymbol{B}_A = 100 \boldsymbol{I}_3$ N s m⁻¹ and $\boldsymbol{K}_{A1} = 1000 \boldsymbol{I}_3$ N m⁻¹, and the follower robots ones are: $\boldsymbol{M}_A = 0.01 \boldsymbol{I}_3$ kg, $\boldsymbol{B}_A = 0.15 \boldsymbol{I}_3$ N s m⁻¹ and $\boldsymbol{K}_{A1} = 0 \boldsymbol{I}_3$ N m⁻¹. We have that the radius of the circle around which the robots are attached is $b = 5$, m. In not differently specified, the desired attitude of the object, $\bar{\boldsymbol{R}}_L$, is described by desired roll, pitch and yaw angles $\theta^d = \phi^d = \psi^d = 0$, which define indeed a configuration of the uttermost practical relevance, in which the object is placed horizontally.

In the set of simulations, where only robot 1 is the leader, we consider a group composed of a variable number of robots, randomly varying between 2 to 50. Instead, a group of 12 robots is considered in the simulations with a different number of leader robots in the group if not differently stated.

9.4.1 Convergence

In this section, we want to show the convergence of the load configuration to a certain static equilibrium, with respect to i) the value of t_L ; ii) the number of leader robots. If there is at least one leader, robot 1 is always considered a leader. Note that the simulations with 1 leader robot validate the results derived in Sec. 9.3. For each

simulation scenario, characterized by a number of leader robots ranging between 0 and 3, three different values of t_L have been tested:

- 1) $t_L = 0\text{N}$,
- 2) $t_L = 0.8\text{N}(> 0)$,
- 3) $t_L = -0.8\text{N}(< 0)$.

Note that, in the cases 2) and 3), the value of t_L is equal to $\pm 0.016\%$ of the total weight-force of the load.

For each one of the cases obtained by a combination of the number of leader robots and value of t_L , at least 10 different simulations of the same scenario have been carried out, each one starting from different initial conditions. In fact, in order to investigate the capability of the system to bring the load to a specific configuration of equilibrium, i.e., the stability of the equilibrium, we initialize the system in several different initial conditions. The initial conditions are characterized by random values of ψ , θ , and ϕ (the last two only in the case of floating systems) between $-\pi/4$ rad and $\pi/4$ rad). For the sake of clarity, due to the large number of simulated cases, only the results of a meaningful subset are displayed through plots in the Thesis. However, the complete set of plots can be found in the published material [225] and in the corresponding online supplementary material.

Zero leader robots First, please note that for a floating system subject to gravity, a leader-less configuration, i.e, one in which there is no position reference, would result not applicable in practice in any case. Indeed, even the slightest error in estimating the mass of the object would result in the falling of the entire setup under the action of gravity, due to non-perfect gravity compensation. Nevertheless, this case has been included in the analysis for the sake of completeness. Assuming, instead, a ground system that might be modeled in a similar way and thus fall into this analysis—please refer to [225] for details about this —, the position of the load would converge to a value that depends on the initial conditions of the system and on the presence of internal forces, but it is not controllable at will by the robots.

If from one side the position of the object is not controllable in this scenario, about the attitude of the load, from the other side, we can observe that:

- for $t_L = 0$, the final attitude of the object is not uniquely determined, but it remains equal to its initial value;
- for $t_L > 0$, the attitude of the object always converges to the desired equilibrium $\bar{\mathbf{R}}_L$.
- for $t_L < 0$, the attitude of the object always converges to $\bar{\mathbf{R}}_L^-$.

The results of the simulation for a floating system with $t_L > 0$ are shown in Fig. 9.3. The plots highlight the important role of the internal force to control the object attitude. In fact, interestingly, not even a leader robot is needed for this purpose when the internal force is non-zero.

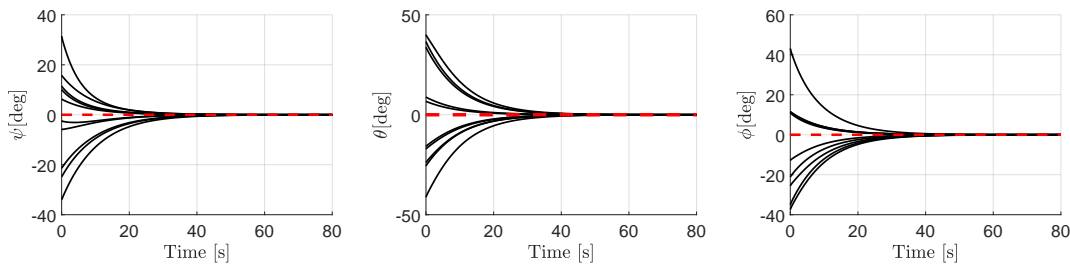


Figure 9.3: Evolution of the attitude of the object with zero leader robots in a group of floating robots and $t_L > 0$.

One leader robot This is the case formally analyzed in Sec. 9.2 and Sec. 9.3 and the results confirm what was theoretically proven:

- for $t_L = 0$, every $x \in \mathcal{X}(0, \bar{q}_L)$ is stable. The pose of the load can not be unambiguously controlled to a desired configuration, as shown in Fig. 9.4,
- for $t_L > 0$, $\mathcal{X}^+(t_L, \bar{q}_L)$ is asymptotically stable, as it is shown in Fig. 9.5
- for $t_L < 0$, $\mathcal{X}^-(t_L, \bar{q}_L)$ is asymptotically stable and $\mathcal{X}^+(t_L, \bar{q}_L)$ is unstable, as it is shown in Fig. 9.5 and 9.7.

Observation 1. *Considering the presented communication-less approach for the manipulation of an object by a swarm of generic robots, from the theoretical previous analysis and observations from numerical simulations, we can conclude that:*

1. *The load orientation can be controlled to $\bar{\mathbf{R}}_L$ even if there are no leader robots, as long as $t_L > 0$, namely if the robots stretch the load producing an internal tension. The load orientation can still be controlled to a precise unique value if $f_{int} < 0$. However, this orientation is different from the desired one. The internal forces applied by the swarm to the object are sufficient alone to stabilize its attitude to a precise value; no leader is required for this specific purpose.*
2. *The presence of at least one leader robot is necessary for the regulation of the position of the object to a specific value.*

Chapter 9. Cooperative Manipulation of a cable-suspended load by N Aerial Robots

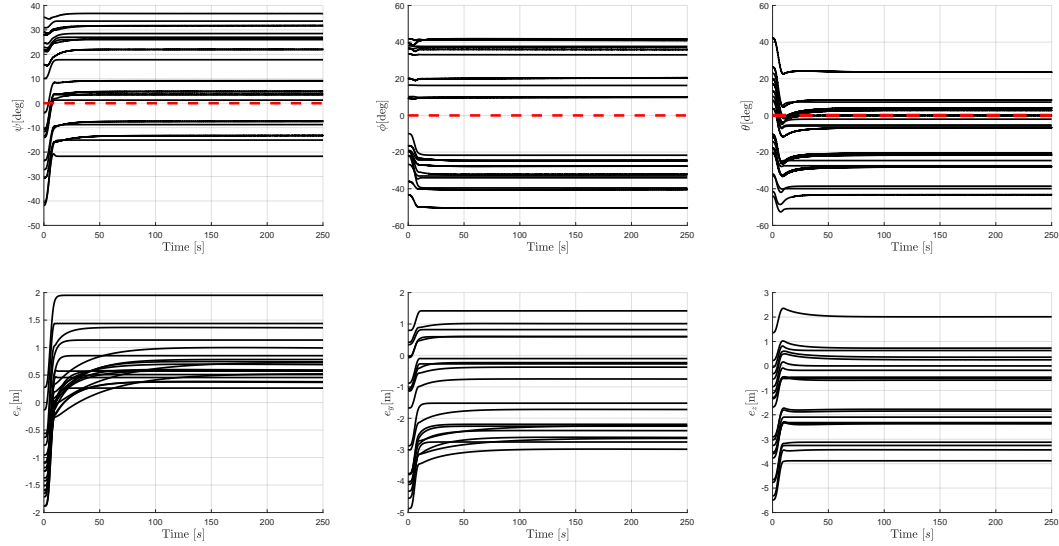


Figure 9.4: Evolution of the attitude (first row) and of the position error (second row) of the object with one leader in a group of floating agents and $t_L = 0$.

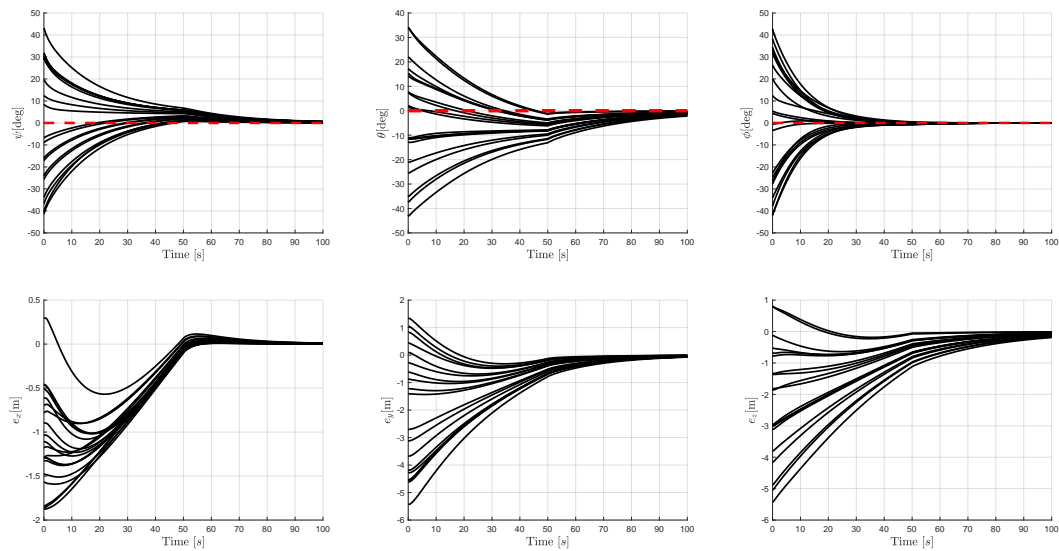


Figure 9.5: Evolution of the attitude (first row) and of the position error (second row) of the object with one leader in a group of floating agents and $t_L > 0$.

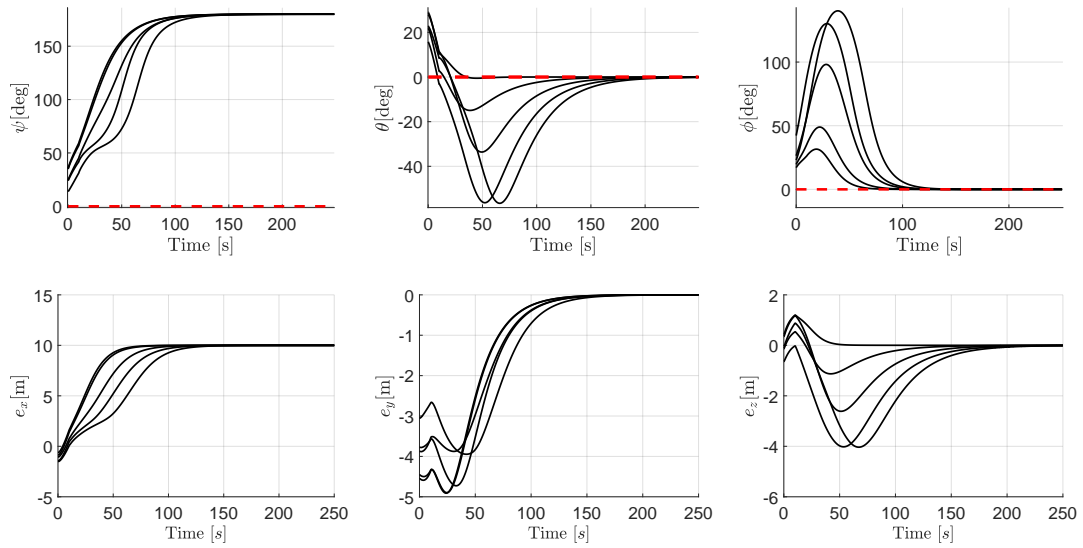


Figure 9.6: Evolution of the attitude (first row) and of the position error (second row) of the object with one leader in a group of floating agents and $t_L < 0$.

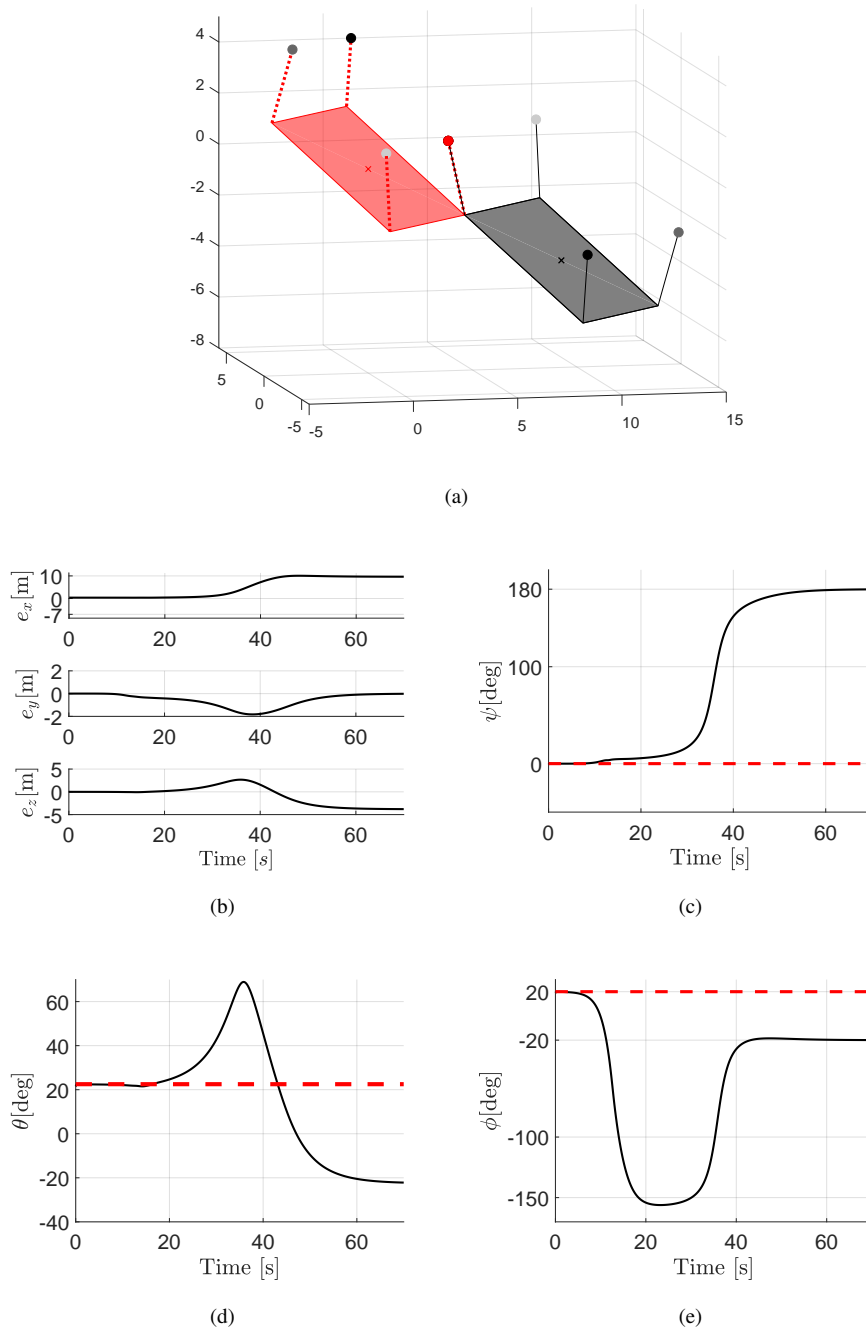


Figure 9.7: Results of a simulation with 4 robots of which one is leader, $t_L = -4\text{N}$, $\bar{\psi} = 0\text{rad}$, $\bar{\theta} = \pi/8\text{rad}$, $\bar{\phi} = \pi/9\text{rad}$. 9.7(a) shows the desired configuration of the system in red (dotted lines are the cables, the red square is the load) and the final equilibrium configuration to which the system converges (grey square is the load, black lines the cables). The red ball is the leader robot, while each follower robot is represented as a ball of a different shade of grey. The load CoM is indicated with a cross in both configurations. The results show that even though the system has been initialized so close to the desired configuration of equilibrium, $\mathcal{X}^+(t_L, \bar{\mathbf{q}}_L)$ (see the other four plots reporting the evolution of attitude and of position errors), it converges to $\mathcal{X}^-(t_L, \bar{\mathbf{q}}_L)$, as expected.

Two leader robots We considered two leader robots anchored to the load along the x_L -axis of the body frame, \mathbf{x}_L , and opposite to each other. Figure 9.8(a) shows a schematic representation of such a configuration. When the two leaders are attached to the load at the same point or very close to each other, the system behavior is very similar to the one observed with just one leader. In fact, being the leader robots anchored almost to the same point, their action is basically equivalent to the one of a single leader robot. The action of the two leader robots is much more effective when they are equally spread around the object.

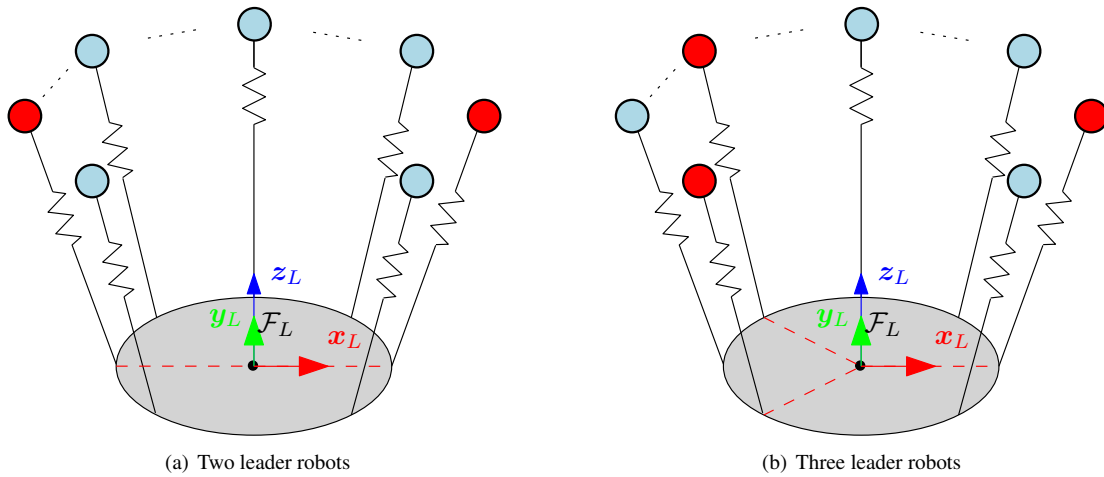


Figure 9.8: Equally spread multiple leader robots. Each leader robot is depicted as a red circle and each follower robot as a light blue one.

Running the usual set of simulations, we observed that:

- for $t_L = 0$, the desired position of the load is now attractive. In fact, no matter the initial configuration, the load position always converges to $\bar{\mathbf{p}}_L$. Regarding the attitude, the θ and ψ converge always to the desired value. In other words, the desired attitude about the axes \mathbf{y}_L and \mathbf{z}_L is stable and attractive. This is not true for the attitude about \mathbf{x}_L , expressed by ϕ , which is still stable but not attractive. Its final value is not unique and depends upon the initial configuration, as shown in Fig. 9.9,
- for $t_L > 0$, both $\bar{\mathbf{p}}_L$ and $\bar{\mathbf{R}}_L$ are attractive,
- for $t_L < 0$, \mathbf{p}_L converges to the desired value. Regarding the attitude, the ψ and θ angles always converge to the desired value. On the other hand, the ϕ angle always converges to $\bar{\phi} \pm 180^\circ$, meaning that all the system flips around \mathbf{x}_L . For $t_L < 0$, $\bar{\mathbf{r}}_{oll}$ is an unstable value while $\phi = \bar{\phi} \pm 180^\circ$ is attractive.

Observation 2. From the previous results, we can conclude that:

1. Two properly distributed leader robots are enough, even without any internal force, for controlling the position of the object to a unique desired value.
2. The attitude about the axes perpendicular to the line ${}^L\mathbf{b}_i - {}^L\mathbf{b}_j$, where i, j are leaders, is always stable, no matter the value of t_L , and it converges to the desired

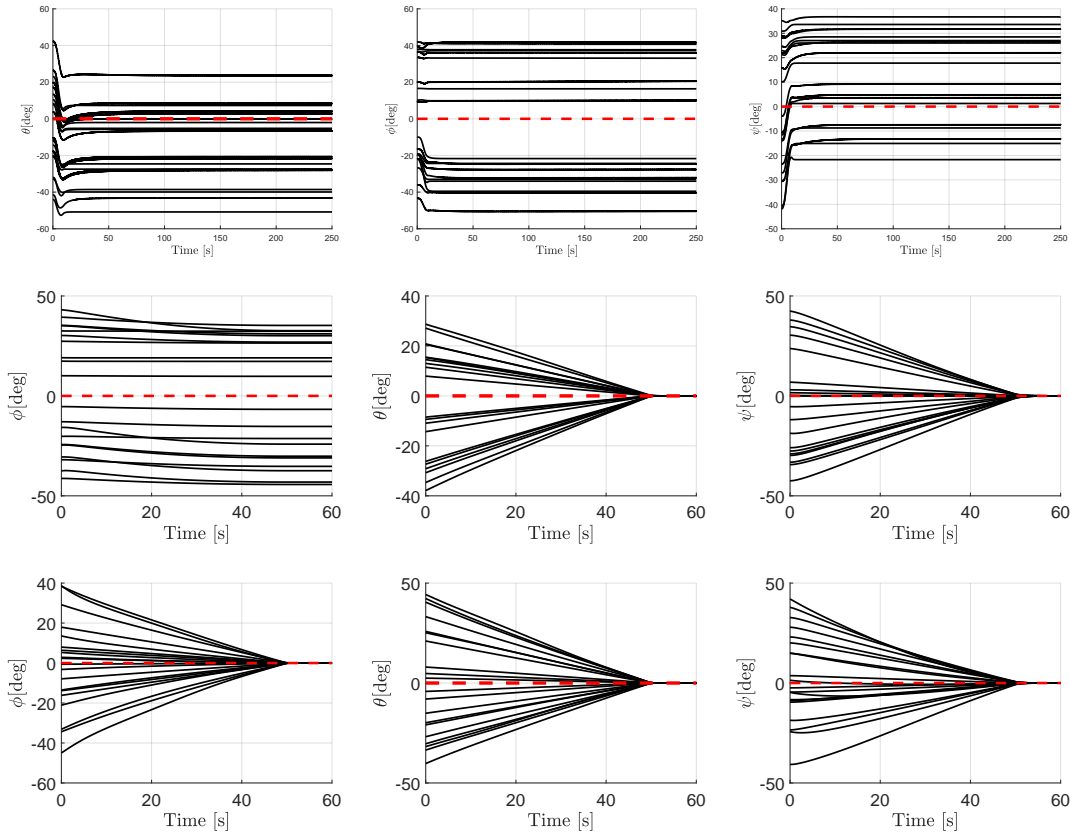


Figure 9.9: This figure aims to show the role of multiple leaders in the meaningful condition when $t_L = 0$. It show the evolution of the attitude of the object. One leader is in the first row, two leaders are in the second row, and three leaders are in the third row.

value. On the other hand, the attitude about the axes ${}^L\mathbf{b}_i - {}^L\mathbf{b}_j$ converges to the desired value only if $t_L > 0$.

Three leader robots As already discussed for the case when the number of leader robots is two, the most interesting scenario to examine is the one in which the leaders are evenly spread around the object. More specifically, we shall consider in these sets of simulations the distribution of leader robots schematically represented in Fig. 9.8(b).

Observation 3. Running the usual set of simulations we observed that if three evenly distributed leaders are in the group, both $\bar{\mathbf{p}}_L$ and $\bar{\mathbf{R}}_L$ are attractive independently from the value of t_L .

The conclusions drawn until now from the numerical results presented in this section are summarized in Table 9.1.

9.4.2 Robustness

In this section, we want to test the capability of the swarm to maintain the orientation and position of the object as close as possible to a desired value when external disturbances act on the object. In particular, the focus is on discovering which

Leaders	t_L	Position	Orientation
0	= 0	The final value depends upon the initial conditions.	The final value depends upon the initial conditions.
	> 0		Converges to $\bar{\mathbf{R}}_L$.
	< 0		Converges to $\bar{\mathbf{R}}_L^-$.
1	= 0	The final value depends upon the initial conditions.	The final value depends upon the initial conditions.
	> 0		Converges to $\bar{\mathbf{p}}_L$.
	< 0		Converges to a different value than $\bar{\mathbf{p}}_L$.
2	= 0	Converges to $\bar{\mathbf{p}}_L$.	Roll depends on the initial conditions. Yaw and pitch converge to the ones of $\bar{\mathbf{R}}_L$.
	> 0		Converges to $\bar{\mathbf{R}}_L$.
	< 0		Roll converges to $\bar{\phi} \pm 180^\circ$.
3	= 0	Converges to $\bar{\mathbf{p}}_L$.	Converges to $\bar{\mathbf{R}}_L$.
	> 0		
	< 0		

Table 9.1: Summary of the load convergence analysis.

conditions, in terms of internal forces and number of leaders, allow the system to manipulate the object without being strongly affected by external disturbances. Constant external forces acting on the object can be compensated adding in the control law an integral action w.r.t. the load position error. Notice that an external force acting on the object could model, e.g., an uncertainty on the mass of the object itself, so that the situation is similar to the one discussed in Sec. 8.6.2 of Chapter 8. As in that case, the leader robot needs to measure the object position \mathbf{p}_L in order to implement the modified control law:

$$\mathbf{u}_{Ri} = \mathbf{M}_{Ai}^{-1} \left(-\mathbf{B}_{Ai} \dot{\mathbf{p}}_{Ri} - \mathbf{K}_{Ai} \mathbf{p}_{Ri} - \mathbf{f}_i + \boldsymbol{\pi}_{Ai} + \mathbf{K}_i^I \int (\bar{\mathbf{p}}_L - \mathbf{p}_L) dt \right), \quad (9.14)$$

in which a standard integral term on the position error of the object with proper gain $\mathbf{K}_i^I \in \mathbb{R}^{3 \times 3}$ has been added to (7.7). A corresponding simulation can be found in Fig. 9.10.

On the other hand, a control action performed just by one robot is not enough to maintain the orientation of the object under external disturbance torques. Intuitively, it is therefore clear that, to react to an external torque and remain close to the desired attitude, at least a pair of contact forces are needed. In other words, some cooperative action is required for this purpose. Because of the required coordination among the robots, we think that the problem of regulating the object attitude subject to external torques is of higher interest in this context. Thus, we focus the following investigation on the attitude regulation problem.

The system is always initialized at the desired equilibrium equal to $\bar{\mathbf{p}}_L = (0, 0, 0)$, $\bar{\mathbf{R}}_L = \mathbf{I}_3$. In every simulation scenario, we tested the system subject to three constant external torques expressed in body frame:

1. $\boldsymbol{\tau}_{e,x} = m_{ext} \mathbf{e}_1$,

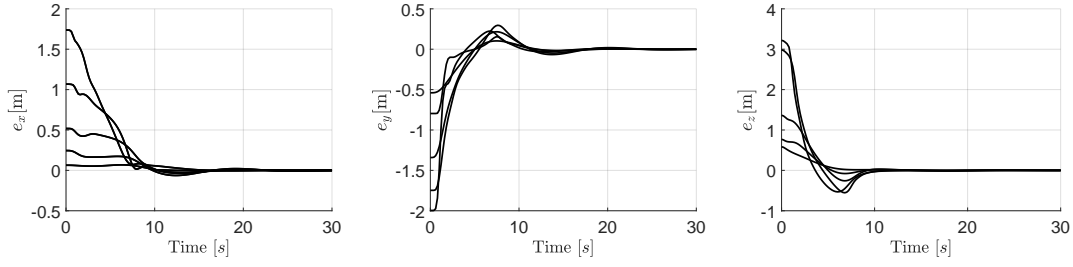


Figure 9.10: Evolution of the position error in case of one leader in the swarm of floating agents and no internal forces. The leader agent applies the control force of eq. (9.14). An external disturbance force of 0.5 N along all the three directions is applied to the object center of mass. $\mathbf{K}_1^I = 10^5$ N/ms and $t_L = 0$. The system is initialized in different configurations.

2. $\tau_{e,y} = m_{ext} e_2$,

3. $\tau_{e,z} = m_{ext} e_3$.

We can not expect the error to converge to zero in the presence of constant disturbances since there is no integral action. However, we wish to obtain a bounded and as small as possible steady-state error. In the following, we want to assess the robustness in terms of the deviation of the load attitude from the desired value. We say that the object attitude (or one of its components) is *robust* if the error stays bounded in time when subject to an external disturbance. On the contrary, it is *not robust* if it diverges in time.

Zero leader robots Running the tests with zero leader robots in the swarms, we observe that (see Fig. 9.11):

- for $t_L = 0$, the attitude of the object is not robust,
- for $t_L > 0$, the attitude of the object is robust
- for $t_L < 0$, the attitude errors are all bounded. However, being $\bar{\mathbf{R}}_L$ not even stable, as shown in the previous section, the system flips by 180° around the axis of the corresponding external torque.

It is not surprising that for $t_L = 0$, none of the components of the object attitude is robust against external torques. In fact, with no robot attracted to a precise position, the only action that may induce resistance to external disturbances is the radial stretch or compression generated by the internal forces. In particular, applying a $\tau_{e,z}$, the yaw angle error is smaller compared to the pitch and the roll ones, even though m_{ext} has been chosen the same for each of the external torque components (see Fig. 9.12, last plot on the right side). This can be related to the fact that all the robots apply the same torque along z_L in compensating the external torque τ_{ext} . On the other hand, along x_L , the robots whose attaching point is closer to be aligned with x_L apply a smaller contribution in compensating the external torque $\tau_{e,x}$. Then, the compensating action is overall less effective. Analogous results have been found for the external torque $\tau_{e,y}$ along y_L .

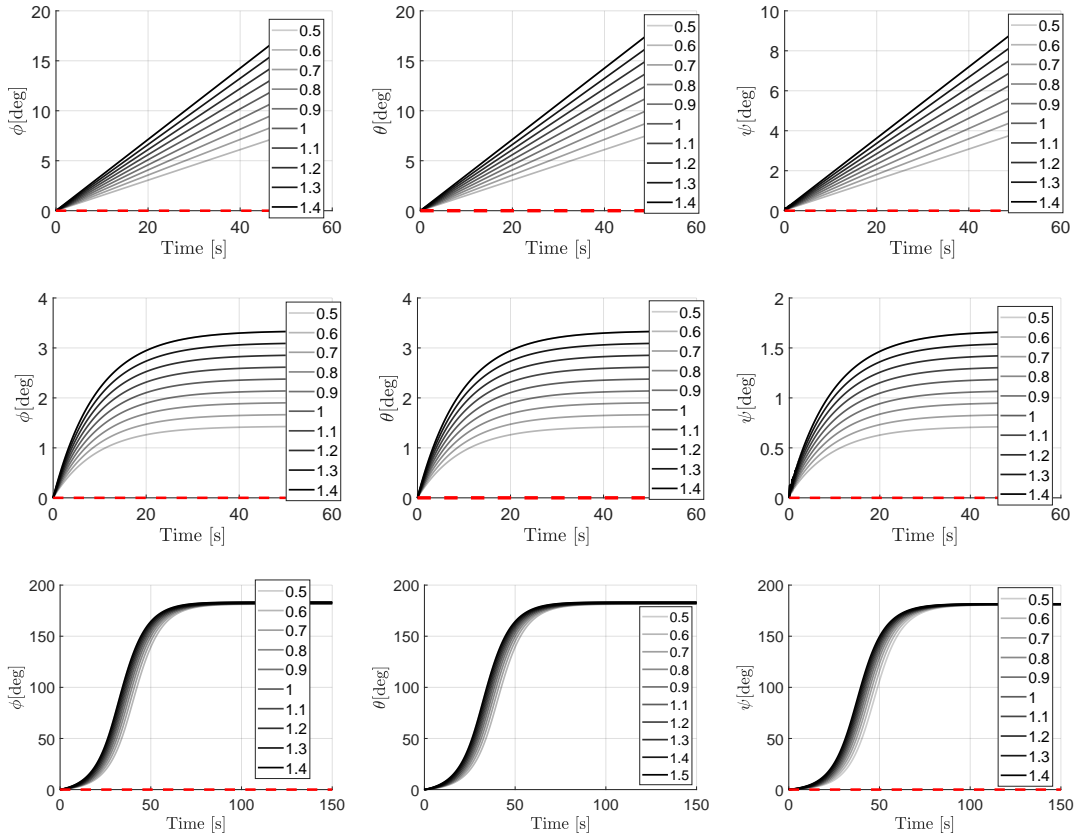


Figure 9.11: Evolution of the attitude of the object, perturbed by external disturbance torques applied at its center of mass, with no leader robots. $t_L = 0$ in the first row, $t_L > 0$ in the second row, and $t_L < 0$ in the third row. From the left to the right, $\tau_{e,x}$, $\tau_{e,y}$, and $\tau_{e,z}$ are applied. Only the rotation around the corresponding axes is displayed, because it is the only one significantly varying. The legends contains the value of m_{ext} expressed in Nm.

In Fig. 9.12 we show the results for a floating swarm with no leader robots and for different positive values of t_L keeping constant the values of $\tau_{e,x}$, $\tau_{e,y}$, $\tau_{e,z}$. We already know from the previous results that the attitude errors should stay bounded. Here, the effect of the intensity of the internal force on the steady-state error has been tested. We noticed that as soon as the intensity of the reference internal force is increased, the magnitude of the errors decreases.

Observation 4. Considering the presented communication-less approach for the manipulation of an object by a swarm of generic robots, from the previous analysis and observations, we can conclude that:

1. The internal forces in the object are sufficient alone to confer robustness to the attitude of the object itself, even without any leader robot in the swarm.
2. The sensitivity of the attitude error when external disturbance torques are applied is inversely proportional to the intensity of the internal forces in the object.

One leader robot In this paragraph, we discuss the robustness to external torques when in the swarm there is one leader robot. From the simulations, we observed that:

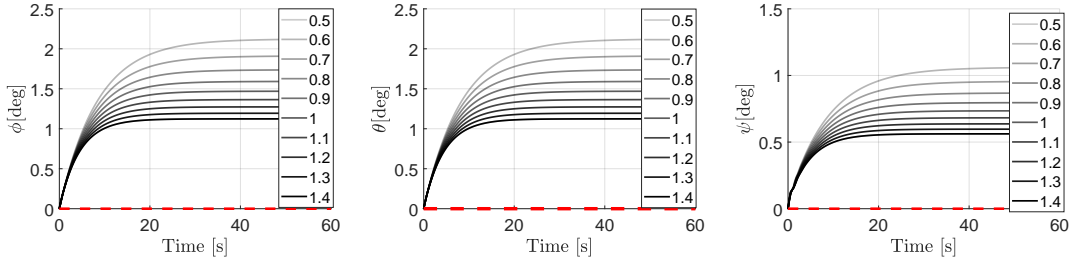


Figure 9.12: Evolution of the attitude of the object with no leaders in a group of floating robots for different values of $t_L > 0$ (displayed in the legends in N). From the left to the right, $\tau_{e,x}$, $\tau_{e,y}$, and $\tau_{e,z}$ are applied, $m_{ext} = 1 \text{ Nm}$. Only the rotation angle about the corresponding axis is displayed.

- for $t_L = 0$, the attitude of the object is not robust,
- for $t_L > 0$, the attitude of the object is robust,
- for $t_L < 0$, the error of each rotation angle is bounded. However, being $\bar{\mathbf{R}}_L$ not even stable in the scenario with one leader robot and without disturbances, as shown in the previous section, the system flips about the axis of the corresponding external torque.

The previous results are similar to the ones obtained for swarms with no leaders. The only difference is that here, when $\tau_{e,z}$ is applied, the leader robot is the pivot around which the system rotates, while in the case of no leaders, all the system rotates about the object center of mass. The results of this set of simulations can be found in [225] and in the corresponding online supplementary material.

The results obtained until now enforce the conclusion that the internal forces in the object are the fundamental tool through which the swarm cooperatively controls the attitude of the object. Instead, the presence of a leader robot, despite essential for controlling the object position (as discussed in the previous section), is not crucial for controlling the attitude.

Two leader robots We shall now show the role of multiple leaders when reacting to the usual external disturbances. As in the previous section, we present here the results for two leader robots evenly distributed around the object. Specifically, we consider again the situation where the two leader robots are placed along \mathbf{x}_L , as in Fig. 9.8(a). From the obtain results (see Fig. 9.13) we observe that:

- for $t_L = 0$, the attitude about the axis connecting the two leader robots, \mathbf{x}_L , is not robust. On the other hand, the angles of rotation about the other two axes, i.e., \mathbf{y}_L and \mathbf{z}_L , are robust,
- for $t_L > 0$, the attitude of the object is robust,
- for $t_L < 0$, the error of each rotation angle stays bounded. However, being $\bar{\mathbf{R}}_L$ not even stable when $\tau_{e,x}$ acts on the object, the object flips of 180° about \mathbf{x}_L , which is the axis between the two leader robots.

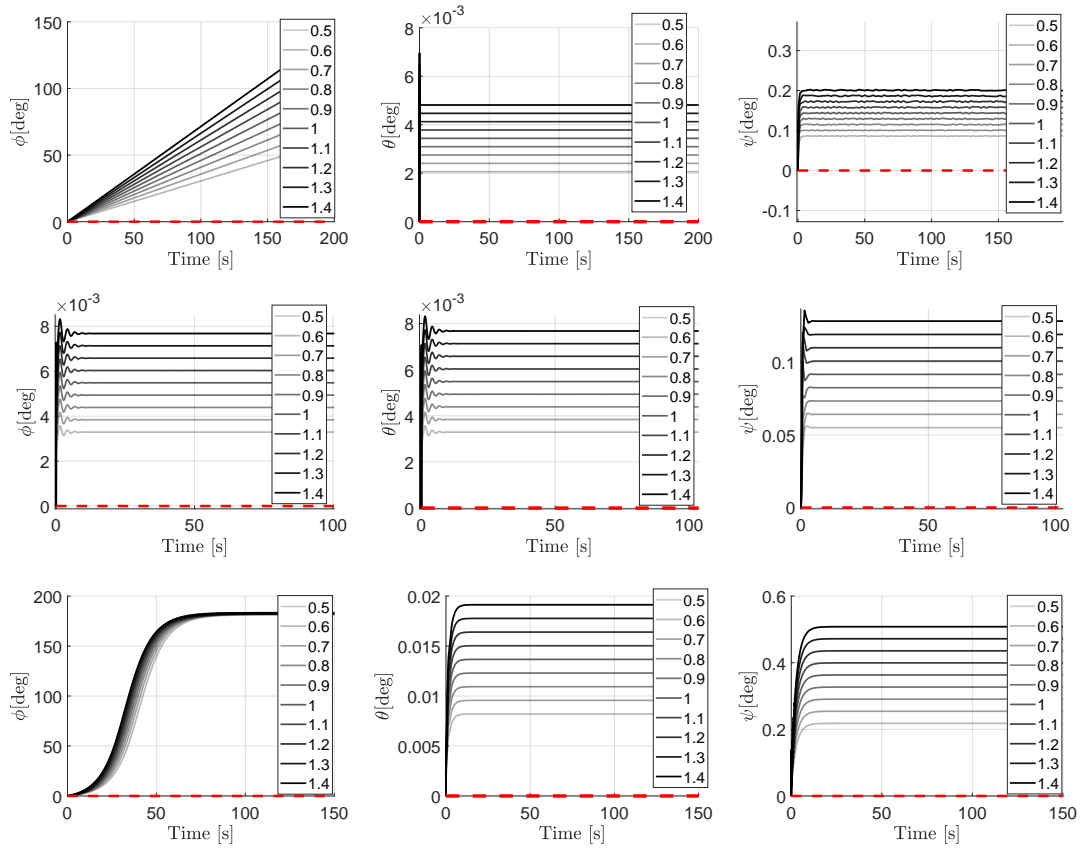


Figure 9.13: Evolution of the attitude of the object with two leader robots. $t_L = 0$ in the first row, $t_L > 0$ in the second row, and $t_L < 0$ in the third row. From the left to the right, $\tau_{e,x}$, $\tau_{e,y}$, and $\tau_{e,z}$ are applied, and only the rotation angle about the corresponding axis is displayed. The legends contains the value of m_{ext} expressed in Nm. In some cases there are oscillations due to the dynamic behavior of the system, which can be tuned by changing the control parameters of the agents.

Three leader robots Let us consider here the case of three evenly distributed leader robots as in Fig. 9.8(b). From the obtained results (see Fig. 9.14) we can conclude that, by means of three leader robots, the control of the attitude of the object is robust, independently from the presence of the internal force or its possible sign. The conclusions drawn until now from the numerical results presented in this section are summarized in Table 9.2. The table also highlights the role of multiple leader robots in the attitude robustness, showing that the addition of one more leader robot enhances the robustness of the system when no internal forces are applied. In the case of two leaders, it emerges that the roll angle ϕ is not robust, whereas the rotations about \mathbf{y}_L and \mathbf{z}_L , i.e., the pitch and yaw angles, respectively, are robust when an external torque is applied about the corresponding axes. This depends on the particular distribution of the two leaders, aligned along \mathbf{x}_L .

We have carried out additional simulations to address the robustness of the attitude of the object in a more realistic scenario. We consider the external torque disturbance as random variables with a Gaussian distribution acting along all the axes of \mathcal{F}_L . We test the system under increasing mean value and with a standard deviation of 0.1 Nm. For what concerns the robots, their state and contact force measurements are affected by

Chapter 9. Cooperative Manipulation of a cable-suspended load by N Aerial Robots

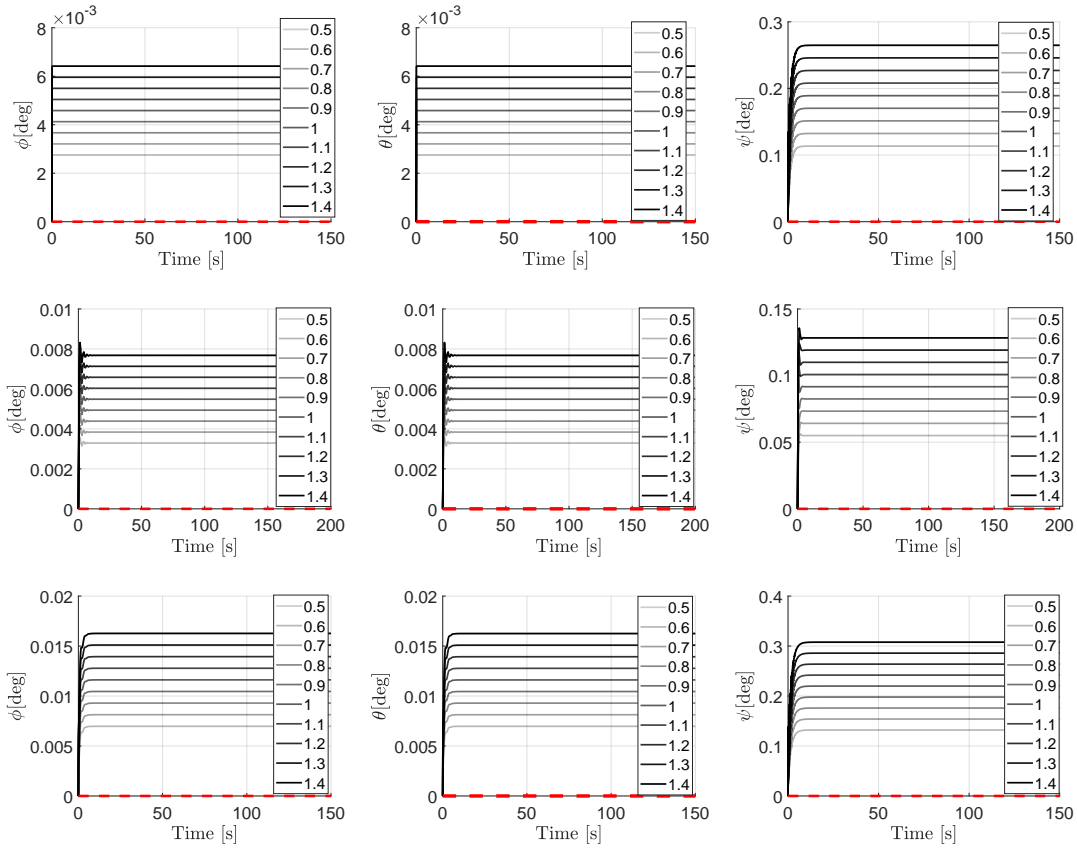


Figure 9.14: Evolution of the attitude of the object with three leader robots. $t_L = 0$ in the first row, $t_L > 0$ in the second row, and $t_L < 0$ in the third row. From the left to the right, $\tau_{e,x}$, $\tau_{e,y}$, and $\tau_{e,z}$ are applied, and only the rotation angle about the corresponding axis is displayed. The legends contains the value of m_{ext} expressed in Nm.

Leaders	t_L	Orientation
0	= 0	not robust
	> 0	robust
	< 0	All the angles flip but stay bounded
1	= 0	not robust
	> 0	robust
	< 0	All the angles flip but stay bounded
2	= 0	robust, except ϕ .
	> 0	robust
	< 0	ϕ flips but all the angles stay bounded.
3	= 0	robust
	> 0	robust
	< 0	robust

Table 9.2: Summary of the load robustness analysis.

noise. In particular, the estimation related to each robot, i.e., own positions and velocities, and the contact force are affected by unbiased Gaussian noise with a

standard deviation of 0.01 m and 0.01 m/s, and 0.2N respectively. The results of all

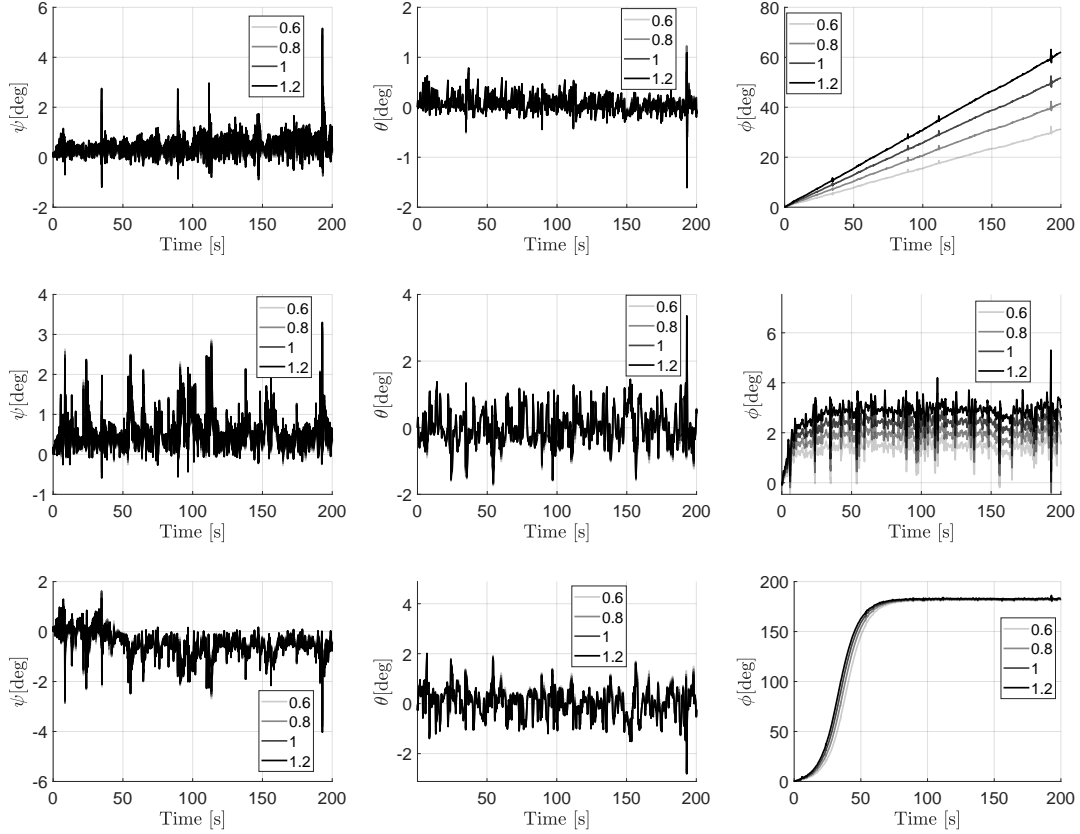


Figure 9.15: Evolution of the attitude of the object with two leader robots. The system is subject to an external Gaussian-distributed disturbance torque applied to the object center of mass, with increasing mean value and 0.1 Nm standard deviation. The mean value of the disturbance along the three orthogonal directions is reported in the legend in Nm. $t_L = 0$ in the first row, $t_L > 0$ in the second, and $t_L < 0$ in the third one.

the simulations (4 per each combination of t_L and number of leaders, for 4 increasing values of the external disturbance mean value) can be found in [225], while here we report in Fig. 9.15 the results for two leader robots. The simulations show the qualitative convergence and robustness behavior that emerged in the previous section. Moreover, in Tab. 9.3 the reader can find the mean value and the standard deviation (std) of the attitude errors in the different simulated conditions (different number of leaders and different values of t_L). The number of simulations in this case could not be sufficient to draw general conclusions by analyzing the statistics. However, the results in Tab. 9.3 suggest that with three leaders the potential benefits induced by a non-zero internal force on the attitude robustness are not very significant. Moreover, they also suggest that the benefits of using three leaders instead of two are not so much evident if a non-zero internal force in the object is also required.

Leaders	t_L	error mean [deg]	error std [deg]
1	$t_L > 0$	ψ : -6.2867	ψ : 2.6101
		θ : -33.6865	θ : 4.1459
		ϕ : 25.4101	ϕ : 3.8239
2	$t_L > 0$	ψ : 0.5273	ψ : 0.3659
		θ : 0.0129	θ : 0.5232
		ϕ : 2.1274	ϕ : 0.3746
3	$t_L > 0$	ψ : 0.0863	ψ : 0.2477
		θ : -0.0380	θ : 0.7354
		ϕ : 0.1902	ϕ : 0.7820
3	$t_L = 0$	ψ : 0.2050	ψ : 0.2526
		θ : 0.0852	θ : 0.1726
		ϕ : 0.0875	ϕ : 0.1762

Table 9.3: Summary of the statistics of the attitude errors for a floating system.

9.5 A shift in the point of view: formation control

Formation control of multi-robot system is a classical task that has received a lot of attention on the literature of multi-agent systems [242, 243]. There are indeed many fields of application in which controlling the robots to reach a certain configuration and maintain it during the motion is a relevant sub-problem. Examples are search and rescue missions, ordnance disposal, demining, and decontamination, transport, plant/building management and services, agriculture use [244]. Typical goals of a formation control problem are establishing the formation, keeping it while moving, changing the shape of the formation, and scaling, i.e., changing the size of the formation [243].

Formation control approaches have been classified, based on the sensing capabilities and the controlled variables, into position-based formation, in which the absolute position of each agent is controlled, displacement-based formation, in which the displacement w.r.t. a global reference system is controlled, and distance-based formation, in which the relative distance between neighbours is directly sensed and controlled [242].

Based on the adopted strategy, formation approaches have been grouped in leader-follower, virtual structure, and behavioral approaches [243]. Leader-follower schemes have been widely adopted in dealing with formation control. Typically, the leader is the reference vehicle and the followers' primary goal is to maintain a desired distance and orientation w.r.t. it [245, 246]. The possibility of changing the shape of the formation can be useful to enhance the robots capabilities in realistic environments, especially to perform obstacle avoidance [243], as shown in the leader-follower approach in [247].

The virtual structure approach has been introduced in [248] and consists of controlling the robot to maintain a certain geometric relationship between them, as they were particles of the same rigid body. These approaches are more fault-tolerance than leader-follower ones and allow precise formation maintenance during trajectory tracking [243].

Behavior-based formation control has been introduced in [249]. The idea at its basis is to give each robot a control input that is the weighted sum of different contributions, corresponding to specific formation behaviors, i.e., avoiding static obstacles, avoiding other robots, maintaining formation, and reaching the target. Theoretical proof of stability is more difficult for these approaches than for the previous ones [243].

Limitations of the communication range and bandwidth represent an obstacle to large-scale formation control applications [250]. Robust communication is essential to implement the presented formation control methods [243]. However, while communication management inserts some additional complexity to the system, both under hardware and software point of view, communication cut-offs and delays in the packet transmission may compromise the performance or even the stability of the formation control in realistic environments.

In this section, I operate a shift in the point of view w.r.t. the presented manipulation strategy, moving the attention from the load and bringing it to the robots. Specifically, following the same interaction method already presented in this part of the Thesis, I propose a formation control for multi-robot systems based on the implicit form of communication enabled by force sensing. *Virtual* forces have been widely considered to achieve formation control. Artificial force fields are used to perform obstacle avoidance and converge to the predefined shape [244, 251]. In [252] virtual spring-damper systems are considered between robots and between each physical robot and a virtual leader robot. I propose a different approach, in which the robots are *physically* connected through elastic cables (springs) to a common object.

9.5.1 proposed solution

I define the formation as a set of desired positions for the robots, p_{Ai} . While in the object manipulation framework the cables were supposed to be attached symmetrically around the object CoM, now the vectors b_i are not known a priori and are in general not all equal. I need to find how to attach the cables to the object, and how to plan the robots' references in order to solve the formation problem. I propose to model the problem as an optimization one, in which the cost function is given by the maximum of the contact-force intensity. In this way, while decreasing the stress imposed on the object and on the robot themselves, the control effort required to perform the formation task is also reduced.

First, I write down (7.6) more generally as:

$$\mathbf{f} = \mathbf{G}(\bar{\mathbf{R}}_L)^\dagger [m_L g \mathbf{z}_W^\top \ 0_{1 \times 3}]^\top + \boldsymbol{\lambda} E, \quad (9.15)$$

where E is a base of the nullspace of \mathbf{G} , and $\boldsymbol{\lambda} \in 3N - 6$ is a vector of internal force intensities λ_i , for $i = 1, \dots, 3N - 6$.

I want to exploit a particular base of \mathbf{G} , considering that the internal forces can be expressed as couples of equal and opposite forces applied at two contact points and acting along the line that connects the points ¹ [253]. Considering for instance three

¹Basically, in the previous analysis that concerned the regulation of the object pose, due to the symmetry of the problem, a particular parametrization had been considered, in which the intensities of the internal forces were all equal. A radial distribution of internal forces resulted.

robots:

$$E = \begin{bmatrix} \mathbf{e}_{1,2} & \mathbf{0}_{2 \times 1} & \mathbf{e}_{1,3} \\ -\mathbf{e}_{2,1} & \mathbf{e}_{2,3} & \mathbf{0}_{2 \times 1} \\ \mathbf{0}_{2 \times 1} & -\mathbf{e}_{2,3} & -\mathbf{e}_{1,3} \end{bmatrix} \begin{bmatrix} \lambda_1 \\ \lambda_2 \\ \lambda_3 \end{bmatrix}$$

with $\mathbf{e}_{i,j} \in \mathbb{R}^2$ the unit vector along the direction $B_i B_j$. Formally,

$$\mathbf{e}_{i,j} = \frac{{}^L \mathbf{b}_i - {}^L \mathbf{b}_j}{\|{}^L \mathbf{b}_i - {}^L \mathbf{b}_j\|}.$$

Matrix E can be similarly written for a different number of robots considering couple of forces between the contact points on the objects.

I define, for every \mathbf{f}_i , the vectors \mathbf{f}_i^i and $\mathbf{f}_i^g \mathbf{e}_3$ both in $nR3$ such that $\mathbf{f}_i = \mathbf{f}_i^i + \mathbf{f}_i^g \mathbf{e}_3$. Specifically, $\mathbf{f}_i^g \mathbf{e}_3$ is the component that contributes to balancing the external wrench and \mathbf{f}_i^i is the component that contributes to the internal force. They are collected into vectors \mathbf{f}^i and \mathbf{f}^g , respectively, both of dimension $3N$. Hence, the following optimization problem can be solved off-line:

$$\min_{\mathbf{b}, \mathbf{f}^i, \mathbf{f}^g, \lambda} (\max \mathbf{f}_i^i + \max \mathbf{f}_i^g) \quad (9.16)$$

subject to:

$$\mathbf{f}_i^i = E(i, :) \lambda \quad (9.16a)$$

$$G \mathbf{f}^g = \begin{bmatrix} m_L g \mathbf{e}_3 \\ \mathbf{0}_{3 \times 1} \end{bmatrix} \quad (9.16b)$$

$${}^L \mathbf{p}_{A_i} = {}^L \mathbf{b}_i + l_0 ({}^L \mathbf{f}_i^i + {}^L \mathbf{f}_i^g) / \|{}^L \mathbf{f}_i^i + v \mathbf{f}_i^g\| + ({}^L \mathbf{f}_i^i + {}^L \mathbf{f}_i^g) / K_c \quad (9.16c)$$

$$\lambda_i \geq th_i \quad (9.16d)$$

where $th_i > 0$ is again defined threshold. By minimizing the maximum of the force intensities, we also distribute the weight of the load uniformly among the robots, avoiding that one robot sustain most of the weight. This is reasonably desirable if the robots have equal payload and level of charge. Eq. (9.16a) imposes that $\mathbf{f}^i = G \lambda$, while (9.16b) implies that the forces are of equilibrium—(9.15) holds. Constraints (9.16c) imposes that kinematics of the system is such that the robots positions coincide with the desired points in the formation. Eventually, (9.16d) constraints the internal forces imposing that they are generated by couples of forces pointing outward the object. The references in the robots' admittance controllers are chosen such that

$\bar{\mathbf{p}}_{R1} = \mathbf{p}_{A1}$, and $\bar{\mathbf{f}} = \hat{\mathbf{f}}^i + \hat{\mathbf{f}}^g$, being $\hat{\mathbf{f}}^i$ and $\hat{\mathbf{f}}^g$ solutions to (9.5.1).

Constraint (9.16d) is important for the stability of the formation. It corresponds to choosing $t_L > 0$ in the previous analysis, in which the anchoring points were uniformly distributed on the same circumference. A proof of the stability for the more general case will be completed. However, the results of the simulations show also the behavior of the system with zero and negative values of λ_i . One can also notice that, at the equilibrium,

$$R_L S ({}^L \mathbf{b}_i) \bar{\mathbf{f}}_i = \mathbf{0}. \quad (9.17)$$

In the case in which $\lambda = 0$, and thus \bar{f}_i are all vertical, the equilibrium is not unique, since after a rotation of the system around the vertical axis, without changing the reference forces, still the equilibrium condition (9.17) holds. In other words, the desired attitude of the formation is not attractive at will since a continuum of equilibrium points exist.

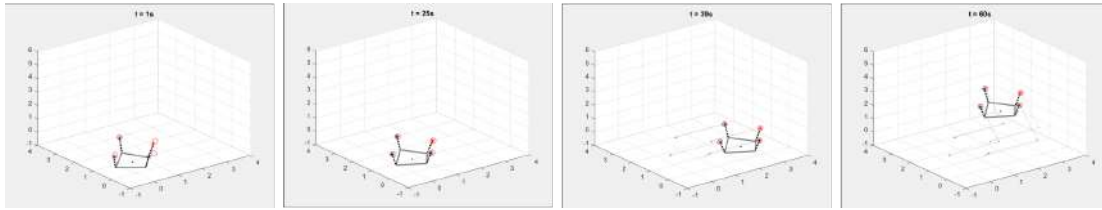
9.5.2 Numerical results

I considered four quadrotor-like vehicles with under-actuated dynamics together with a geometric position controller as in [223] and in Chapter 8, even though our method can be applied to general aerial vehicles. This choice has been made to test the system in the worst-case scenario represented by the under-actuated aerial vehicles. In the simulations, $m_{Ri} = 1.02$ kg, $\mathbf{J}_{Ri} = 0.015\mathbf{I}_3$ kg m², $l_0 = 0.8$ m, $K_c = 20$ N/m, $m_L = 1$ kg, $\mathbf{J}_L = 0.1$ kg m². The values of the controller gains \mathbf{M}_A , \mathbf{B}_A , and \mathbf{K}_A for the leader and the followers are the same as in Chapter 8.

The trajectory that the formation has to perform is a piece-wise 5th-order polynomial trajectory. Each piece starts and ends with zero velocity and zero acceleration. The desired initial formation is given by $\mathbf{p}_{A1} = [0.8 \ 0 \ 1]^\top$ m, $\mathbf{p}_{A2} = [-0.056 \ 0.798 \ 1.2]^\top$ m, $\mathbf{p}_{A3} = [-0.796 \ 0.08 \ 0.7]^\top$ m, and $\mathbf{p}_{A4} = [0.159 \ -0.784 \ 0.9]^\top$ m, where $^\top$ is the transpose operator. First, the robots are initialized in positions $\mathbf{p}_{Ri}(0)$, generally different from the desired position. For the first 25 seconds the leader is commanded \mathbf{p}_{A1} and thus the robots goal is to establish the formation. Then, the formation is commanded (through the leader's desired trajectory) to translate of 2 meters along x_W in 15s and then of 1 meter along y_W and 2 meters along z_W in the following 20 seconds. White noise has been added to the robots' measured state, and to the measured cable force. A low-pass filter with a first-order dynamics and a time constant 0.0667 s has been put in cascade to each noisy signal.

I show here three different simulations, for $\lambda_i >, =, < 0$, respectively. In the first simulation, $\lambda_i > 0$, the robots are initialized in $\mathbf{p}_{R1}(0) = [0.7 \ -0.08 \ 0.94]^\top$ m, $\mathbf{p}_{R2}(0) = [0.064 \ 0.968 \ 1.17]^\top$ m, $\mathbf{p}_{R3}(0) = [-0.856 \ 0.05 \ 0.64]^\top$ m, and $\mathbf{p}_{R4}(0) = [-0.141 \ -0.814 \ 0.83]^\top$ m. The results are shown in Fig. 9.16.

In the second simulation $\lambda_i = 0$ and the robots are initialized in $\mathbf{p}_{R1}(0) = [0.6470.278 \ 0.940]^\top$ m, $\mathbf{p}_{R2}(0) = [-0.425 \ 0.872 \ 1.170]^\top$ m, $\mathbf{p}_{R3}(0) = [-0.768 \ -0.382 \ 0.640]^\top$ m, and $\mathbf{p}_{R4}(0) = [0.282 \ -0.777 \ 0.830]^\top$ m. The results are shown in Fig. 9.17, from which one can see how the robots converge to an equilibrium different from the desired one, as expected from previous considerations. Moreover, the equilibrium is not unique but depends on the initialization. Finally, the third simulation is one in which $\lambda_i < 0$. Despite the robots are initialized in the desired formation, they cannot maintain it, suggesting that the equilibrium is unstable. The robots move towards a configuration in which the object is stretched by the cable forces. The results are shown in Fig. 9.18.



(a) Some time lapses of the simulation with $\lambda_i > 0$. The leader robot is the red star, the followers are the black ones. The surface of the common object given by connecting the cables anchoring points is in grey, with the CoM of the object as a black dot. The cables are dotted black lines. The red circles indicate the desired formation. At $t = 1$ s the robots are initialized in positions different from the desired formation; they establish it (see $t = 25$ s), and then move.

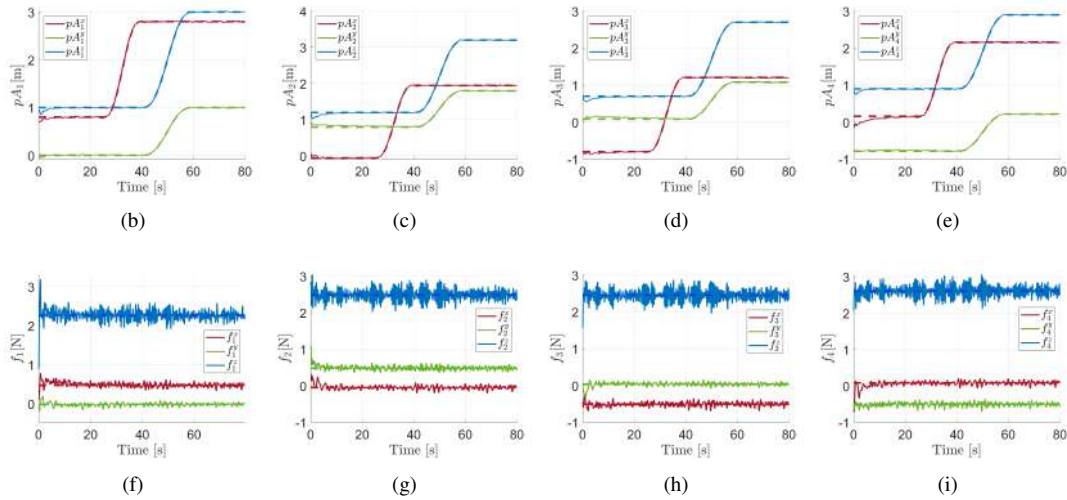
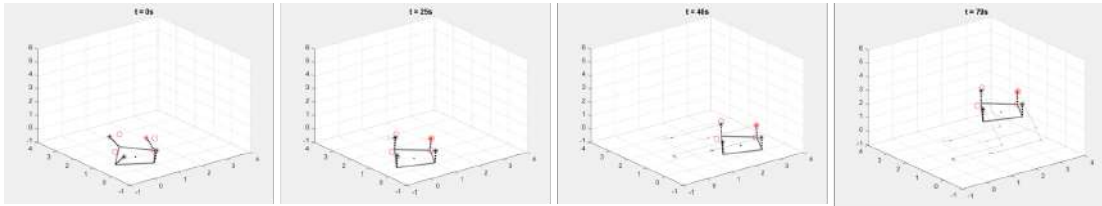


Figure 9.16: The first row contains a visualization of the system is some salient instants, in the second row the positions of the robots are shown, and the forces in the cables are in the third row. The dotted line of a similar color indicates the desired value of the corresponding solid-line signal. Notice that the follower robots do not know their reference position and what is displayed as a dotted line is the desired position of the follower robots in the (translated) formation.

9.5. A shift in the point of view: formation control



(a) Some time lapses of the simulation with $\lambda_i = 0$. The leader robot is the red star, the followers are the black ones. The surface of the common object given by connecting the cables anchoring points is in grey, with the CoM of the object as a black dot. The cables are dotted black lines. The red circles indicate the desired formation. At $t = 1$ s the robots are initialized in positions different from the desired formation; they do not converge to the desired formation.

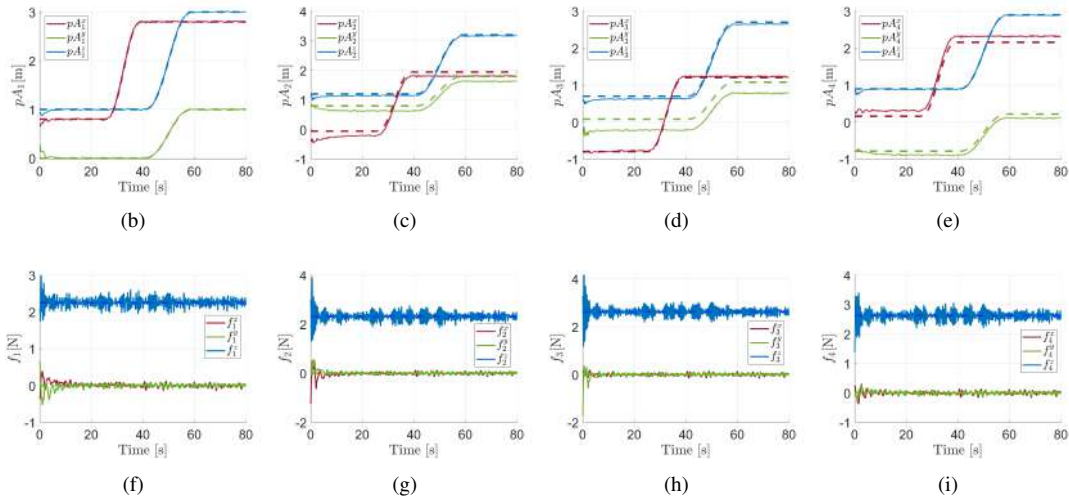
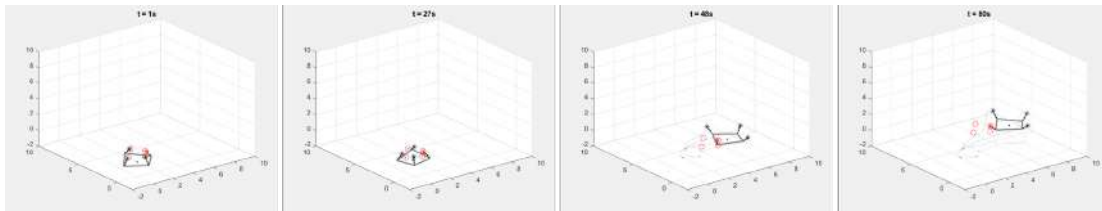


Figure 9.17: The first row contains a visualization of the system is some salient instants, in the second row the positions of the robots are shown, and the forces in the cables are in the third row. The dotted line of a similar color indicates the desired value of the corresponding solid-line signal. Notice that the follower robots do not know their reference position and what is displayed as a dotted line is the desired position of the follower robots in the (translated) formation.



(a) Some time lapses of the simulation with $\lambda_i = 0$. The leader robot is the red star, the followers are the black ones. The surface of the common object given by connecting the cables anchoring points is in grey, with the CoM of the object as a black dot. The cables are dotted black lines. The red circles indicate the desired formation. At $t = 1$ s the robots are initialized in the desired formation; however, they do not maintain it and converge to a configuration in which the cables stretch the load.

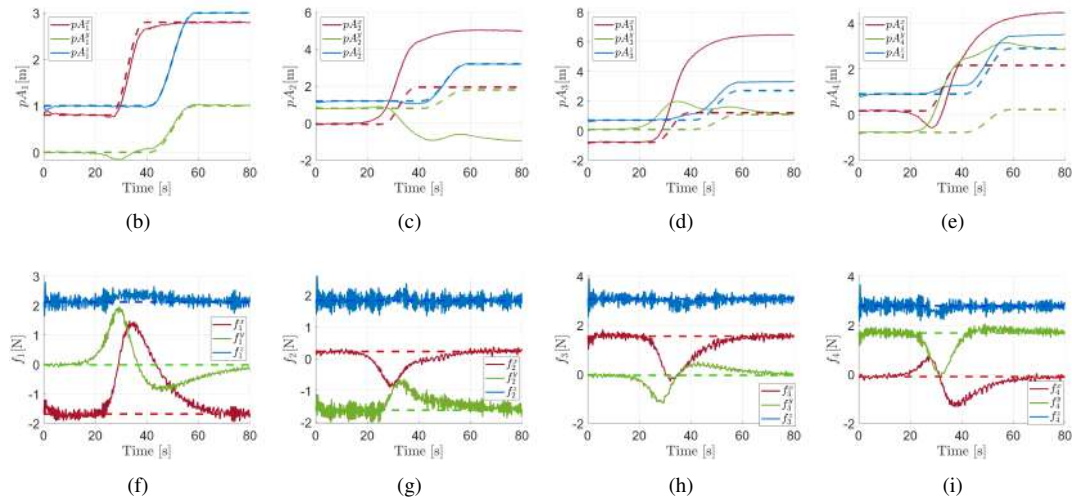


Figure 9.18: The first row contains a visualization of the system is some salient instants, in the second row the positions of the robots are shown, and the forces in the cables are in the third row. The dotted line of a similar color indicates the desired value of the corresponding solid-line signal. Notice that the follower robots do not know their reference position and what is displayed as a dotted line is the desired position of the follower robots in the (translated) formation.

9.6 Discussion

In this and in the previous chapters of this part of the Thesis, we presented a generic model and a control law for robots cooperatively manipulating an object. The presented approach is not based on explicit communication, but rather on the force exchanged through the physical interactions. The manipulated object becomes an implicit means of information exchange. The proposed method employs a leader–follower approach where the follower robots, while damping the oscillations of the system, try to bring the sensed contact force (exchanged with the object) to the desired value. On the other hand, a leader robot, in addition to the action performed by a follower robot, follows a reference trajectory, and, as a result, the global system moves toward a specific point. The role of the internal force induced on the object in the stability and robustness of the closed loop system has been highlighted.

Eventually, a possible extension of the proposed interaction method to the problem of formation control has been presented.

In the future, further implementation with multiple hardware robots will be carried out. For the real implementation, especially with many robots, some effective obstacle avoidance protocols could be required in order to avoid possible collisions among the robots. The formal analysis that considers parametric uncertainties will be extended to the $N > 2$ robot case. As highlighted in [225], the described manipulation protocol is applicable, with minor changes, to ground robots as well. Experimental tests on ground vehicles are left as future work.

CHAPTER 10

Conclusions

This thesis studied the role of contact information and in general interaction forces in enabling the execution of robotic logistic applications in environments that might be non perfectly structured.

First, a planning strategy to unwrap pallets with an uncertain and irregular profile has been introduced and tested. The planning allows the robot to cut the plastic film that wraps the pallets even when the robot's knowledge of the environment is affected by uncertainties. To do so, detection and interpretation of end-effector collisions are derived from force and torque online measurements and used to change the trajectory on the fly . Extensive experimental tests on different pallets has been successfully conducted. Hence, a somehow similar concept has been adopted in a trajectory planner for a dual-arm depalletizer robot. According to such a planning procedure, the robot is expected to online refine its end-effector trajectory during the bi-manual picking operations, based on the acquired information coming from contacts with the objects on the pallet. This makes the execution of the task possible even if the exact position of the items is not accurately known *a priori*. The planner has been tested on several objects coming from the food industry. During the tests, the robot has shown a large versatility in handling objects that differ for shape, weight, and dimensions. In order to enlarge even more the spectrum of the picking applications, a grasping strategy to pick also smaller objects has been envisioned and tested in the thesis. The policy does not require the prior knowledge of any model of the object and is based on a slim data set of ground-truth grasps. This is possible because a human operator trained in the use of the robotic hand generates the data set by grasping only basic shapes instead of representative objects. Hence, the method is generalized to grasp any object by decomposing the object point cloud into the same basic shapes.

Secondly, the Thesis moves the focus on the aerial manipulation of cable-suspended

objects, interesting for the delivery phase. A cooperative approach in which the robots coordinate themselves based exclusively on the implicit information embedded in the interaction forces is considered. In this way, while gaining the pros of cooperative decentralized methods, such as greater payload and robustness in the case of failure of one robot, the possible drawbacks related to corruption or delays in the communication are avoided. The crucial role of the internal force applied to the transported object in determining the stability, passivity, and robustness of the controlled system is highlighted. A similar interaction approach might be extended to achieve force-based communication-less formation control. A thorough numerical study and preliminary experiments on two robots transporting a beam load validate the theoretical results.

The topics addressed in this Thesis will lead to future developments, first of all in terms of tests in real-world scenarios. The assessment of the efficiency of the autonomous unwrapping and depalletizer systems in real warehouses is a crucial future step. Plastic ties and different types of wrapping film will be included in the tests. The integration of a prismatic joint at the base of the unwrapping manipulator might be considered, depending on the use-case requirements, in order to enlarge the workspace of the robot in the vertical direction. Concerning the dual-arm depalletizer, its installation on a forklift will be considered. While the single-object grasping policy has shown good results when tested on the PISA/IIT SoftHand, experiments using different end-effectors will be conducted. The information regarding the expected wrench associated with a predicted grasp could be included in the policy for picking the candidate grasp as an interesting future work that may be beneficial to generalize the method to different end-effectors. As a matter of fact, such a criterion, not being based on any consideration about the specific geometry of the gripper, appears to be quite general. The decomposition of the object point cloud into basic shapes depends on parameters that may be automatically tuned based on dimension or shape characteristics of the point cloud itself. Segmentation and collision avoidance algorithms will be included in the grasping policy to analyze multi-object scenes and to reach the candidate grasping pose avoiding undesired collisions with other objects or with parts of the same object to be grasped, respectively.

Regarding the aerial cooperative manipulation framework, an extensive experimental campaign to test the method on hardware robots will be carried out. The theoretical study about the effect of parametric uncertainties on the system equilibrium will be extended to the $N > 2$ -robot case. Application to ground robots may also be assessed with hardware experiments. The extension of the method to tackle the problem of multi-robot formation will be completed including the proof of stability and will be validated with experiments.

The results of this Thesis are examples of how the contacts can help the robots to adapt to the environment and effectively execute their tasks despite the uncertainties that might affect the knowledge of the environment itself. This is a key feature for collaborative robots of the future, that must be able to move in a non-perfectly characterized environment showing great flexibility. Only in this way, in fact, the robots may be able to improve the efficiency of work while effectively contributing to improving the working conditions for humans. With a special focus on logistic applications, this Thesis has tackled the automation of tasks related to depalletizing and object transportation, repetitive and potentially dangerous operations that are still

mostly executed by human workers. Unwrapping pallets, object picking, and object delivery causes strain for the workers and require plenty of labor availability. Their automation may improve the condition of work, solve possible labor shortage in the future, and improve work efficiency. Moreover, object delivery, especially in the era of e-commerce, not only imposes a high workload to the drivers, but it also suffers from being unpredictably affected by the traffic jam. Studying a delivery system that exploits autonomous aerial robots is beneficial also in this respect. Eventually, it is also expected to have a positive environmental impact, resulting in a reduction of emissions. Eventually, the recent outbreak of the COVID-19 pandemic is setting higher standards of automation to guarantee physical distancing in the workplaces, including the warehouses. This applies also to the freight sector, in which an autonomous robot-based delivery system would reduce the risk of exposure of the human workers by limiting person-to-person close interactions.

Bibliography

- [1] Klaus Schwab. *The Fourth Industrial Revolution*. Penguin Random House, 2017.
- [2] Heiner Lasi, Peter Fettke, Hans-Georg Kemper, Thomas Feld, and Michael Hoffmann. Industry 4.0. *Business & information systems engineering*, 6(4):239–242, 2014.
- [3] Saurabh Vaidya, Prashant Ambad, and Santosh Bhosle. Industry 4.0—a glimpse. *Procedia Manufacturing*, 20:233–238, 2018.
- [4] Andreja Rojko. Industry 4.0 concept: background and overview. *International Journal of Interactive Mobile Technologies (iJIM)*, 11(5):77–90, 2017.
- [5] František Zezulka, Petr Marcon, I Vesely, and Ondrej Sajdl. Industry 4.0—an introduction in the phenomenon. *IFAC-PapersOnLine*, 49(25):8–12, 2016.
- [6] Yang Lu. Industry 4.0: A survey on technologies, applications and open research issues. *Journal of industrial information integration*, 6:1–10, 2017.
- [7] Tanya M Anandan. The end of separation: Man and robot as collaborative coworkers on the factory floor. *Robotics Industry Insights*, 2013.
- [8] James E Colgate and Michael A Peshkin. Cobots, 1999. US Patent 5,952,796.
- [9] Shimon Y Nof. *Handbook of industrial robotics*. John Wiley & Sons, 1999.
- [10] Richard K Miller. *Industrial robot handbook*. Springer Science & Business Media, 1989.
- [11] Mohd Aiman Kamarul Bahrin, Mohd Fauzi Othman, NH Nor Azli, and Muhamad Farihin Talib. Industry 4.0: A review on industrial automation and robotic. *Jurnal Teknologi*, 78(6-13):137–143, 2016.
- [12] Bruno Siciliano and Oussama Khatib. *Springer handbook of robotics*. Springer, 2016.
- [13] Matthew T Mason. Compliance and force control for computer controlled manipulators. *IEEE Transactions on Systems, Man, and Cybernetics*, 11(6):418–432, 1981.
- [14] McNair Corey and Peart Monica. *Worldwide Retail and Ecommerce Sales: eMarketer’s Updated Forecast and New Mcommerce Estimates for 2016 - 2021*. eMaketer, 2018.
- [15] Wolfgang Echelmeyer, Alice Kirchheim, and Eckhard Wellbrock. Robotics-logistics: Challenges for automation of logistic processes. In *2008 IEEE International Conference on Automation and Logistics*, pages 2099–2103. IEEE, 2008.
- [16] Thomas Wagner, Carolin Hausner, Jurgen Elger, Ulrich Lowen, and Arndt Luder. Engineering processes for decentralized factory automation systems. In *Factory Automation*. IntechOpen, 2010.
- [17] Wolfgang Echelmeyer, Alice Kirchheim, Achim J Lilienthal, Hülya Akbiyik, and Marco Bonini. Performance indicators for robotics systems in logistics applications. In *IROS Workshop on Metrics and Methodologies for Autonomous Robot Teams in Logistics (MMARTLOG)*, page 55, 2011.
- [18] Tom Bonkenburg. Robotics in logistics a dpdhl perspective on implications and use cases for the logistics industry.

Bibliography

- [19] Nils Boysen, René de Koster, and Felix Weidinger. Warehousing in the e-commerce era: A survey. *European Journal of Operational Research*, 277(2):396–411, 2019.
- [20] Hossein Bonyan Khamseh, Farrokh Janabi-Sharifi, and Abdelkader Abdessameud. Aerial manipulation—a literature survey. *Robotics and Autonomous Systems*, 107:221–235, 2018.
- [21] Juan Jesús Roldán, Jaime del Cerro, David Garzón-Ramos, Pablo Garcia-Aunon, Mario Garzón, Jorge de León, and Antonio Barrientos. Robots in agriculture: State of art and practical experiences. *Service Robots*, 2018.
- [22] R. R. Murphy. A decade of rescue robots. In *2012 IEEE/RSJ International Conference on Intelligent Robots and Systems*, pages 5448–5449, 2012.
- [23] Malcolm Thomas Connolly et al. The use of multi rotor remotely operated aerial vehicles (roavs) as a method of close visually inspecting (cvi) live and difficult to access assets on offshore platforms. In *Abu Dhabi International Petroleum Exhibition and Conference*. Society of Petroleum Engineers, 2014.
- [24] Salua Hamaza, Ioannis Georgilas, and Thomas Richardson. Energy-tank based force control for 3d contour following. In *Annual Conference Towards Autonomous Robotic Systems*, pages 41–51. Springer, 2019.
- [25] P Ramon-Soria, AE Gomez-Tamm, FJ Garcia-Rubiales, BC Arrue, and A Ollero. Autonomous landing on pipes using soft gripper for inspection and maintenance in outdoor environments. 2019.
- [26] T Bartelds, Alex Capra, Salua Hamaza, Stefano Stramigioli, and Matteo Fumagalli. Compliant aerial manipulators: Toward a new generation of aerial robotic workers. *IEEE Robotics and Automation Letters*, 1(1):477–483, 2016.
- [27] Matko Orsag, Christopher Korpela, Paul Oh, Stjepan Bogdan, and Anibal Ollero. *Aerial Manipulation*. Springer, 2018.
- [28] Nathan Michael, Jonathan Fink, and Vijay Kumar. Cooperative manipulation and transportation with aerial robots. *Autonomous Robots*, 30(1):73–86, 2011.
- [29] Paul El Pounds, Daniel R Bersak, and Aaron M Dollar. Grasping from the air: Hovering capture and load stability. In *2011 IEEE international conference on robotics and automation*, pages 2491–2498. IEEE, 2011.
- [30] Nathan Michael, Soonkyum Kim, Jonathan Fink, and Vijay Kumar. Kinematics and statics of cooperative multi-robot aerial manipulation with cables. In *ASME 2009 International Design Engineering Technical Conferences and Computers and Information in Engineering Conference*, pages 83–91. American Society of Mechanical Engineers Digital Collection, 2009.
- [31] Ivan Maza, Konstantin Kondak, Markus Bernard, and Anibal Ollero. Multi-uav cooperation and control for load transportation and deployment. In *Selected papers from the 2nd International Symposium on UAVs, Reno, Nevada, USA June 8–10, 2009*, pages 417–449. Springer, 2009.
- [32] Konstantin Kondak, Markus Bernard, Fernando Caballero, Ivan Maza, and Anibal Ollero. Cooperative autonomous helicopters for load transportation and environment perception. In *Advances in Robotics Research*, pages 299–310. Springer, 2009.
- [33] Markus Bernard, Konstantin Kondak, Ivan Maza, and Anibal Ollero. Autonomous transportation and deployment with aerial robots for search and rescue missions. *Journal of Field Robotics*, 28(6):914–931, 2011.
- [34] Qimi Jiang and Vijay Kumar. The inverse kinematics of cooperative transport with multiple aerial robots. *IEEE Transactions on Robotics*, 29(1):136–145, 2012.
- [35] Rodney G Roberts, Todd Graham, and Jefferson M Trumpower. On the inverse kinematics and statics of cable-suspended robots. In *1997 IEEE International Conference on Systems, Man, and Cybernetics. Computational Cybernetics and Simulation*, volume 5, pages 4291–4296. IEEE, 1997.
- [36] Jinlong Piao, Xuejun Jin, Jinwoo Jung, Eunpyo Choi, Jong-Oh Park, and Chang-Sei Kim. Development of a high payload cable-driven parallel robot. In *2017 17th International Conference on Control, Automation and Systems (ICCAS)*, pages 423–425. IEEE, 2017.
- [37] Dario Fusato, Giorgio Guglieri, and Roberto Celi. Flight dynamics of an articulated rotor helicopter with an external slung load. *Journal of the American Helicopter Society*, 46(1):3–13, 2001.
- [38] Joshua K Stolaroff, Constantine Samaras, Emma R O’Neill, Alia Lubers, Alexandra S Mitchell, and Daniel Ceperley. Energy use and life cycle greenhouse gas emissions of drones for commercial package delivery. *Nature communications*, 9(1):1–13, 2018.
- [39] Carlos Miguel Ferreira and Sandro Serpa. Society 5.0 and social development. *Management and Organizational Studies (5)*, pages 26–31, 2018.

- [40] Mayumi Fukuyama. Society 5.0: Aiming for a new human-centered society. *Japan Spotlight*, 1:47–50, 2018.
- [41] Elisha Ondieki Makori. Blockchain applications and trends that promote information management. In *Emerging Trends and Impacts of the Internet of Things in Libraries*, pages 34–51. IGI Global, 2020.
- [42] Norbert Wiener. *The human use of human beings: Cybernetics and society*. Number 320. Da Capo Press, 1988.
- [43] Terrell Ward Bynum. Computer ethics: Its birth and its future. *Ethics and Information Technology*, 3(2):109–112, 2001.
- [44] Gianmarco Veruggio, Fiorella Operto, and George Bekey. Roboethics: Social and ethical implications. In *Springer handbook of robotics*, pages 2135–2160. Springer, 2016.
- [45] S. Wischniewski and A. Ajoudani. How can assistive robotics improve personal and work life? a million dollar question. *IEEE Robotics Automation Magazine*, 26(2):106–106, 2019.
- [46] Muhammad Iftikhar Hanif and Linta Iftikhar. Post covid-19 industrial revolution 5.0. the dawn of cobot, chipbot and curbot. *Pakistan Journal of Surgery and Medicine*, 1(2):122–126, 2020.
- [47] Zhanjing Zeng, Po-Ju Chen, and Alan A. Lew. From high-touch to high-tech: Covid-19 drives robotics adoption. *Tourism Geographies*, pages 1–11, 2020.
- [48] Luigi Villani and Joris De Schutter. Force control. In *Springer handbook of robotics*, pages 195–220. Springer, 2016.
- [49] Antonio Bicchi, Manuel Giuseppe Catalano, and Cosimo Della Santina. *Soft Robots*. Springer Berlin Heidelberg, Berlin, Heidelberg, 2020. In Press (<https://tinyurl.com/tbdw3g6>).
- [50] Cecilia Laschi, Jonathan Rossiter, Fumiya Iida, Matteo Cianchetti, and Laura Margheri. *Soft Robotics: Trends, Applications and Challenges*. Springer, 2016.
- [51] Panagiotis Polygerinos, Nikolaus Correll, Stephen A Morin, Bobak Mosadegh, Cagdas D Onal, Kirstin Petersen, Matteo Cianchetti, Michael T Tolley, and Robert F Shepherd. Soft robotics: Review of fluid-driven intrinsically soft devices; manufacturing, sensing, control, and applications in human-robot interaction. *Advanced Engineering Materials*, 19(12):1700016, 2017.
- [52] Sangbae Kim, Cecilia Laschi, and Barry Trimmer. Soft robotics: a bioinspired evolution in robotics. *Trends in biotechnology*, 31(5):287–294, 2013.
- [53] Puneet Kumar Singh and C Murali Krishna. Continuum arm robotic manipulator: A review. *Universal Journal of Mechanical Engineering*, 2(6):193–198, 2014.
- [54] Chiwon Lee, Myungjoon Kim, Yoon Jae Kim, Nhayoung Hong, Seungwan Ryu, H Jin Kim, and Sungwan Kim. Soft robot review. *International Journal of Control, Automation and Systems*, 15(1):3–15, 2017.
- [55] C. Fitzgerald. Developing baxter. In *2013 IEEE Conference on Technologies for Practical Robot Applications (TePRA)*, pages 1–6, 2013.
- [56] Erico Guizzo and Evan Ackerman. The rise of the robot worker. *IEEE Spectrum*, 49(10):34–41, 2012.
- [57] Karen Bodie, C Dario Bellicoso, and Marco Hutter. Anypulator: Design and control of a safe robotic arm. In *2016 IEEE/RSJ International Conference on Intelligent Robots and Systems (IROS)*, pages 1119–1125. IEEE, 2016.
- [58] Alin Albu-Schäffer and Antonio Bicchi. Actuators for soft robotics. In *Springer Handbook of Robotics*, pages 499–530. Springer, 2016.
- [59] Alessandro De Luca and Wayne J Book. Robots with flexible elements. In *Springer Handbook of Robotics*, pages 243–282. Springer, 2016.
- [60] Christian Ott. *Cartesian impedance control of redundant and flexible-joint robots*. Springer, 2008.
- [61] Oussama Khatib. A unified approach for motion and force control of robot manipulators: The operational space formulation. *IEEE Journal on Robotics and Automation*, 3(1):43–53, 1987.
- [62] Neville Hogan. Impedance Control: An Approach to Manipulation: Part I—Theory. *Journal of Dynamic Systems, Measurement, and Control*, 107(1):1–7, 03 1985.
- [63] Neville Hogan. Impedance Control: An Approach to Manipulation: Part II—Implementation. *Journal of Dynamic Systems, Measurement, and Control*, 107(1):8–16, 03 1985.
- [64] Neville Hogan. Impedance Control: An Approach to Manipulation: Part III—Applications. *Journal of Dynamic Systems, Measurement, and Control*, 107(1):17–24, 03 1985.

Bibliography

- [65] Alexander Dietrich, Christian Ott, and Alin Albu-Schäffer. Multi-objective compliance control of redundant manipulators: Hierarchy, control, and stability. In *2013 IEEE/RSJ International Conference on Intelligent Robots and Systems*, pages 3043–3050. IEEE, 2013.
- [66] Christian Ott, Alexander Dietrich, and Alin Albu-Schäffer. Prioritized multi-task compliance control of redundant manipulators. *Automatica*, 53:416–423, 2015.
- [67] Bruno Siciliano, Lorenzo Sciavicco, Luigi Villani, and Giuseppe Oriolo. *Robotics: modelling, planning and control*. Springer Science & Business Media, 2010.
- [68] Georg Kartnig, Bruno Grösel, and Nenad Zrnić. Past, state-of-the-art and future of intralogistics in relation to megatrends. *FME Transactions*, 40(4):193–200, 2012.
- [69] Augusto Urru, Marco Bonini, Timo Burbach, Elena Höng, Philipp Stein, and Wolfgang Echelmeyer. Autonomous unloading of heavy deformable goods: Market opportunities. In *2015 IEEE International Conference on Service Operations And Logistics, And Informatics (SOLI)*, pages 54–59. IEEE, 2015.
- [70] Jana Jost, Thomas Kirks, Preity Gupta, Dennis Lünsch, and Jonas Stenzel. Safe human-robot-interaction in highly flexible warehouses using augmented reality and heterogenous fleet management system. In *2018 IEEE International Conference on Intelligence and Safety for Robotics (ISR)*, pages 256–260. IEEE, 2018.
- [71] Edoardo Lamon, Mattia Leonori, Wansoo Kim, and Arash Ajoudani. Towards an intelligent collaborative robotic system for mixed case palletizing. In *2020 IEEE International Conference on Robotics and Automation (ICRA)*, pages 9128–9134. IEEE, 2020.
- [72] Pietro Balatti, Fabio Fusaro, Nicola Villa, Edoardo Lamon, and Arash Ajoudani. A collaborative robotic approach to autonomous pallet jack transportation and positioning. *IEEE Access*, 8:142191–142204, 2020.
- [73] Stephen Balakirsky, Thomas Kramer, and Frederick Proctor. Metrics for mixed pallet stacking. In *Proceedings of the 10th Performance Metrics for Intelligent Systems Workshop*, pages 54–61. ACM, 2010.
- [74] Rahaf Rahal, Firas Abi-Farraj, Paolo Robuffo Giordano, and Claudio Pacchierotti. Haptic shared-control methods for robotic cutting under nonholonomic constraints. In *2019 IEEE/RSJ International Conference on Intelligent Robots and Systems (IROS)*, pages 8151–8157. IEEE, 2019.
- [75] Seul Jung and Tien C Hsia. Adaptive force tracking impedance control of robot for cutting nonhomogeneous workpiece. In *Proceedings 1999 IEEE International Conference on Robotics and Automation (Cat. No. 99CH36288C)*, volume 3, pages 1800–1805. IEEE, 1999.
- [76] Robert J Anderson and Mark W Spong. Hybrid impedance control of robotic manipulators. *IEEE Journal on Robotics and Automation*, 4(5):549–556, 1988.
- [77] L Eusebi and Claudio Melchiorri. Force reflecting telemanipulators with time-delay: Stability analysis and control design. *IEEE Transactions on Robotics and Automation*, 14(4):635–640, 1998.
- [78] Berend Denkena and Thomas Lepper. Enabling an industrial robot for metal cutting operations. *Procedia CIRP*, 35:79–84, 2015.
- [79] Philip Long, Wisama Khalil, and Philippe Martinet. Modeling & control of a meat-cutting robotic cell. In *2013 16th International Conference on Advanced Robotics (ICAR)*, pages 1–6. IEEE, 2013.
- [80] P. Long, W. Khalil, and P. Martinet. Robotic cutting of soft materials using force control image moments. In *2014 13th International Conference on Control Automation Robotics Vision (ICARCV)*, pages 474–479, 2014.
- [81] Tommaso Pardi, Valerio Ortenzi, C Fairbairn, T Pipe, R Stolkin, et al. Maximally manipulable vision-based motion planning for robotic rough-cutting on arbitrarily shaped surfaces. *arXiv preprint arXiv:1909.05523*, 2019.
- [82] Narunas Vaskevicius, Christian A Mueller, Manuel Bonilla, Vinicio Tincani, Todor Stoyanov, Gualtiero Fantoni, Kaustubh Pathak, Achim Lilienthal, Antonio Bicchi, and Andreas Birk. Object recognition and localization for robust grasping with a dexterous gripper in the context of container unloading. In *2014 IEEE International Conference on Automation Science and Engineering (CASE)*, pages 1270–1277. IEEE, 2014.
- [83] Andreas Dömel, Simon Kriegel, Manuel Brucker, and Michael Suppa. Autonomous pick and place operations in industrial production. In *2015 12th International Conference on Ubiquitous Robots and Ambient Intelligence (URAI)*, pages 356–356. IEEE, 2015.
- [84] Melonee Wise, Michael Ferguson, Derek King, Eric Diehr, and David Dymesich. Fetch and freight: Standard platforms for service robot applications. In *Workshop on autonomous mobile service robots*, 2016.
- [85] C. G. Petersen and G. Aase. A comparison of picking, storage, and routing policies in manual order picking. *International Journal of Production Economics*, 92(1):11–19, 2004.

- [86] C Piazza, G Grioli, MG Catalano, and A Bicchi. A century of robotic hands. *Annual Review of Control, Robotics, and Autonomous Systems*, 2:1–32, 2019.
- [87] O. Madsen, S. Bøgh, C. Schou, R. S. Andersen, J. Skov Damgaard, M. R. Pedersen, and V. Krüger. Integration of mobile manipulators in an industrial production. *Industrial Robot: An International Journal*, 42(1):11–18, 2015.
- [88] A. Dömel, S. Kriegel, M. Kaßecker, M. Brucker, T. Bodenmüller, and M. Suppa. Toward fully autonomous mobile manipulation for industrial environments. *International Journal of Advanced Robotic Systems*, 14(4):1729881417718588, 2017.
- [89] Kim Wansoo, Marta Lorenzini, Balatti Pietro, Wu Yuqiang, and Arash Ajoudani. Towards ergonomic control of collaborative effort in multi-human mobile-robot teams. In *IEEE/RSJ International Conference on Intelligent Robots and Systems*, pages N–A, 2019.
- [90] Andrea Cherubini, Robin Passama, Benjamin Navarro, Mohamed Sorour, Abdellah Khelloufi, Osama Mazhar, Sonny Tarbouriech, Jihong Zhu, Olivier Tempier, André Crosnier, et al. A collaborative robot for the factory of the future: Bazar. *The International Journal of Advanced Manufacturing Technology*, 105(9):3643–3659, 2019.
- [91] Jordi Pages, Luca Marchionni, and Francesco Ferro. Tiago: the modular robot that adapts to different research needs. In *International workshop on robot modularity, IROS*, 2016.
- [92] Vinicio Tincani, Manuel G Catalano, Edoardo Farnioli, Manolo Garabini, Giorgio Grioli, Gualtiero Fantoni, and Antonio Bicchi. Velvet fingers: A dexterous gripper with active surfaces. In *2012 IEEE/RSJ International Conference on Intelligent Robots and Systems*, pages 1257–1263. IEEE, 2012.
- [93] Vinicio Tincani, Giorgio Grioli, Manuel G Catalano, Manolo Garabini, Simone Grechi, Gualtiero Fantoni, and Antonio Bicchi. Implementation and control of the velvet fingers: a dexterous gripper with active surfaces. In *2013 IEEE International Conference on Robotics and Automation*, pages 2744–2750. IEEE, 2013.
- [94] M. Hvilshøj, S. Bøgh, O. Skov Nielsen, and O. Madsen. Autonomous industrial mobile manipulation (AIMM): past, present and future. *Industrial Robot: An International Journal*, 39(2):120–135, 2012.
- [95] R. Krug, T. Stoyanov, V. Tincani, H. Andreasson, R. Mosberger, G. Fantoni, and A. J. Lilienthal. The next step in robot commissioning: Autonomous picking and palletizing. *IEEE Robotics and Automation Letters*, 1(1):546–553, 2016.
- [96] Hao Zhang, Pinxin Long, Dandan Zhou, Zhongfeng Qian, Zheng Wang, Weiwei Wan, Dinesh Manocha, Chonhyon Park, Tommy Hu, Chao Cao, et al. Dorapicker: An autonomous picking system for general objects. In *2016 IEEE International Conference on Automation Science and Engineering (CASE)*, pages 721–726. IEEE, 2016.
- [97] Riccardo Caccavale, Pierluigi Arpentì, Gianmarco Paduano, Fontanelli Andrea, Vincenzo Lippiello, Luigi Villani, and Bruno Siciliano. A flexible robotic depalletizing system for supermarket logistics.
- [98] G. Andrea Fontanelli, Gianmarco Paduano, Riccardo Caccavale, Pierluigi Arpentì, Vincenzo Lippiello, Luigi Villani, and Bruno Siciliano. A reconfigurable gripper for robotic autonomous depalletizing in supermarket logistics.
- [99] R. Krug, T. Stoyanov, V. Tincani, H. Andreasson, R. Mosberger, G. Fantoni, and A. J. Lilienthal. The next step in robot commissioning: Autonomous picking and palletizing. *IEEE Robotics and Automation Letters*, 1(1):546–553, 2016.
- [100] N. Correll, K. E. Bekris, D. Berenson, O. Brock, A. Causo, K. Hauser, K. Okada, A. Rodriguez, J. M. Romano, and P. R. Wurman. Analysis and observations from the first amazon picking challenge. *IEEE Transactions on Automation Science and Engineering*, 15(1):172–188, 2016.
- [101] J. Bohg, A. Morales, T. Asfour, and D. Kragic. Data-driven grasp synthesis—a survey. *T-Ro*, 30(2):289–309, 2013.
- [102] A Bicchi. On the closure properties of robotic grasping. *IJRR*, 14(4):319–334, 1995.
- [103] A. Sahbani, S. El-Khoury, and P. Bidaud. An overview of 3d object grasp synthesis algorithms. *Robotics and Autonomous Systems*, 60(3):326–336, 2012.
- [104] J. Redmon and A. Angelova. Real-time grasp detection using convolutional neural networks. In *ICRA*, pages 1316–1322. IEEE, 2015.
- [105] I. Lenz, Ho. Lee, and A. Saxena. Deep learning for detecting robotic grasps. *IJRR*, 34(4-5):705–724, 2015.

Bibliography

- [106] S. Kumra and C. Kanan. Robotic grasp detection using deep convolutional neural networks. In *IROS*, pages 769–776. IEEE, 2017.
- [107] Sergey Levine, Peter Pastor, Alex Krizhevsky, Julian Ibarz, and Deirdre Quillen. Learning hand-eye coordination for robotic grasping with deep learning and large-scale data collection. *The International Journal of Robotics Research*, 37(4-5):421–436, 2018.
- [108] J. Mahler, M. Matl, X. Liu, A. Li, D. Gealy, and K. Goldberg. Dex-net 3.0: Computing robust robot vacuum suction grasp targets in point clouds using a new analytic model and deep learning. *arXiv preprint arXiv:1709.06670*, 2017.
- [109] J. Mahler, J. Liang, S. Niyaz, M. Laskey, R. Doan, X. Liu, J. A. Ojea, and K. Goldberg. Dex-net 2.0: Deep learning to plan robust grasps with synthetic point clouds and analytic grasp metrics. *arXiv preprint arXiv:1703.09312*, 2017.
- [110] Arsalan Mousavian, Clemens Eppner, and Dieter Fox. 6-dof graspnet: Variational grasp generation for object manipulation. In *Proceedings of the IEEE International Conference on Computer Vision*, pages 2901–2910, 2019.
- [111] A. Depierre, E. Dellandréa, and L. Chen. Jacquard: A large scale dataset for robotic grasp detection. In *2018 IEEE/RSJ International Conference on Intelligent Robots and Systems (IROS)*, pages 3511–3516, 2018.
- [112] Douglas Morrison, Peter Corke, and Jurgen Leitner. Egad! an evolved grasping analysis dataset for diversity and reproducibility in robotic manipulation. *IEEE Robotics and Automation Letters*, 2020.
- [113] A. T. Miller and P. K. Allen. Graspit! a versatile simulator for robotic grasping. *IEEE Robotics Automation Magazine*, 11(4):110–122, 2004.
- [114] Corey Goldfeder, Matei Ciocarlie, Hao Dang, and Peter K Allen. The columbia grasp database. In *2009 IEEE international conference on robotics and automation*, pages 1710–1716. IEEE, 2009.
- [115] A. Rocchi and K. Hauser. A generic simulator for underactuated compliant hands. In *SIMPAR*, pages 37–42. IEEE, 2016.
- [116] C Della Santina, C Piazza, G. M. Gasparri, M. Bonilla, M. G. Catalano, G. Grioli, M. Garabini, and A. Bicchi. The quest for natural machine motion: An open platform to fast-prototyping articulated soft robots. *RAM*, 24(1):48–56, 2017.
- [117] Raphael Deimel and Oliver Brock. A novel type of compliant and underactuated robotic hand for dexterous grasping. *The International Journal of Robotics Research*, 35(1-3):161–185, 2016.
- [118] C. Della Santina, V. Arapi, G. Averta, F. Damiani, G. Fiore, A. Settimi, M. G. Catalano, D. Bacciu, A. Bicchi, and M. Bianchi. Learning from humans how to grasp: a data-driven architecture for autonomous grasping with anthropomorphic soft hands. *RA-L*, 4(2):1533–1540, 2019.
- [119] Mark R Cutkosky et al. On grasp choice, grasp models, and the design of hands for manufacturing tasks. *IEEE Transactions on robotics and automation*, 5(3):269–279, 1989.
- [120] Christopher Lee and Yangsheng Xu. Reduced-dimension representations of human performance data for human-to-robot skill transfer. In *Proceedings. 1998 IEEE/RSJ International Conference on Intelligent Robots and Systems. Innovations in Theory, Practice and Applications (Cat. No. 98CH36190)*, volume 3, pages 1956–1961. IEEE, 1998.
- [121] Markus Przybylski, Tamim Asfour, Rüdiger Dillmann, René Gilster, and Heiner Deubel. Human-inspired selection of grasp hypotheses for execution on a humanoid robot. In *2011 11th IEEE-RAS International Conference on Humanoid Robots*, pages 643–649. IEEE, 2011.
- [122] Maria Ralph and Medhat A Moussa. An integrated system for user-adaptive robotic grasping. *IEEE transactions on Robotics*, 26(4):698–709, 2010.
- [123] G. Lentini, G. Grioli, M. G. Catalano, and A. Bicchi. Robot programming without coding. In *2020 IEEE International Conference on Robotics and Automation (ICRA)*, pages 7576–7582, 2020.
- [124] Micha Hersch, Florent Guenter, Sylvain Calinon, and Aude Billard. Dynamical system modulation for robot learning via kinesthetic demonstrations. *IEEE Transactions on Robotics*, 24(6):1463–1467, 2008.
- [125] R. Balasubramanian, L. Xu, P. D. Brook, J. R. Smith, and Y. Matsuoka. Physical human interactive guidance: Identifying grasping principles from human-planned grasps. *IEEE Transactions on Robotics*, 28(4):899–910, 2012.
- [126] A. Herzog, P. Pastor, M. Kalakrishnan, L. Righetti, T. Asfour, and S. Schaal. Template-based learning of grasp selection. In *IEEE ICRA*, pages 2379–2384, May 2012.

- [127] R. Detry, C. H. Ek, M. Madry, and D. Kragic. Learning a dictionary of prototypical grasp-predicting parts from grasping experience. In *IEEE ICRA*, pages 601–608, May 2013.
- [128] A. Pas and R. Platt. Localizing handle-like grasp affordances in 3d point clouds. In *Experimental Robotics*. Springer, 2016.
- [129] G. Vezzani, U. Pattacini, and L. Natale. A grasping approach based on superquadric models. In *ICRA*, pages 1579–1586. IEEE, 2017.
- [130] Ales Jaklic, Ales Leonardis, and Franc Solina. *Segmentation and recovery of superquadrics*, volume 20. Springer Science & Business Media, 2013.
- [131] K. Huebner, S. Ruthotto, and D. Kragic. Minimum volume bounding box decomposition for shape approximation in robot grasping. In *ICRA*, pages 1628–1633. IEEE, 2008.
- [132] M. Bonilla, D. Resasco, M. Gabiccini, and A. Bicchi. Grasp planning with soft hands using bounding box object decomposition. In *IROS*, pages 518–523. IEEE, 2015.
- [133] Sebastian Geidenstam, Kai Huebner, Daniel Banksell, and Danica Kragic. Learning of 2d grasping strategies from box-based 3d object approximations. In *Robotics: Science and Systems*, volume 2008, 2009.
- [134] Markus Przybylski, Tamim Asfour, and Rüdiger Dillmann. Planning grasps for robotic hands using a novel object representation based on the medial axis transform. In *2011 IEEE/RSJ International Conference on Intelligent Robots and Systems*, pages 1781–1788. IEEE, 2011.
- [135] Andrew T Miller, Steffen Knoop, Henrik I Christensen, and Peter K Allen. Automatic grasp planning using shape primitives. In *2003 IEEE International Conference on Robotics and Automation (Cat. No. 03CH37422)*, volume 2, pages 1824–1829. IEEE, 2003.
- [136] Corey Goldfeder, Peter K Allen, Claire Lackner, and Raphael Pelossof. Grasp planning via decomposition trees. In *Proceedings 2007 IEEE International Conference on Robotics and Automation*, pages 4679–4684. IEEE, 2007.
- [137] Robert Krug, Todor Stoyanov, and Achim Lilienthal. Grasp envelopes for constraint-based robot motion planning and control. In *2015 Robotics: Science and Systems Conference (RSS, Rome, Italy, July 13-17, 2015)*, 2015.
- [138] Bryan Penin, Paolo Robuffo Giordano, and François Chaumette. Vision-based reactive planning for aggressive target tracking while avoiding collisions and occlusions. *IEEE Robotics and Automation Letters*, 3(4):3725–3732, 2018.
- [139] Antonio Bicchi, J Kenneth Salisbury, and Paolo Dario. Augmentation of grasp robustness using intrinsic tactile sensing. In *1989 IEEE International Conference on Robotics and Automation*, pages 302–303. IEEE Computer Society, 1989.
- [140] Johan Tegin and Jan Wikander. Tactile sensing in intelligent robotic manipulation—a review. *Industrial Robot: An International Journal*, 2005.
- [141] Javier Felip and Antonio Morales. Robust sensor-based grasp primitive for a three-finger robot hand. In *2009 IEEE/RSJ International Conference on Intelligent Robots and Systems*, pages 1811–1816. IEEE, 2009.
- [142] Kaijen Hsiao, Paul Nangeroni, Manfred Huber, Ashutosh Saxena, and Andrew Y Ng. Reactive grasping using optical proximity sensors. In *2009 IEEE International Conference on Robotics and Automation*, pages 2098–2105. IEEE, 2009.
- [143] Joshua R Smith, Eric Garcia, Ryan Wistort, and Ganesh Krishnamoorthy. Electric field imaging pretouch for robotic graspers. In *2007 IEEE/RSJ International Conference on Intelligent Robots and Systems*, pages 676–683. IEEE, 2007.
- [144] Ryan Wistort and Joshua R Smith. Electric field servoing for robotic manipulation. In *2008 IEEE/RSJ International Conference on Intelligent Robots and Systems*, pages 494–499. IEEE, 2008.
- [145] Cristian Vergara, Santiago Iregui, Joris De Schutter, and Erwin Aertbelien. Generating reactive approach motions towards allowable manifolds using generalized trajectories from demonstrations. In *2020 IEEE/RSJ International Conference on Intelligent Robots and Systems (IROS)*, Accepted.
- [146] C. Gabellieri, A. Palleschi, A. Mannucci, M. Pierallini, E. Stefanini, M. G. Catalano, D. Caporale, A. Settini, T. Stoyanov, M. Magnusson, M. Garabini, and L. Pallottino. Towards an autonomous unwrapping system for intralogistics. *IEEE Robotics and Automation Letters*, 4(4):4603–4610, 2019.
- [147] C Gabellieri, A. Palleschi, M.G. Catalano, M. Garabini, and L. Pallottino. Flexible automated depalletizing: an unwrapping robot to remove plastic from palletized goods. In *I-RIM 3D Conference, Submitted*, 2020.

Bibliography

- [148] G. Garibotto, S. Masciangelo, M. Ilic, and P. Bassino. Service robotics in logistic automation: Robolift: vision based autonomous navigation of a conventional fork-lift for pallet handling. In *Advanced Robotics, 1997. ICRA'97. Proceedings., 8th International Conference on*, pages 781–786. IEEE, 1997.
- [149] M. R. Walter, S. Karaman, E. Frazzoli, and S. Teller. Closed-loop pallet manipulation in unstructured environments. In *Intelligent Robots and Systems (IROS), 2010 IEEE/RSJ International Conference on*, pages 5119–5126. IEEE, 2010.
- [150] R. Varga and S. Nedeveschi. Robust pallet detection for automated logistics operations. In *VISIGRAPP (4: VISAPP)*, pages 470–477, 2016.
- [151] G. Baechler, I. Dokmanic, L. Baboulaz, and M. Vetterli. Accurate recovery of a specularity from a few samples of the reflectance function. In *2016 IEEE International Conference on Acoustics, Speech and Signal Processing (ICASSP)*, pages 1596–1600, March 2016.
- [152] Miika Aittala, Tim Weyrich, and Jaakko Lehtinen. Practical svbrdf capture in the frequency domain. *ACM Trans. Graph.*, 32(4):110:1–110:12, July 2013.
- [153] Girum Demisse, Razvan Mihalyi, Billy Okal, Dev Poudel, Johannes Schauer, and Andreas Nüchter. Mixed palletizing and task completion for virtual warehouses. In *Virtual Manufacturing and Automation Competition (VMAC) Workshop at the Int. Conference of Robotics and Automation (ICRA)*, volume 16, 2012.
- [154] Martin Schuster, Richard Bormann, Daniela Steidl, Saul Reynolds-Haertle, and Mike Stilman. Stable stacking for the distributor’s pallet packing problem. In *2010 IEEE/RSJ International Conference on Intelligent Robots and Systems*, pages 3646–3651. IEEE, 2010.
- [155] Aleksey Ivanovich Soldatov, AA Soldatov, PV Sorokin, EL Loginov, MA Kostina, Olesya Anatolievna Kozhemyak, and SI Bortalevich. System for automatic sorting of pallets. In *2016 International Siberian Conference on Control and Communications (SIBCON)*, pages 1–4. IEEE, 2016.
- [156] S. Haddadin, A. De Luca, and A. Albu-Schäffer. Robot collisions: A survey on detection, isolation, and identification. *IEEE Transactions on Robotics*, 33(6):1292–1312, 2017.
- [157] A. Bicchi, J. K. Salisbury, D. L., and Brock. Contact sensing from force measurements. *The International Journal of Robotics Research*, 12(3):249–262, 1993.
- [158] Manolo Garabini, Danilo Caporale, Vinicio Tincani, Alessandro Palleschi, Chiara Gabellieri, Marco Gugliotta, Alessandro Settini, Manuel G Catalano, Giorgio Grioli, and Lucia Pallottino. Wrapp-up: a dual-arm robot for intralogistics. *IEEE Robotics & Automation Magazine*, 2020.
- [159] A. Palleschi, M. Gugliotta, C. Gabellieri, D.C. Hoang, T. Stoyanov, M. Garabini, and L. Pallottino. Fully autonomous picking with a dual-arm platform for intralogistics. In *I-RIM 3D Conference, Submitted*, 2020.
- [160] J. Rudd. *A Practical Guide to Logistics: An Introduction to Transport, Warehousing, Trade and Distribution*. Kogan Page Publishers, 2019.
- [161] Manuel G Catalano, Giorgio Grioli, Edoardo Farnioli, Alessandro Serio, Cristina Piazza, and Antonio Bicchi. Adaptive synergies for the design and control of the pisa/iit soft hand. *The International Journal of Robotics Research*, 33(5):768–782, 2014.
- [162] Fabrizio Flacco and Alessandro De Luca. Unilateral constraints in the reverse priority redundancy resolution method. In *2015 IEEE/RSJ International Conference on Intelligent Robots and Systems (IROS)*, pages 2564–2571. IEEE, 2015.
- [163] Emir Mobedi, Nicola Villa, Wansoo Kim, and Arash Ajoudani. An adaptive control approach to robotic assembly with uncertainties in vision and dynamics. In *2020 29th IEEE International Conference on Robot and Human Interactive Communication (RO-MAN)*, pages 144–150. IEEE.
- [164] Chiara Gabellieri, Franco Angelini, Visar Arapi, Alessandro Palleschi, Manuel G Catalano, Giorgio Grioli, Lucia Pallottino, Antonio Bicchi, Matteo Bianchi, and Manolo Garabini. Grasp it like a pro: Grasp of unknown objects with robotic hands based on skilled human expertise. *IEEE Robotics and Automation Letters*, 5(2):2808–2815, 2020.
- [165] M. Bianchi, G. Averta, E. Battaglia, C.s Rosales, M. Bonilla, A. Tondo, M. Poggiani, G. Santaera, S. Ciotti, and M. G. et al. Catalano. Touch-based grasp primitives for soft hands: Applications to human-to-robot handover tasks and beyond. In *2018 ICRA*, pages 7794–7801. IEEE.
- [166] Ravi Balasubramanian, Ling Xu, Peter D Brook, Joshua R Smith, and Yoky Matsuoka. Human-guided grasp measures improve grasp robustness on physical robot. In *2010 IEEE International Conference on Robotics and Automation*, pages 2294–2301. IEEE, 2010.

- [167] B. Calli, A. Walsman, A. Singh, S. Srinivasa, P. Abbeel, and A. M. Dollar. Benchmarking in manipulation research: Using the yale-cmu-berkeley object and model set. *RAM*, 22(3):36–52, 2015.
- [168] H. Dang and P. K. Allen. Semantic grasping: Planning robotic grasps functionally suitable for an object manipulation task. In *2012 IEEE/RSJ International Conference on Intelligent Robots and Systems*, pages 1311–1317, 2012.
- [169] Renaud Detry, Jeremie Papon, and Larry Matthies. Task-oriented grasping with semantic and geometric scene understanding. In *2017 IEEE/RSJ International Conference on Intelligent Robots and Systems (IROS)*, pages 3266–3273. IEEE, 2017.
- [170] Rajal G Cohen and David A Rosenbaum. Where grasps are made reveals how grasps are planned: generation and recall of motor plans. *Experimental Brain Research*, 157(4):486–495, 2004.
- [171] Kai Huebner and Danica Kragic. Selection of robot pre-grasps using box-based shape approximation. In *2008 IEEE/RSJ International Conference on Intelligent Robots and Systems*, pages 1765–1770. IEEE, 2008.
- [172] Fabio Ruggiero, Vincenzo Lippiello, and Anibal Ollero. Aerial manipulation: A literature review. *IEEE Robotics and Automation Letters*, 3(3):1957–1964, 2018.
- [173] AE Jimenez-Cano, J Braga, Guillermo Heredia, and Anibal Ollero. Aerial manipulator for structure inspection by contact from the underside. In *2015 IEEE/RSJ international conference on intelligent robots and systems (IROS)*, pages 1879–1884. IEEE, 2015.
- [174] Anibal Ollero, Guillermo Heredia, Antonio Franchi, Gianluca Antonelli, Konstantin Kondak, Alberto Sanfeliu, Antidio Viguria, J Ramiro Martinez-de Dios, Francesco Pierri, Juan Cortés, et al. The aeroarms project: Aerial robots with advanced manipulation capabilities for inspection and maintenance. *IEEE Robotics & Automation Magazine*, 25(4):12–23, 2018.
- [175] Alejandro Suarez, Alvaro Caballero, Ambar Garofano, Pedro J Sanchez-Cuevas, Guillermo Heredia, and Anibal Ollero. Aerial manipulator with rolling base for inspection of pipe arrays. *IEEE Access*, 8:162516–162532, 2020.
- [176] Ammar Mirjan, Federico Augugliaro, Raffaello D’Andrea, Fabio Gramazio, and Matthias Kohler. Building a bridge with flying robots. In *Robotic Fabrication in Architecture, Art and Design 2016*, pages 34–47. Springer, 2016.
- [177] Jan Willmann, Federico Augugliaro, Thomas Cadalbert, Raffaello D’Andrea, Fabio Gramazio, and Matthias Kohler. Aerial robotic construction towards a new field of architectural research. *International journal of architectural computing*, 10(3):439–459, 2012.
- [178] Matteo Fumagalli, Roberto Naldi, Alessandro Macchelli, Raffaella Carloni, Stefano Stramigioli, and Lorenzo Marconi. Modeling and control of a flying robot for contact inspection. In *2012 IEEE/RSJ International Conference on Intelligent Robots and Systems*, pages 3532–3537. IEEE, 2012.
- [179] AE Jimenez-Cano, Jesús Martin, Guillermo Heredia, Anibal Ollero, and R Cano. Control of an aerial robot with multi-link arm for assembly tasks. In *2013 IEEE International Conference on Robotics and Automation*, pages 4916–4921. IEEE, 2013.
- [180] Konstantin Kondak, Anibal Ollero, Ivan Maza, Kai Krieger, Alin Albu-Schaeffer, Marc Schwarzbach, and Maximilian Laiacker. Unmanned aerial systems physically interacting with the environment: Load transportation deployment and aerial manipulation. *Handbook of Unmanned Aerial Vehicles*, pages 2755–2785, 2015.
- [181] Patricio J Cruz and Rafael Fierro. Cable-suspended load lifting by a quadrotor uav: hybrid model, trajectory generation, and control. *Autonomous Robots*, 41(8):1629–1643, 2017.
- [182] Marco Tognon and Antonio Franchi. Dynamics, control, and estimation for aerial robots tethered by cables or bars. *IEEE Transactions on Robotics*, 33(4):834–845, 2017.
- [183] Konstantin Kondak, Felix Huber, Marc Schwarzbach, Maximilian Laiacker, Dominik Sommer, Manuel Bejar, and Anibal Ollero. Aerial manipulation robot composed of an autonomous helicopter and a 7 degrees of freedom industrial manipulator. In *2014 IEEE international conference on robotics and automation (ICRA)*, pages 2107–2112. IEEE, 2014.
- [184] Yuri S Sarkisov, Min Jun Kim, Davide Bicego, Dzmitry Tsetserukou, Christian Ott, Antonio Franchi, and Konstantin Kondak. Development of sam: Cable-suspended aerial manipulator. In *2019 International Conference on Robotics and Automation (ICRA)*, pages 5323–5329. IEEE, 2019.
- [185] Guillermo Heredia, AE Jimenez-Cano, I Sanchez, Domingo Llorente, V Vega, J Braga, JA Acosta, and Anibal Ollero. Control of a multirotor outdoor aerial manipulator. In *2014 IEEE/RSJ International Conference on Intelligent Robots and Systems*, pages 3417–3422. IEEE, 2014.

Bibliography

- [186] Suseong Kim, Hoseong Seo, and H Jin Kim. Operating an unknown drawer using an aerial manipulator. In *2015 IEEE International Conference on Robotics and Automation (ICRA)*, pages 5503–5508. IEEE, 2015.
- [187] R Cano, C Pérez, F Pruano, A Ollero, and G Heredia. Mechanical design of a 6-dof aerial manipulator for assembling bar structures using uavs. In *2nd RED-UAS 2013 workshop on research, education and development of unmanned aerial systems*, volume 218, 2013.
- [188] Alejandro Suarez, Guillermo Heredia, and Anibal Ollero. Lightweight compliant arm for aerial manipulation. In *2015 IEEE/RSJ International Conference on Intelligent Robots and Systems (IROS)*, pages 1627–1632. IEEE, 2015.
- [189] Todd W Danko, Kenneth P Chaney, and Paul Y Oh. A parallel manipulator for mobile manipulating uavs. In *2015 IEEE international conference on technologies for practical robot applications (TePRA)*, pages 1–6. IEEE, 2015.
- [190] Alejandro Suarez, Fran Real, Víctor M Vega, Guillermo Heredia, Angel Rodriguez-Castaño, and Anibal Ollero. Compliant bimanual aerial manipulation: Standard and long reach configurations. *IEEE Access*, 8:88844–88865, 2020.
- [191] C. Gabellieri, Y. Sarkisov, A. Coelho, L. Pallottino, K. Kondak, and M.J. Kim. Compliance control of a cable-suspended aerial manipulator using hierarchical control framework. In *IEEE/RSJ International Conference on Intelligent Robots and Systems (Accepted)*, 2020.
- [192] Markus Ryll, Giuseppe Muscio, Francesco Pierri, Elisabetta Cataldi, Gianluca Antonelli, Fabrizio Caccavale, and Antonio Franchi. 6d physical interaction with a fully actuated aerial robot. In *2017 IEEE International Conference on Robotics and Automation (ICRA)*, pages 5190–5195. IEEE, 2017.
- [193] Daniel Mellinger, Michael Shomin, Nathan Michael, and Vijay Kumar. Cooperative grasping and transport using multiple quadrotors. In *Distributed autonomous robotic systems*, pages 545–558. Springer, 2013.
- [194] Abdullah Mohiuddin, Taha Tarek, Yahya Zweiri, and Dongming Gan. A survey of single and multi-uav aerial manipulation. *Unmanned Systems*, 8(02):119–147, 2020.
- [195] Nicolas Staub, Mostafa Mohammadi, Davide Bicego, Quentin Delamare, Hyunsoo Yang, Domenico Prattichizzo, Paolo Robuffo Giordano, Dongjun Lee, and Antonio Franchi. The tele-magmas: An aerial-ground comanipulator system. *IEEE Robotics & Automation Magazine*, 25(4):66–75, 2018.
- [196] Nicola Lissandrini, Christos K Verginis, Pedro Roque, Angelo Cenedese, and Dimos V Dimarogonas. Decentralized nonlinear mpc for robust cooperative manipulation by heterogeneous aerial-ground robots. In *submitted to the IEEE/RSJ International Conference on Intelligent Robots and Systems (IROS)*, 2020.
- [197] Hai-Nguyen Nguyen, Sangyul Park, and Dongjun Lee. Aerial tool operation system using quadrotors as rotating thrust generators. In *2015 IEEE/RSJ International Conference on Intelligent Robots and Systems (IROS)*, pages 1285–1291. IEEE, 2015.
- [198] Robin Ritz and Raffaello D’Andrea. Carrying a flexible payload with multiple flying vehicles. In *2013 IEEE/RSJ International Conference on Intelligent Robots and Systems*, pages 3465–3471. IEEE, 2013.
- [199] Fabrizio Caccavale, Gerardo Giglio, Giuseppe Muscio, and Francesco Pierri. Cooperative impedance control for multiple uavs with a robotic arm. In *2015 IEEE/RSJ International Conference on Intelligent Robots and Systems (IROS)*, pages 2366–2371. IEEE, 2015.
- [200] Koushil Sreenath and Vijay Kumar. Dynamics, control and planning for cooperative manipulation of payloads suspended by cables from multiple quadrotor robots. *m*, 1(r2):r3, 2013.
- [201] Montserrat Manubens, Didier Devaurs, Lluís Ros, and Juan Cortés. Motion planning for 6-d manipulation with aerial towed-cable systems. 2013.
- [202] Carlo Masone, Heinrich H Bühlhoff, and Paolo Stegagno. Cooperative transportation of a payload using quadrotors: A reconfigurable cable-driven parallel robot. In *2016 IEEE/RSJ International Conference on Intelligent Robots and Systems (IROS)*, pages 1623–1630. IEEE, 2016.
- [203] D. Sanalitra, H. J. Savino, M. Tognon, J. Cortés, and A. Franchi. Full-pose manipulation control of a cable-suspended load with multiple uavs under uncertainties. *IEEE Robotics and Automation Letters*, 5(2):2185–2191, 2020.
- [204] Pedro O Pereira and Dimos V Dimarogonas. Pose stabilization of a bar tethered to two aerial vehicles. *Automatica*, 112:108695, 2020.
- [205] Abdullah Mohiuddin, Randa Almadhoun, Yahya Zweiri, Tarek Taha, and Dongming Gan. Energy distribution in dual-uav collaborative transportation through load sharing. *Journal of Mechanisms and Robotics*, pages JMR–19, 2020.

- [206] Vojtech Spurny, Matej Petrlik, Vojtech Vonasek, and Martin Saska. Cooperative transport of large objects by a pair of unmanned aerial systems using sampling-based motion planning. In *2019 24th IEEE International Conference on Emerging Technologies and Factory Automation (ETFA)*, pages 955–962. IEEE, 2019.
- [207] Jonathan Fink, Nathan Michael, Soonkyum Kim, and Vijay Kumar. Planning and control for cooperative manipulation and transportation with aerial robots. *The International Journal of Robotics Research*, 30(3):324–334, 2011.
- [208] Suseong Kim, Hoseong Seo, Jongho Shin, and H Jin Kim. Cooperative aerial manipulation using multirotors with multi-dof robotic arms. *IEEE/ASME Transactions on Mechatronics*, 23(2):702–713, 2018.
- [209] Hyeonbeom Lee, Hyoin Kim, and H Jin Kim. Path planning and control of multiple aerial manipulators for a cooperative transportation. In *2015 IEEE/RSJ International Conference on Intelligent Robots and Systems (IROS)*, pages 2386–2391. IEEE, 2015.
- [210] Pierre-P Grassé. La reconstruction du nid et les coordinations interindividuelles chez *Bellicositermes natalensis* et *Cubitermes* sp. la théorie de la stigmergie: Essai d’interprétation du comportement des termites constructeurs. *Insectes sociaux*, 6(1):41–80, 1959.
- [211] C Ronald Kube and Eric Bonabeau. Cooperative transport by ants and robots. *Robotics and autonomous systems*, 30(1-2):85–101, 2000.
- [212] S. Berman, Q. Lindsey, M. S. Sakar, V. Kumar, and S. C. Pratt. Experimental study and modeling of group retrieval in ants as an approach to collective transport in swarm robotic systems. *Proceedings of the IEEE*, 99(9):1470–1481, 2011.
- [213] Michael Rubenstein, Adrian Cabrera, Justin Werfel, Golnaz Habibi, James McLurkin, and Radhika Nagpal. Collective transport of complex objects by simple robots: theory and experiments. In *Proceedings of the 2013 international conference on Autonomous agents and multi-agent systems*, pages 47–54, 2013.
- [214] Christos K Verginis, Alexandros Nikou, and Dimos V Dimarogonas. Communication-based decentralized cooperative object transportation using nonlinear model predictive control. In *2018 European control conference (ECC)*, pages 733–738. IEEE, 2018.
- [215] Dominik Sieber and Sandra Hirche. Human-guided multirobot cooperative manipulation. *IEEE Transactions on Control Systems Technology*, 27(4):1492–1509, 2018.
- [216] Anastasios Tsiamis, Christos K Verginis, Charalampos P Bechlioulis, and Kostas J Kyriakopoulos. Cooperative manipulation exploiting only implicit communication. In *2015 IEEE/RSJ International Conference on Intelligent Robots and Systems (IROS)*, pages 864–869. IEEE, 2015.
- [217] Zijian Wang and Mac Schwager. Force-amplifying n-robot transport system (force-ants) for cooperative planar manipulation without communication. *The International Journal of Robotics Research*, 35(13):1564–1586, 2016.
- [218] Michael Gassner, Titus Cieslewski, and Davide Scaramuzza. Dynamic collaboration without communication: Vision-based cable-suspended load transport with two quadrotors. In *2017 IEEE International Conference on Robotics and Automation (ICRA)*, pages 5196–5202. IEEE, 2017.
- [219] Andrea Tagliabue, Mina Kamel, Sebastian Verling, Roland Siegwart, and Juan Nieto. Collaborative transportation using mavs via passive force control. In *2017 IEEE International Conference on Robotics and Automation (ICRA)*, pages 5766–5773. IEEE, 2017.
- [220] Andrea Tagliabue, Mina Kamel, Roland Siegwart, and Juan Nieto. Robust collaborative object transportation using multiple mavs. *The International Journal of Robotics Research*, 38(9):1020–1044, 2019.
- [221] Sandesh Thapa, He Bai, and JA Acosta. Cooperative aerial load transport with force control. *IFAC-PapersOnLine*, 51(12):38–43, 2018.
- [222] Jossué Cariño Escobar, Rogelio Lozano, and Moisés Bonilla Estrada. Two pvtols cooperative slung-load transport control based on passivity. *Advanced Control for Applications: Engineering and Industrial Systems*, 2(1):e22, 2020.
- [223] Marco Tognon, Chiara Gabellieri, Lucia Pallottino, and Antonio Franchi. Aerial co-manipulation with cables: The role of internal force for equilibria, stability, and passivity. *IEEE Robotics and Automation Letters*, 3(3):2577–2583, 2018.
- [224] Chiara Gabellieri, Marco Tognon, Lucia Pallottino, and Antonio Franchi. A study on force-based collaboration in flying swarms. In *International Conference on Swarm Intelligence*, pages 3–15. Springer, 2018.

Bibliography

- [225] Chiara Gabellieri, Marco Tognon, Dario Sanalidro, Lucia Pallottino, and Antonio Franchi. A study on force-based collaboration in swarms. *Swarm Intelligence*, 14(1):57–82, 2020.
- [226] Julian Erskine, Abdelhamid Chriette, and Stéphane Caro. Wrench analysis of cable-suspended parallel robots actuated by quadrotor unmanned aerial vehicles. *Journal of Mechanisms and Robotics*, 11(2), 2019.
- [227] Markus Ryll, Davide Bicego, and Antonio Franchi. Modeling and control of fast-hex: A fully-actuated by synchronized-tilting hexarotor. In *2016 IEEE/RSJ International Conference on Intelligent Robots and Systems (IROS)*, pages 1689–1694. IEEE, 2016.
- [228] Ramy Rashad, Jelmer Goerres, Ronald G Aarts, Johan BC Engelen, and Stefano Stramigioli. Fully actuated multirotor uavs: A literature review. *IEEE Robotics & Automation Magazine*, 2020.
- [229] M. Ryll, H. H. Bühlhoff, and P. Robuffo Giordano. Modeling and control of a quadrotor uav with tilting propellers. In *2012 IEEE International Conference on Robotics and Automation*, pages 4606–4613, 2012.
- [230] G. Jiang, R. M. Voyles, and J. J. Choi. Precision fully-actuated uav for visual and physical inspection of structures for nuclear decommissioning and search and rescue. In *2018 IEEE International Symposium on Safety, Security, and Rescue Robotics (SSRR)*, pages 1–7, 2018.
- [231] Sangyul Park, Jongbeom Her, Juhyeok Kim, and Dongjun Lee. Design, modeling and control of omni-directional aerial robot. In *2016 IEEE/RSJ International Conference on Intelligent Robots and Systems (IROS)*, pages 1570–1575. IEEE, 2016.
- [232] M. Ryll, H. H. Bühlhoff, and P. Robuffo Giordano. A novel overactuated quadrotor unmanned aerial vehicle: Modeling, control, and experimental validation. *IEEE Transactions on Control Systems Technology*, 23(2):540–556, 2015.
- [233] Taeyoung Lee. Geometric control of quadrotor uavs transporting a cable-suspended rigid body. *IEEE Transactions on Control Systems Technology*, 26(1):255–264, 2017.
- [234] G. Antonelli, E. Cataldi, P. Robuffo Giordano, S. Chiaverini, and A. Franchi. Experimental validation of a new adaptive control scheme for quadrotors mavs. In *2013 IEEE/RSJ International Conference on Intelligent Robots and Systems*, pages 2439–2444, 2013.
- [235] Pratik Prajapati, Sagar Parekh, and Vineet Vashista. Collaborative transportation of cable-suspended payload using two quadcopters with human in the loop. In *2019 28th IEEE International Conference on Robot and Human Interactive Communication (RO-MAN)*, pages 1–6. IEEE, 2019.
- [236] F. Pierri, M. Nigro, G. Muscio, and F. Caccavale. Cooperative manipulation of an unknown object via omnidirectional unmanned aerial vehicles. *Journal of Intelligent & Robotic Systems*, pages 1–15, 2020.
- [237] Abdulghafoor Salehzadeh Aghdam, Mohammad B Menhaj, Farshad Barazandeh, and Farzane Abdollahi. Cooperative load transport with movable load center of mass using multiple quadrotor uavs. In *2016 4th International Conference on Control, Instrumentation, and Automation (ICCIA)*, pages 23–27. IEEE, 2016.
- [238] Reiner Horst, Panos M Pardalos, and Nguyen Van Thoai. *Introduction to global optimization*. Springer Science & Business Media, 2000.
- [239] Kenneth Eriksson, Don Estep, and Claes Johnson. Applied mathematics body and soul: Vol i-iii. *Springer-Verlag Publishing*, 1:3, 2003.
- [240] Hassan K Khalil and Jessy W Grizzle. *Nonlinear systems*, volume 3. Prentice hall Upper Saddle River, NJ, 2002.
- [241] Alessandro De Luca and Raffaella Mattone. Sensorless robot collision detection and hybrid force/motion control. In *Proceedings of the 2005 IEEE international conference on robotics and automation*, pages 999–1004. IEEE, 2005.
- [242] Kwang-Kyo Oh, Myoung-Chul Park, and Hyo-Sung Ahn. A survey of multi-agent formation control. *Automatica*, 53:424–440, 2015.
- [243] Yuanchang Liu and Richard Bucknall. A survey of formation control and motion planning of multiple unmanned vehicles. *Robotica*, 36(7):1019–1047, 2018.
- [244] F. E. Schneider and D. Wildermuth. A potential field based approach to multi robot formation navigation. In *IEEE International Conference on Robotics, Intelligent Systems and Signal Processing, 2003. Proceedings. 2003*, volume 1, pages 680–685 vol.1, 2003.
- [245] Paul KC Wang. Navigation strategies for multiple autonomous mobile robots moving in formation. *Journal of Robotic Systems*, 8(2):177–195, 1991.

- [246] Luca Consolini, Fabio Morbidi, Domenico Prattichizzo, and Mario Tosques. Leader–follower formation control of nonholonomic mobile robots with input constraints. *Automatica*, 44(5):1343–1349, 2008.
- [247] Jaydev P Desai, Jim Ostrowski, and Vijay Kumar. Controlling formations of multiple mobile robots. In *Proceedings. 1998 IEEE International Conference on Robotics and Automation (Cat. No. 98CH36146)*, volume 4, pages 2864–2869. IEEE, 1998.
- [248] Kar-Han Tan and M Anthony Lewis. Virtual structures for high-precision cooperative mobile robotic control. In *Proceedings of IEEE/RSJ International Conference on Intelligent Robots and Systems. IROS'96*, volume 1, pages 132–139. IEEE, 1996.
- [249] Tucker Balch and Ronald C Arkin. Behavior-based formation control for multirobot teams. *IEEE transactions on robotics and automation*, 14(6):926–939, 1998.
- [250] Wei Ren and Nathan Sorensen. Distributed coordination architecture for multi-robot formation control. *Robotics and Autonomous Systems*, 56(4):324–333, 2008.
- [251] Anh Duc Dang, Hung Manh La, Thang Nguyen, and Joachim Horn. Formation control for autonomous robots with collision and obstacle avoidance using a rotational and repulsive force–based approach. *International Journal of Advanced Robotic Systems*, 16(3):1729881419847897, 2019.
- [252] Kanin Piemngam, Itthisek Nilkhamhang, and Pished Bunnun. A virtual spring damper method for formation control of the multi omni-directional robots in cooperative transportation. In *2019 11th International Conference on Information Technology and Electrical Engineering (ICITEE)*, pages 1–6. IEEE, 2019.
- [253] Tsuneo Yoshikawa. Virtual truss model for characterization of internal forces for multiple finger grasps. *IEEE Transactions on Robotics and Automation*, 15(5):941–947, 1999.